NASA TECHNICAL NOTE

NASA TN D-5098

c. 1

NASA TN D-5098

TECH LIBRARY KAFB, NM
0131789

LOAN COPY: RETURN TO
AFWL (WLIL-2)
KIRTLAND AFB, N MEX

EFFECT OF PLUG AND SHROUD GEOMETRY VARIABLES ON PLUG-NOZZLE PERFORMANCE AT TRANSONIC SPEEDS

by Bobby L. Berrier

Langley Research Center
Langley Station, Hampton, Va.

NATIONAL AERONAUTICS AND SPACE ADMINISTRATION • WASHINGTON, D. C. • MARCH 1969

TECH LIBRARY KAFB, NM

0131789

EFFECT OF PLUG AND SHROUD GEOMETRY VARIABLES ON PLUG-NOZZLE PERFORMANCE AT TRANSONIC SPEEDS

By Bobby L. Berrier

Langley Research Center
Langley Station, Hampton, Va.

NATIONAL AERONAUTICS AND SPACE ADMINISTRATION

For sale by the Clearinghouse for Federal Scientific and Technical Information
Springfield, Virginia 22151 – CFSTI price $3.00

EFFECT OF PLUG AND SHROUD GEOMETRY VARIABLES ON PLUG-NOZZLE PERFORMANCE AT TRANSONIC SPEEDS*

By Bobby L. Berrier
Langley Research Center

SUMMARY

An investigation of the effect of plug and shroud geometry variables on the performance characteristics of a basic 15° cone plug nozzle has been made in a transonic wind tunnel. Geometry variables were plug truncation (0, 30, 72.5, and 100 percent of full length from annular throat), shroud boattail angle (8°, 20°, and 30°), and truncated plug base shape (flat and semitoroidal). All nozzle configurations were designed to operate at a jet total-pressure ratio of 16.5. The ratio of annular throat area to maximum cross-sectional area was 0.25. The wind-tunnel Mach number was varied from 0 to 1.30. The jet total-pressure ratio was varied from 1.0 to approximately 8.0 depending on the external airstream Mach number. Model angle of attack was 0° for all tests. A comparison of experimental plug pressures and theoretical plug pressures obtained by the method of characteristics is made.

The performance of the 15° cone plug nozzle was shown to be higher than the performance of a comparable isentropic plug nozzle. The results also show that plug truncation decreases cone-plug-nozzle performance although the 15° cone plug was truncated 30 percent with a loss of generally less than 1 percent. The 72.5- and 100-percent-truncated plug-nozzle configurations show severe losses in nozzle performance. Increasing boattail angle generally decreased cone-plug-nozzle performance except for the 100-percent-truncated plug-nozzle configurations.

INTRODUCTION

As a result of relatively low lift-drag ratio and high net specific fuel consumption, airplanes which operate in the supersonic speed range require exhaust nozzles which operate at near optimum efficiency in the supersonic cruise condition. The payload of an airplane cruising at Mach 2.2, for example, is decreased by about 8 percent for a

---

*The basic information presented herein was included in a thesis offered in partial fulfillment of the requirements for the degree of Master of Science, North Carolina State University, Raleigh, North Carolina, May 1968.

loss of 1 percent in nozzle efficiency. (See ref. 1.) In addition, high nozzle efficiency is desirable for acceleration through the transonic speed range where airplane drag is high and during the cruise and loiter conditions at subsonic speeds.

The wide range of flight speed and jet total-pressure ratio (i.e., the ratio of jet-exhaust total pressure to external stream static pressure) required for supersonic airplanes thus creates a serious problem in nozzle development for such airplanes. The simple convergent-divergent nozzles with fixed geometry give high nozzle efficiency when operating at the design pressure ratio. However, a decrease or increase of jet total-pressure ratio from the design jet total-pressure ratio causes a rather large loss in nozzle efficiency due to overexpansion or underexpansion losses. Further, at forward speeds, the airplane nozzle system incurs an additional loss due to pressure drag on the boattail surfaces. Overexpansion and underexpansion losses may be eliminated by providing variable nozzle geometry through mechanical means. This solution leads, however, to a complex design with fabrication difficulties, an increase in weight, and an increase in boattail pressure drag at low jet total-pressure ratios.

Hence, lightweight exhaust nozzles that can provide high nozzle performance levels over a wide range of operating pressure ratios are needed. One promising nozzle type is the plug nozzle for which the outer boundary of the exhaust stream continually adjusts to ambient or free-stream pressure.

The objective of this investigation was to determine the effects of plug and shroud geometry variables on the performance of a 15° cone plug nozzle operating at off-design jet total-pressure ratios in the subsonic and transonic speed regimes. Geometry variables were plug truncation (0, 30, 72.5, and 100 percent of full length from annular throat), shroud boattail angle (8°, 20°, and 30°), and truncated plug base shape (flat and semitoroidal). In this investigation, only plug nozzles with all exhaust flow expansion occurring external to the nozzle shroud were considered.

Theoretical pressure distributions on the plug surface, as calculated by the method of characteristics, are compared with experimental pressure distributions at an external airstream Mach number of 0 and for various values of jet total-pressure ratio.

The experimental investigation was conducted in the Langley 16-foot transonic tunnel at static conditions and at Mach numbers of 0.50 to 1.30 at an angle of attack of 0°. The jet total-pressure ratio was varied from 1.0 (jet off) to about 8.0, depending on the Mach number. The nozzles were designed to operate at a jet total-pressure ratio of 16.5. The jet exhaust was simulated by the decomposition products of 90-percent-concentration hydrogen peroxide which had a specific-heat ratio of 1.266 at a temperature of 1013° K.

SYMBOLS

A cross-sectional area, meters^2

$C_{D,\beta}$ boattail pressure drag coefficient $\sum_{x=0}^{b} -C_p \frac{A_l}{A_{max}}$

where $b = -1.113d_{max}$ for afterbody A

$b = -0.550d_{max}$ for afterbody B

$b = -0.343d_{max}$ for afterbody C

C_F thrust coefficient, $\frac{F}{q_\infty A_{max}}$

$C_{F,i}$ ideal thrust coefficient, $\frac{F_i}{q_\infty A_{max}}$; for static conditions, $\frac{F_i}{p_\infty A_{max}}$

$C_{(F-D)}$ thrust-minus-drag coefficient, $\frac{F - D}{q_\infty A_{max}}$; for static conditions, $\frac{F - D}{p_\infty A_{max}}$

$C_{F,plug}$ plug thrust coefficient, $\sum_{x/l_1=0}^{1.0} \frac{C_p A_l}{A_{max}}$

$C_{f,\beta}$ skin-friction drag coefficient on nozzle boattail, $\frac{\text{Boattail skin-friction drag}}{q_\infty A_{max}}$

$C_{f,cyl}$ skin-friction drag coefficient on cylindrical part of afterbody, $\frac{\text{Cylinder skin-friction drag}}{q_\infty A_{max}}$

C_p pressure coefficient, $\frac{p_l - p_\infty}{q_\infty}$; for static conditions, $\frac{p_l - p_\infty}{p_\infty}$

D boattail pressure drag and skin-friction drag, $\left(C_{D,\beta} + C_{f,\beta}\right)q_\infty A_{max}$, newtons

d	diameter, meters
F	jet thrust, newtons
l	general length or reference length of plug from shroud lip, positive downstream, meters
l_1	length of plug from throat to plug tip, 19.51 centimeters
Δl_1	amount of plug length cut off, meters
M	free-stream Mach number
M_e	jet-exit exhaust Mach number for fully expanded flow
m	measured mass flow rate, kilograms/second
p	static pressure, newtons/meter^2
p_t	total pressure, newtons/meter^2
q	dynamic pressure, newtons/meter^2
R	gas constant, joules/(kilogram)(degree Kelvin)
r	radius, meters
r_1	radius on plug base to pressure orifice location, meters
r_2, r_3	radius defining semitoroidal-base plug geometry, meters
T	temperature, degrees Kelvin
x	axial coordinate from shroud lip, positive downstream, meters
x_1	axial coordinate from shroud attachment point $\left(x/d_{max} = -0.7\right)$, positive downstream, meters
x_2	axial coordinate from plug attachment point, meters

y	radial coordinate, meters
β	external boattail lip angle, degrees
γ	ratio of specific heats
δ	internal boattail angle, degrees
θ	flow deflection angle, degrees
μ	Mach angle, $\sin \mu = \frac{1}{M}$, degrees
ϕ	radial angle of nozzle, degrees

Subscripts:

a	afterbody
b	base region
bal	balance reading
e	nozzle exit
i	internal or ideal
j	jet flow
l	local
max	maximum
s	condition at surface
t	stagnation
β	boattail
∞	free stream

Superscript:

* nozzle throat

A bar over a symbol indicates an average condition.

EXPERIMENTAL ARRANGEMENT

Tunnel

The experimental investigation was conducted in the Langley 16-foot transonic tunnel. The facility is a single-return, atmospheric tunnel with air exchange for cooling and has a continuously variable speed range from a Mach number of 0.20 to 1.30. The average Reynolds number per meter varies from 9.71×10^6 at a Mach number of 0.50 to 12.6×10^6 at a Mach number of 1.30. Additional information about the facility is given in references 2 and 3.

Model and Support System

The exhaust stream of a turbojet engine was simulated by a hydrogen peroxide monopropellant rocket system similar to the jet simulator described in reference 4. A sketch illustrating the major components of the jet simulator is given in figure 1.

The strut-supported, turbojet-engine simulator model used in this investigation is illustrated in the sketch in figure 2, and a photograph of the model installed in the test section is shown as figure 3. The model consisted of a conical forebody, a cylindrical section of 15.24-cm diameter, and an afterbody-plug combination consisting of a cylindrical section, a boattail, and a cone plug. The afterbody-plug combinations were detachable at the 104.39-cm station to facilitate configuration changes. All external surfaces downstream of this station were attached to the thrust balance. All the plug-nozzle configurations investigated were designed, by using the specific-heat ratio for the exhaust gases ($\gamma = 1.266$), for a jet total-pressure ratio of 16.5 $\left(M_e = 2.46\right)$. A streamline is assumed to be parallel to the axis of symmetry and to be issuing from the boattail lip at design conditions. The ratio of throat critical area to maximum cross-sectional area was designed to represent a nonaugmentation condition (no afterburning).

Eleven configurations were investigated by interchanging different shrouds and plugs on the basic nacelle model. A list of these configurations and their basic geometric parameters is given in table I. Three shrouds and six plugs were used and these are shown in the photographs in figure 4. Sketches giving dimensions and pressure-orifice locations on the shrouds and plugs are presented in figure 5.

The configuration designation has been coded as follows:

(1) The first character, a number, indicates the boattail angle in degrees.

(2) The second character, a letter, indicates the type of base used on the plug as follows:

R	no base
F	flat base
S	semitoroidal base

(3) The third character, a number, indicates the amount of plug truncation in percent of full-length cut off. The 72.5-percent truncation is rounded to 73 percent.

Figure 6 presents photographs of several of the configurations investigated.

Instrumentation

The gross thrust minus drag of the nozzle system was measured by a one-component, strain-gage thrust balance shown in figure 1. Static pressure was measured on the plug and afterbody surfaces at the locations shown in figure 5 by use of electronic pressure transducers. In addition, four total-pressure probes, as shown in figure 2, were used to measure the jet total pressure. Jet total temperature was measured at the location shown in figure 2 by a chromel-alumel thermocouple. Two turbine-type electronic flowmeters located in the liquid hydrogen peroxide supply line were used to obtain liquid hydrogen peroxide mass flow. The electrical signals of all instruments were recorded by an automatic magnetic tape-recording system.

Tests

All configurations were investigated at static conditions ($M = 0$) and at free-stream Mach numbers from 0.50 to 1.30. However, some data were lost due to bad pressure orifices and excessive zero shifts of the thrust balance measurement. The angle of attack was held at a constant value of 0° during the entire investigation. The ratio of jet total pressure to free-stream static pressure was varied from 1.0 (jet off) to about 8.0.

DATA ANALYSIS

The data, recorded as electrical signals on magnetic tape, were used to compute standard force and pressure coefficients with an electronic computer. Pressure coefficients were referenced to free-stream dynamic pressure for Mach numbers greater

than 0 and to ambient pressure for static conditions (M = 0). All force coefficients were referenced to the maximum cross-sectional area of the model and free-stream dynamic pressure or ambient pressure.

Approximately 15 frames of data were taken over a time period of about 0.75 second for each data point, and the average value was used for computations. Pressure forces on the boattail and cone plug were obtained by assigning to each pressure orifice an incremental area projected on a plane normal to the model axis and by numerically integrating the incremental forces. Model support interference is small for this support system and hence no correction for strut interference was made for this investigation. (See refs. 5 and 6.)

The thrust balance measured the sum of the following axial forces: total momentum flux at the nozzle throat, plug pressure forces, external aerodynamic drag of the afterbody aft of station 104.39 cm, some internal tare pressure area forces in the nacelle, and friction forces. Thrust-minus-drag force for the nozzle was obtained by the use of the following equation:

$$F - D = F_{bal} + \left(p_i - p_\infty\right)A_{max} + \left(C_{f,cyl}\right)q_\infty A_{max} \tag{1}$$

The calculated skin-friction drag on the cylindrical portion of the shroud was not charged to the total drag of the nozzle system because the cylindrical portion of the shroud is not regarded as a part of the nozzle system.

To obtain internal performance, which includes total momentum flux at the nozzle throat plus plug forces, the following equation was used.

$$F = (F - D) + \left(C_{D,\beta}\right)q_\infty A_{max} + \left(C_{f,\beta}\right)q_\infty A_{max} \tag{2}$$

For comparative purposes, the forces obtained by using equations (1) and (2) were nondimensionalized by dividing by the optimum isentropic thrust F_i. This thrust is given by the equation

$$F_i = m\sqrt{2R\frac{\gamma}{\gamma - 1}T_{t,j}\left[1 - \left(\frac{p_\infty}{p_{t,j}}\right)^{\frac{\gamma-1}{\gamma}}\right]} \tag{3}$$

and obtained by assuming low chamber fluid velocity and isentropic nozzle flow so that chamber temperature is equal to the stagnation temperature. Also, complete isentropic expansion of the exhaust flow is assumed so that p_e equals p_∞. Since jet total-pressure ratio and jet stagnation temperature are dependent on the efficiency of the

silver-screen catalyst bed used in the H_2O_2 simulator, an average straight-line fairing of optimum isentropic thrust data from tunnel runs for all configurations was used to eliminate data scatter due to catalyst bed decay and error in throat areas. The maximum deviation from this average line was approximately 4 percent; however, the majority of the data points were much closer to the average fairing.

RESULTS AND DISCUSSION

Afterbody Pressure Distributions

Figure 7 presents the jet-off pressure distributions on the external surface of the three afterbodies for various Mach numbers. Pressure coefficients are shown for several configurations at the three radial rows of pressure orifices on each shroud (0°, 90°, and 180°). Several configurations are shown for the 8° and 20° boattail shrouds to indicate the effect of plug geometry on the jet-off pressure distributions.

The good agreement of the pressure coefficients measured on the three radial rows of orifices on each afterbody indicates a symmetrical flow field around the model and also indicates that model support interference effects were small. Although no specific conclusion can be made about the effect of plug geometry on afterbody pressure distributions from the data shown; the effect of plug geometry on the level of the pressure distributions is generally small or nonexistent, as might be expected. The pressure distributions shown in figure 7(a) for configuration 8-R-0 were obtained with a shroud different from that used to obtain the pressure distributions for configurations 8-F-73 and 8-S-73. Due to warpage, the 8° boattail shroud was rebuilt early in the investigation and it is thought that small differences in rebuilding the second shroud produced the shift in the pressure-distribution levels shown in figure 7(a). Configuration 8-R-0 was the only configuration investigated with the original 8° boattail shroud.

The small dip in the pressure distribution on the cylindrical portion of the 20° boattail shroud as shown in figure 7(b) at supersonic Mach numbers was probably caused by some misalinement of the shroud at the point of attachment to the model $\left(x/d_{max} = -0.7\right)$.

All three shrouds exhibit the abrupt decrease in pressure over the initial boattail curvature characteristic of the external flow expansion around a corner or radius. Since disturbances can be propagated upstream through the boundary layer for shorter distances at high speeds than at low speeds, the decrease in pressure on the boattail is more abrupt at supersonic speeds than at subsonic speeds. Pressure recovery is observed over most of the boattail length of the 8° and 20° boattail shrouds whereas external flow separation occurred on the 30° boattail shroud as shown in figure 7(c). After separation, the boattail pressures remained essentially constant.

Figure 8 shows the jet-on pressure distribution on the external surface of the three afterbodies for various Mach numbers and jet total-pressure ratios. Since the pressures measured around the afterbodies at 0°, 90°, and 180° locations agreed closely at the same longitudinal locations as shown in figure 7, the pressure coefficients are presented as averages in figure 8. The abrupt decrease in pressure over the external boattails and the external flow separation on the 30° boattail shroud shown for the jet-off pressure distributions of figure 7 are also exhibited for the jet-on pressure distributions. These pressure distributions are typical for boattail bodies. (See refs. 5 and 7.)

Boattail pressures on all three shrouds decreased with an initial increase of jet total-pressure ratio. However, when jet total-pressure ratio is increased to higher values, the boattail pressures increased with increasing jet total pressure. The boattail pressure decreasing and then increasing with increasing jet total-pressure ratio was reported in reference 5 and is caused by the jet plume initially aspirating the boattail and base region at low jet total-pressure ratios and then expanding into the free-stream flow at higher jet total-pressure ratios, thus reducing the aspiration effects. Positive boattail pressure coefficients, and hence beneficial thrust terms, are obtained on the 8° boattail shroud at the higher values of jet total-pressure ratio whereas the pressure coefficients generally remained negative on the 20° and 30° boattail shrouds.

Boattail Drag

Boattail pressure drag, obtained by integrating the pressures over the axially projected boattail area, is presented in coefficient form in figures 9 and 10. The variation of jet-off boattail drag coefficient with Mach number for the three shrouds investigated is shown in figure 9 for several configurations. The results of reference 8 indicate some model interference from the bow shock wave reflected from the tunnel wall in the region $1.05 < M < 1.13$. However, no interference from the bow shock wave is apparent for the data presented. A decrease of jet-off boattail pressure drag is observed for the 8° boattail shroud at $M = 1.00$. This decrease of drag is probably caused by some tunnel wall interference associated with the model nose-cone—cylinder juncture expansion field. This effect at $M = 1.00$ was observed in the Langley 16-foot transonic tunnel and reported in reference 8 for a model 152.4 cm in length and 15.24 cm in diameter.

The three shrouds investigated have approximately the same projected boattail area and hence the jet-off drag is only a function of the expansion of the external flow around the boattail. For subsonic Mach numbers, the 8° boattail shroud exhibits the lowest pressure drag level, as might be expected, since the external flow is required to expand through a larger angle and to lower pressure levels for the 20° and 30° boattail shrouds. However, from $M = 0.90$ to $M = 1.30$, the lowest drag level is exhibited by the 30° boattail shroud. This low drag level is caused by separation of the external flow on the

30° boattail at these speeds, which prevents complete expansion around the boattail and avoids the attendant low pressures and high drag. The 8° boattail shroud exhibits approximately the same jet-off pressure drag level at Mach numbers above 1.1 as the 30° boattail shroud.

Considering the entire Mach number range of the investigation, the 8° boattail shroud generally exhibits the lowest jet-off boattail drag level whereas the 20° boattail shroud exhibits the highest boattail drag level. The amount of plug truncation and the plug base shape have little or no effect on the jet-off boattail drag levels.

The effects of jet operation on boattail drag are shown in figure 10. Truncation of the cone plug up to 72.5 percent of full length had little or no effect on the jet-on boattail drag of the 8° boattail shroud. However, the 20° boattail shroud exhibits an increase in jet-on boattail drag when the cone plug was truncated from 72.5 to 100 percent of full length and a semitoroidal base was installed. Only one plug configuration was investigated with the 30° boattail and no conclusion can be made concerning the effect of plug geometry on the drag of this shroud.

Jet operation initially increases boattail pressure drag on all three shrouds investigated. All three shrouds also show some decrease of boattail drag in the high range of jet total-pressure ratios. The amount of drag decrease is dependent on boattail angle. Jet operation becomes favorable (i.e., the boattail drag at some jet total-pressure ratio is less than the jet-off value of boattail drag) on the 8° boattail shroud for jet total-pressure ratios larger than approximately 3.5 at all test Mach numbers. Jet operation is detrimental on the 20° boattail shroud throughout the range of jet total-pressure ratios for subsonic Mach numbers with the possible exception of the highest jet total-pressure ratio. At supersonic speeds, operation of the jet again has a favorable effect on the boattail drag of the 20° boattail shroud at the higher jet total-pressure ratios. Jet operation had a detrimental effect on the boattail drag of the 30° boattail shroud for all Mach numbers and jet total-pressure ratios of the investigation.

A hysteresis effect is exhibited by the boattail drag of the 20° boattail shroud as jet total-pressure ratio is varied continuously (i.e., being increased and then decreased) at sonic and low supersonic speeds. This effect was reported in reference 5 and is attributed to the axial movement of the external flow separation point on the boattail. Although separation also occurred on the 30° boattail shroud, the separation point apparently remained at a fixed point and hence no hysteresis effect is present on the 30° boattail shroud.

Cone-Plug Static-Pressure Distributions

Figures 11, 12, and 13 present the cone-plug static-pressure distributions for several Mach numbers, jet total-pressure ratios, and configurations. These plug pressure distributions are typical of plug-type nozzles. (See refs. 5, 9, and 10.) The series of increases and decreases of local plug static pressure along the length of the cone plug, particularly at low Mach numbers, are a result of alternating regions of expansion and compression of the jet flow starting with a Prandtl-Meyer expansion fan originating at the boattail lip. The average plug base pressure, for truncated plugs, is shown in figures 11, 12, and 13 as a solid symbol and generally has approximately the same level as the last pressure measured on the plug surface.

The theoretical pressure distributions calculated by the method of characteristics as given in the appendix are compared with the experimental pressure distributions in figures 14, 15, and 16. The theoretical jet-plume shapes are also given in these figures for each case computed. The location of shock waves or regions of strong compression predicted by the method of characteristics is indicated in the figures by a dash-dot-dash line in the jet flow field.

At regions of strong compression, deviation from the experimental distributions occurs because the flow becomes nonisentropic. Two such regions of strong compression were predicted for configuration 8-R-0, as shown in figure 14(a). The location of the second strong compression may not be accurate because of errors introduced by the first region of strong compression. For the 72.5-percent-truncated plugs and jet total-pressure ratios greater than 2.77 (fig. 16), the region of strong compression did not occur on the plug surface and hence the pressure distributions for these cases are not affected by nonisentropic flow. An abrupt deviation of the jet boundary at the intersection of the boundary with a region of strong compression is also predicted by theory.

Theory deviates from experimental data in the initial expansion region because no iterations were performed and the initial line was assumed to be straight. However, the main cause of disagreement between theory and experiment in this region is probably the assumption of flow direction perpendicular to the geometric throat which was inclined 15° from the normal (perpendicular to plug surface). From this assumption and two-dimensional calculations, the flow deflection angle at the initial line $\left(M_j = 1.02\right)$ did not vary much from the value of -15° at the geometric throat. In actuality, for the 8° boattail shroud configurations, the flow deflection angle varied from -8° at the shroud lip to -15° at the plug surface along the geometric throat and also should have approximately the same variation along the $M_j = 1.02$ initial line. A comparison of the pressure distributions for the 20° boattail shroud configuration (15° internal boattail angle) shown in figure 16(b) and the 8° boattail shroud configurations (fig. 16(a)) shows better agreement between theory and experiment for the 20° boattail shroud configuration. For the 20°

boattail shroud configuration, the actual flow deflection angle approaches the theoretical flow deflection distribution of -15° along the geometric throat.

After the initial decrease in the theoretical static-pressure distribution, a discontinuity of slope occurs and the static pressure on the plug tends to remain fairly constant. This region of the jet flow field consists of intersecting compression and expansion characteristic lines of opposite families whereas the preceding region of the jet flow field consisted almost entirely of expansion characteristic lines.

The next region of the jet flow field consists almost entirely of compression characteristic lines and accounts for the abrupt increase in the static-pressure distribution shown by experiment and predicted by theory. In this region, strong compressions or shock waves begin forming and the theoretical pressures calculated downstream of this point have errors introduced by nonisentropic flow.

Cone-Plug Base Pressure Distributions

The radial distributions of cone-plug base pressure are presented in figures 17 to 21 for several Mach numbers, jet total-pressure ratios, and configurations. The pressures obtained on the base of the 100-percent-truncated plug configurations were symmetrical about the plug center line. Therefore, the pressures at corresponding radial stations about the plug center line were averaged and are shown as such in figures 20 and 21. Some asymmetric pressure distributions were obtained on the longer plugs and hence the base pressures measured on each side of the plug center line are shown for those configurations utilizing the 30-percent and 72.5-percent-truncated plugs.

Plug base pressure generally decreased at most conditions with increasing plug truncation. For example, a comparison of data for the 8° boattail flat-base configurations shown in figures 17, 18, and 20 shows the plug base region to be generally pressurized for the 30-percent-truncated plug, pressurized or aspirated depending on jet total-pressure ratio for the 72.5-percent-truncated plug, and aspirated by the jet flow for the 100-percent-truncated plug.

Variation of the shroud boattail angle and, hence, of the internal lip angle had little or no effect on the 72.5-percent-truncated plug base pressures. However, a large effect of internal angle was observed for the 100-percent-truncated plug configurations at subsonic Mach numbers. This effect might be expected since large boattail and internal shroud angles direct both the external flow stream and the jet flow stream toward the plug base and thus tend to pressurize this region. Figure 21 indicates that the increase in base pressure of the 30° boattail over that of the 20° boattail is not as large as the increase in base pressure of the 20° boattail shroud over that of the 8° boattail. Boattail and internal shroud angle had little or no effect on plug base pressures at Mach numbers greater than 0.90.

The plug base shape had little effect on the plug base pressures, and no consistent trend is evident from the data shown. However, a comparison of the flat- and semitoroidal-base configurations indicates that the semitoroidal base established and maintained a vortex-ring type of flow more readily than the flat plug base. A vortex-ring type of flow is indicated by pressure peaks near the center and at the edges of the plug base. (See ref. 11.) Little or no vortex flow was established on the 30-percent-truncated plug. Vortex flow was maintained on the 72.5-percent-truncated plug at most test conditions. Vortex flow was indicated on the 100-percent-truncated, flat-base plug only at the higher values of jet total-pressure ratio and on the 100-percent-truncated, semitoroidal-base plug at all conditions at subsonic Mach numbers and at the higher values of jet total-pressure ratio at transonic and supersonic Mach numbers.

The plug base pressures measured on plug configurations having some plug surface for jet flow expansion (truncation < 100 percent) increased or decreased depending on the value of jet total-pressure ratio. The plug base pressures are hence a function of the jet flow expansion along the length of the plug, as might be expected from the average plug base pressures shown in figures 12 and 13. The plug base pressures on the 100-percent-truncated plug configurations generally decreased with increasing jet total-pressure ratio. One exception is configuration 30-S-100 at subsonic speeds for which increasing jet total-pressure ratio increased the plug base pressures.

Plug Thrust

Figure 22 presents the variation of plug thrust coefficient with jet total-pressure ratio and Mach number for all configurations investigated. Plug thrust was obtained by integrating the pressures over the axially projected plug area downstream of the annular throat.

Nozzle Performance Characteristics

Basic data.- Figure 23 presents the variation of the static thrust-minus-drag coefficient and the ideal static thrust coefficient with jet total-pressure ratio for all configurations tested.

Thrust-minus-drag coefficients, thrust coefficients, and ideal thrust coefficients for all configurations are shown in figure 24 as functions of jet total-pressure ratio for the Mach numbers and jet total pressures of the investigation. It should be noted that the ideal-thrust-coefficient line is a faired, or averaged, line obtained from the ideal thrust data for all configurations investigated. The same faired line of the ideal thrust coefficient is used as the common reference for each configuration in figure 24. This procedure merely averages any scatter in mass-flow and jet-temperature measurements.

Thrust coefficient was not obtained on several configurations due to loss of pressure data from which external drag is obtained.

Thrust-minus-drag ratio.- The variation of thrust-minus-drag ratio with jet total-pressure ratio and amount of plug truncation is shown in figures 25 to 28 for several Mach numbers and configurations. The thrust-minus-drag ratio generally increases with increasing jet total-pressure ratio. Due to the increase of external drag with increasing Mach number, thrust-minus-drag ratio generally decreases with Mach number for the 0- and 30-percent-truncated plugs. Similar trends are shown for isentropic plug nozzles in reference 5. The variation of thrust-minus-drag performance with Mach number for the 72.5- and 100-percent-truncated plugs was more erratic at transonic and low supersonic Mach numbers due to the larger effect of the plug base pressures. Thrust-minus-drag ratio decreases with increasing amount of plug truncation. Large losses were incurred by all configurations utilizing the 72.5- and 100-percent-truncated plugs. However, the thrust-minus-drag performance of the 30-percent-truncated plug configuration approaches the thrust-minus-drag performance of the full-length plug except at Mach numbers of 1.00 and 1.15. Generally, the 15° cone plug may be truncated as much as 30 percent of full length with little or no loss of thrust-minus-drag performance; further increase in plug truncation, however, incurs large losses on the nozzle thrust-minus-drag performance.

Figures 29 to 32 present the effect of jet total-pressure ratio and boattail angle on thrust-minus-drag ratio for several Mach numbers and configurations. At Mach numbers up to 1.15, and, in particular, for the 72.5-percent-truncated plug configurations, the 8° boattail configurations generally exhibit the best thrust-minus-drag performance characteristics due to lower external drag. The 100-percent-truncated, semitoroidal-base plug configurations shown in figure 32 exhibit trends which may be expected from examination of the plug base pressures shown in figure 21. The 20° boattail gives the best performance due to higher plug base pressures at Mach numbers of 0 and 0.50. At Mach numbers above 0.50, the 8° boattail configuration generally gives the highest performance. The 30° boattail configuration is not shown at Mach numbers of 0.50 and 0.70 due to excessive zero shifts of the data.

The effect of jet total-pressure ratio and plug base shape on thrust-minus-drag ratio is shown in figures 33 to 36 for several Mach numbers and configurations. A definite trend of thrust-minus-drag ratio with plug base shape is not evident from the data shown. The semitoroidal base configurations usually exhibit the highest thrust-minus-drag performance for 72.5-percent-truncated configurations and the lowest performance for the 100-percent-truncated configurations. However, several exceptions are shown in figures 33 to 36. The effect of plug base shape appears to be dependent to a large extent on the flow field and the formation of the ring-type vortices; hence, determination of the

best plug base shape should be made in the flow field of the airplane model in which the nozzle system is to be installed. This requirement is not uncommon for some nozzle systems. (See ref. 12.)

Thrust ratio.- The variation of thrust ratio or internal performance with jet total-pressure ratio is shown in figures 37 to 43 for several Mach numbers and configurations. The internal performance was obtained by adding the external pressure drag and skin friction to the thrust-minus-drag values. Values of thrust ratio are not shown for several configurations because pressure instrumentation was lost and hence no external pressure drag could be calculated. Thrust ratio is also not given at a Mach number of 0 since, in this case, external pressure drag and skin friction equal zero and thrust ratio is equivalent to the thrust-minus-drag ratio shown previously.

Internal performance generally follows the same trends as thrust-minus-drag performance since the thrust term constitutes the major terms in both parameters. Internal performance is generally at a higher level, however, since external drag is not charged to the internal performance. Internal performance generally increases with increasing jet total-pressure ratio and decreases with increasing Mach number.

The effect of plug truncation on internal performance is shown in figures 37 and 38. Increasing the amount of plug truncation decreases the internal performance due to adverse pressures on the plug bases. The loss incurred by cutting the plug 30 percent of full length is small except at Mach numbers of 1.00 and 1.15.

Figures 39 to 41 present the effect of boattail angle on internal performance. Internal performance decreased with increasing boattail angle with the exception of the 72.5-percent-truncated flat-base plug configurations shown in figures 39(c) at $M = 1.20$ and $M = 1.30$.

The effect of plug base shape on internal performance is presented in figures 42 and 43. Internal performance for the 100-percent-truncated configurations is not given because of the loss of pressure instrumentation for these configurations. The semitoroidal-base plug configurations exhibit the highest internal performance at Mach numbers up to 1.15 for the configurations shown. No conclusion can be made on the effect of plug base shape at Mach numbers of 1.20 and 1.30.

Performance at a scheduled pressure ratio.- Figure 44 presents a jet total-pressure-ratio schedule for a typical turbojet engine for external Mach numbers from 0.5 to 1.3. (See refs. 5 and 13.) The variation of nozzle internal performance and thrust-minus-drag ratio with Mach number for this typical turbojet total-pressure-ratio schedule is presented in figure 45.

Figure 45(a) compares the performance of the full-length 15° cone plug with that of an isentropic plug reported in reference 5 and of a 10° cone plug nozzle reported in

reference 13. The isentropic plug nozzle was designed for the same conditions as the cone plug nozzle of the present investigation. The isentropic plug incurred much greater losses than the full-length cone plug. The low performance level of the isentropic plug is a result of high drag on the steep boattail angle required for isentropic plugs and of a large amount of overexpansion losses on the plug as evidenced by the low level of thrust ratio or internal performance in figure 45(a) (see ref. 1). The full-length 15° cone plug shows a higher level of performance as theorized in reference 10 because of the low value of boattail angle and less overexpansion penalty on the plug due to the external flow. The performance of the 15° cone plug nozzle is somewhat below the performance of the 10° ($\beta = 5.5^{\circ}$) cone plug nozzle, except for Mach numbers slightly greater than 1.2, because of higher boattail drag and overexpansion losses on the plug. The nozzle performance of all configurations decreases with increasing subsonic Mach numbers and increases with increasing supersonic Mach numbers except for the 10° cone plug nozzle.

The effect of plug truncation on nozzle performance for the typical turbojet total-pressure-ratio schedule is shown in figure 45(b) as a function of Mach number. Thrust ratio is not shown for configuration 8-F-100 because pressure instrumentation was lost for this configuration. Both thrust-minus-drag ratio and thrust ratio decrease with increasing amount of plug truncation. However, the loss incurred by truncating the plug 30 percent of full length is generally less than 1 percent except in the transonic speed range. The 72.5- and 100-percent-truncated plugs exhibit large losses as a result of plug truncation.

Figure 45(c) presents the effect of boattail angle on nozzle performance for the typical turbojet total-pressure-ratio schedule. As a result of pressure instrumentation loss, thrust ratio is not shown for configuration 8-S-100, Cone plug nozzle performance generally decreases with increasing boattail angle. For Mach numbers less than 0.80, the 8° and 20° boattail shroud configurations exhibit approximately the same thrust-minus-drag performance. This is a result of the increase of plug base pressures shown in figure 21 for these Mach numbers due to increasing boattail angle. The resultant increase in plug thrust is greater than the increase of boattail drag due to a larger boattail angle, and the thrust-minus-drag performance of configuration 20-S-100 is hence increased to a level favorably comparable to that of configuration 8-S-100 (generally less than 1 percent loss). In the transonic speed range where the drag rise occurs, the increase in boattail drag becomes larger than the increase in plug thrust due to increased boattail angle, and thrust-minus-drag performance decreases with increasing boattail angle. Mixed results were obtained at a Mach number of 1.30.

CONCLUSIONS

An investigation of the effect of plug truncation, boattail angle, and plug base shape on the performance of a 15° cone plug nozzle has been made. The nozzle was designed for a jet total-pressure ratio of 16.5 and a ratio of nozzle throat area to maximum cross-sectional area of 0.25. The investigation was conducted at Mach numbers from 0 to 1.30, jet total-pressure ratios from 1.0 to approximately 8.0, and an angle of attack of 0°. The following trends are indicated:

1. Nozzle performance loss as a result of a 30-percent truncation of the 15° cone plug was generally less than 1 percent whereas further truncation incurred large losses in nozzle performance.

2. Cone-plug-nozzle performance generally decreased with increasing boattail angle.

3. Although plug base shape had a large effect on nozzle performance, a definite trend of cone-plug-nozzle performance with plug base shape is not evident from this investigation.

4. The 15° cone-plug-nozzle performance was higher than that of a comparable isentropic plug nozzle but somewhat lower than a 10° cone plug nozzle.

5. Beneficial jet interference was observed at high values of jet total-pressure ratio on the 8° boattail shroud pressure; the boattail pressures remained negative at all conditions for the 20° and 30° boattail shrouds.

6. Plug base pressures appear to be a strong function of the jet flow expansion process along the length of the plugs which were not fully truncated. For the 100-percent-truncated plugs, base pressure was a strong function of boattail angle at subsonic Mach numbers; base pressure and plug thrust increased with increasing boattail angle in the subsonic speed range.

Langley Research Center,
National Aeronautics and Space Administration,
Langley Station, Hampton, Va., December 17, 1968,
720-03-00-01-23.

APPENDIX

METHOD-OF-CHARACTERISTICS COMPUTER PROGRAM FOR CONE PLUG NOZZLES

The method of characteristics (refs. 14, 15, 16, 17, and 18) was used to calculate the theoretical plug pressure distributions presented in the body of this report. The computer program used for this purpose is reproduced as written in Fortran IV language. Also given are the program assumptions, restrictions, and inputs. Figure 46 is a sketch showing the initial and boundary conditions assumed for the cone plug nozzle.

Assumptions

The following conditions were assumed for the computer program used:

1. Axisymmetric, supersonic, nonviscous, irrotational, isentropic, steady flow
2. Perfect gas
3. Jet flow is parallel everywhere along the geometric throat and inclined to the X-axis at an angle equal to the plug half-angle
4. Two-dimensional flow at corner of shroud and along throat
5. Throat or initial starting line is assumed downstream of geometric throat so that the initial Mach number is greater than 1.00
6. No iterations

Restrictions

Use of the computer program is restricted by the following conditions:

1. Cone plug nozzles only; no plug curvature
2. No internal jet expansion
3. No external flow

Initial and Boundary Conditions

A straight line inclined with the geometric throat at a Prandtl-Meyer turning angle corresponding to $M_j = 1.02$ was used for the initial conditions. This line is a characteristic line of the $(\theta - \mu)$ family. Additional initial conditions were needed to define the shape of the characteristic line of the $(\theta + \mu)$ family. These initial conditions were obtained by generating a two-dimensional Prandtl-Meyer expansion fan from the boattail

lip. At the intersections of the characteristic line of the $(\theta + \mu)$ family and the Prandtl-Meyer waves, the flow properties were calculated from two-dimensional isentropic relations and, thus, the initial conditions along the $(\theta + \mu)$ characteristic line were defined. The flow deflection angle θ was allowed to vary lineally along the initial $(\theta - \mu)$ characteristic line from the value (approximately 15°) calculated at the first intersection of the $(\theta - \mu)$ and $(\theta + \mu)$ characteristic lines to the value on the plug surface (15°).

Boundary conditions that must be met occur at the plug surface (flow deflection angle) and at the outer boundary at the exhaust stream (pressure). The ratio of specific heats used for all calculations was 1.266 (for products of decomposition of 90-percent hydrogen peroxide) and 1.0133×10^5 N/m^2 was used for atmospheric pressure.

Characteristic Nets

Figure 47 shows two examples of the characteristic net obtained by the method of characteristics for no external flow. The characteristic net and the initial and boundary conditions are presented in figure 47(a) for configuration 8-F-73 at a jet total-pressure ratio of 4.07. Figure 47(b) presents the characteristic net calculated for configuration 8-F-30 at a jet total-pressure ratio of 4.03. The transition from isentropic flow to non-isentropic flow is clearly predicted by the theory for this case. A shock wave is formed when compression waves of the same family converge and intersect. (See ref. 15.) The shaded region shown in figure 47(b) is a region of strong compression of the jet flow as predicted by theory and which may form a shock wave in the actual flow case. These characteristic lines converged and intersected for several cases with lower jet total-pressure ratios calculated for this investigation and might for this case if a smaller mesh size were selected. An abrupt change of jet boundary at the strong compression or shock is also predicted.

Input Cards

The inputs required for the program are as follows. All input is in floating-point form with six decimal places unless otherwise specified.

Card	Columns	Contents
1	1 to 5	Π = an integer If $\Pi = 0$, Mach number along initial $(\theta + \mu)$ characteristic line (see fig. 46) read in as data If $\Pi = 1$, Mach number calculated by program

APPENDIX

Card	Columns	Contents
1	6 to 14	GAMMA = ratio of specific heats
	15 to 23	PR = jet total-pressure ratio $p_{t,j}/p_\infty$
	24 to 32	YO = radius of plug base, inches
	33 to 41	FL = length of plug from shroud lip to plug base, inches
	42 to 50	YS = radius of shroud at throat, inches
	51 to 59	PGANRD = plug half-angle, radians
	60 to 64	ICONFG = an integer signifying configuration number
	65 to 69	ICASE = an integer signifying case number
2	1 to 9	THRTAN = throat angle (negative), radians
3	1 to 9	XMACH(1,1) = Mach number along initial $(\theta - \mu)$ characteristic line (see fig. 46)
	10 to 18	XMACH(2,1) = Mach number as above
	19 to 27	XMACH(3,1) = Mach number as above
	28 to 36	XMACH(4,1) = Mach number as above, located on plug surface
4	1 to 10	TL = length of reference plug from shroud lip to plug tip, inches
	11 to 20	PLUGAN = plug half-angle, degrees
	21 to 30	TRUN = percent of plug truncation
	31 to 40	BETA = shroud internal angle, degrees
	41 to 50	XS = axial coordinate of shroud lip (generally taken as zero), inches
4(a) optional (Card 1 must have II = 0)		
	1 to 9	XMACH(1,1) = Mach number along initial $(\theta + \mu)$ characteristic line (see fig. 46)
	10 to 18	XMACH(1,2) = Mach number as above

Card	Columns	Contents
4(a) optional (Card 1 must have II = 0)		
	19 to 27	XMACH(1,3) = Mach number as above
	28 to 36	XMACH(1,4) = Mach number as above
	37 to 45	XMACH(1,5) = Mach number as above
	46 to 54	XMACH(1,6) = Mach number as above, located on jet boundary

Computer Program

The method-of-characteristics computer program was written and debugged by use of the English gravitational system of units. The program as written in Fortran IV language is as follows:

```
C
C        METHOD OF CHARACTERISTICS - MAIN DECK
C          CONE PLUG NOZZLE PRESSURE DISTRIBUTION
C
C     SUPERSONIC, STEADY, ISENTROPIC, INVISCID, AXI-SYMMETRIC FLOW
C
C     INITIAL LINE AND IDENTIFICATION SECTION
C
C
      DIMENSION X(48,45),Y(48,45),THETA(48,45),XMU(48,45),W(48,45),XL(48
     1,45),XM(48,45),XRATIO(48,45),XMACH(48,45),PRATIO(48,45),C(7,7),D(7
     2,7)
C
C
C      SUBPROGRAM TO DETERMINE INITIAL VALUES FOR MAIN DECK
C         SUBDECK TO METHOD OF CHARACTERISTICS
C
C
      READ(5,1)II,GAMMA,PR,YO,FL,YS,PGANRD,ICONFG,ICASE,THRTAN
    1 FORMAT(I5,6F9.6,2I5/F9.6)
      READ(5,920)(XMACH(I,1),I=1,4)
  920 FORMAT(4F9.6)
      READ(5,4)TL,PLUGAN,TRUN,BETA,XS
    4 FORMAT(5F10.6)
      DPRATO = PR
      IONFIG = ICONFG
      IF(II.EQ.1)GO TO 902
      READ(5,903)(XMACH(1,J),J=1,6)
  903 FORMAT(6F9.6)
      IF(II.EQ.0)GO TO 904
  902 XMACH(1,6)=SQRT(2./(GAMMA-1.)*(PR**((GAMMA-1.)/GAMMA)-1.))
      XMACH(1,1)=1.00
      DELTA=(XMACH(1,6)-1.0)/5.0
      DO 905 J=2,6
```

```
      K=J-1
  905 XMACH(1,J)=XMACH(1,K)+DELTA
      XMACH(1,1)=1.02
  904 A=-.5*SQRT((GAMMA+1.)/(GAMMA-1.))
      B= (1.-GAMMA**2)/2.
      DO 906 J=1,6
      C(1,J)=XMACH(1,J)**2/(1.+(GAMMA-1.)/2.*XMACH(1,J)**2)
      D(1,J)=1./C(1,J)
      THETA(1,J)=A*(ARSIN(B*C(1,J)+GAMMA)-1.570788)-.5*(ARSIN(GAMMA-2.*D
     1(1,J))+1.570788)+THRTAN
      XMU(1,J)=ARSIN(1./XMACH(1,J))
  906 W(1,J)=SQRT((GAMMA+1.)/2.*XMACH(1,J)**2/(1.+(GAMMA-1.)/2.*XMACH(1,
     1J)**2))
      XX=(YO+FL*TAN(PGANRD)-YS)/(TAN(PGANRD)+TAN(THETA(1,1)-XMU(1,1)))
      YY=YO+(FL-XX)*TAN(PGANRD)
      ALPHA=-(THETA(1,1)-XMU(1,1)+1.570788)
      H=(YS-YY)/COS(ALPHA)
      DELH=H/4.
      DO 907 I=1,4
      XI=I
      DELY=XI*DELH*COS(ALPHA)
      Y(I,1)=YS-DELY
  907 X(I,1)=-DELY*TAN(ALPHA)
      DO 8 J=2,6
      K=J-1
      X(1,J)=(Y(1,K)-YS-X(1,K)*TAN(THETA(1,K)+XMU(1,K)))/(TAN(THETA(1,J)
     1-XMU(1,J))-TAN(THETA(1,K)+XMU(1,K)))
    8 Y(1,J)=Y(1,K)+(X(1,J)-X(1,K))*TAN(THETA(1,K)+XMU(1,K))
      DELTHE=(-PGANRD-THETA(1,1))/3.
      DO 909 I=2,4
      J=I-1
      THETA(I,1)=THETA(J,1)+DELTHE
      W(I,1)=SQRT((GAMMA+1.)/2.*XMACH(I,1)**2/(1.+(GAMMA-1.)/2.*XMACH(I,
     11)**2))
  909 XMU(I,1)=ARSIN(1./XMACH(I,1))
```

```
      PRINT 910,GAMMA,PR,FL,PGANRD,THRTAN,ICONFG,ICASE
  910 FORMAT(1H1,2X,5HGAMMA,5X,10HPRES RATIO,4X,6HPLUG L,3X,12HPLUG ANG
     1RAD,12H TH0 ANG RAD,3X,6HCONFIG,7X,4HCASE//5F12.7,I7,I12)
      PRINT 911,(X(1,J),Y(1,J),W(1,J),THETA(1,J),XMU(1,J),J=1,6)
  911 FORMAT(1H0,14HINITIAL I LINE///2X,1HI,4X,1HJ,7X,1HX,11X,1HY,11X,1H
     1W,9X,5HTHETA,9X,2HMU//2X,1H1,4X,1H1,2X,5F12.7/2X,1H1,4X1H2,2X,5F12
     2.7/2X,1H1,4X,1H3,2X,5F12.7/2X,1H1,4X,1H4,2X,5F12.7/2X,1H1,4X,1H5,2
     3X,5F12.7/2X,1H1,4X,1H6,2X,5F12.7)
      PRINT 912,(X(I,1),Y(I,1),W(I,1),THETA(I,1),XMU(I,1),I=1,4)
  912 FORMAT(1H0,14HINITIAL J LINE///2X,1HI,4X,1HJ,7X,1HX,11X,1HY,11X,1H
     1W,9X,5HTHETA,9X,2HMU//2X,1H1,4X,1H1,2X,5F12.7/2X,1H2,4X1H1,2X,5F12
     2.7/2X,1H3,4X,1H1,2X,5F12.7/2X,1H4,4X,1H1,2X,5F12.7)
      PRINT 5,IONFIG,DPRATO,TRUN,BETA,GAMMA,PLUGAN,FL,TL
    5 FORMAT(1H1,7X,64HCALCULATION OF LOCAL PLUG PRESSURES BY METHOD OF
     1CHARACTERISTICS////2X,6HCONFIG,2X,10HPRES RATIO,3X,4HTRUN,6X,4HBET
     2A,6X,5HGAMMA,2X,10HPLUG ANGLE,2X,7HFRACT L,3X,5HREF L//3X,I4,4X,F6
     3.2,5X,F6.2,4X,F6.2,4X,F6.3,3X,F6.2,4X,F7.3,3X,F7.3)
      PRINT 10,(X(I,1),Y(I,1),THETA(I,1),XMU(I,1),W(I,1),I=1,4)
   10 FORMAT(1H0,22X,35HINITIAL J LINE CONDITIONS I=1,2,3,4//5X,1HX,10X,
     11HY,6X,9HTHETA RAD,2X,9HM ANG RAD,5X,4HV/A*//(5F11.7))
C
C
C     CALCULATION OF PRANDTL-MEYER EXPANSION WAVES AND PLUG INTERSECTION
C
C     PRANDTL-MEYER WAVE SECTION
C
C
      DO 100 J=2,6
      L = J-1
      N = J+3
      M = N-1
      DO 200 I=2,M
      K = I-1
      X(I,J)=(Y(I,L)-Y(K,J)+X(K,J)*TAN(THETA(K,J)-XMU(K,J))-X(I,L)*TAN(T
     1HETA(I,L)+XMU(I,L)))/(TAN(THETA(K,J)-XMU(K,J))-TAN(THETA(I,L)+XMU(
```

```
   2I,L)))
    Y(I,J)=Y(I,L)+(X(I,J)-X(I,L))*TAN(THETA(I,L)+XMU(I,L))
    XL(I,L)=SIN(XMU(I,L))*SIN(THETA(I,L))*TAN(XMU(I,L))/COS(THETA(I,L)
   1+XMU(I,L))
    XM(K,J)=SIN(XMU(K,J))*SIN(THETA(K,J))*TAN(XMU(K,J))/COS(THETA(K,J)
   1-XMU(K,J))
    XTHETA=(1.-W(I,L)/W(K,J)-(THETA(I,L)-THETA(K,J))*TAN(XMU(K,J))+(X(
   1I,J)-X(K,J))*XM(K,J)/Y(K,J)-XL(I,L)/Y(I,L)*(X(I,J)-X(I,L))*W(I,L)/
   2W(K,J))/(TAN(XMU(K,J))+W(I,L)/W(K,J)*TAN(XMU(I,L)))
    THETA(I,J)=THETA(I,L)+XTHETA
    DW=W(I,L)*(TAN(XMU(I,L))*XTHETA+XL(I,L)/Y(I,L)*(X(I,J)-X(I,L)))
    W(I,J)=W(I,L)+DW
    XMACH(I,J)=W(I,J)*(1./(SQRT((GAMMA+1.)/2.-((GAMMA-1.)/2.)*W(I,J)**
   12)))
    XII = II
    IF((XMACH(I,J).LT.1.00).AND.(XII.GT.2.5))GO TO 611
    IF(XMACH(I,J).LT. 1.00) GO TO 506
    ARG=1.0/(SQRT(XMACH(I,J)**2-1.0))
    IF(XMACH(I,J).GE. 1.00) GO TO 200
506 PRINT 507
507 FORMAT(1H1////37H MACH NUMBER IS SUBSONIC -- NOT VALID///49H READ
   1MACH(1,1) THROUGH MACH(1,6) INTO SUBPROGRAM//74H MACH(1,1) = 1.02,
   2 MACH(1,2)= 1.09 AND MACH(1,6) DEPENDS ON PRESSURE RATIO//65H MACH
   3INE IS RECALCULATING USING THESE VALUES AND ONES SHOWN BELOW)
    XMACH(1,6)=SQRT(2./(GAMMA-1.)*(PR**((GAMMA-1.)/GAMMA)-1.))
    XMACH(1,1)=1.02
    XMACH(1,2)=1.09
    BBZ=(XMACH(1,6)-XMACH(1,2))/4.0
    XMACH(1,3)=XMACH(1,2)+BBZ
    XMACH(1,4)=XMACH(1,3)+BBZ
    XMACH(1,5)=XMACH(1,4)+BBZ
    PRINT 601,(XMACH(1,K),K=1,6)
601 FORMAT(1H ///60H MACH(1,1) MACH(1,2) MACH(1,3) MACH(1,4) MACH(1,5)
   1 MACH(1,6)//6F10.6)
    II=3
```

```
      GO TO 904
  611 PRINT 612
  612 FORMAT(1H ///81H MACHINE HAS RECOMPUTED USING MACH VALUES ABOVE AN
     1D MACH NUMBER IS STILL SUBSONIC//10H NOT VALID///55H MACHINE IS TI
     2RED AND IS THEREFORE CONCLUDING OPERATION)
      GO TO 11
  200 XMU(I,J)=ATAN(ARG)
      PRINT 2,(X(I,J),Y(I,J),THETA(I,J),XMU(I,J),W(I,J),I=1,M)
    2 FORMAT(1H0,12X,54HCALCULATED FIELD POINTS FOR ONE J LINE AND I=1,2
     1,3...M//5X,1HX,10X,1HY,6X,9HTHETA RAD,2X,9HM ANG RAD,5X,4HV/A*//(5
     2F11.7))
      PRINT 3,J,M
    3 FORMAT(1H0,4X,1HJ,8X,1HM//I6,4X,I5)
C
C     PLUG INTERSECTION OF PRANDTL-MEYER WAVES AND STATIC PRESSURES
C
      X(N,J)=(YO+X(M,J)*TAN(THETA(M,J)-XMU(M,J))+FL*TAN(PGANRD)-Y(M,J))/
     1(TAN(PGANRD)+TAN(THETA(M,J)-XMU(M,J)))
      Y(N,J)=YO+(FL-X(N,J))*TAN(PGANRD)
      THETA(N,J)=-PGANRD
      XTHETA=THETA(N,J)-THETA(M,J)
      DW=W(M,J)*(XM(M,J)/Y(M,J)*(X(N,J)-X(M,J))-TAN(XMU(M,J))*XTHETA)
      W(N,J)=W(M,J)+DW
      XMACH(N,J)=W(N,J)*(1./(SQRT((GAMMA+1.)/2.-((GAMMA-1.)/2.)*W(N,J)**
     12)))
      ARG=1.0/(SQRT(XMACH(N,J)**2-1.0))
      XMU(N,J)=ATAN(ARG)
      XRATIO(N,J)=X(N,J)/TL
      PRATIO(N,J)=(1.0-(GAMMA-1.)/(GAMMA+1.)*W(N,J)**2)**(GAMMA/(GAMMA-1
     1.))
      PRINT 7,N,J,X(N,J),Y(N,J),THETA(N,J),XMU(N,J),W(N,J),XMACH(N,J),XR
     1ATIO(N,J),PRATIO(N,J)
    7 FORMAT(1H0,23X,32HCALCULATED POINT ON PLUG SURFACE///2X,1HI,4X,1HJ
     1,7X,1HX,9X,1HY,4X,9HTHETA RAD,2X,9HM ANG RAD,3X,4HV/A*//I3,I5,F12.
     26,4F10.6///1X,10HLOCAL MACH,2X,7HX/REF L,3X,7HP/P TOT//3F10.6)
```

```
  100 CONTINUE
C
C
C     INITIAL CALCULATION ON PRESSURE BOUNDARY -- 2-DIM. SECTION
C
      X(1,7)=(Y(1,6)-YS+XS*TAN(THETA(1,6))-X(1,6)*TAN(THETA(1,6)+XMU(1,6
     1)))/(TAN(THETA(1,6))-TAN(THETA(1,6)+XMU(1,6)))
      Y(1,7)=X(1,7)*TAN(THETA(1,6))-XS*TAN(THETA(1,6))+YS
      WW=W(1,6)
      XL(1,6)=SIN(XMU(1,6))*SIN(THETA(1,6))*TAN(XMU(1,6))/COS(THETA(1,6)
     1+XMU(1,6))
      XTHETA=(WW-W(1,6))/(W(1,6)*TAN(XMU(1,6)))-XL(1,6)*(X(1,7)-X(1,6))/
     1(Y(1,6)*TAN(XMU(1,6)))
      W(1,7)=W(1,6)
      THETA(1,7)=THETA(1,6)+XTHETA
      XMU(1,7)=XMU(1,6)
      PRINT 14,X(1,7),Y(1,7),THETA(1,7),XMU(1,7),W(1,7)
   14 FORMAT(1H1,23X,34HINITIAL POINT ON PRESSURE BOUNDARY///2X,1HI,4X,1
     1HJ,7X,1HX,9X,1HY,4X,9HTHETA RAD,2X,9HM ANG RAD,3X,4HV/A*//2X,1H1,4
     2X,1H7,F12.6,4F10.6)
C
C
C     PRESSURE BOUNDARY CALCULATION SECTION
C
C
      DO 300 J=7,45
      L=J-1
      N=J+3
      M=N-1
      II=J-5
      IF(J.LE.7)GO TO 12
      II=J-6
      JJ=J-7
      X(II,J)=(Y(II,L)-Y(JJ,L)+X(JJ,L)*TAN(THETA(JJ,L))-X(II,L)*TAN(THET
     1A(II,L)+XMU(II,L)))/(TAN(THETA(JJ,L))-TAN(THETA(II,L)+XMU(II,L)))
```

```
      Y(II,J)=X(II,J)*TAN(THETA(JJ,L))-X(JJ,L)*TAN(THETA(JJ,L))+Y(JJ,L)
      XL(II,L)=SIN(XMU(II,L))*SIN(THETA(II,L))*TAN(XMU(II,L))/COS(THETA(
     1II,L)+XMU(II,L))
      W(II,J)=W(JJ,L)
      XTHETA=(W(II,J)-W(II,L))/(W(II,L)*TAN(XMU(II,L)))-XL(II,L)*(X(II,J
     1)-X(II,L))/(Y(II,L)*TAN(XMU(II,L)))
      THETA(II,J)=THETA(II,L)+XTHETA
      XMU(II,J)=XMU(JJ,L)
      PRINT 13,II,J,X(II,J),Y(II,J),THETA(II,J),XMU(.II,J),W(II,J)
   13 FORMAT(1H0,21X,37HCALCULATED POINT ON PRESSURE BOUNDARY///2X,1HI,4
     1X,1HJ,7X,1HX,9X,1HY,4X,9HTHETA RAD,2X,9HM ANG RAD,3X,4HV/A*//I3,I5
     2,F12.6,4F10.6)
C
C
C     CALCULATION OF FIELD POINTS SECTION
C
C
      II=J-5
   12 DO 400 I=II,M
      K=I-1
      X(I,J)=(Y(I,L)-Y(K,J)+X(K,J)*TAN(THETA(K,J)-XMU(K,J))-X(I,L)*TAN(T
     1HETA(I,L)+XMU(I,L)))/(TAN(THETA(K,J)-XMU(K,J))-TAN(THETA(I,L)+XMU(
     2I,L)))
      Y(I,J)=Y(I,L)+(X(I,J)-X(I,L))*TAN(THETA(I,L)+XMU(I,L))
      XL(I,L)=SIN(XMU(I,L))*SIN(THETA(I,L))*TAN(XMU(I,L))/COS(THETA(I,L)
     1+XMU(I,L))
      XM(K,J)=SIN(XMU(K,J))*SIN(THETA(K,J))*TAN(XMU(K,J))/COS(THETA(K,J)
     1-XMU(K,J))
      XTHETA=(1.-W(I,L)/W(K,J)-(THETA(I,L)-THETA(K,J))*TAN(XMU(K,J))+(X(
     1I,J)-X(K,J))*XM(K,J)/Y(K,J)-XL(I,L)/Y(I,L)*(X(I,J)-X(I,L))*W(I,L)/
     2W(K,J))/(TAN(XMU(K,J))+W(I,L)/W(K,J)*TAN(XMU(I,L)))
      THETA(I,J)=THETA(I,L)+XTHETA
      DW=W(I,L)*(TAN(XMU(I,L))*XTHETA+XL(I,L)/Y(I,L)*(X(I,J)-X(I,L)))
      W(I,J)=W(I,L)+DW
      XMACH(I,J)=W(I,J)*(1./(SQRT((GAMMA+1.)/2.-((GAMMA-1.)/2.)*W(I,J)**
```

```
     12)))
      ARG=1.0/(SQRT(XMACH(I,J)**2-1.0))
  400 XMU(I,J)=ATAN(ARG)
      PRINT 2,(X(I,J),Y(I,J),THETA(I,J),XMU(I,J),W(I,J),I=II,M)
      PRINT 9,J,II,M
    9 FORMAT(1H0,4X,1HJ,8X,2HII,8X,1HM//I6,4X,I5,4X,I5)
C
C
C     FIELD CHARACTERISTICS INTERSECTION ON PLUG SECTION
C
C
      X(N,J)=(YO+X(M,J)*TAN(THETA(M,J)-XMU(M,J))+FL*TAN(PGANRD)-Y(M,J))/
     1(TAN(PGANRD)+TAN(THETA(M,J)-XMU(M,J)))
      IF(X(N,J).GT.FL)GO TO 11
      Y(N,J)=YO+(FL-X(N,J))*TAN(PGANRD)
      THETA(N,J)=-PGANRD
      XTHETA=THETA(N,J)-THETA(M,J)
      DW=W(M,J)*(XM(M,J)/Y(M,J)*(X(N,J)-X(M,J))-TAN(XMU(M,J))*XTHETA)
      W(N,J)=W(M,J)+DW
      XMACH(N,J)=W(N,J)*(1./(SQRT((GAMMA+1.)/2.-((GAMMA-1.)/2.)*W(N,J)**
     12)))
      ARG=1.0/(SQRT(XMACH(N,J)**2-1.0))
      XMU(N,J)=ATAN(ARG)
      XRATIO(N,J)=X(N,J)/TL
      PRATIO(N,J)=(1.0-(GAMMA-1.)/(GAMMA+1.)*W(N,J)**2)**(GAMMA/(GAMMA-1
     1.))
      PRINT 7,N,J,X(N,J),Y(N,J),THETA(N,J),XMU(N,J),W(N,J),XMACH(N,J),XR
     1ATIO(.N,J),PRATIO(N,J)
  300 CONTINUE
   11 STOP
      END
```

REFERENCES

1. Reid, J.: The Effects of Base Bleed on Plug Nozzles. Tech. Rep. No. 65043, Brit. R.A.E., Feb. 1965.

2. Schaefer, William T., Jr.: Characteristics of Major Active Wind Tunnels at the Langley Research Center. NASA TM X-1130, 1965.

3. Ward, Vernon G.; Whitcomb, Charles F.; and Pearson, Merwin D.: Air-Flow and Power Characteristics of the Langley 16-Foot Transonic Tunnel With Slotted Test Section. NACA RM L52E01, 1952.

4. Runckel, Jack F.; and Swihart, John M.: A Hydrogen Peroxide Hot-Jet Simulator for Wind-Tunnel Tests of Turbojet-Exit Models. NASA MEMO 1-10-59L, 1959.

5. Berrier, Bobby L.; and Mercer, Charles E.: Off-Design Performance of Two Isentropic Plug Nozzles Designed for a Pressure Ratio of 16.5. NASA TN D-3852, 1967.

6. Norton, Harry T., Jr.; Runckel, Jack F.; and Pendergraft, Odis C., Jr.: Transonic Performance of Two Convergent-Divergent Ejector Nozzles Designed for Corrected Secondary Flows of 3 and 9.4 Percent. NASA TM X-909, 1964.

7. Henry, Beverly Z., Jr.; and Cahn, Maurice S.: Pressure Distributions Over a Series of Related Afterbody Shapes As Affected by a Propulsive Jet at Transonic Speeds. NACA RM L56K05, 1957.

8. Capone, Francis J.; and Coates, Edward M., Jr.: Determination of Boundary-Reflected-Disturbance Lengths in the Langley 16-Foot Transonic Tunnel. NASA TN D-4153, 1967.

9. Angelino, G.: Theoretical and Experimental Investigation of the Design and Performance of a Plug-Type Nozzle. Tech. Note 12, Training Center Exp. Aerodyn. (Belgium), July 1963.

10. Rabone, George R.: Low-Angle Plug Nozzle Performance Characteristics. AIAA Paper No. 66-664. June 1966.

11. Mercer, Charles E.; and Salters, Leland B., Jr.: Performance of a Plug Nozzle Having a Concave Central Base With and Without Terminal Fairings at Transonic Speeds. NASA TN D-1804, 1963.

12. Schmeer, James W.; Lauer, Rodney F., Jr.; and Berrier, Bobby L.: Performance of Blow-in-Door Ejector Nozzles Installed on a Twin-Jet Variable-Wing-Sweep Fighter Airplane Model. NASA TM X-1383, 1967.

13. Schmeer, James W.; Kirkham, Frank S.; and Salters, Leland B., Jr.: Performance Characteristics of a 10° Conical Plug Nozzle at Mach Numbers up to 1.29. NASA TM X-913, 1964.

14. Ferri, Antonio: Elements of Aerodynamics of Supersonic Flows. The Macmillan Co., 1949.

15. Liepmann, H. W.; and Lapin, Ellis: Summary of Characteristics Methods for Steady State Supersonic Flows. Rep. No. SM-13343, Douglas Aircraft Co., Inc., Mar. 3, 1949.

16. Liepmann, H. W.; and Roshko, A.: Elements of Gasdynamics. John Wiley & Sons, Inc., 1957.

17. Shapiro, Ascher H.: The Dynamics and Thermodynamics of Compressible Fluid Flow. Vol. I. Ronald Press Co., c.1953.

18. Shapiro, Ascher H.: The Dynamics and Thermodynamics of Compressible Fluid Flow. Vol. II. Ronald Press Co., c.1954.

TABLE I.- IMPORTANT GEOMETRIC PARAMETERS OF CONE-PLUG-NOZZLE CONFIGURATIONS

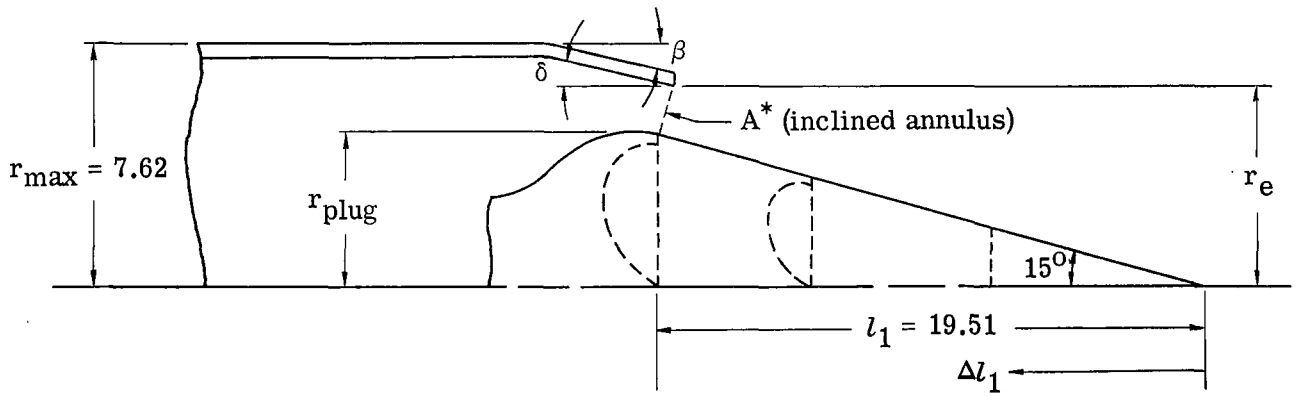

Geometric parameters								
Configuration	Plug	Shroud	d_{plug}/d_{max}	A^*/A_{max}	A_e/A^*	$\Delta l_1/l_1$	β, deg	δ, deg
8-R-0	1	A	0.70	0.25	2.94	0.000	8	8
8-F-30	2	A	.70	.25	2.94	.300	8	8
8-F-73	3	A	.70	.25	2.94	.725	8	8
20-F-73	3	B	.70	.25	2.94	.725	20	15
8-F-100	4	A	.70	.25	2.94	1.000	8	8
20-F-100	4	B	.70	.25	2.94	1.000	20	15
8-S-73	5	A	.70	.25	2.94	.725	8	8
20-S-73	5	B	.70	.25	2.94	.725	20	15
8-S-100	6	A	.70	.25	2.94	1.000	8	8
20-S-100	6	B	.70	.25	2.94	1.000	20	15
30-S-100	6	C	.70	.25	2.94	1.000	30	25

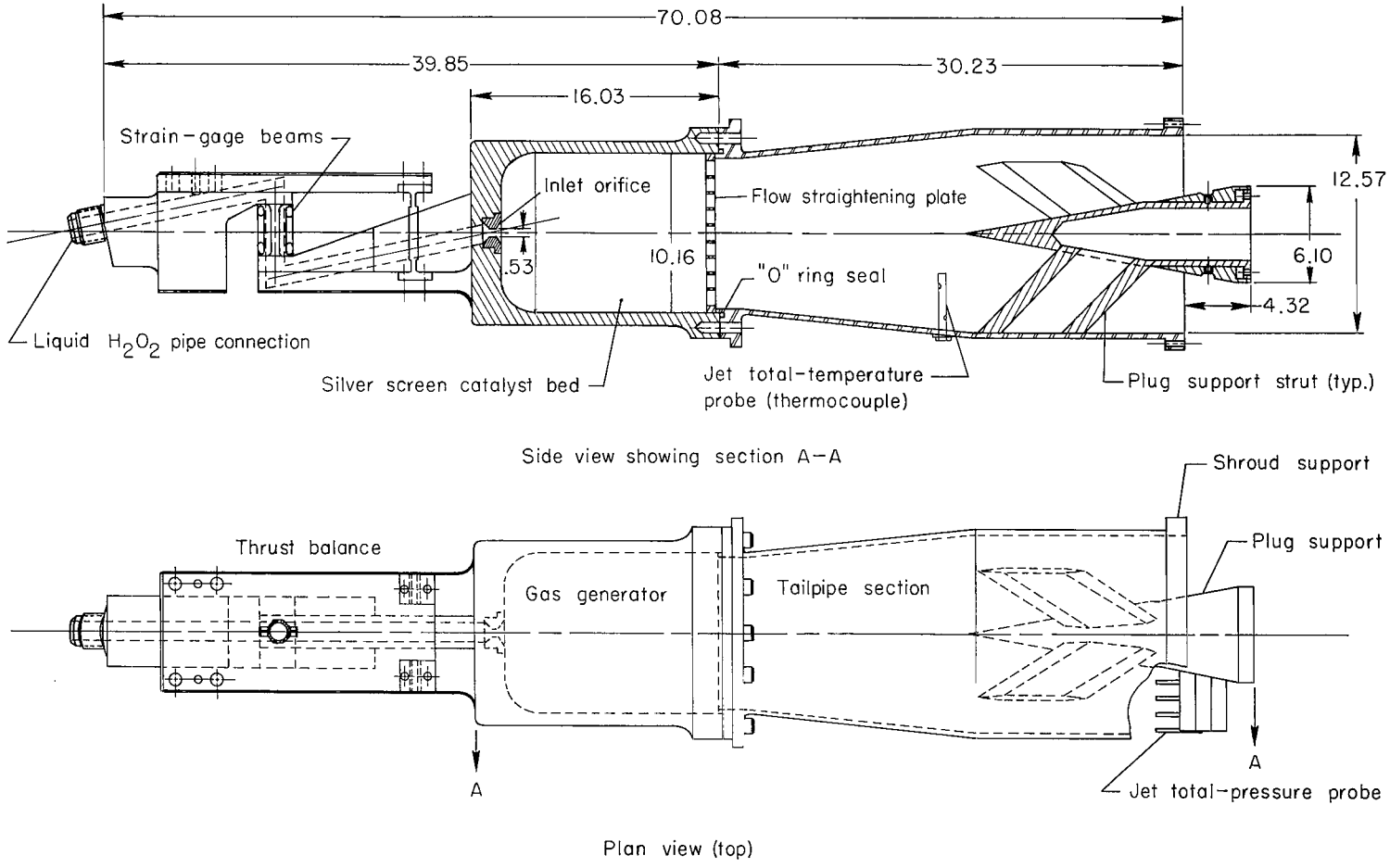

Figure 1.- Sketch of hydrogen peroxide jet simulator. All dimensions are in centimeters.

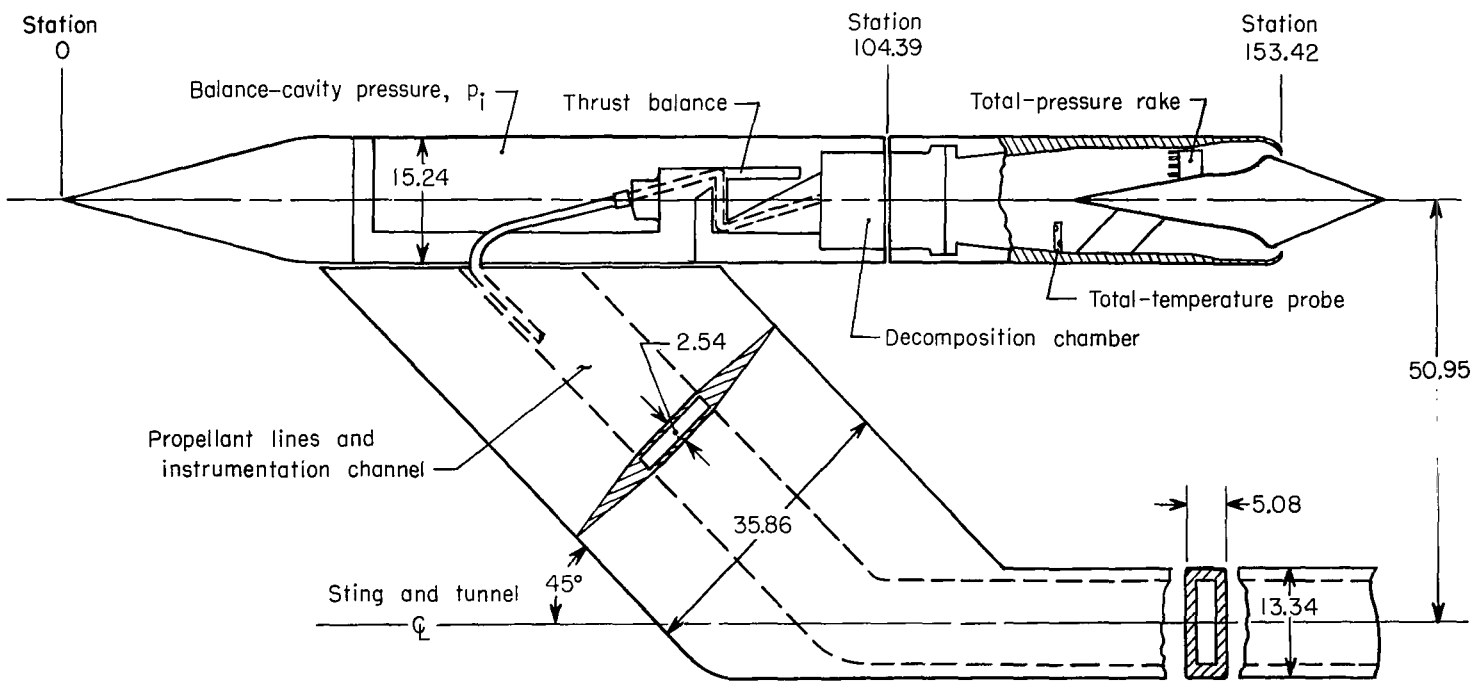

Figure 2.- Sketch of cone plug nozzle installed on pylon nacelle. All dimensions are in centimeters.

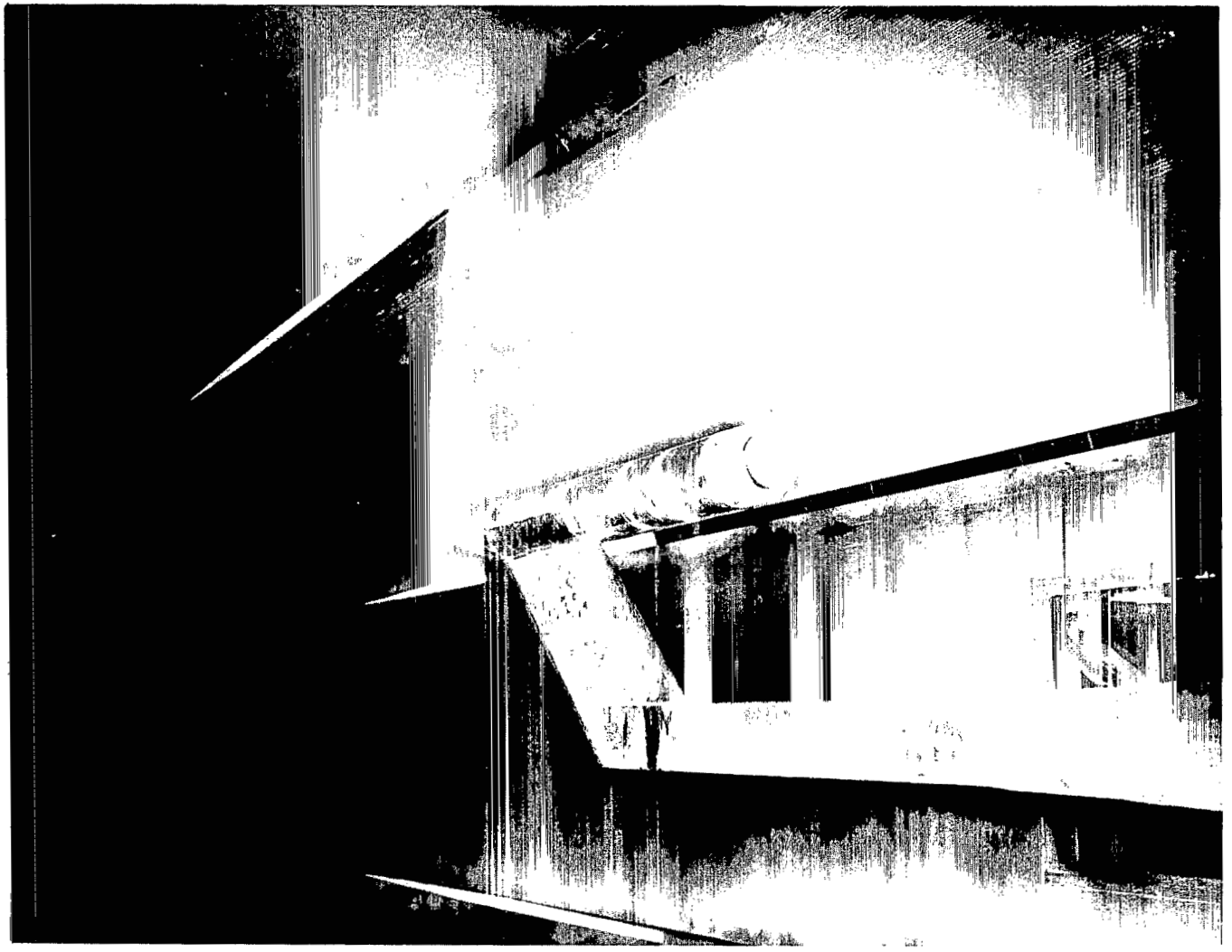

Figure 3.- Photograph of cone-plug-nozzle pylon nacelle installed in test section. L-66-4083

Shrouds

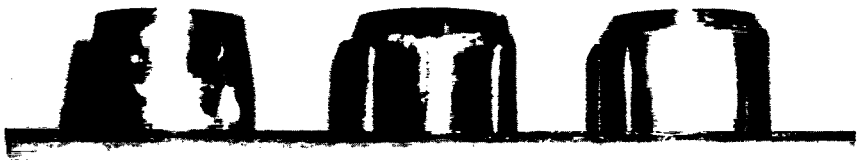

Boattail = 8° 20° 30°

Flat-base plugs

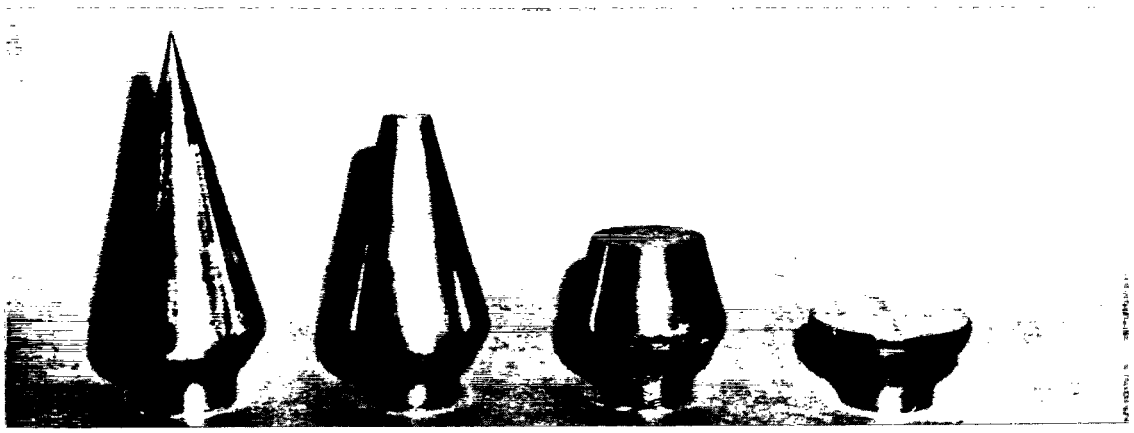

Truncation = 0% 30% 72.5% 100%

Semitoroidal-base plugs

Truncation = 72.5% 100%

Figure 4.- Photographs of cone plugs and shrouds. L-68-10,098

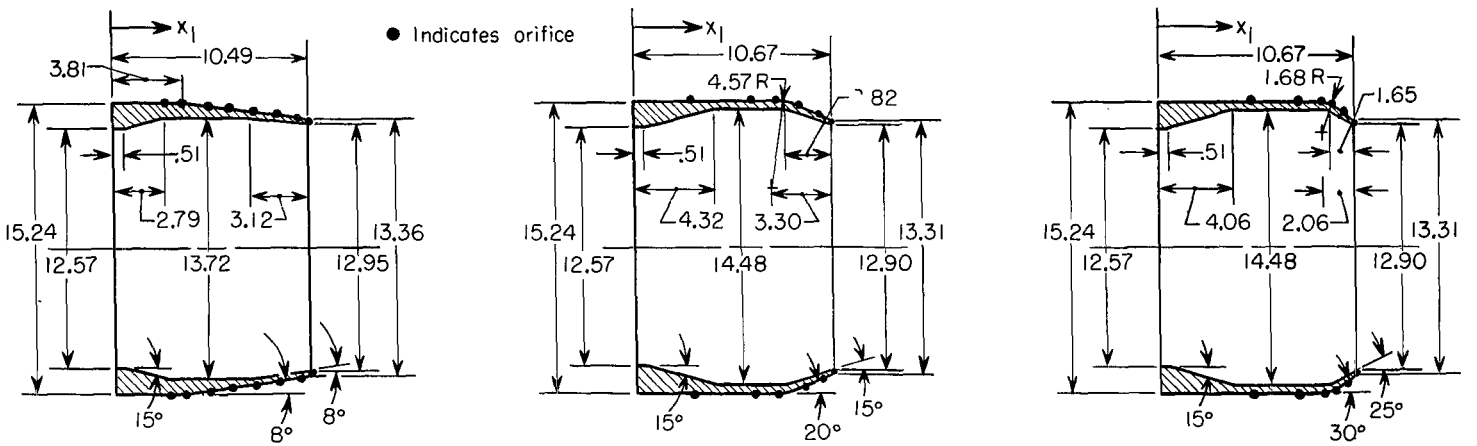

Afterbody A

Orifice locations	
x_1	Row
3.05	0, 90, and 180
3.81	0, 90, and 180
5.08	0, 90, and 180
6.35	0, 90, and 180
7.62	0, 90, and 180
8.89	0, 90, and 180
10.03	0, 90, and 180
10.49	0, 90, and 180

Afterbody B

Orifice locations	
x_1	Row
3.05	0, 90, and 180
6.35	0, 90, and 180
7.62	0, 90, and 180
8.89	0, 90, and 180
10.03	0, 90, and 180
10.67	0, 90, and 180

Afterbody C

Orifice locations	
x_1	Row
5.08	0, 90, and 180
7.62	0, 90, and 180
8.89	0, 90, and 180
9.40	0, 90, and 180
10.03	0, 90, and 180
10.67	0, 90, and 180

(a) Shrouds.

Figure 5.- Sketch of cone plugs and shrouds giving dimensions and orifice locations. All dimensions are in centimeters.

● Indicates orifice

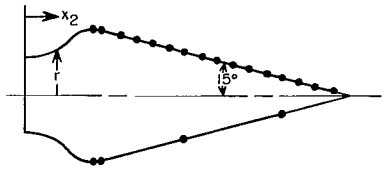

Plug 1—15° cone

Plug coordinates			
x_2	r	x_2	r
0	3.05	4.83	5.28
1.02	3.12	5.08	5.33
1.78	3.30	5.33	5.36
2.54	3.63	5.59	5.33
3.05	3.91	5.84	5.31
3.56	4.39	6.05	5.26
4.06	4.88	25.65	0
4.57	5.21		

Orifice locations			
x_2	Row	x_2	Row
5.59	22.50 and 202.50	15.24	22.50
6.05	22.50 and 202.50	16.51	22.50
7.62	22.50	17.78	22.50
8.89	22.50	19.05	22.50
10.16	22.50	20.32	22.50 and 202.50
11.43	22.50	21.59	22.50
12.70	22.50 and 202.50	22.86	22.50
13.97	22.50	24.26	22.50

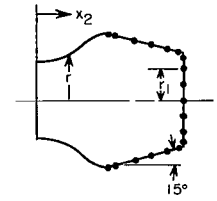

Plug 3—72.5% truncated

Plug coordinates			
x_2	r	x_2	r
0	3.05	4.83	5.28
1.02	3.12	5.08	5.33
1.78	3.30	5.33	5.36
2.54	3.63	5.59	5.33
3.05	3.91	5.84	5.31
3.56	4.39	6.05	5.26
4.06	4.88	11.43	3.81
4.57	5.21		

Orifice locations			
Surface		Base (x_2 = 11.43)	
x_2	Row	r_1	Row
5.59	22.50 and 202.50	0	Center
6.05	22.50 and 202.50	1.27	22.50 and 202.50
7.62	22.50 and 202.50	2.54	22.50 and 202.50
8.89	22.50 and 202.50	3.56	22.50 and 202.50
10.16	22.50 and 202.50		
11.25	22.50 and 202.50		

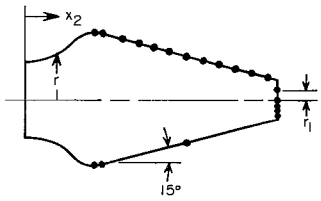

Plug 2—30% truncated

Plug coordinates			
x_2	r	x_2	r
0	3.05	4.83	5.28
1.02	3.12	5.08	5.33
1.78	3.30	5.33	5.36
2.54	3.63	5.59	5.33
3.05	3.91	5.84	5.31
3.56	4.39	6.05	5.26
4.06	4.88	19.76	1.57
4.57	5.21		

Orifice locations			
Surface		Base (x_2=19.76)	
x_2	Row	r_1	Row
5.59	22.50 and 202.50	0	Center
6.05	22.50 and 202.50	.51	202.50
7.62	22.50	.76	22.50
8.89	22.50	1.02	202.50
10.16	22.50	1.40	202.50
11.43	22.50		
12.70	22.50 and 202.50		
13.97	22.50		
15.24	22.50		
16.51	22.50		
17.78	22.50		
19.05	22.50		

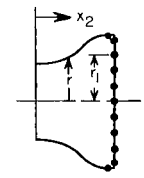

Plug 4—100% truncated

Plug coordinates			
x_2	r	x_2	r
0	3.05	4.57	5.21
1.02	3.12	4.83	5.28
1.78	3.30	5.08	5.33
2.54	3.63	5.33	5.36
3.05	3.91	5.59	5.33
3.56	4.39	5.84	5.31
4.06	4.88	6.05	5.26

Orifice locations			
Surface		Base (x_2 = 6.05)	
x_2	Row	r_1	Row
5.59	22.50, 112.50 202.50, and 292.50	0	Center
		1.27	22.50, 112.50 202.50, and 292.50
		2.54	22.50, 112.50 202.50, and 292.50
		3.81	22.50, 112.50 202.50, and 292.50
		5.08	22.50, 112.50 202.50, and 292.50

(b) Flat-base plugs.

Figure 5.- Continued.

● Indicates orifice

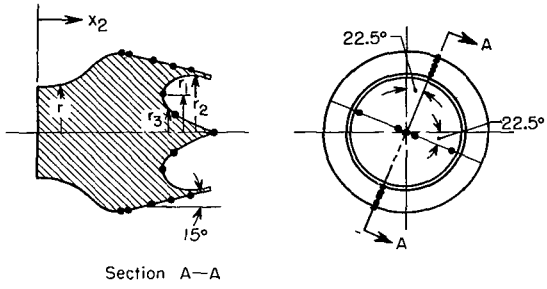

Section A—A

Plug 5—72.5% semitoroidal

Orifice locations			
Surface		Base	
x_2	Row	r_1	Row
5.58	22.50 and 202.50	0	Center
6.05	22.50 and 202.50	.64	112.50 and 292.50
7.62	22.50 and 202.50	1.27	22.50 and 202.50
8.89	22.50 and 202.50	2.54	22.50 and 202.50
10.16	22.50 and 202.50	3.56	112.50 and 292.50

Plug coordinates							
x_2	r	r_2	r_3	x_2	r	r_2	r_3
0	3.05	—	—	6.05	5.26	—	—
1.02	3.12	—	—	8.38	—	2.54	2.54
1.78	3.30	—	—	8.64	—	3.18	1.68
2.54	3.63	—	—	8.89	—	3.45	1.42
3.05	3.91	—	—	9.14	—	3.63	1.22
3.56	4.39	—	—	9.40	—	3.76	1.04
4.06	4.88	—	—	9.91	—	3.89	.76
4.57	5.21	—	—	10.41	—	3.89	.48
5.08	5.33	—	—	10.92	—	3.76	.25
5.33	5.36	—	—	11.18	—	3.71	.13
5.59	5.33	—	—	11.43	3.81	3.68	.03

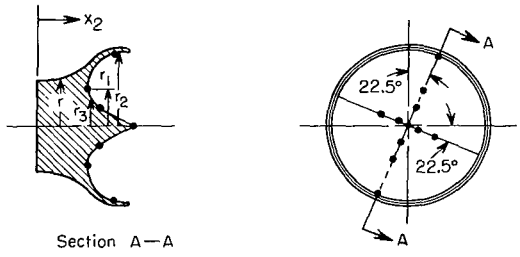

Section A—A

Plug 6—100% semitoroidal

Orifice locations
Base
r_1	Row
0	Center
.64	112.50 and 292.50
1.27	22.50 and 202.50
1.91	112.50 and 292.50
2.54	22.50 and 202.50
5.08	22.50 and 202.50

Plug coordinates							
x_2	r	r_2	r_3	x_2	r	r_2	r_3
0	3.05	—	—	4.06	4.88	4.39	1.27
1.02	3.12	—	—	4.32	5.03	4.62	1.09
1.27	3.15	—	—	4.57	5.21	4.80	.94
1.78	3.30	—	—	4.83	5.28	4.95	.81
2.29	3.51	—	—	5.08	5.33	5.08	.66
2.54	3.63	—	—	5.33	5.36	5.13	.51
2.79	3.78	—	—	5.59	5.33	5.16	.41
3.05	3.91	—	—	5.84	5.31	5.16	.28
3.30	4.14	2.67	2.67	6.05	5.26	—	—
3.56	4.39	3.66	1.75	6.10	—	5.13	.13
3.81	4.67	4.09	1.50	6.35	—	—	.03

(c) Semitoroidal-base plugs.

Figure 5.- Concluded.

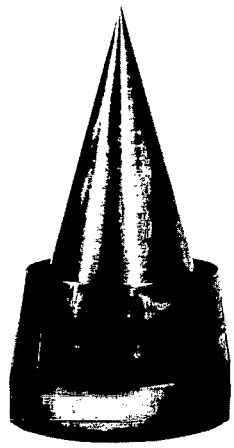

Configuration 8-R-0

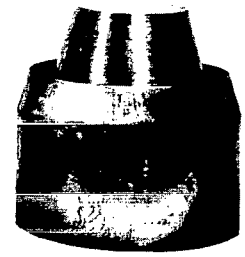

Configuration 20-F-73

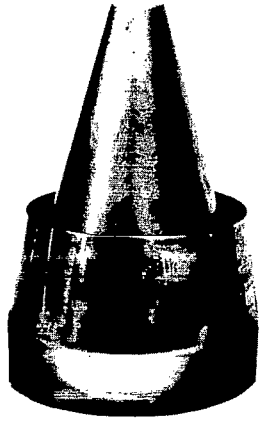

Configuration 8-F-30

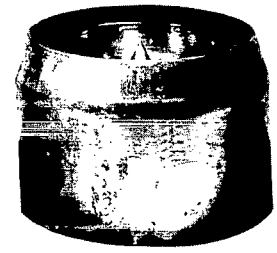

Configuration 20-S-100

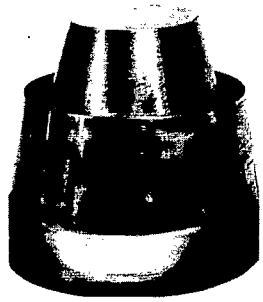

Configuration 8-F-73

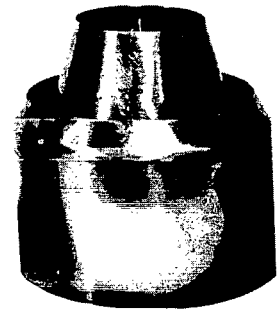

Configuration 30-S-73

Figure 6.- Photographs of several cone-plug-nozzle configurations. L-68-10,099

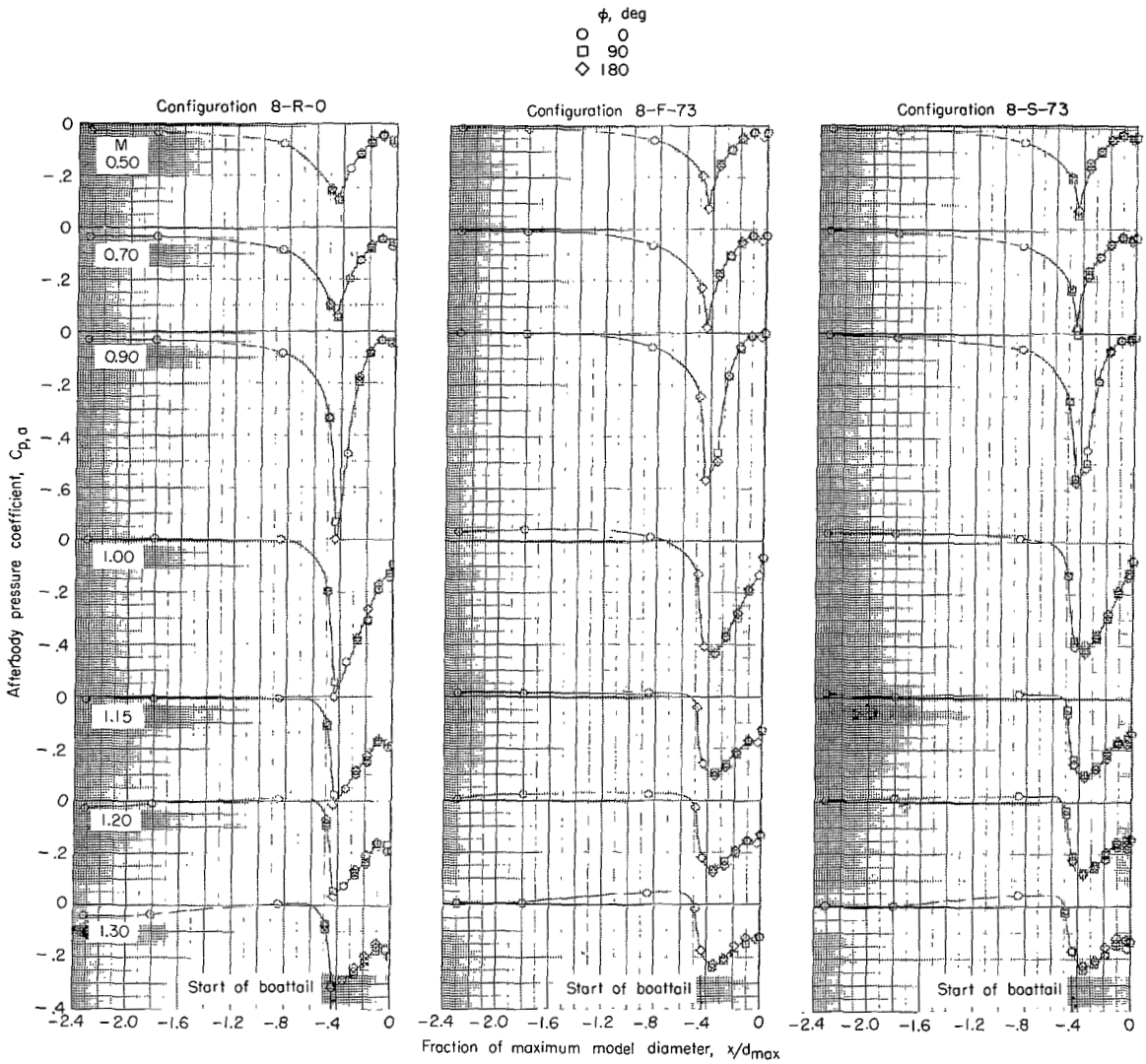

(a) $\beta = 8^0$.

Figure 7.- Effect of Mach number on external pressure distributions. Jet off.

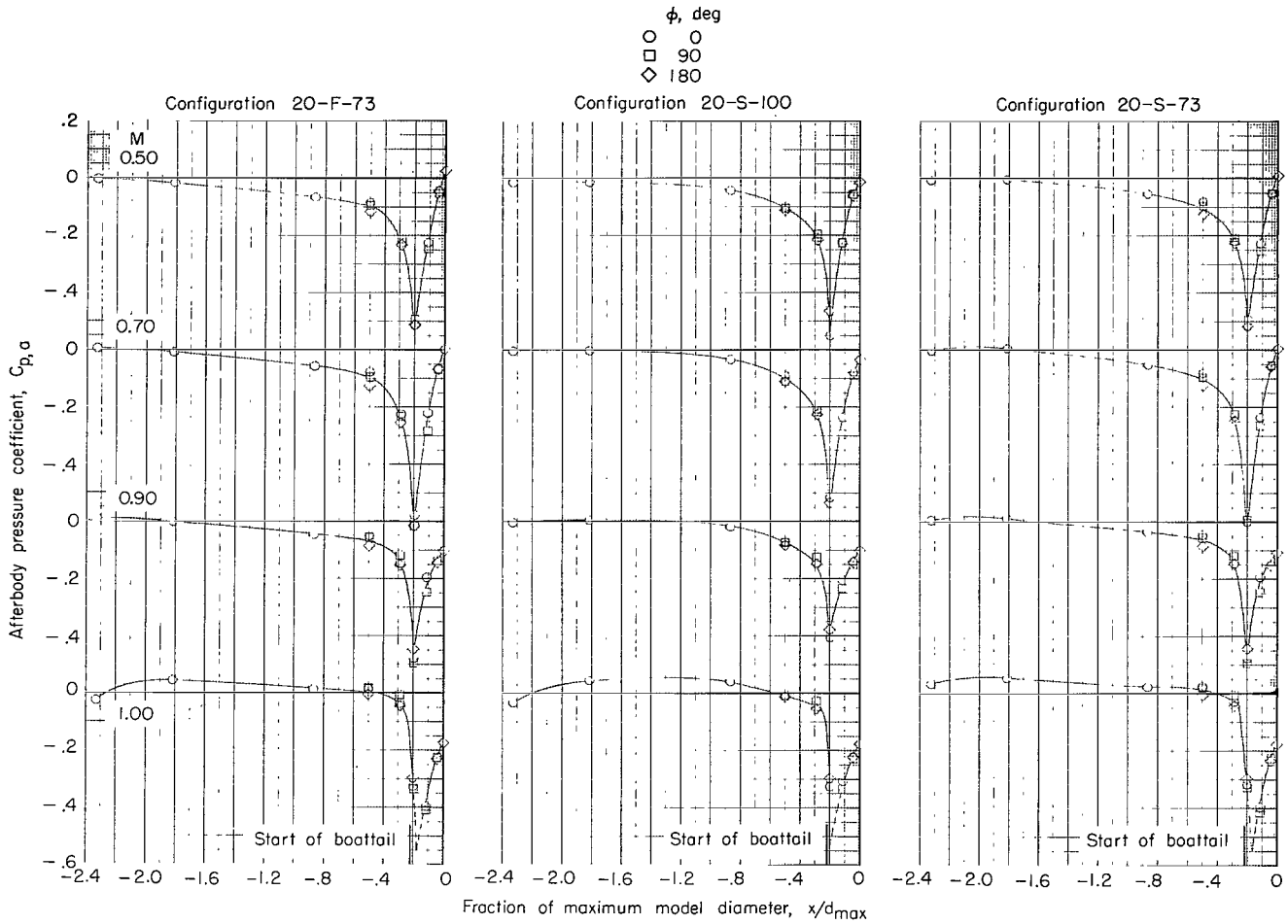

(b) $\beta = 20^0$.

Figure 7.- Continued.

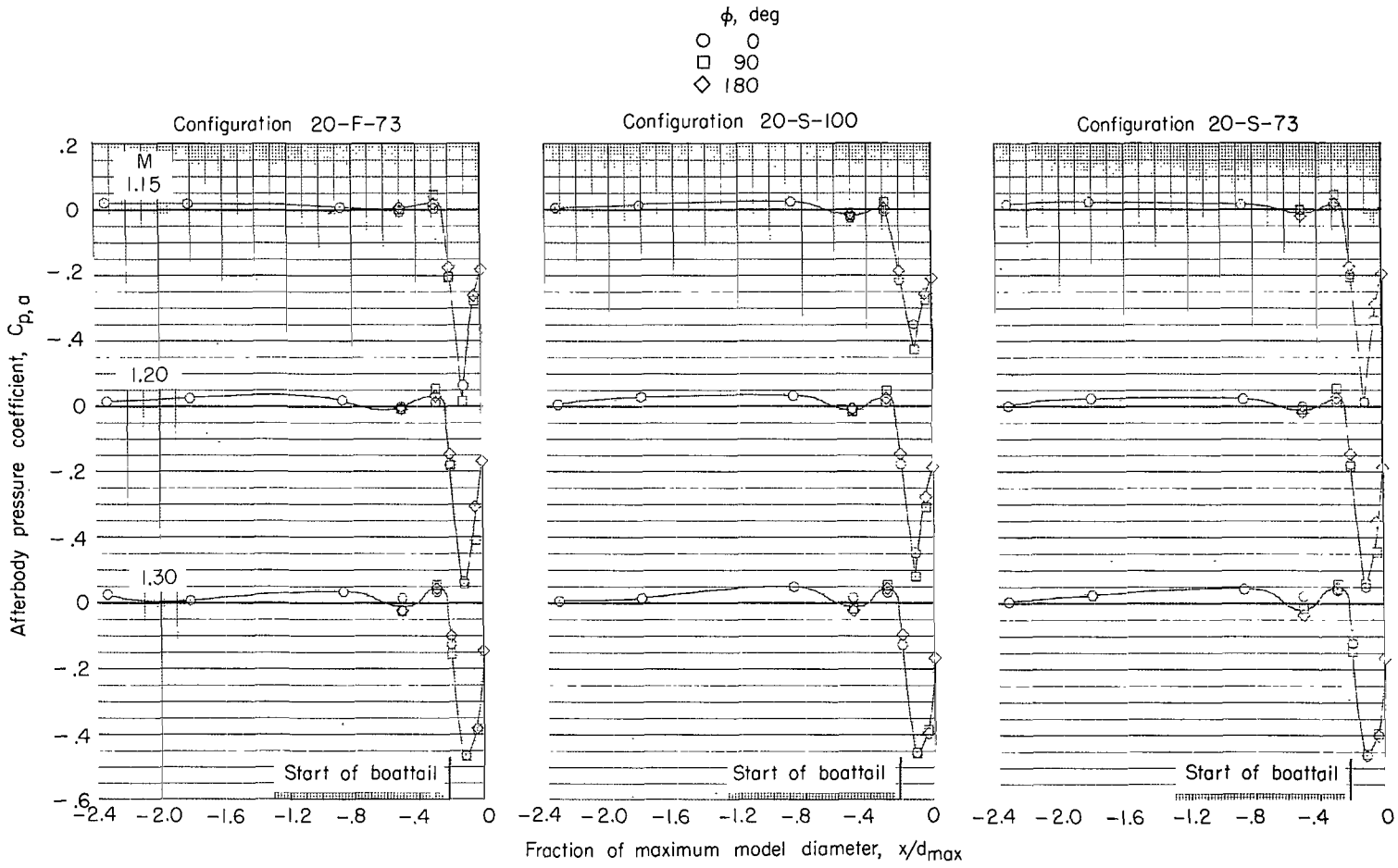

(b) $\beta = 20^{\circ}$. Concluded.

Figure 7.- Continued.

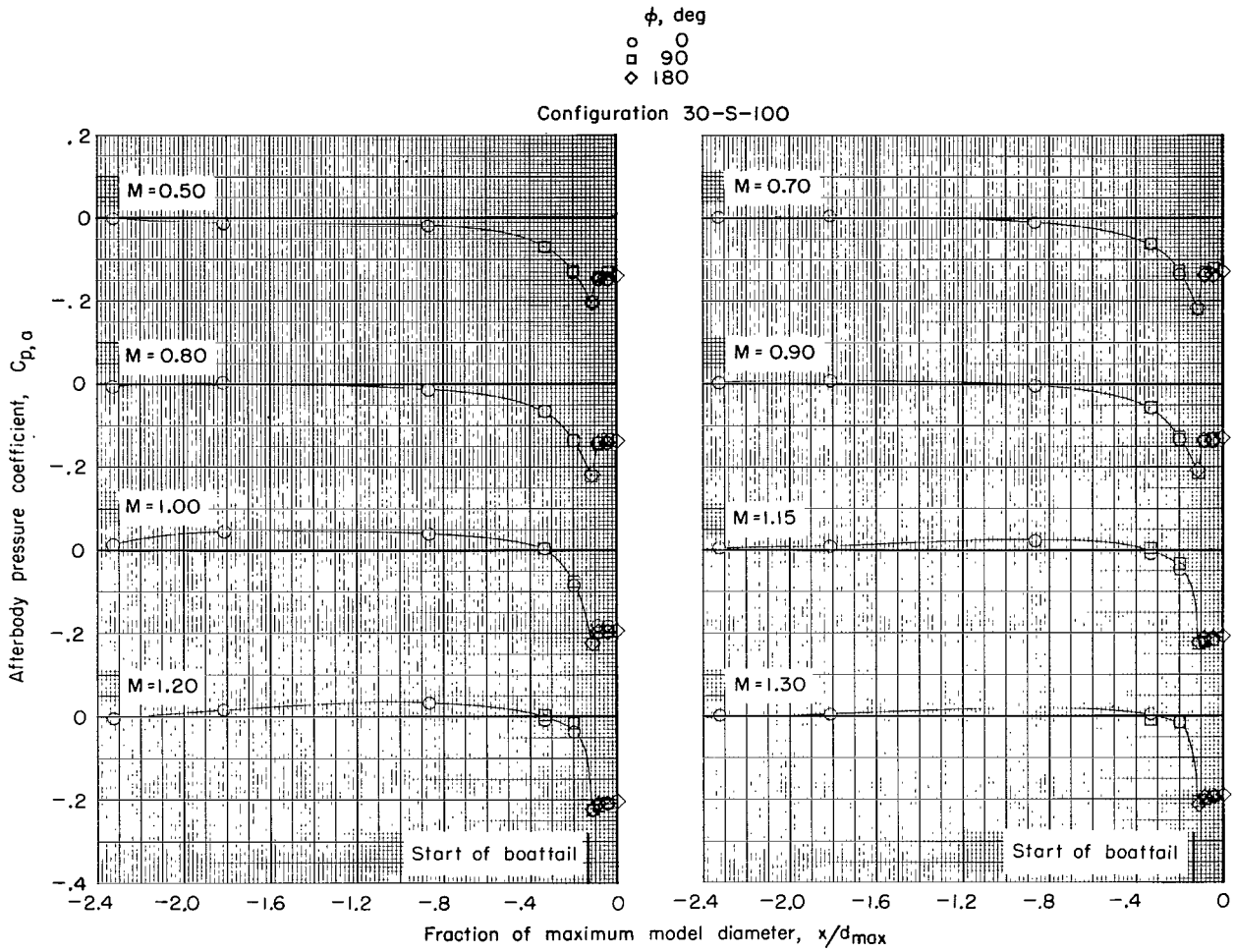

(c) $\beta = 30^0$.

Figure 7.- Concluded.

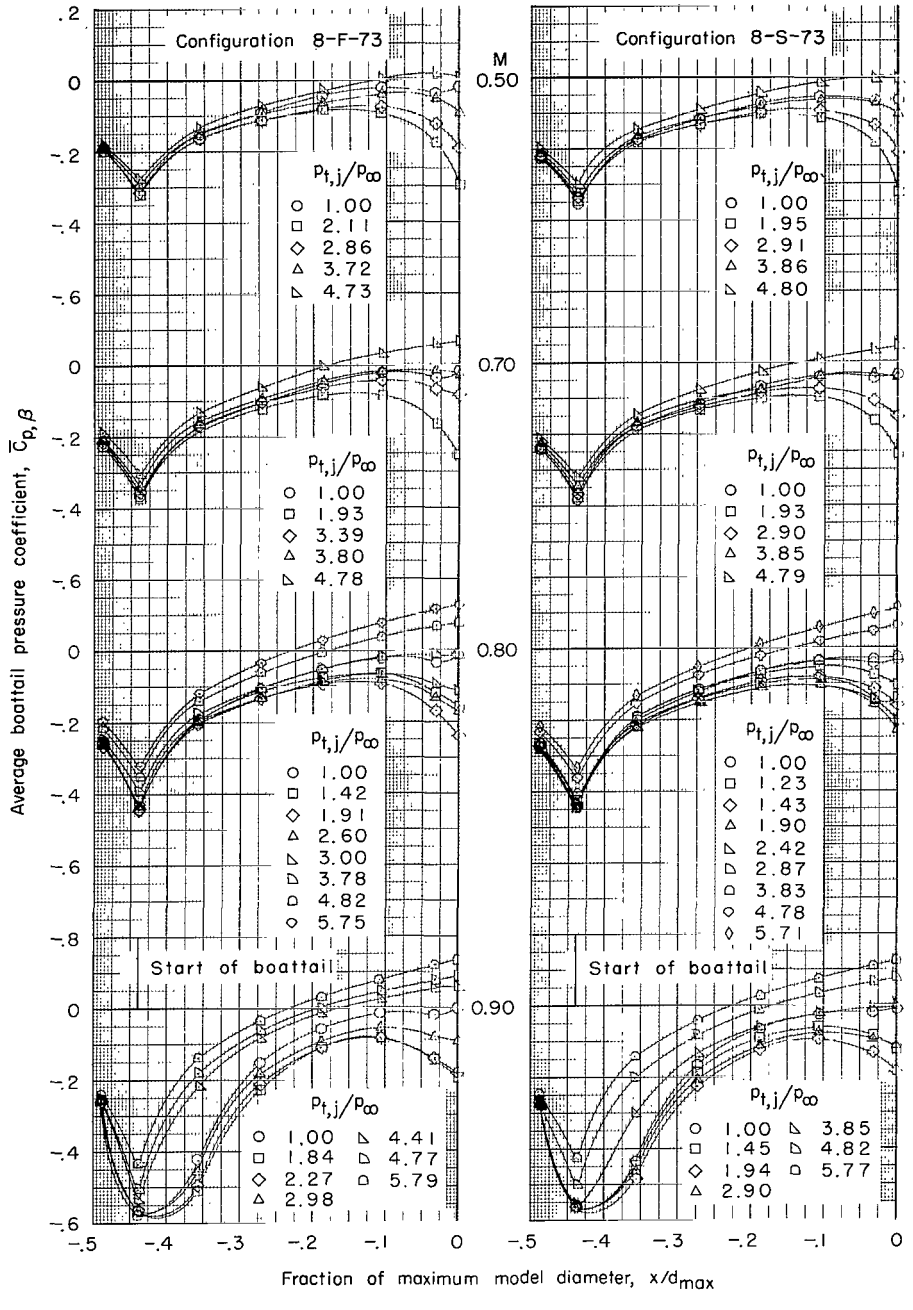

(a) $\beta = 8^0$.

Figure 8.- Effect of jet total-pressure ratio on average boattail pressure distributions for various Mach numbers.

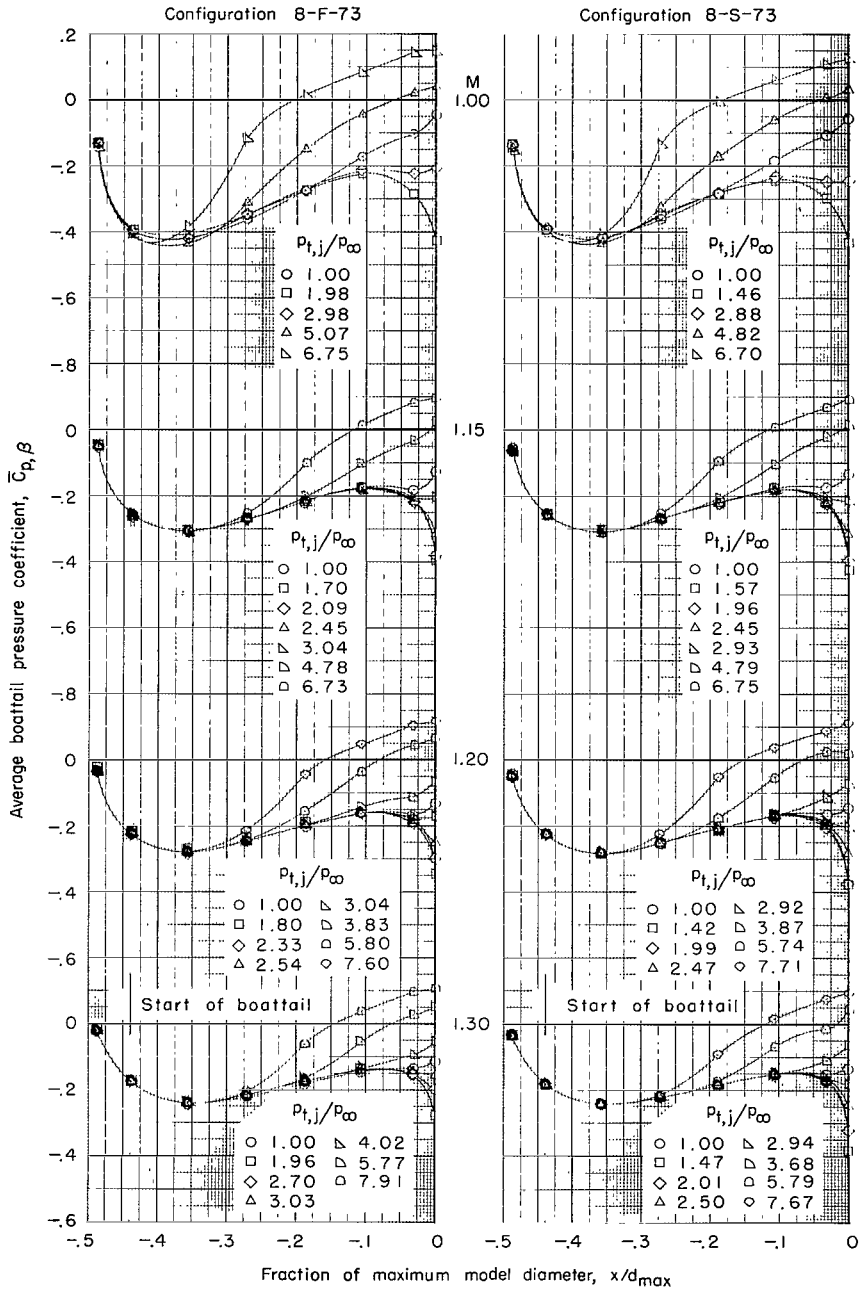

(a) $\beta = 8^0$. Concluded.

Figure 8.- Continued.

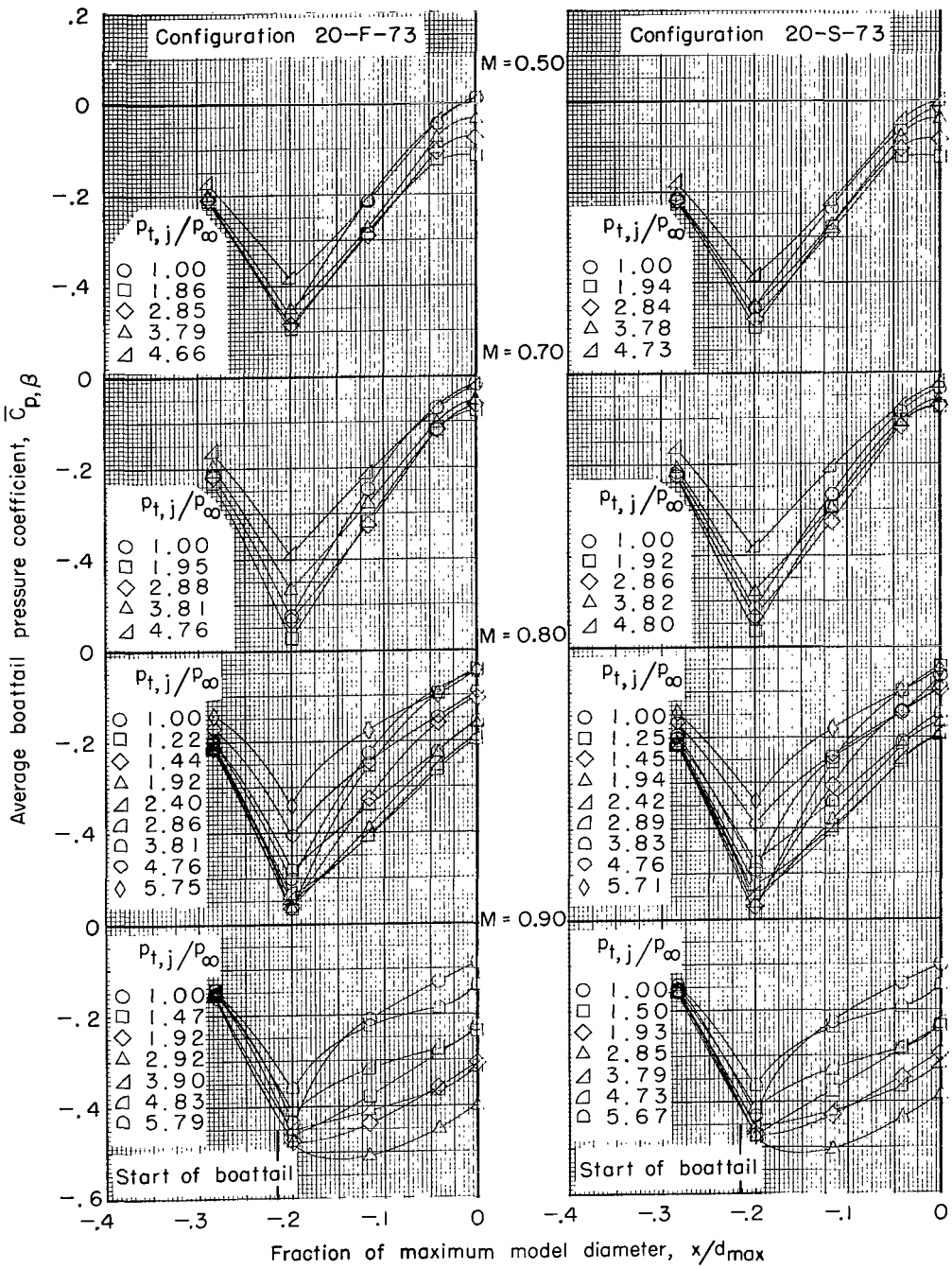

(b) $\beta = 20^0$.

Figure 8.- Continued.

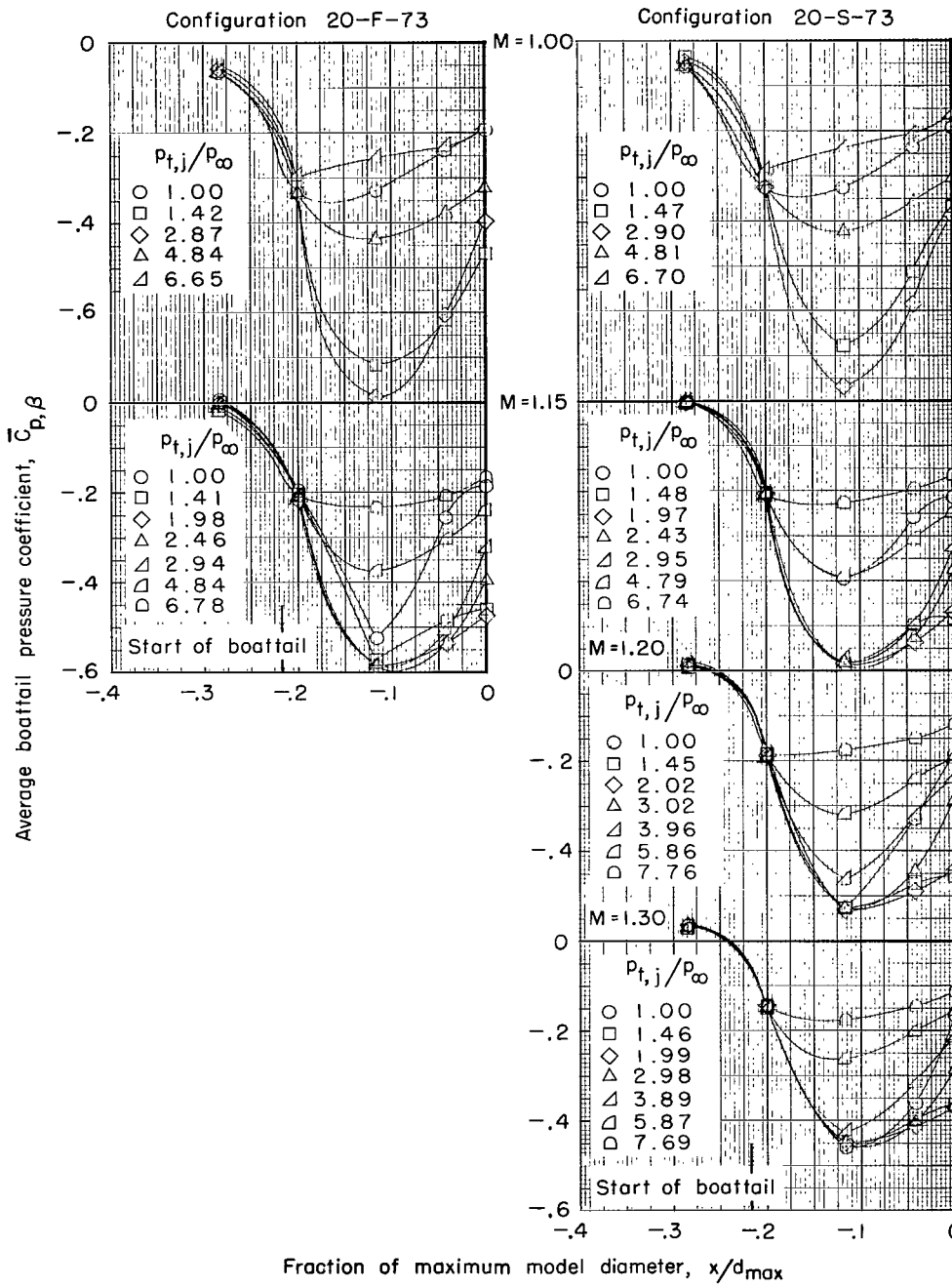

(b) $\beta = 20^0$. Concluded.

Figure 8.- Continued.

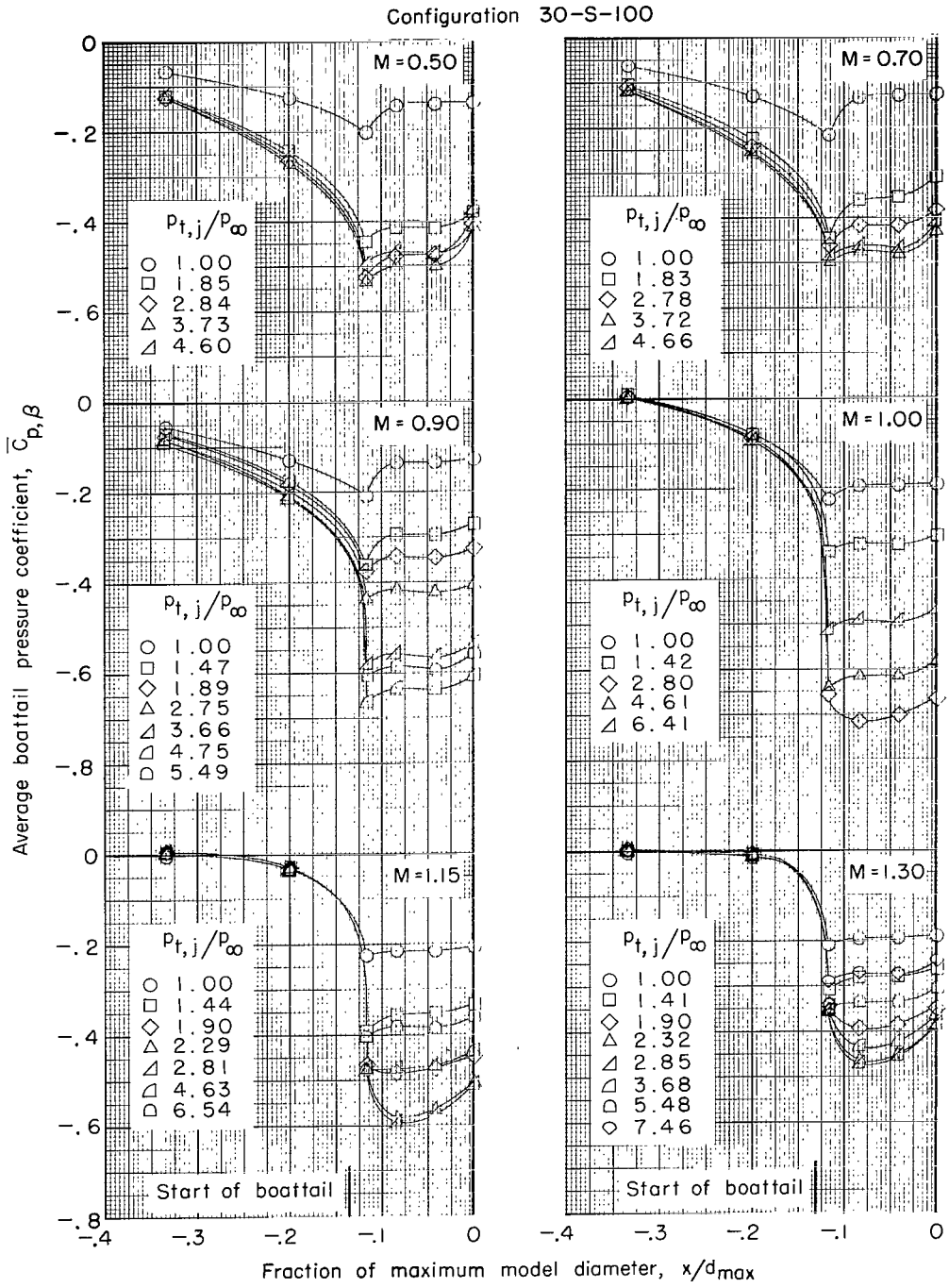

(c) $\beta = 30^0$.

Figure 8.- Concluded.

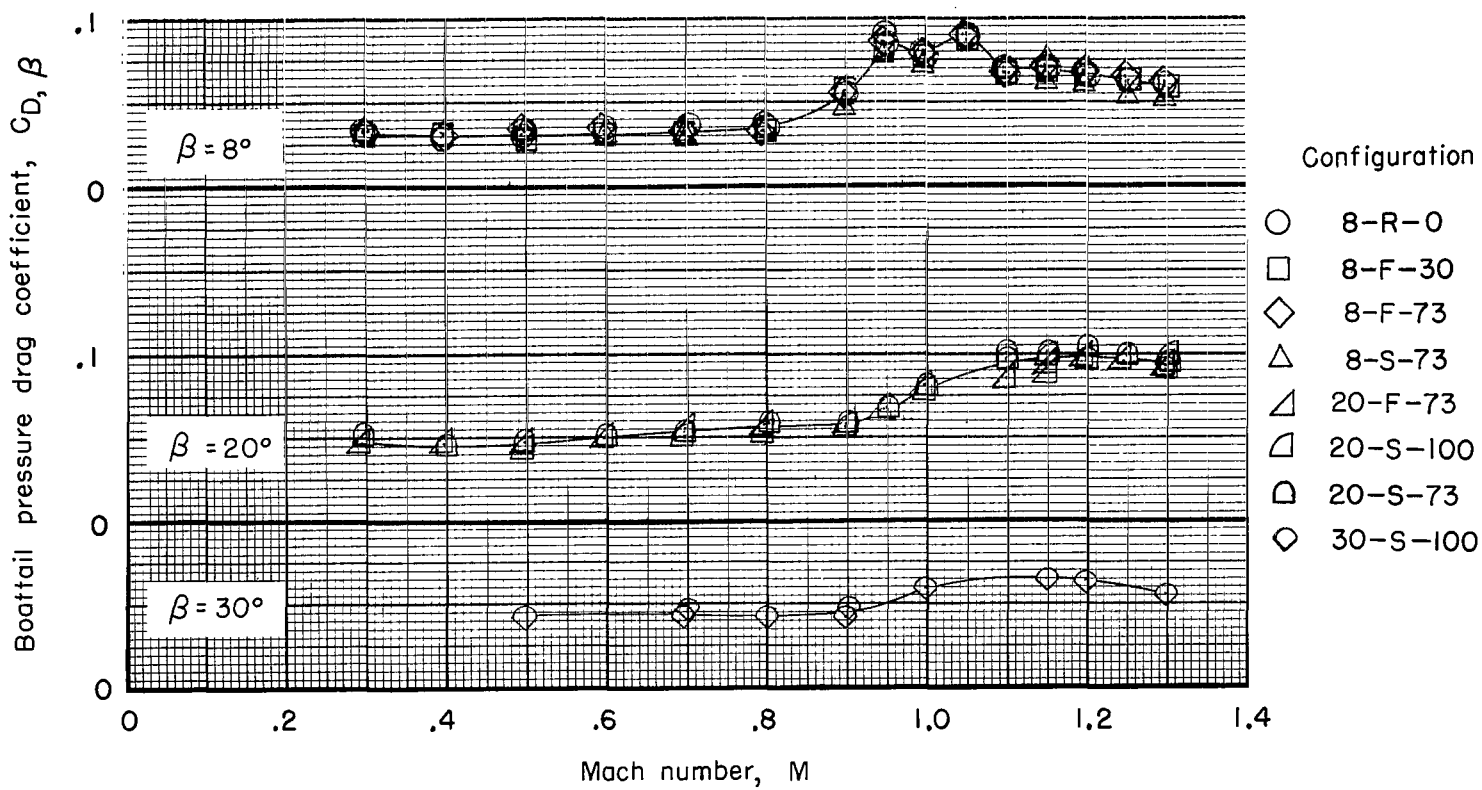

Figure 9.- Variation of boattail drag coefficient with Mach number for jet-off conditions.

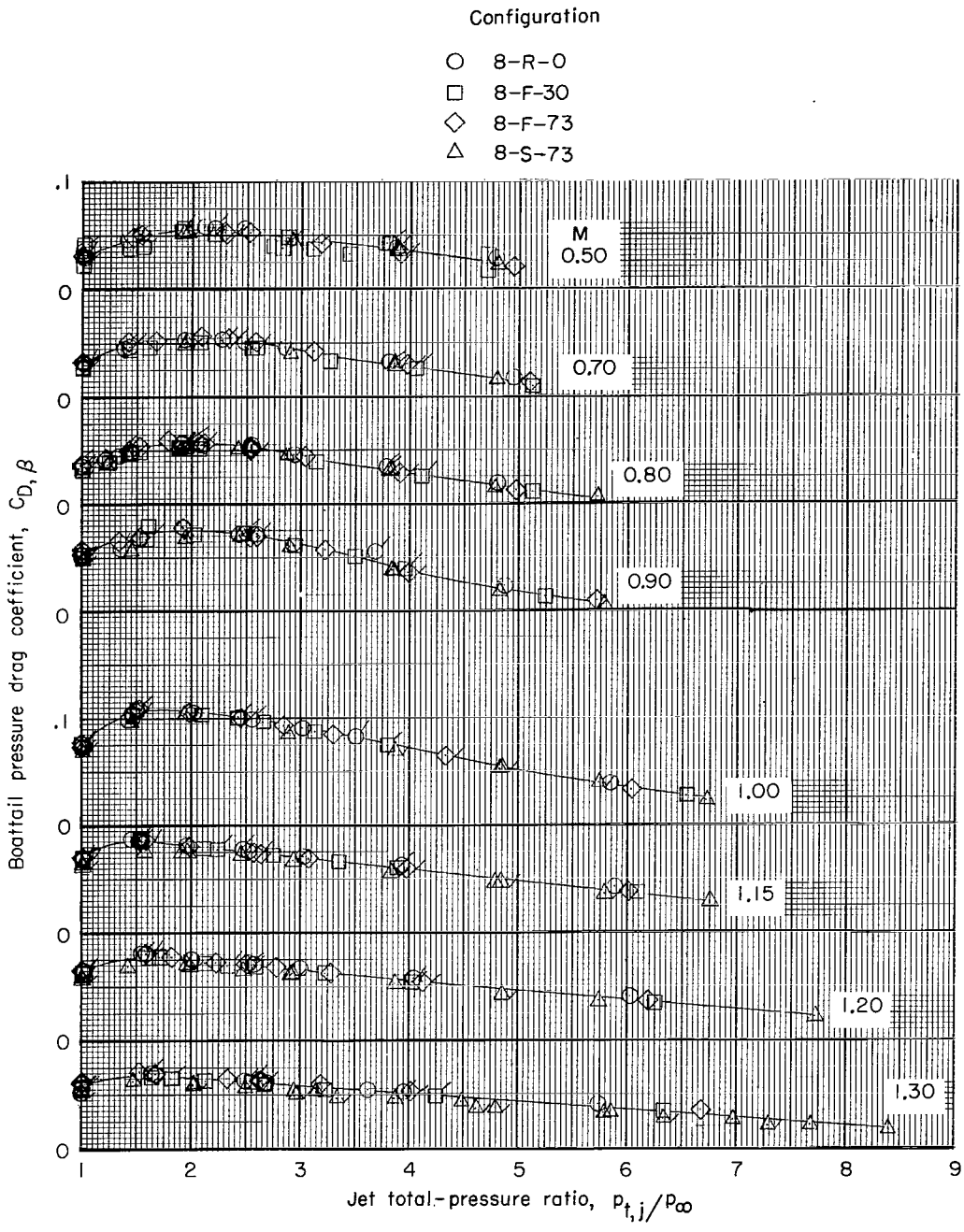

(a) $\beta = 8^0$.

Figure 10.- Variation of boattail drag coefficient with jet total-pressure ratio. Flagged symbols denote decreasing pressure ratios.

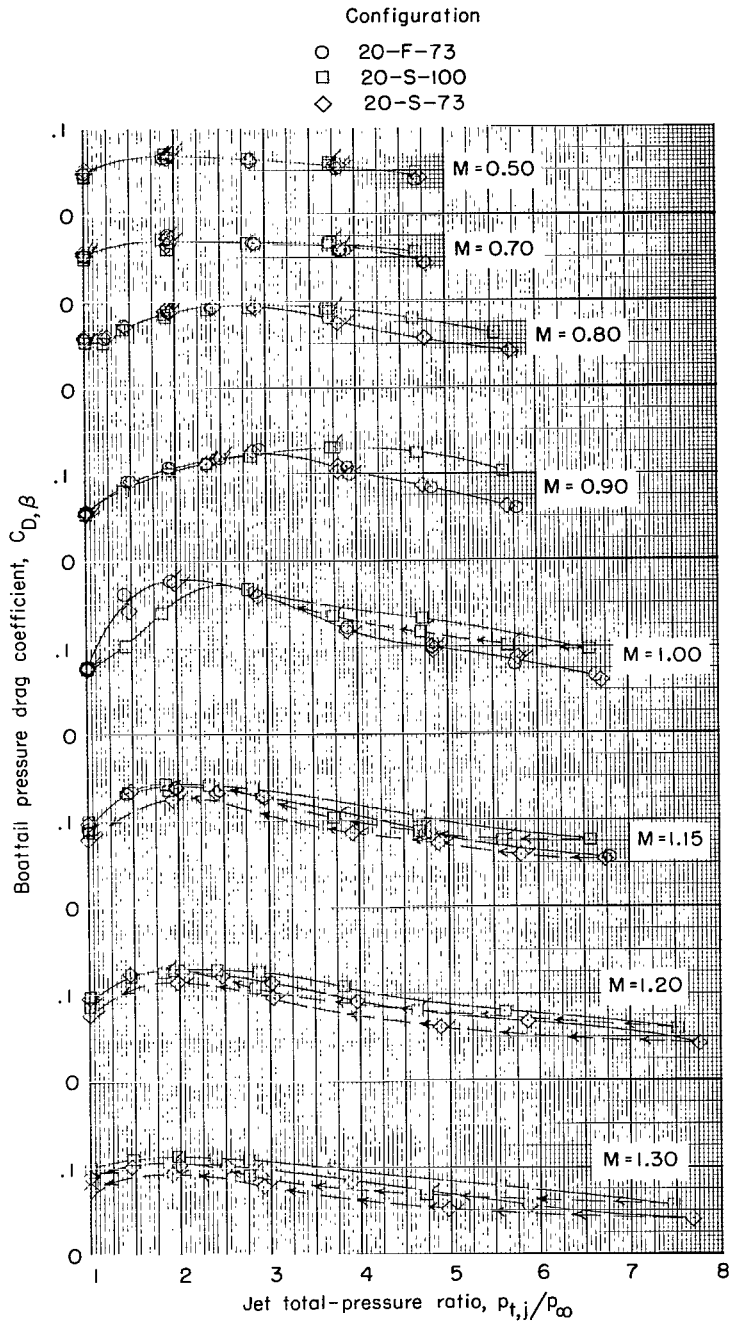

(b) $\beta = 20^0$.

Figure 10.- Continued.

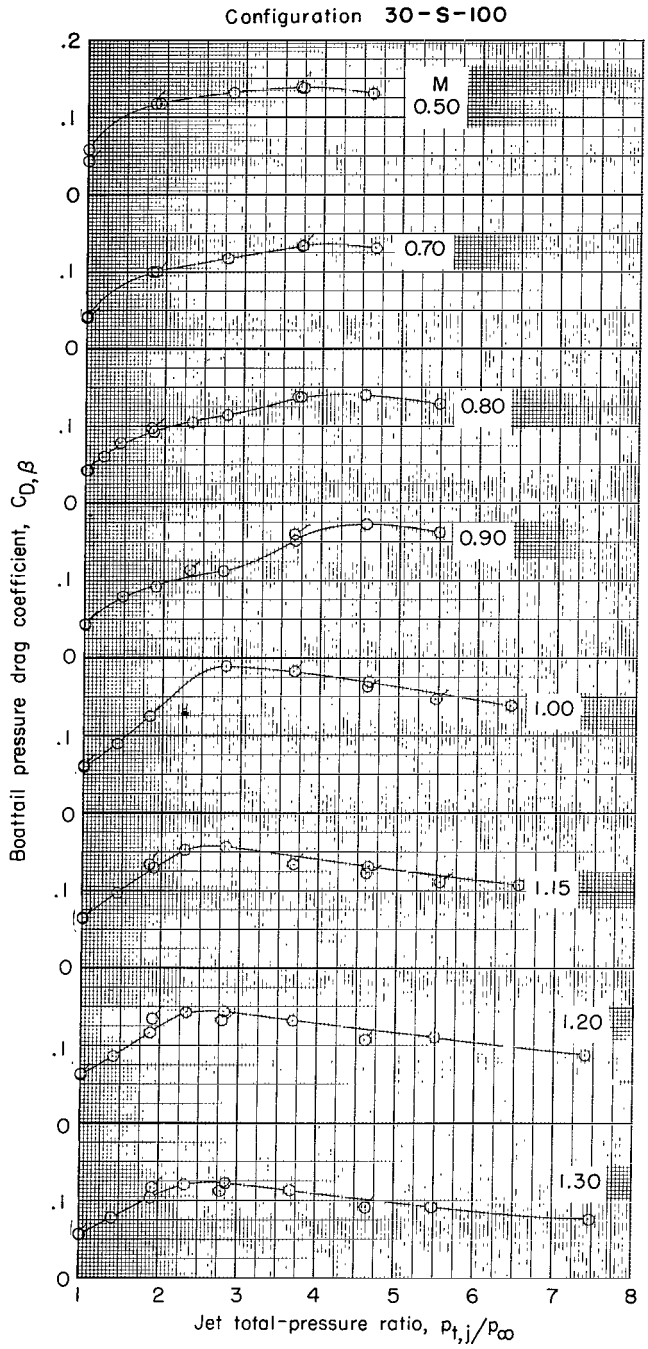

(c) $\beta = 30^0$.

Figure 10.- Concluded.

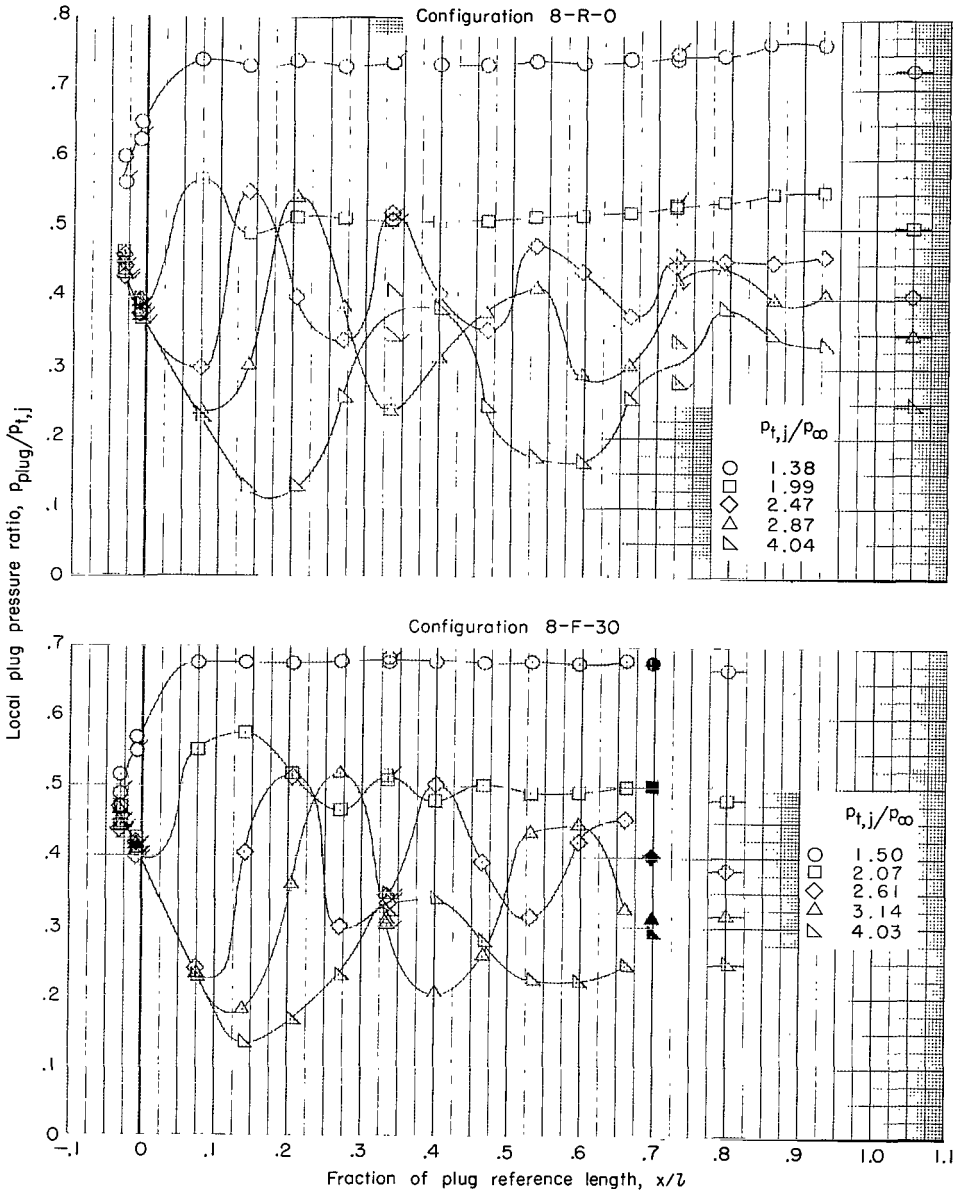

(a) M = 0.

Figure 11.- Effect of jet total-pressure ratio on plug static-pressure distributions for various Mach numbers. Symbols with flags indicate row 180° orifices; isolated symbols with ticks indicate values of $p_\infty/p_{t,j}$; solid symbols indicate values of average $p_{plug,b}/p_{t,j}$; configurations 8-R-0 and 8-F-30.

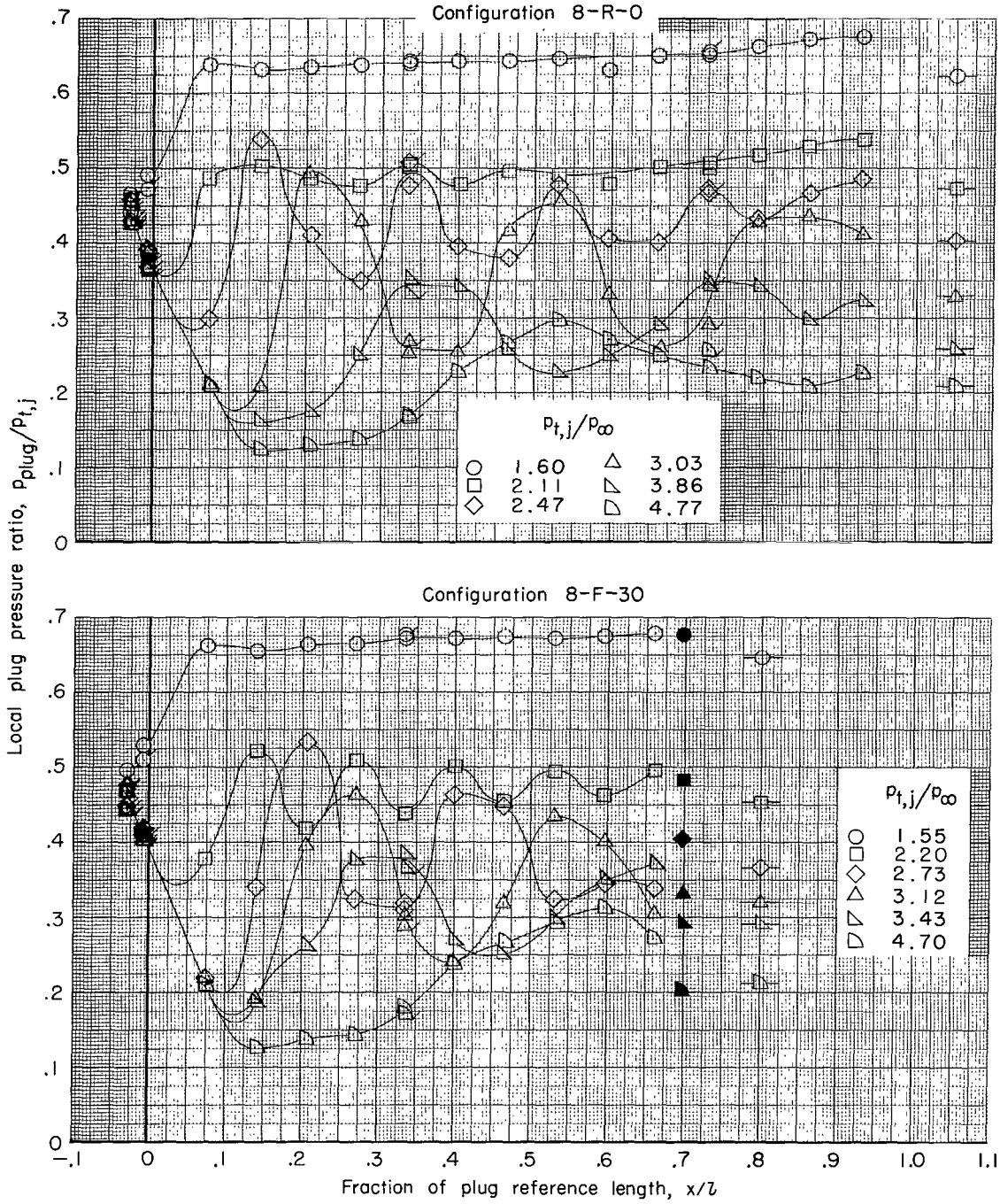

(b) M = 0.50.

Figure 11.- Continued.

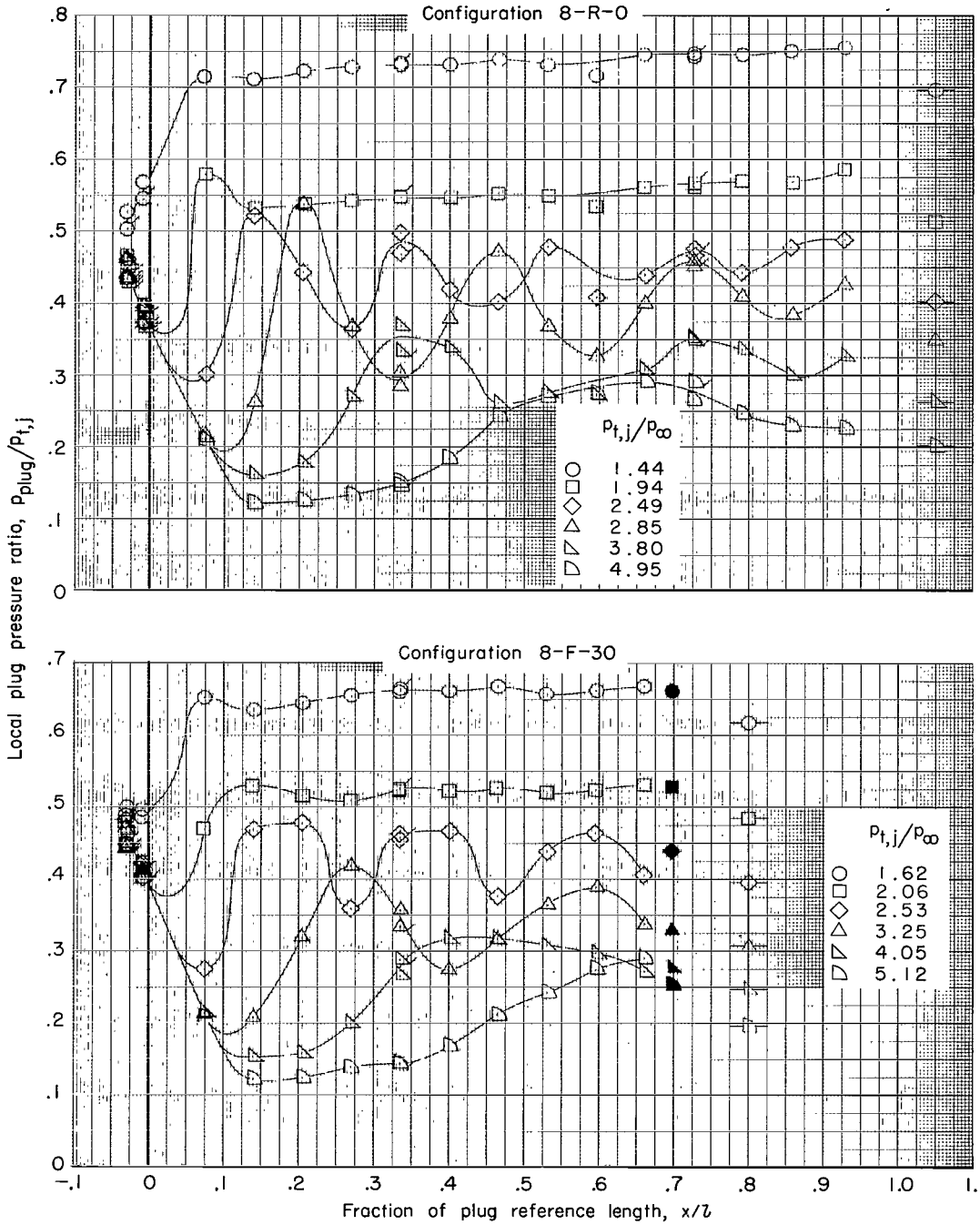

(c) M = 0.70.

Figure 11.- Continued.

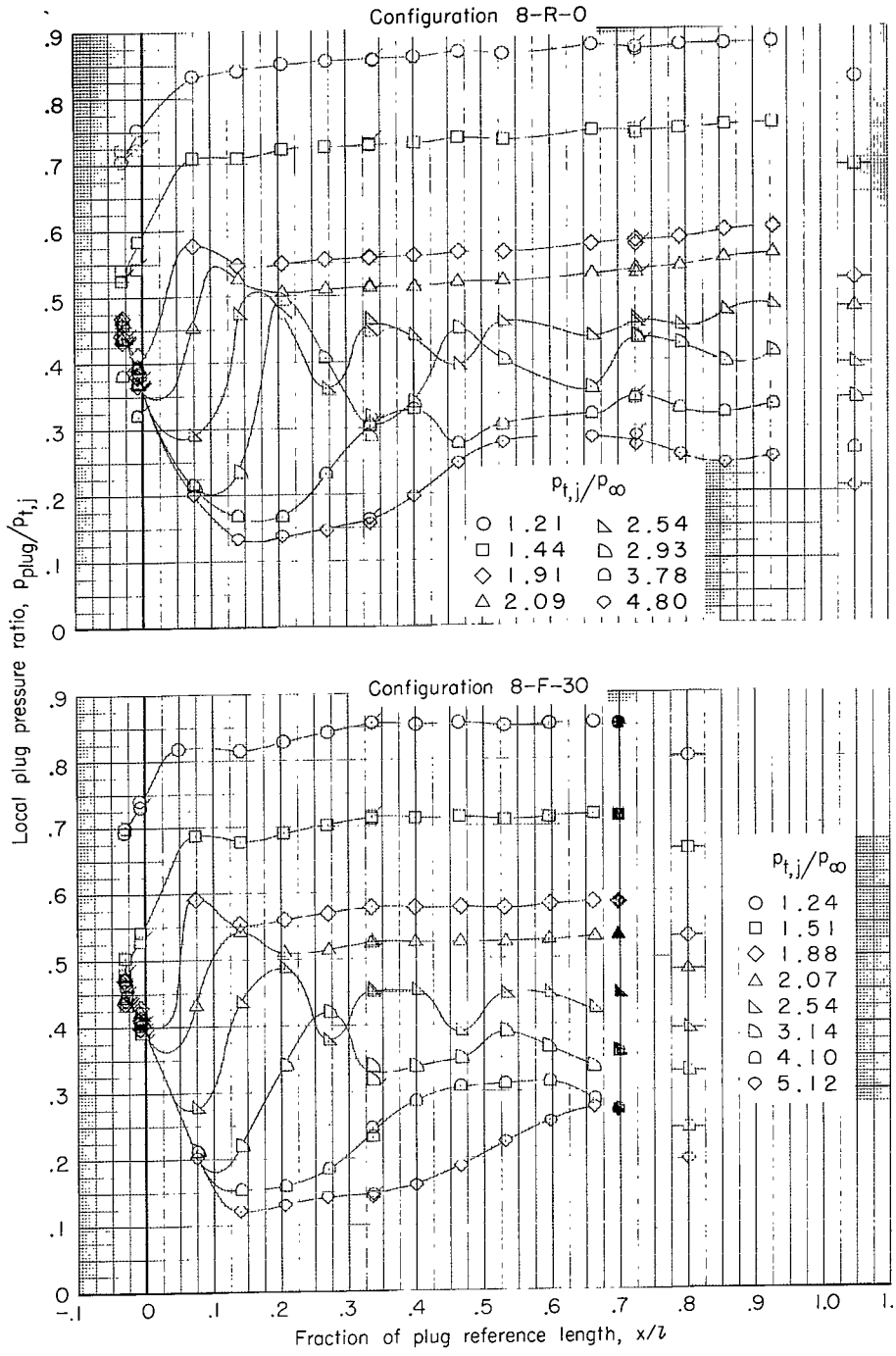

(d) M = 0.80.

Figure 11.- Continued.

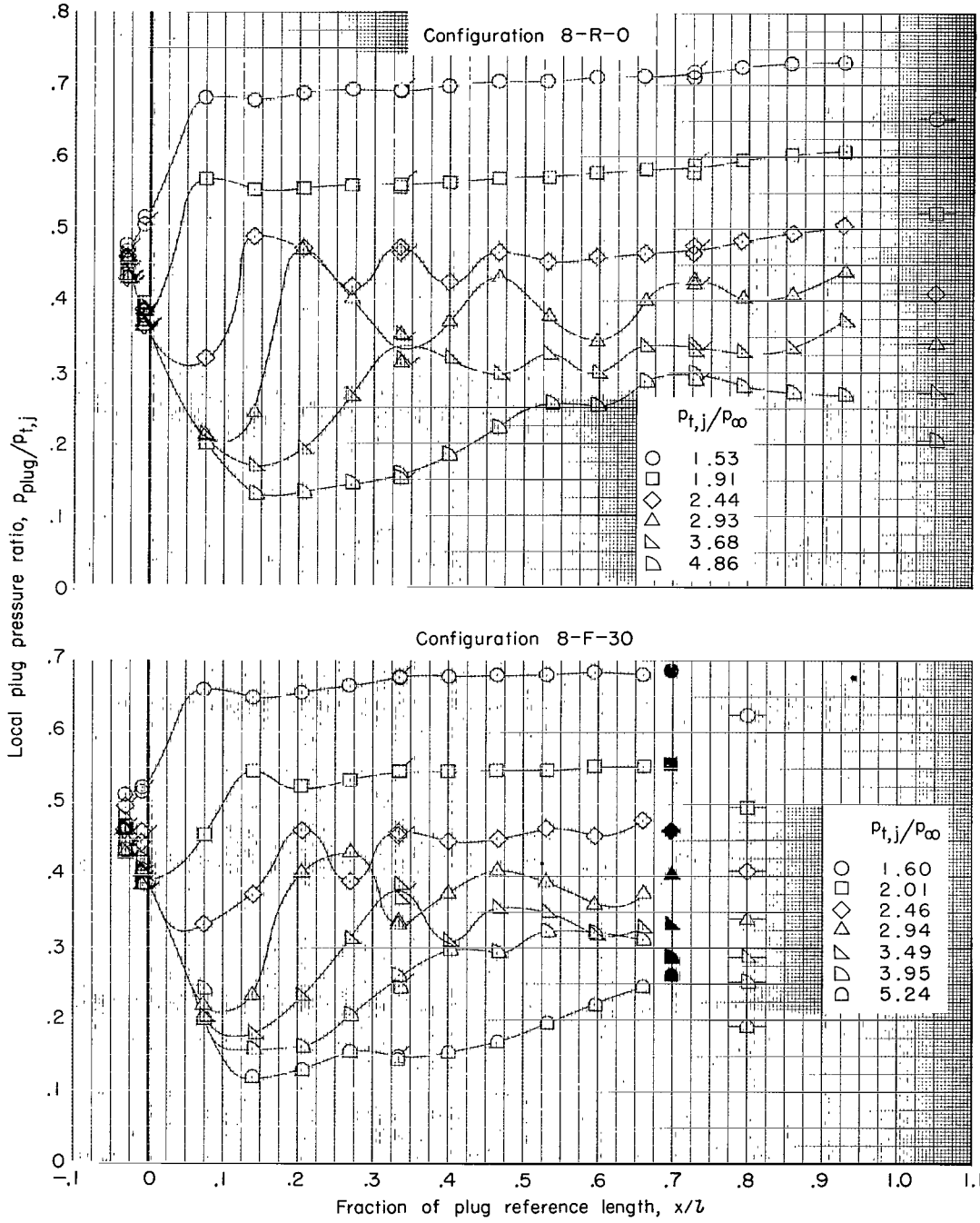

(e) M = 0.90.

Figure 11.- Continued.

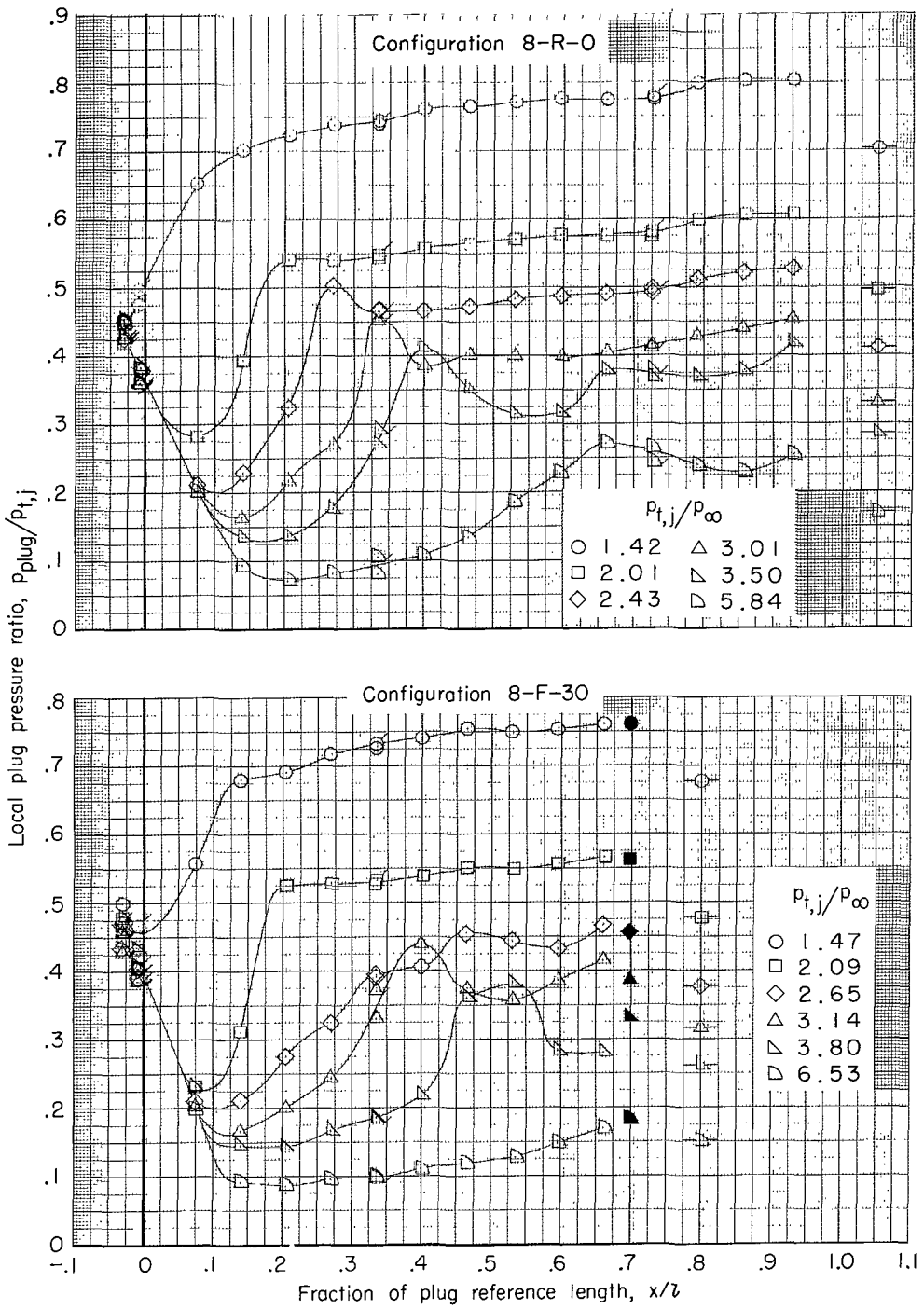

(f) M = 1.00.

Figure 11.- Continued.

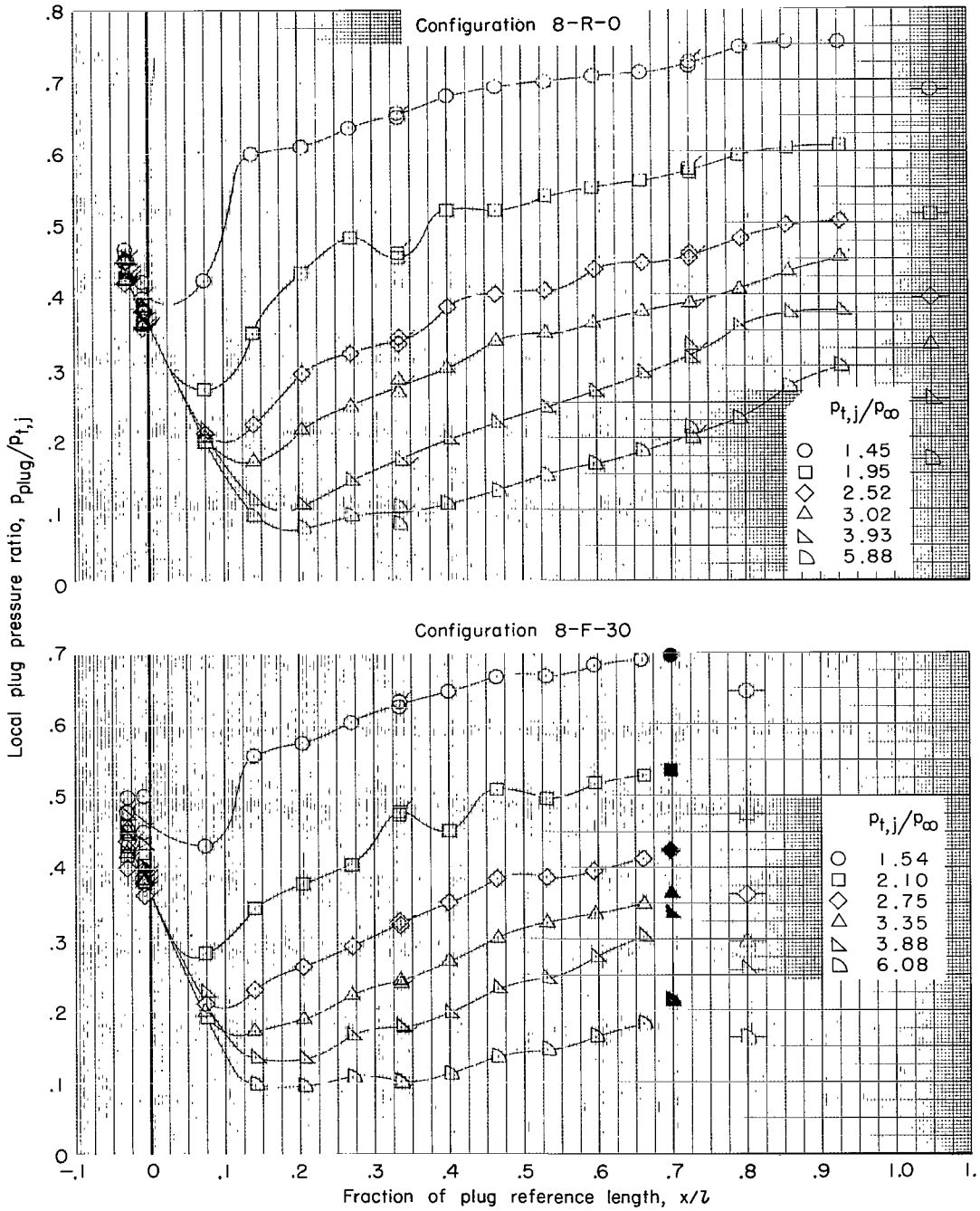

(g) M = 1.15.

Figure 11.- Continued.

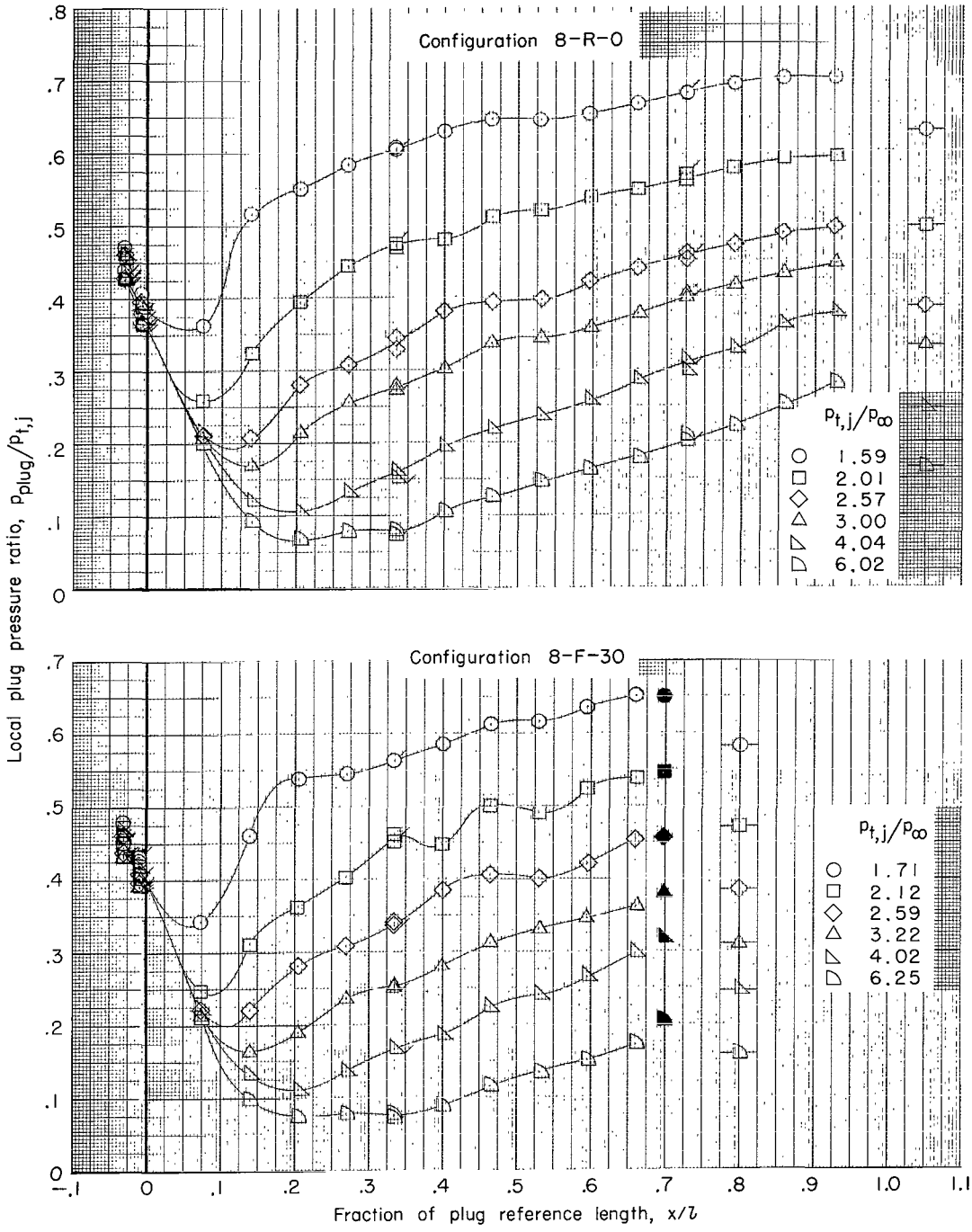

(h) M = 1.20.

Figure 11.- Continued.

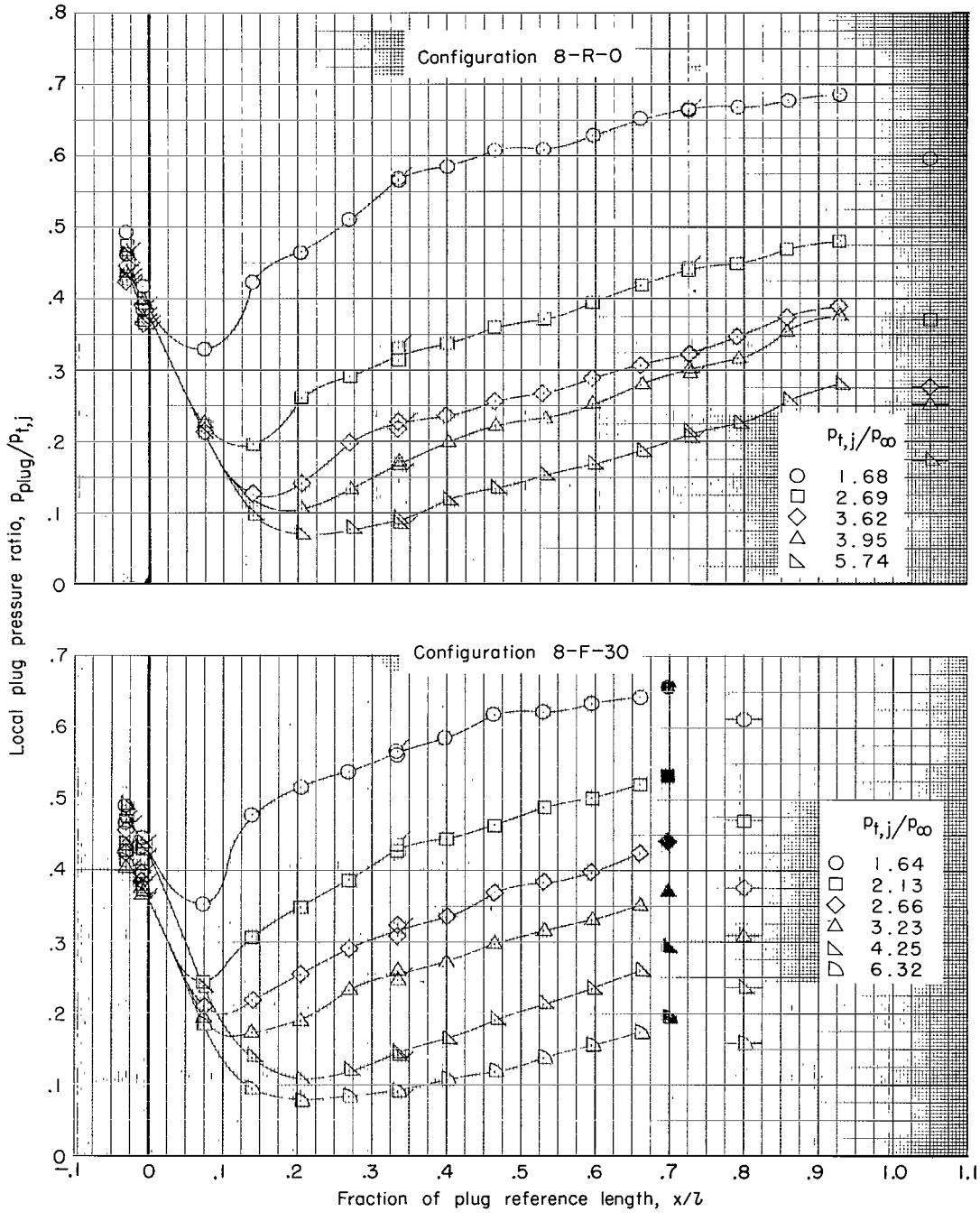

(i) M = 1.30.

Figure 11.- Concluded.

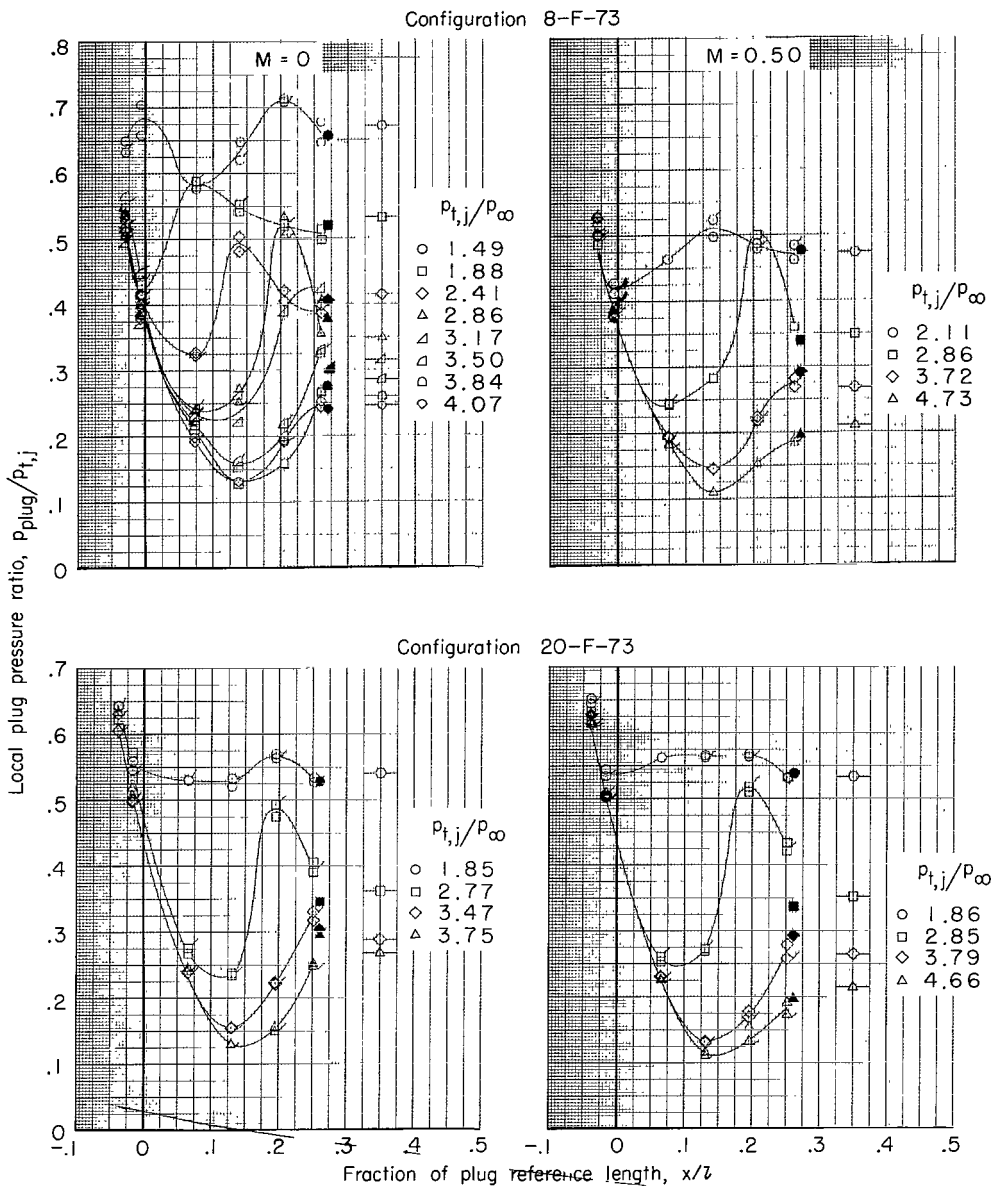

(a) M = 0 and M = 0.50.

Figure 12.- Effect of jet total-pressure ratio on plug static-pressure distributions for various Mach numbers. Symbols with flags indicate row 180° orifices; isolated symbols with ticks indicate values of $p_\infty/p_{t,j}$; solid symbols indicate values of average $p_{plug,b}/p_{t,j}$; configurations 8-F-73 and 20-F-73.

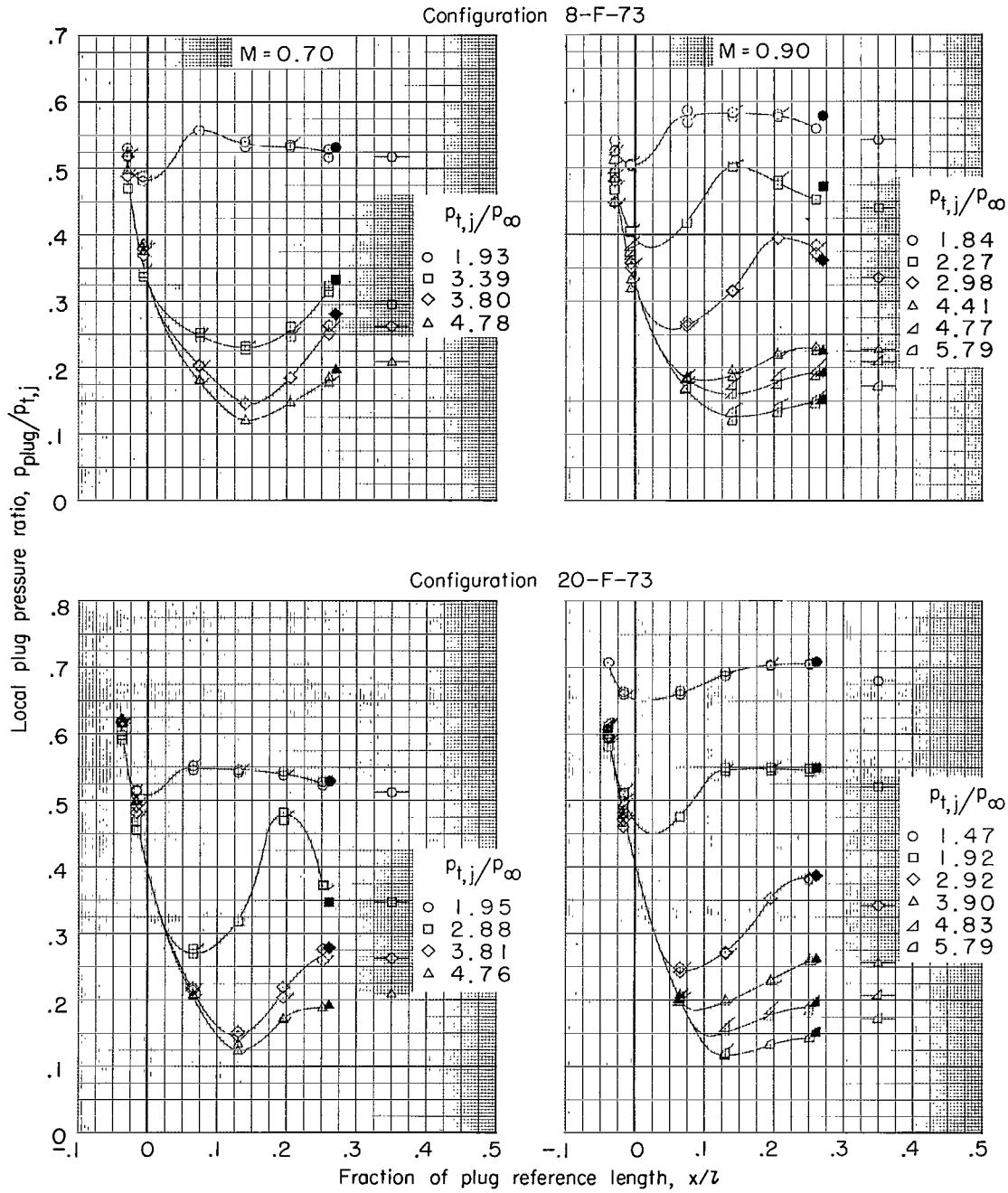

(b) M = 0.70 and M = 0.90.

Figure 12.- Continued.

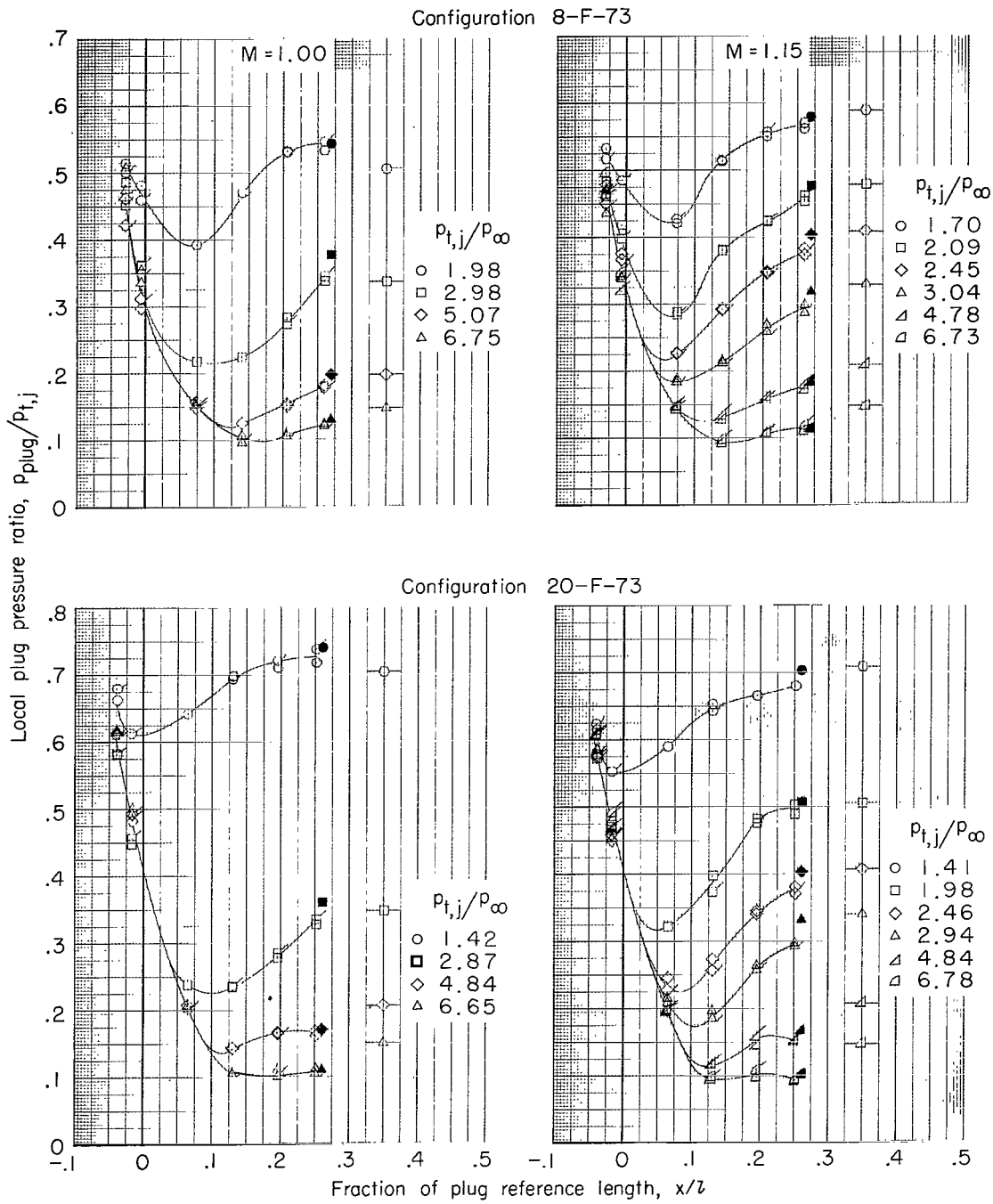

(c) M = 1.00 and M = 1.15.

Figure 12.- Continued.

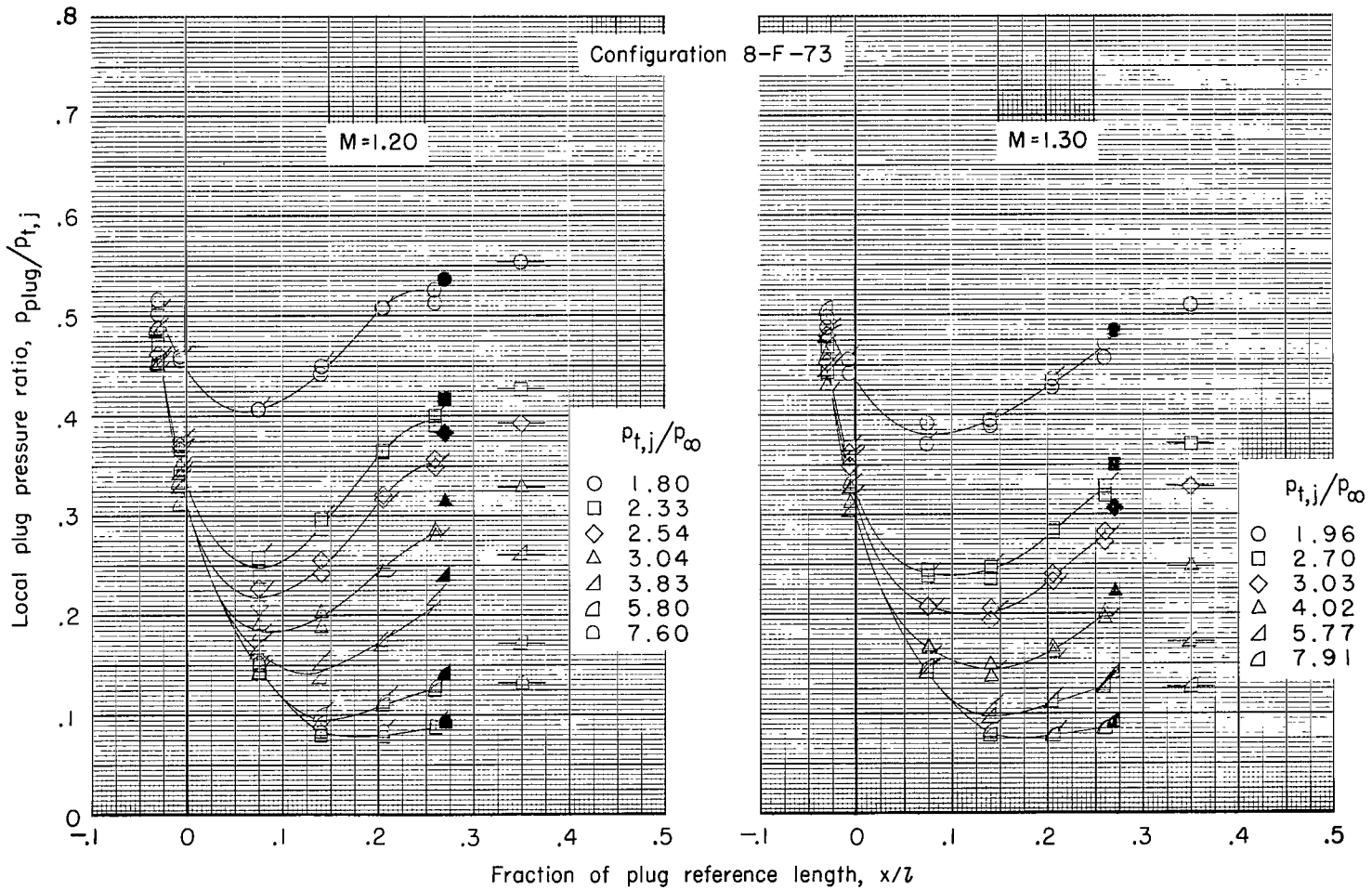

(d) M = 1.20 and M = 1.30.

Figure 12.- Concluded.

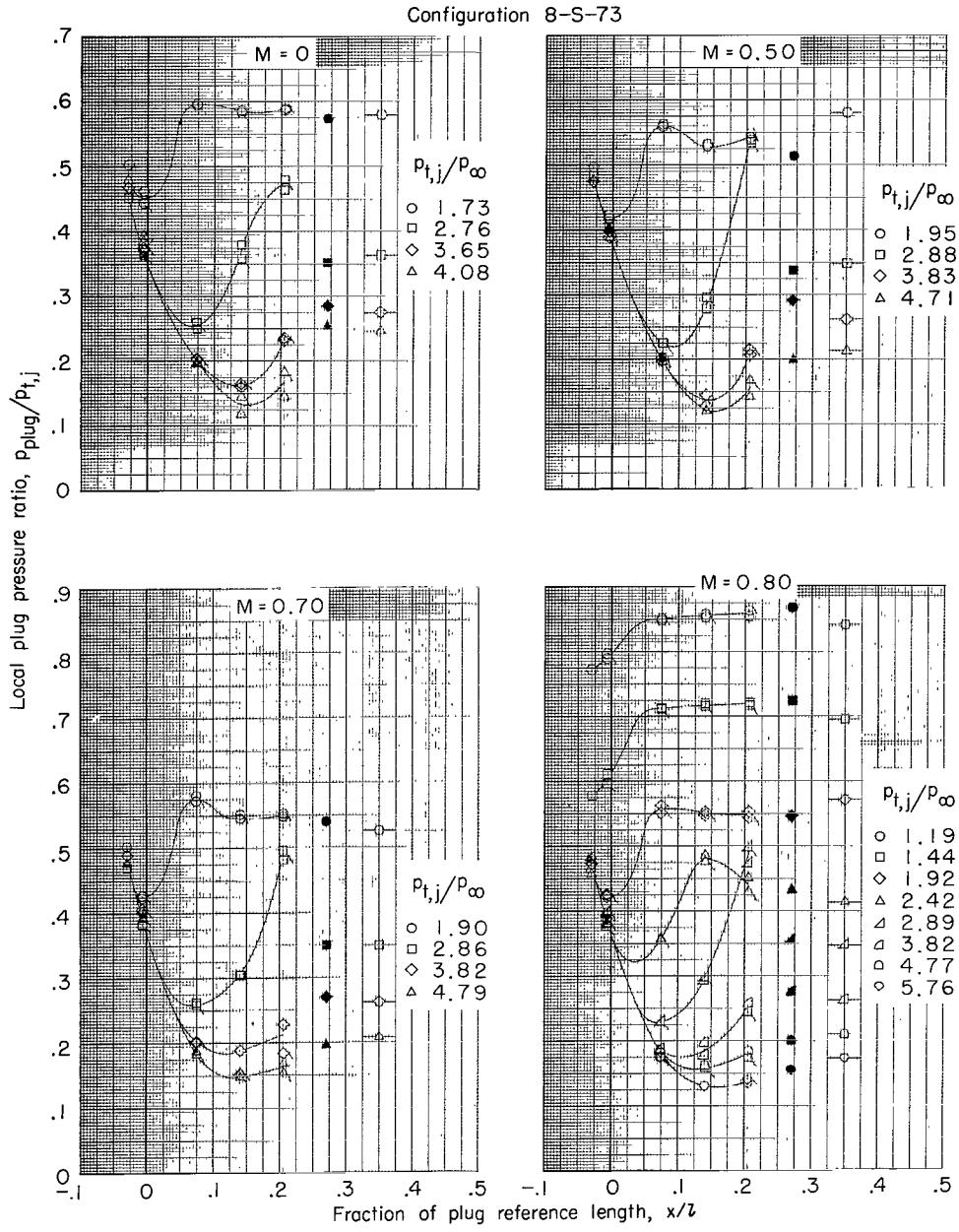

(a) M = 0 to M = 0.80.

Figure 13.- Effect of jet total-pressure ratio on plug static-pressure distributions for various Mach numbers. Symbols with tails indicate row 180° orifices; isolated symbols with ticks indicate values of $p_\infty/p_{t,j}$; solid symbols indicate values of average $p_{plug,b}/p_{t,j}$; configuration 8-S-73.

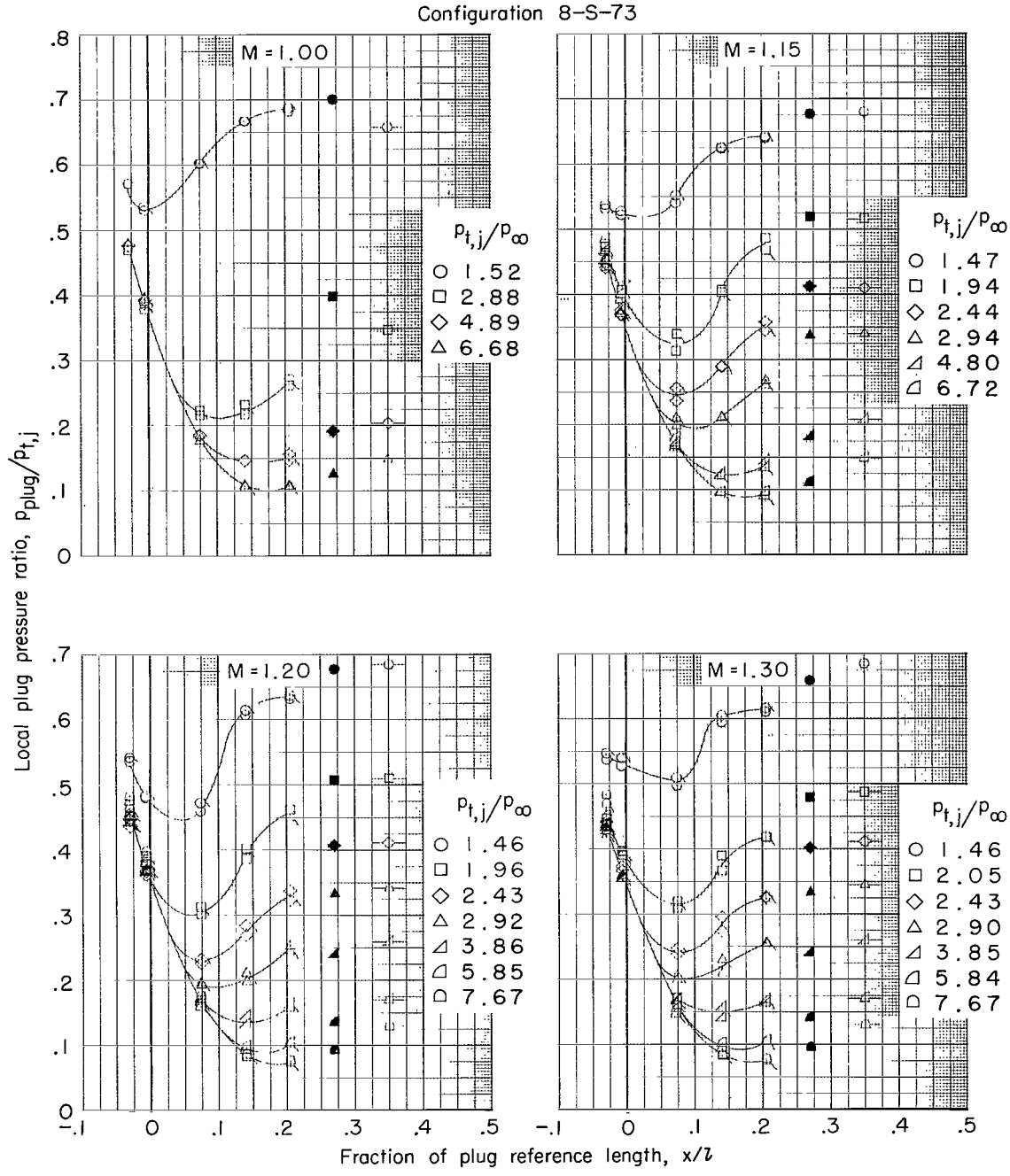

(b) M = 1.00 to M = 1.30.

Figure 13.- Concluded.

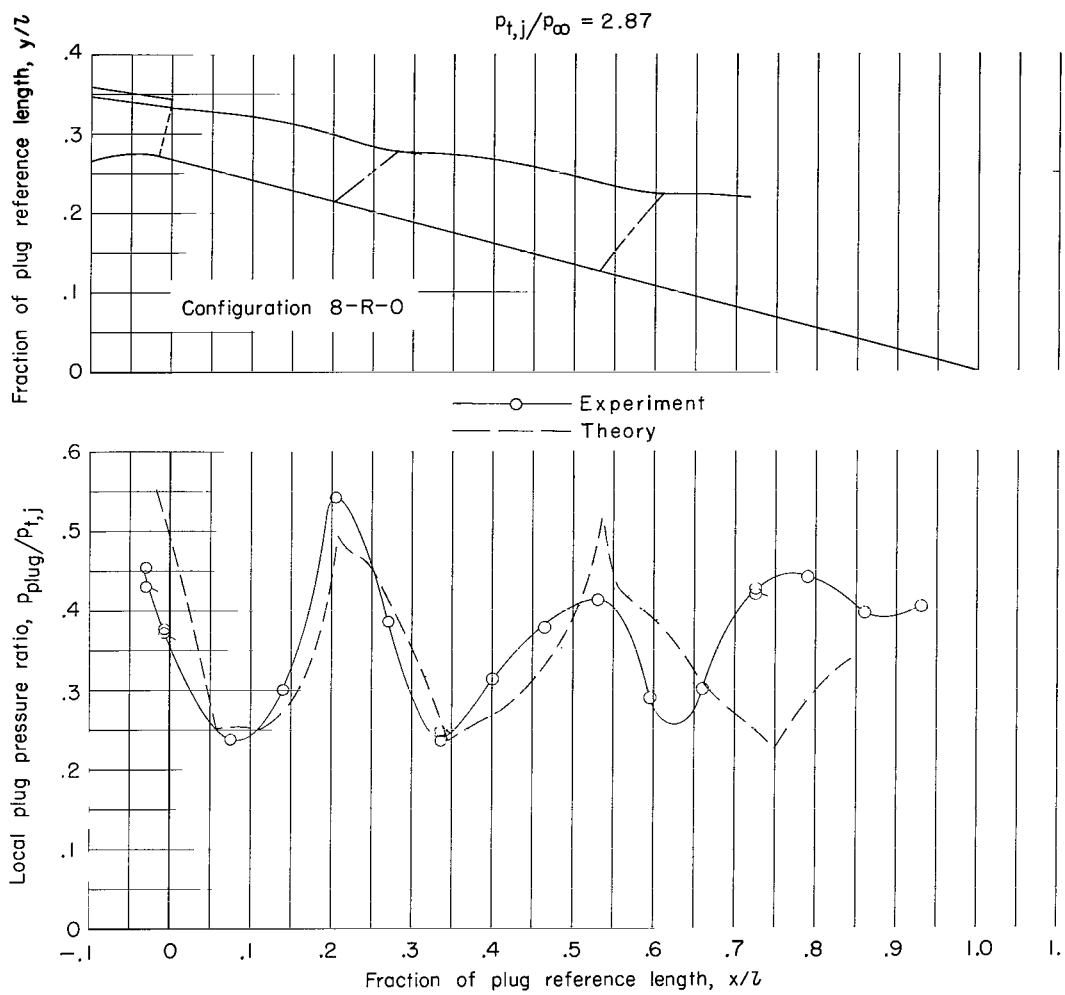

(a) $p_{t,j}/p_\infty$ = 2.87.

Figure 14.- Comparison of theoretical and experimental plug static-pressure distributions on configuration 8-R-0. Dash-dot-dash lines represent location of shock waves or regions of strong compression; symbols with tails indicate row 180° orifices.

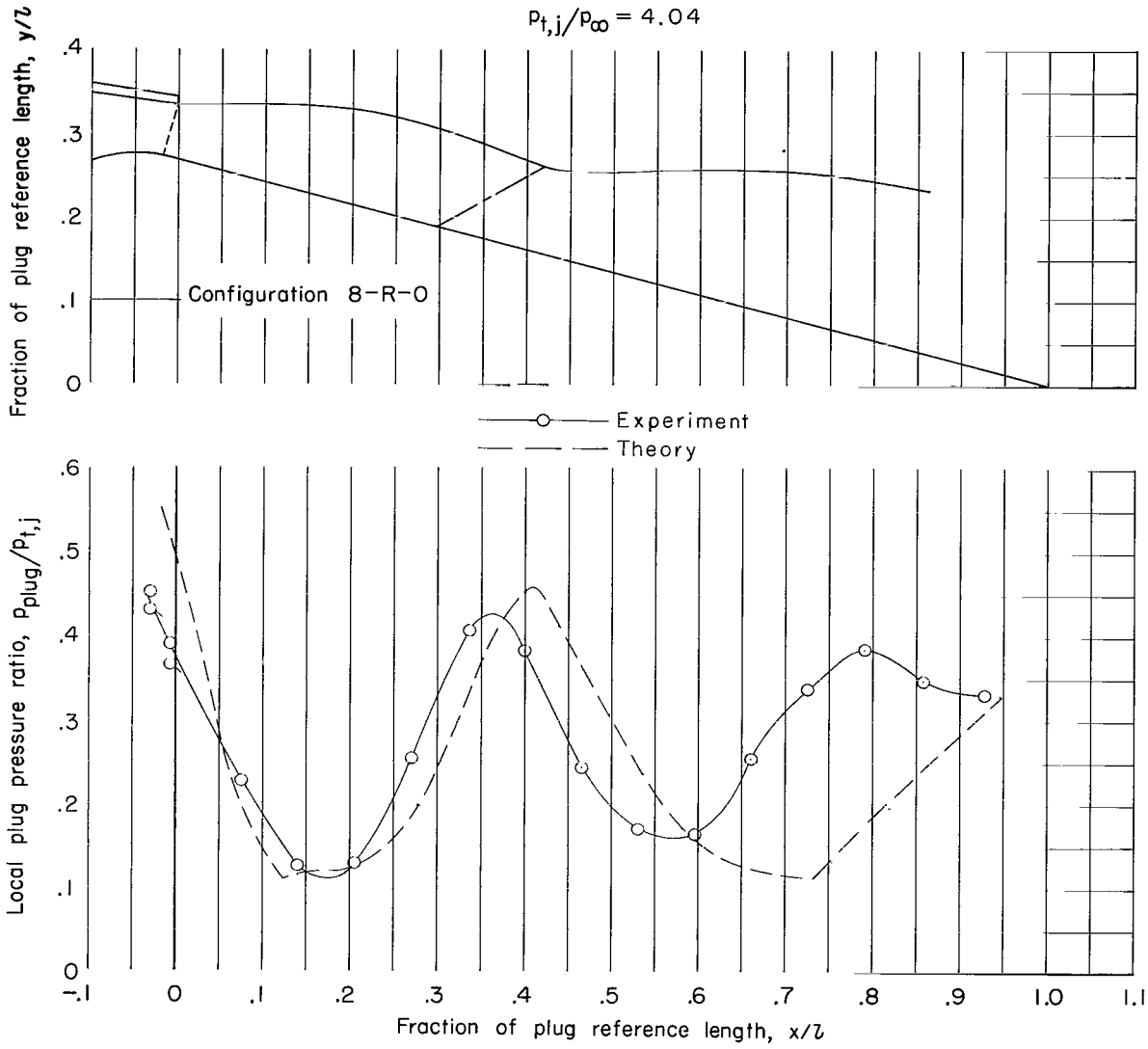

(b) $p_{t,j}/p_\infty = 4.04$.

Figure 14.- Concluded.

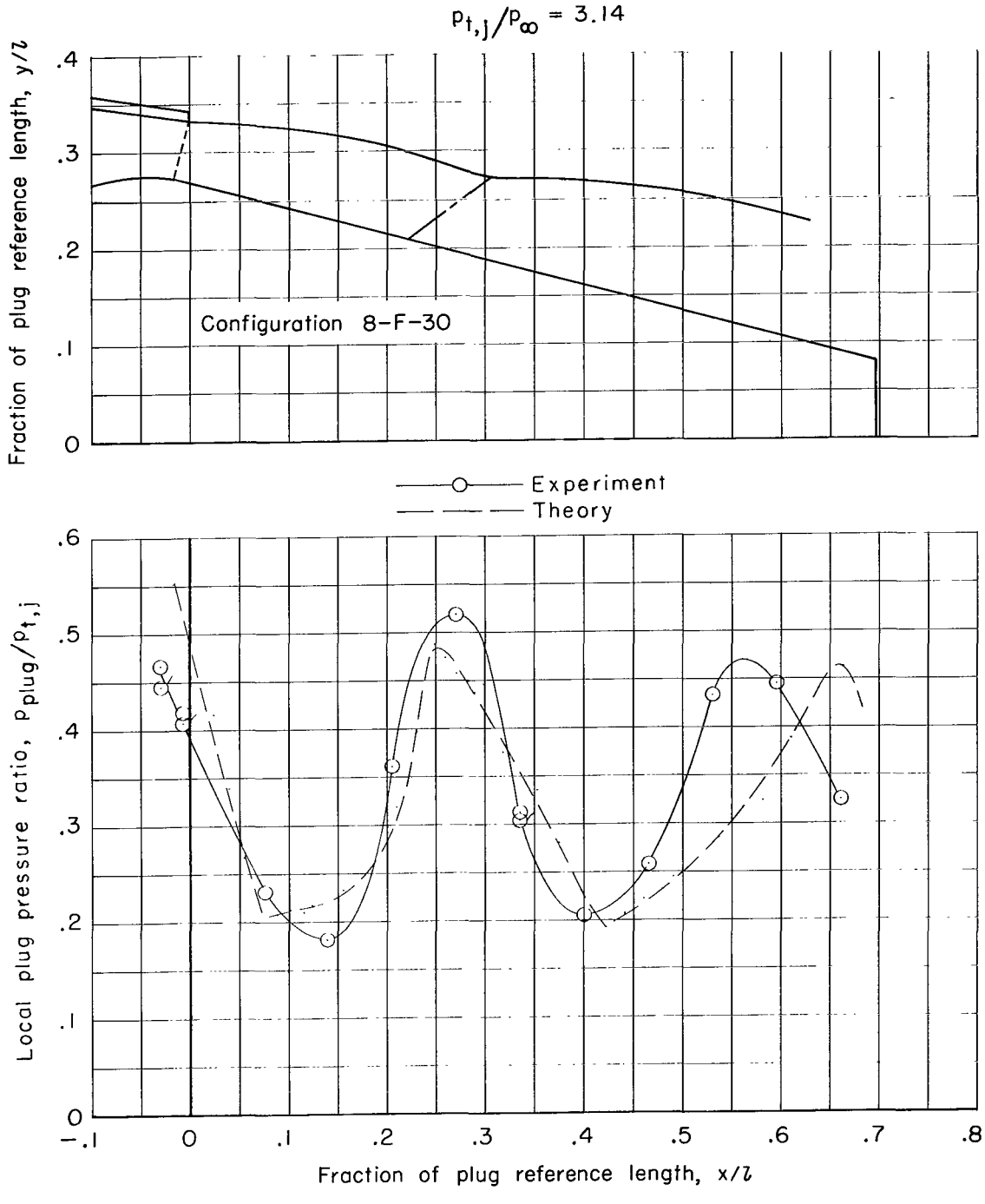

(a) $p_{t,j}/p_\infty = 3.14$.

Figure 15.- Comparison of theoretical and experimental plug static-pressure distributions on configuration 8-F-30. Dash-dot-dash lines represent location of shock waves or regions of strong compression; symbols with flags indicate row 180° orifices.

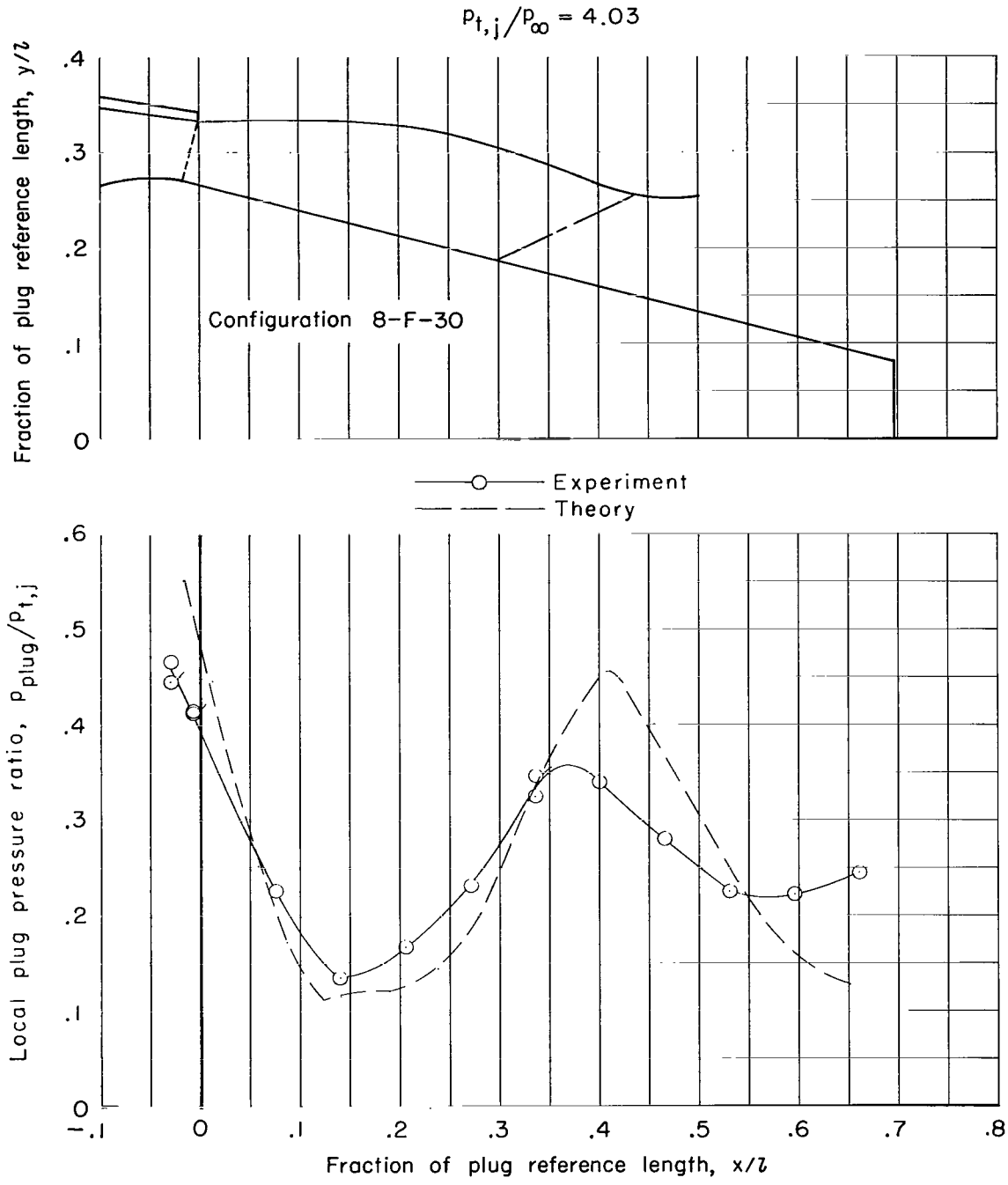

(b) $p_{t,j}/p_\infty = 4.03$.

Figure 15.- Concluded.

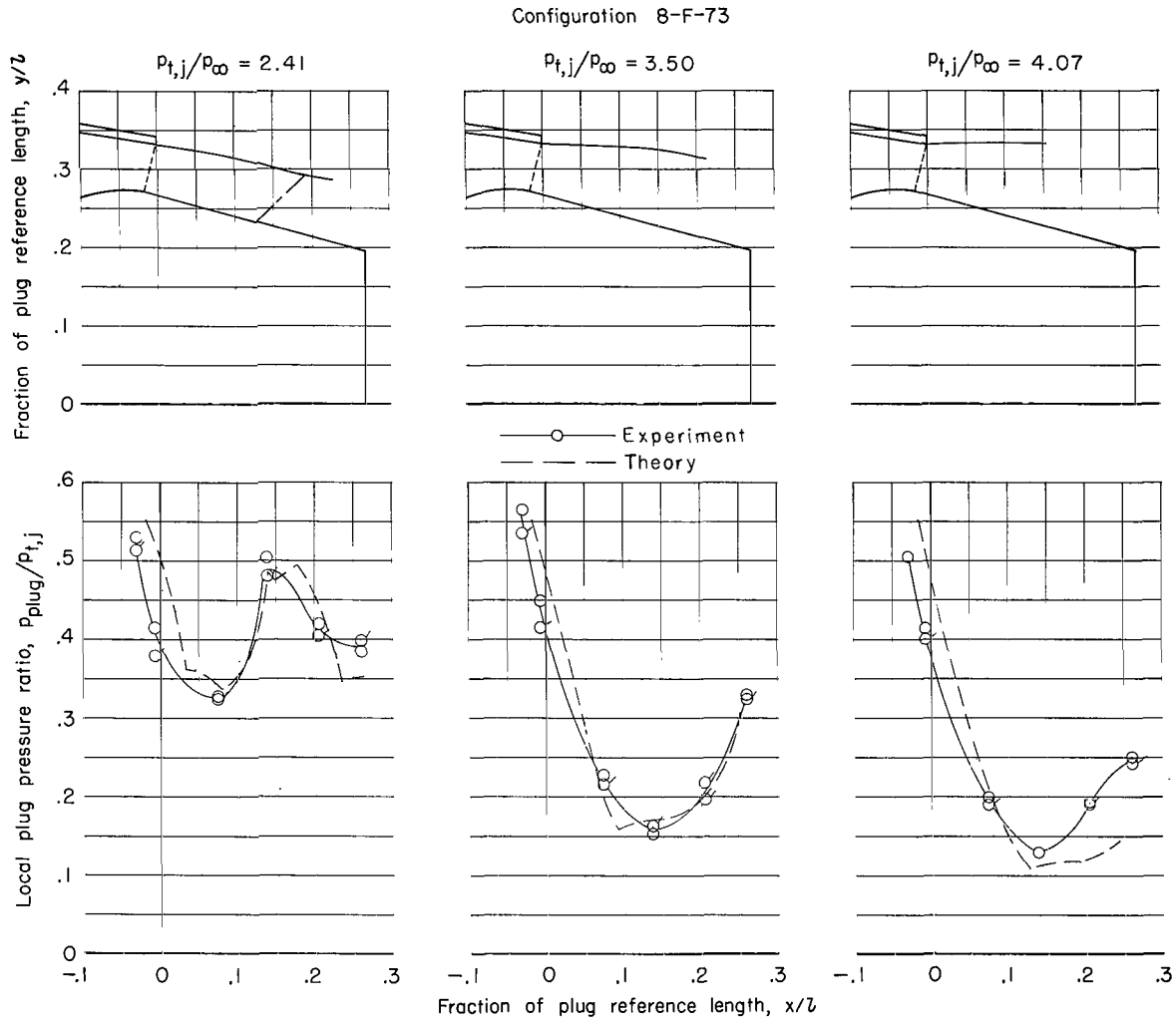

(a) Configuration 8-F-73.

Figure 16.- Comparison of theoretical and experimental plug static-pressure distributions on configurations 8-F-73 and 20-F-73. Dash-dot-dash lines represent location of shock waves or regions of strong compression; symbols with flags indicate row 180° orifices.

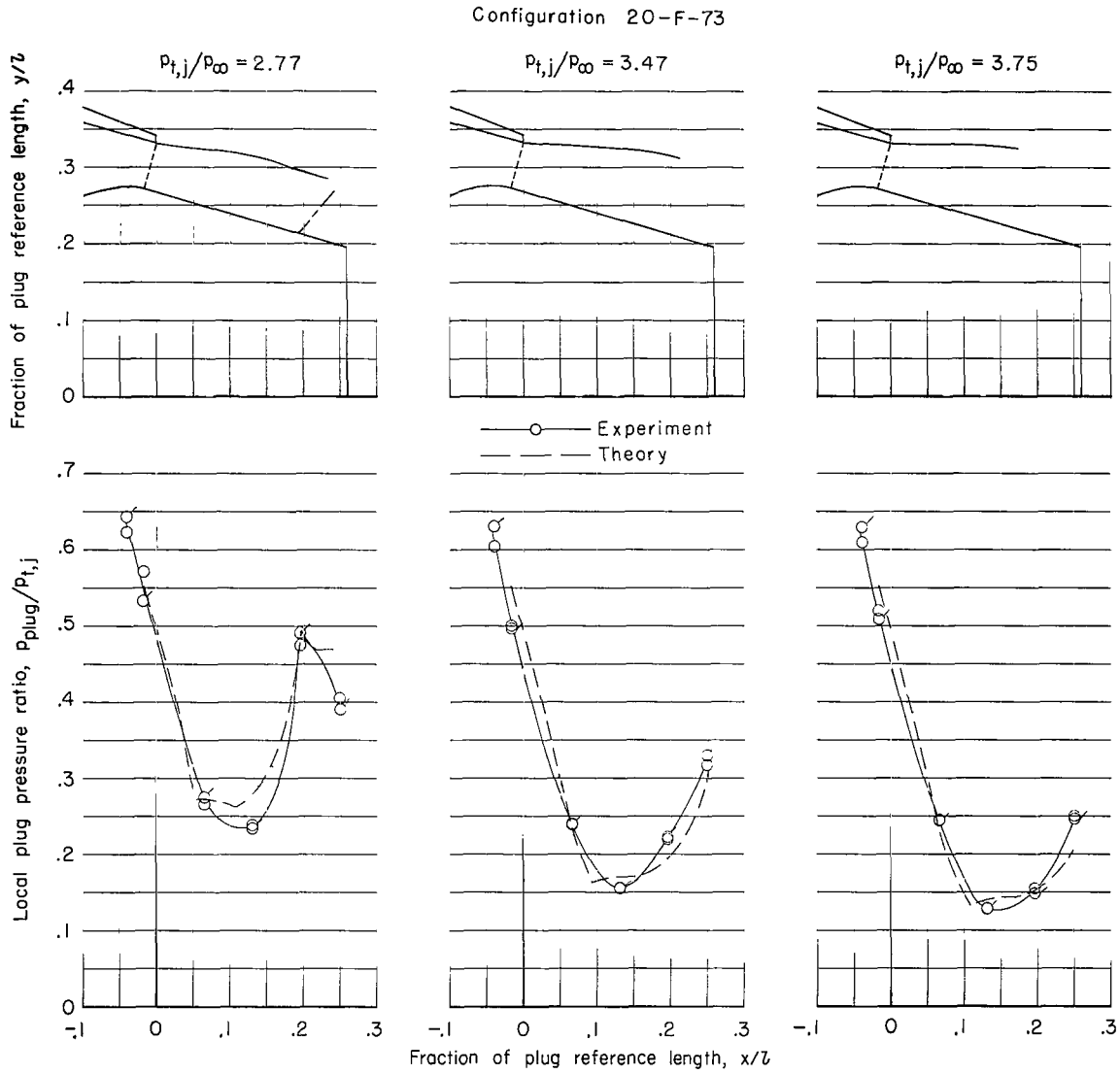

(b) Configuration 20-F-73.

Figure 16.- Concluded.

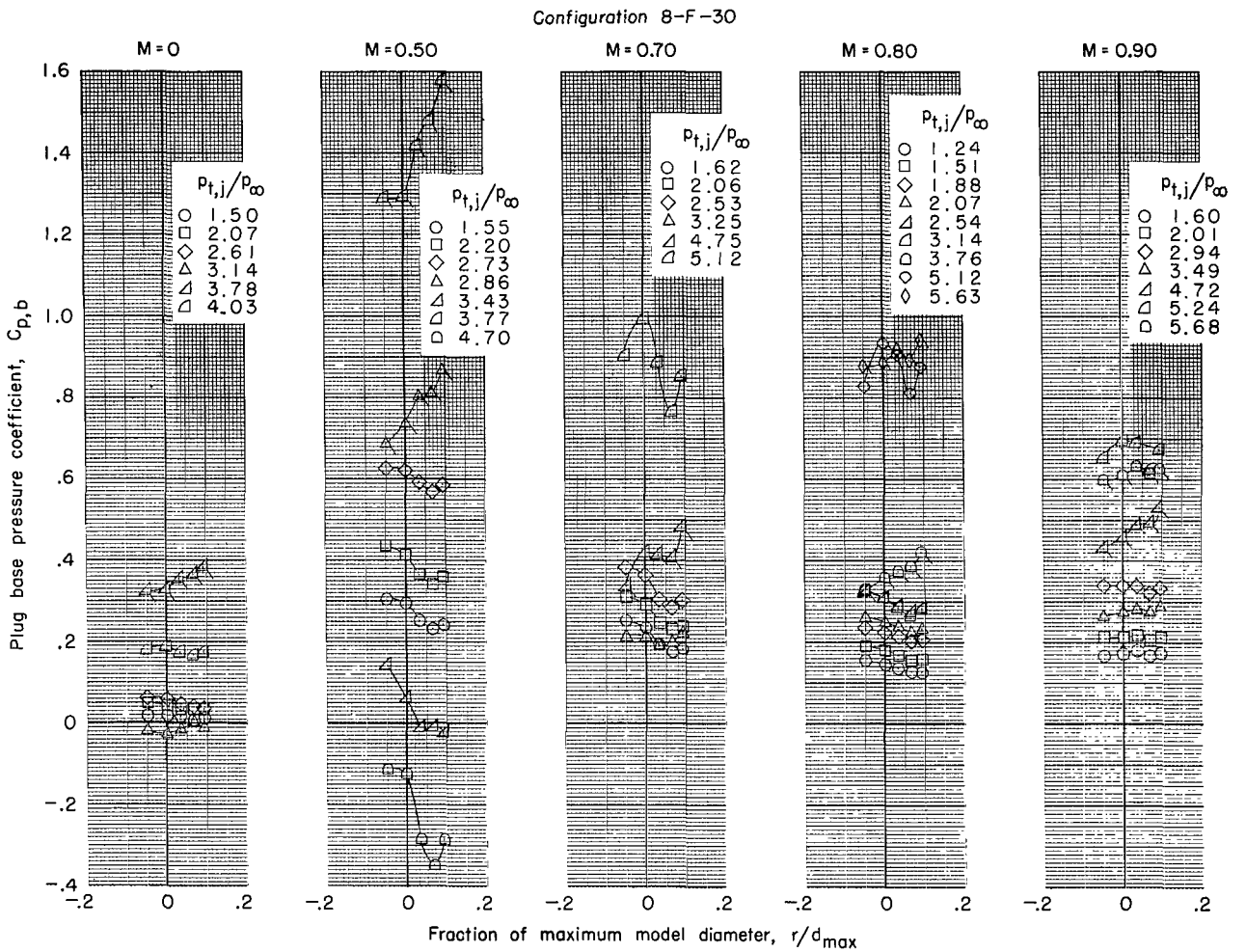

(a) M = 0 to M = 0.90.

Figure 17.- Effect of jet total-pressure ratio on plug base-pressure distributions of configuration 8-F-30 for various Mach numbers. Tailed symbols denote decreasing pressure ratio.

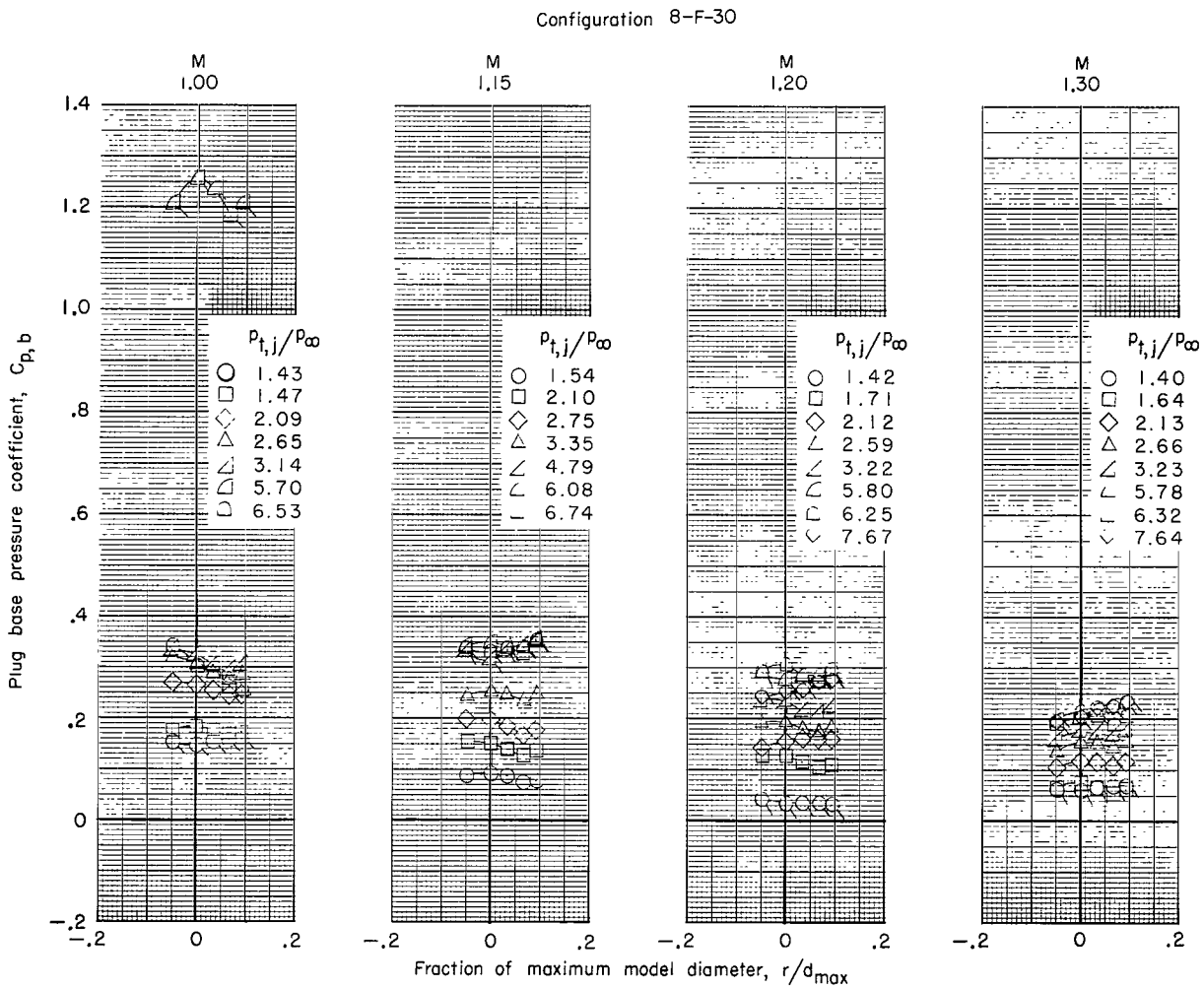

(b) M = 1.00 to M = 1.30.

Figure 17.- Concluded.

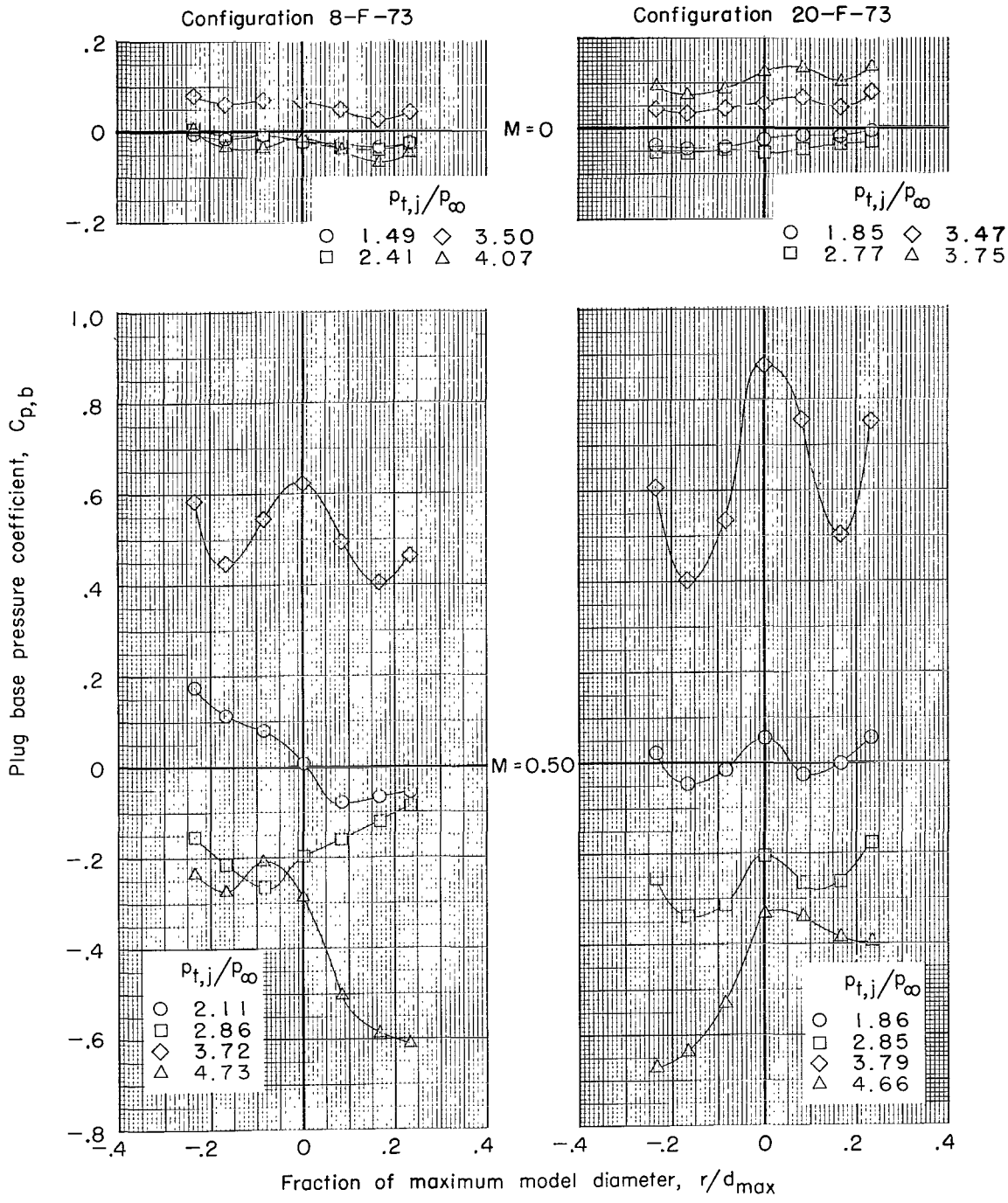

(a) M = 0 and M = 0.50.

Figure 18.- Effect of jet total-pressure ratio on plug base pressure distributions of configurations 8-F-73 and 20-F-73 for various Mach numbers.

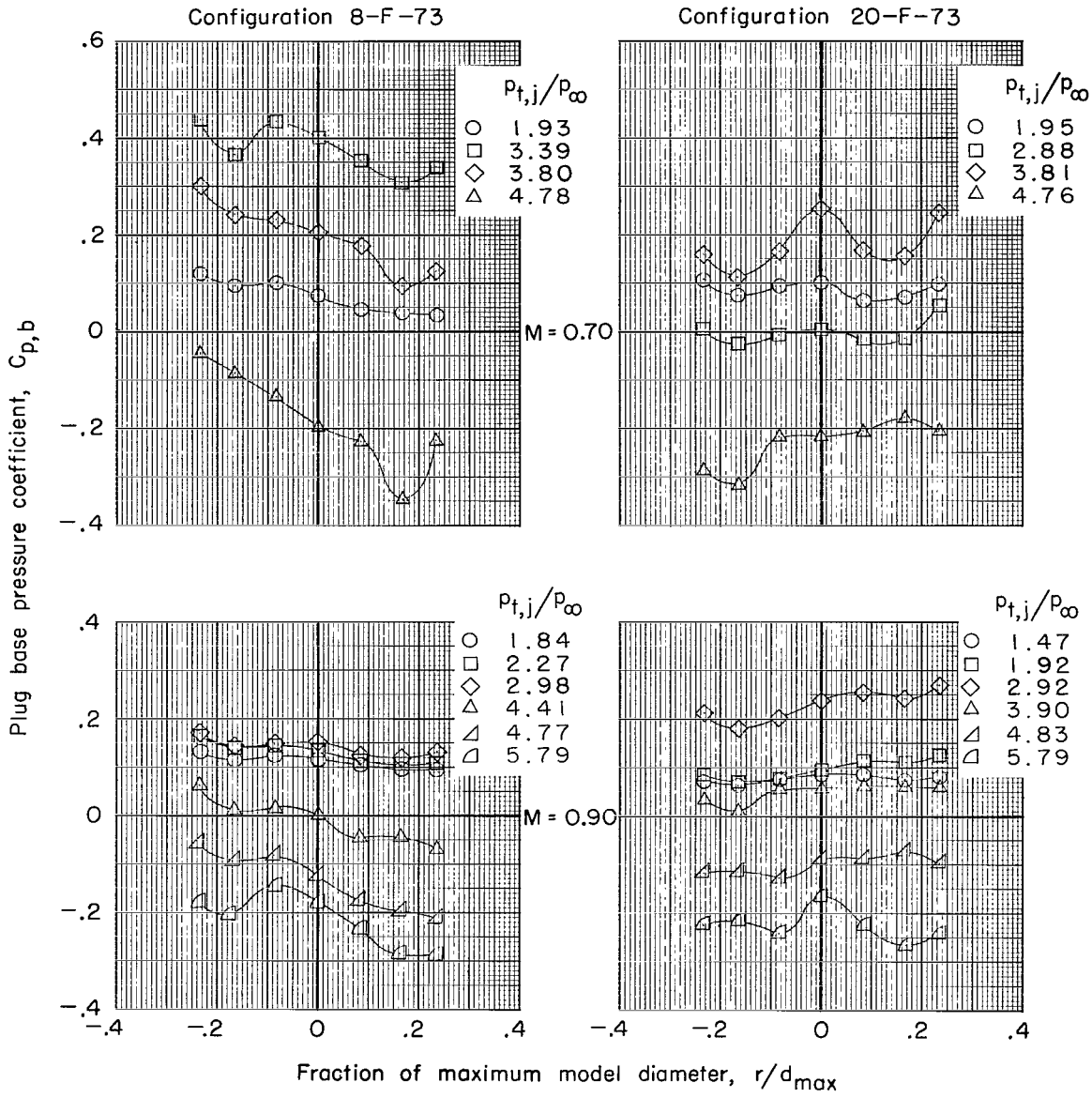

(b) M = 0.70 and M = 0.90.

Figure 18.- Continued.

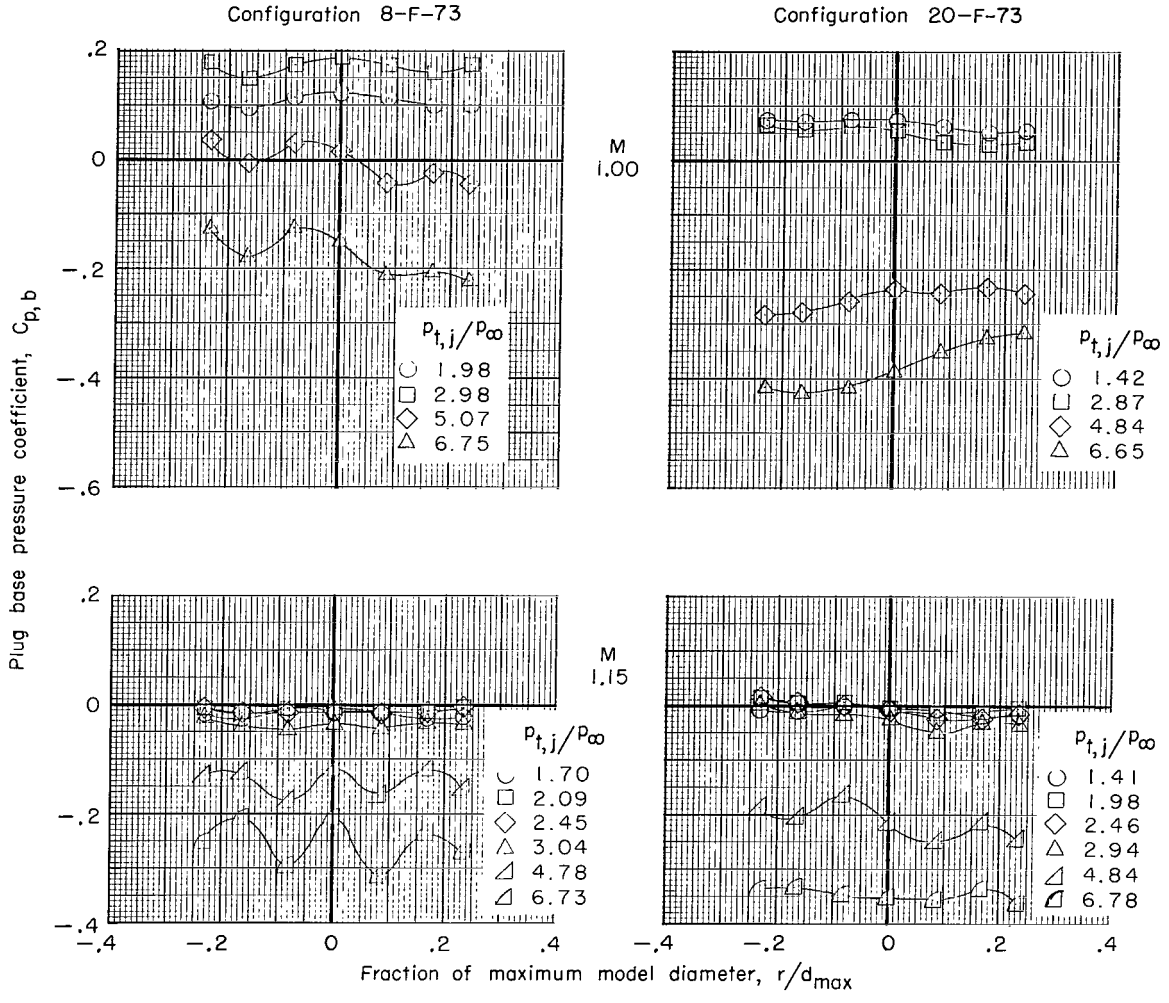

(c) M = 1.00 and M = 1.15.

Figure 18.- Continued.

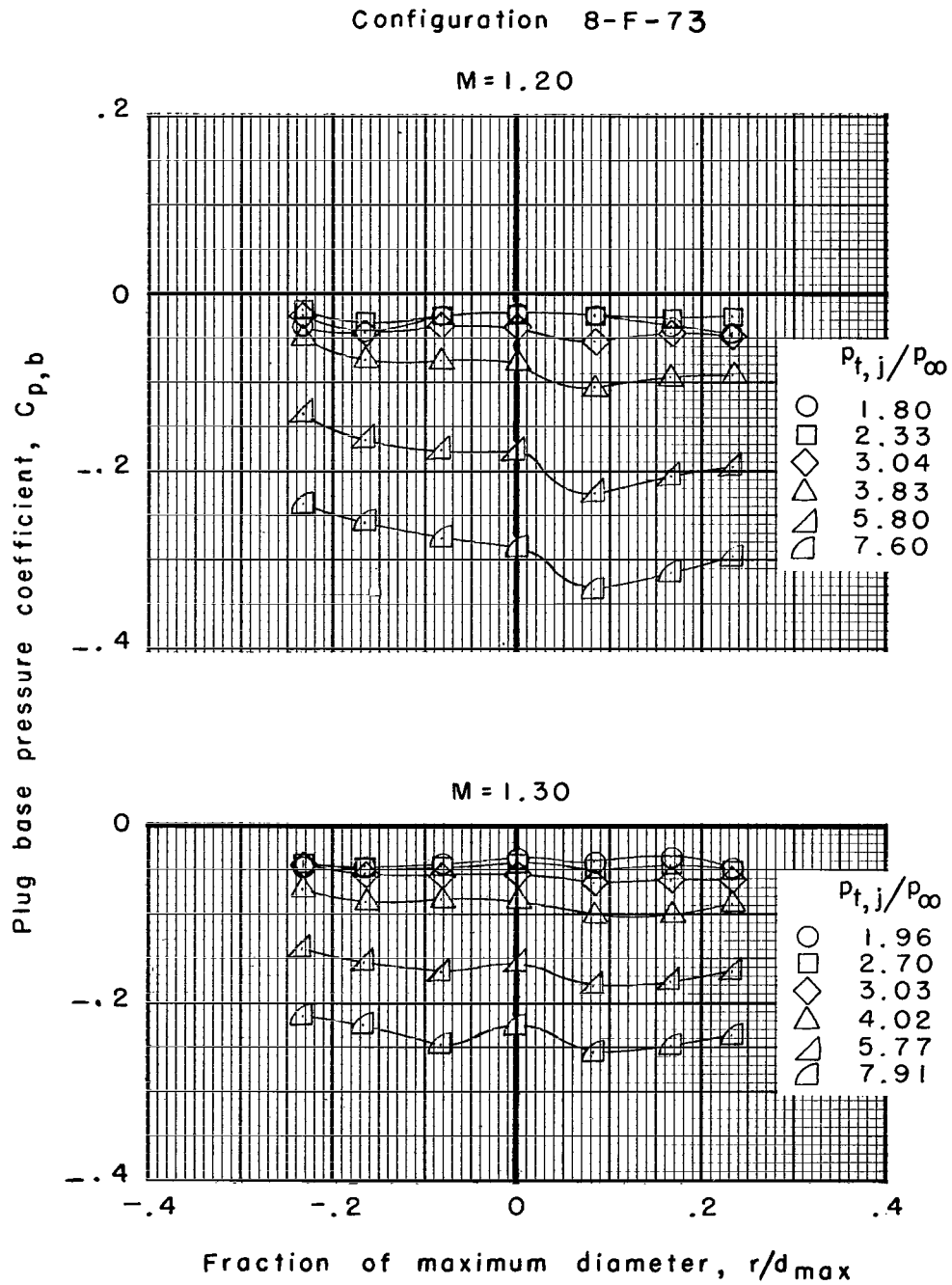

(d) M = 1.20 and M = 1.30.

Figure 18.- Concluded.

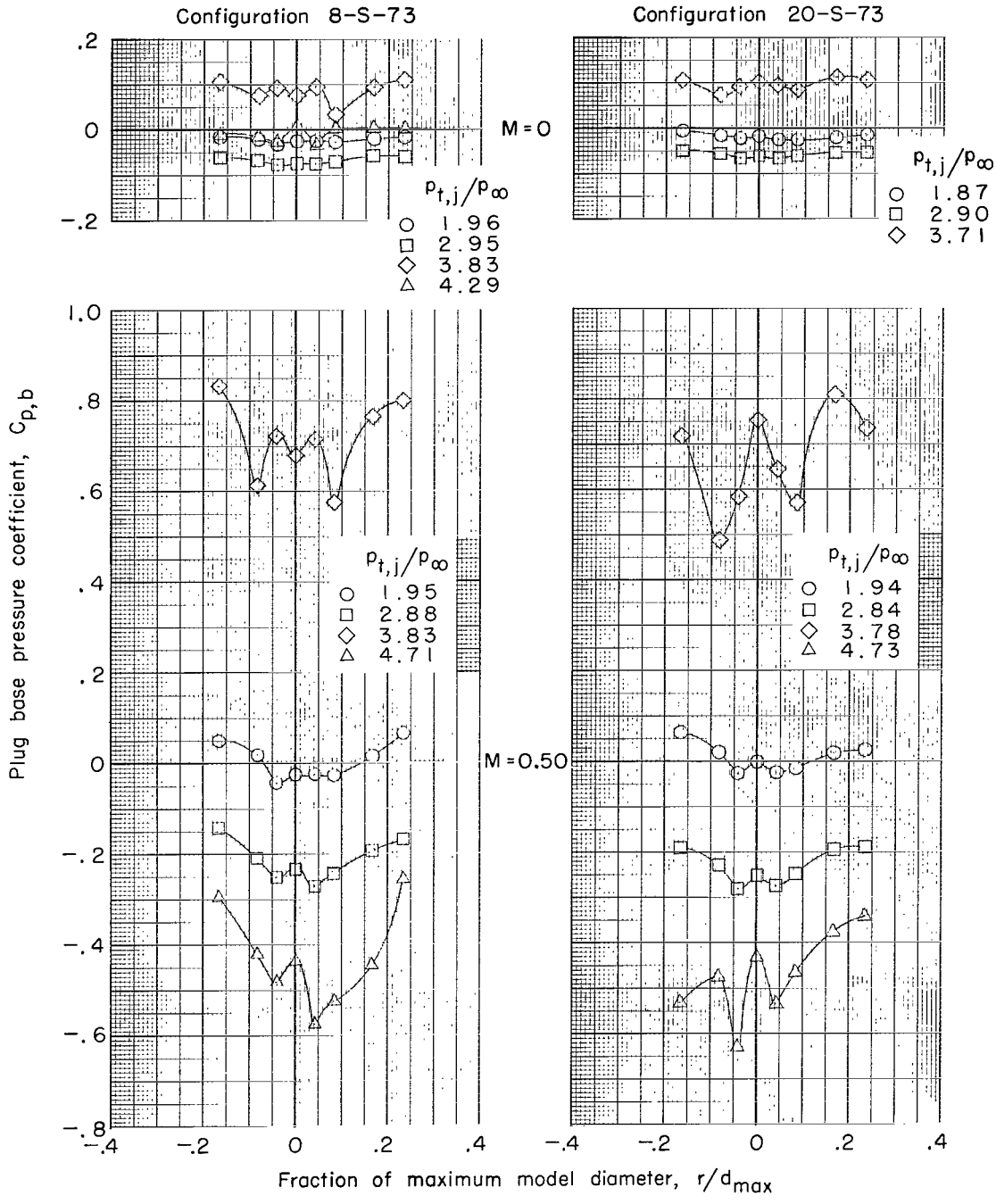

(a) M = 0 and M = 0.50.

Figure 19.- Effect of jet total-pressure ratio on plug base pressure distributions of configurations 8-S-73 and 20-S-73 for various Mach numbers.

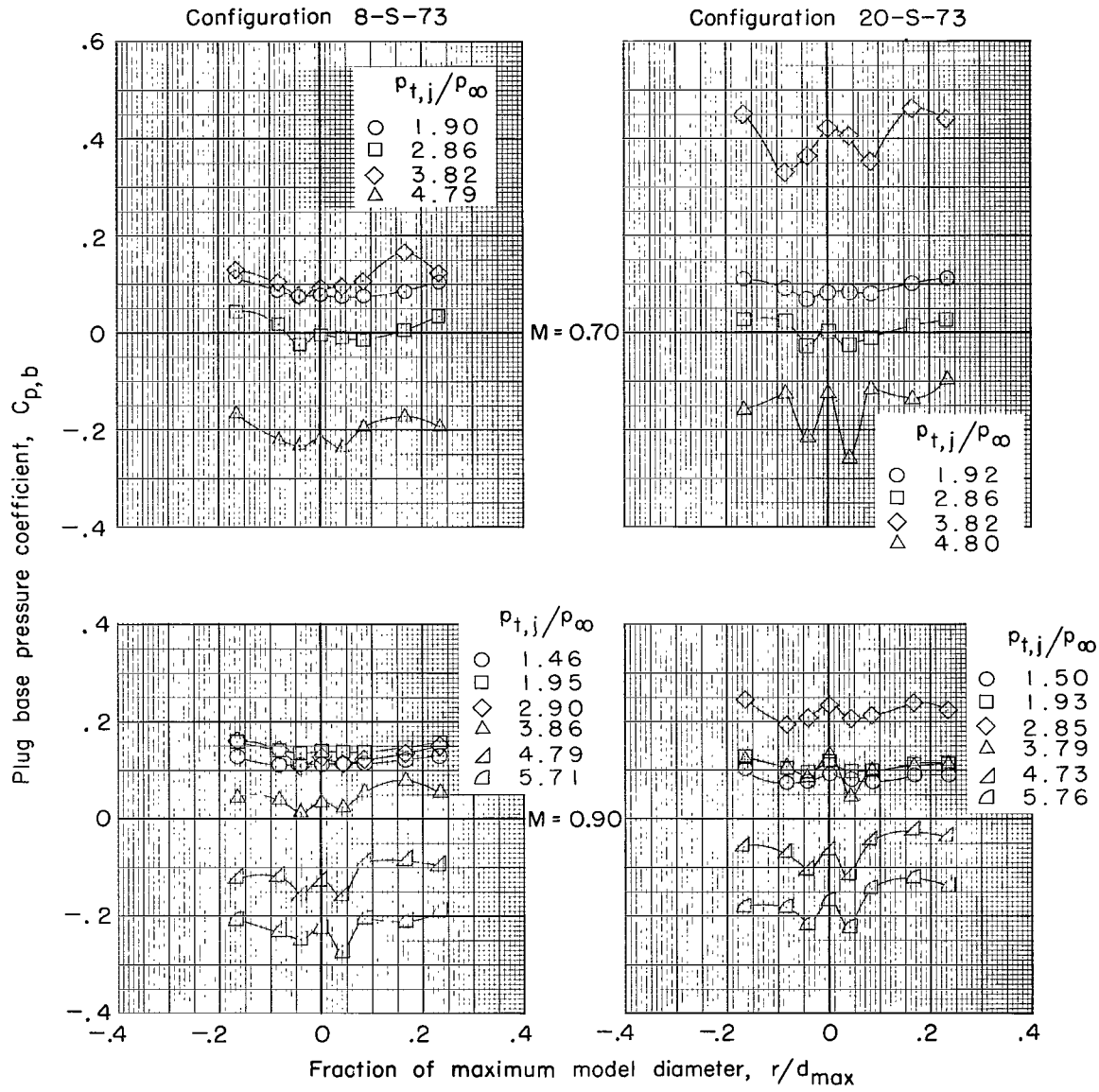

(b) M = 0.70 and M = 0.90.

Figure 19.- Continued.

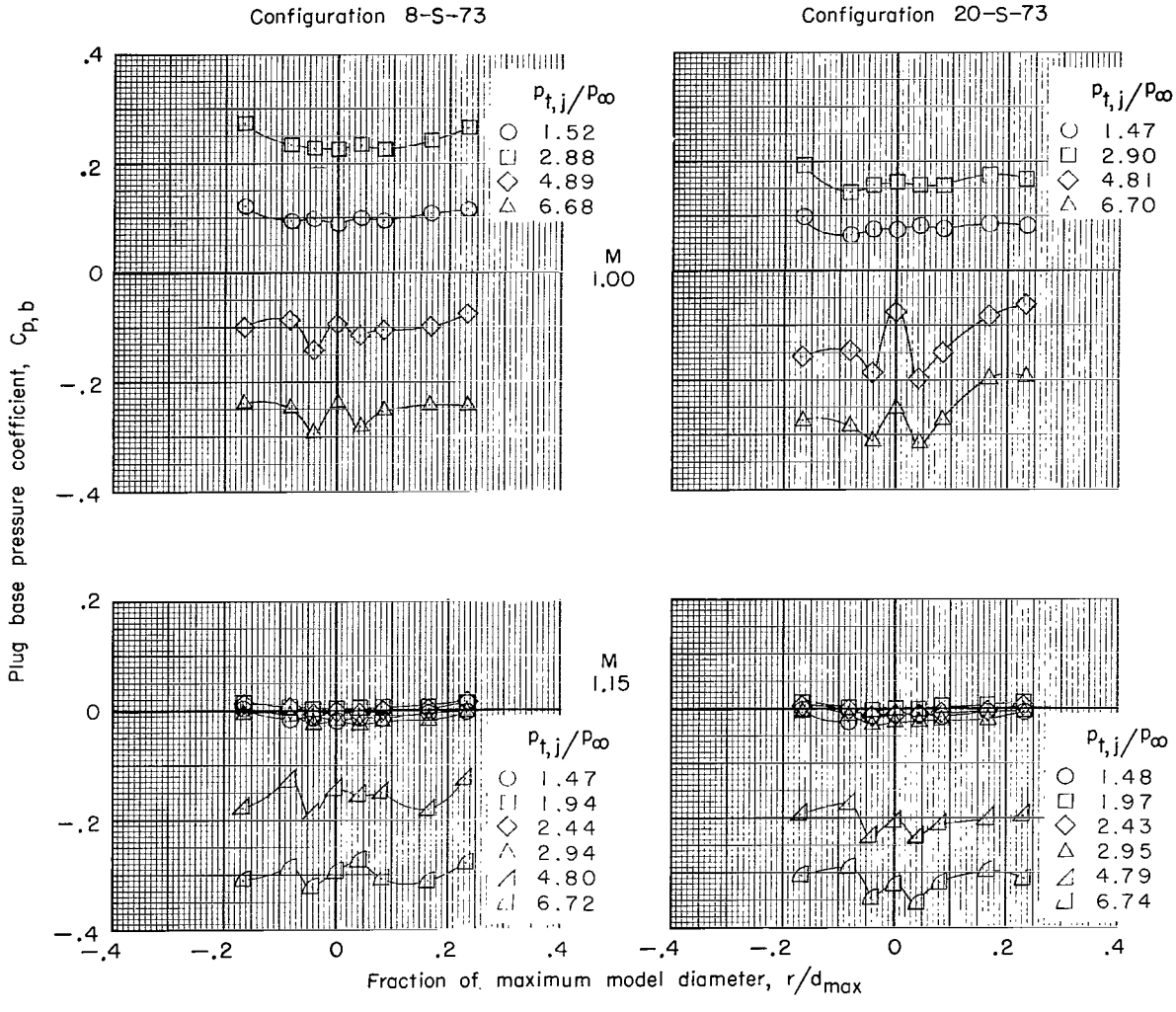

(c) M = 1.00 and M = 1.15.

Figure 19.- Continued.

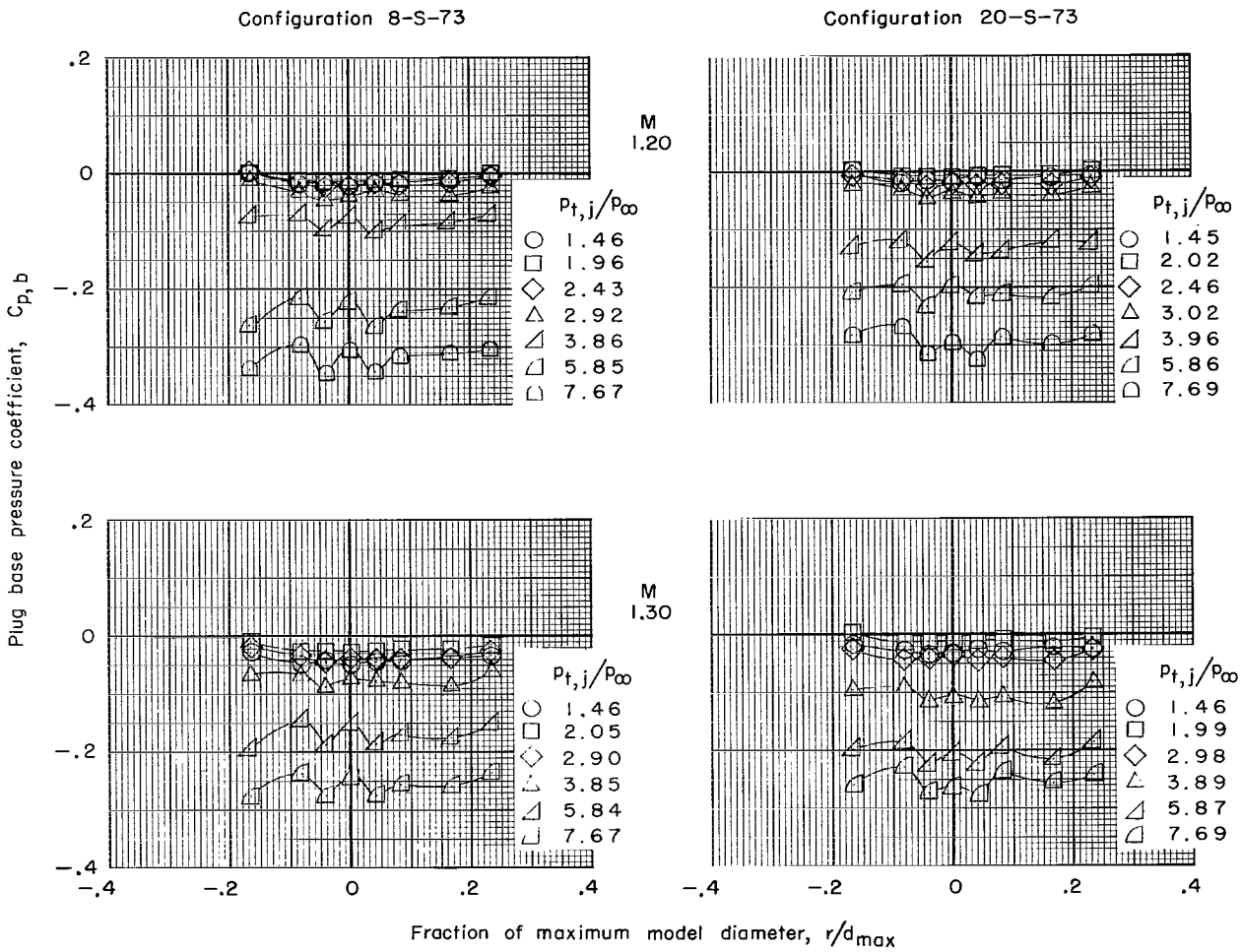

(d) M = 1.20 and M = 1.30.

Figure 19.- Concluded.

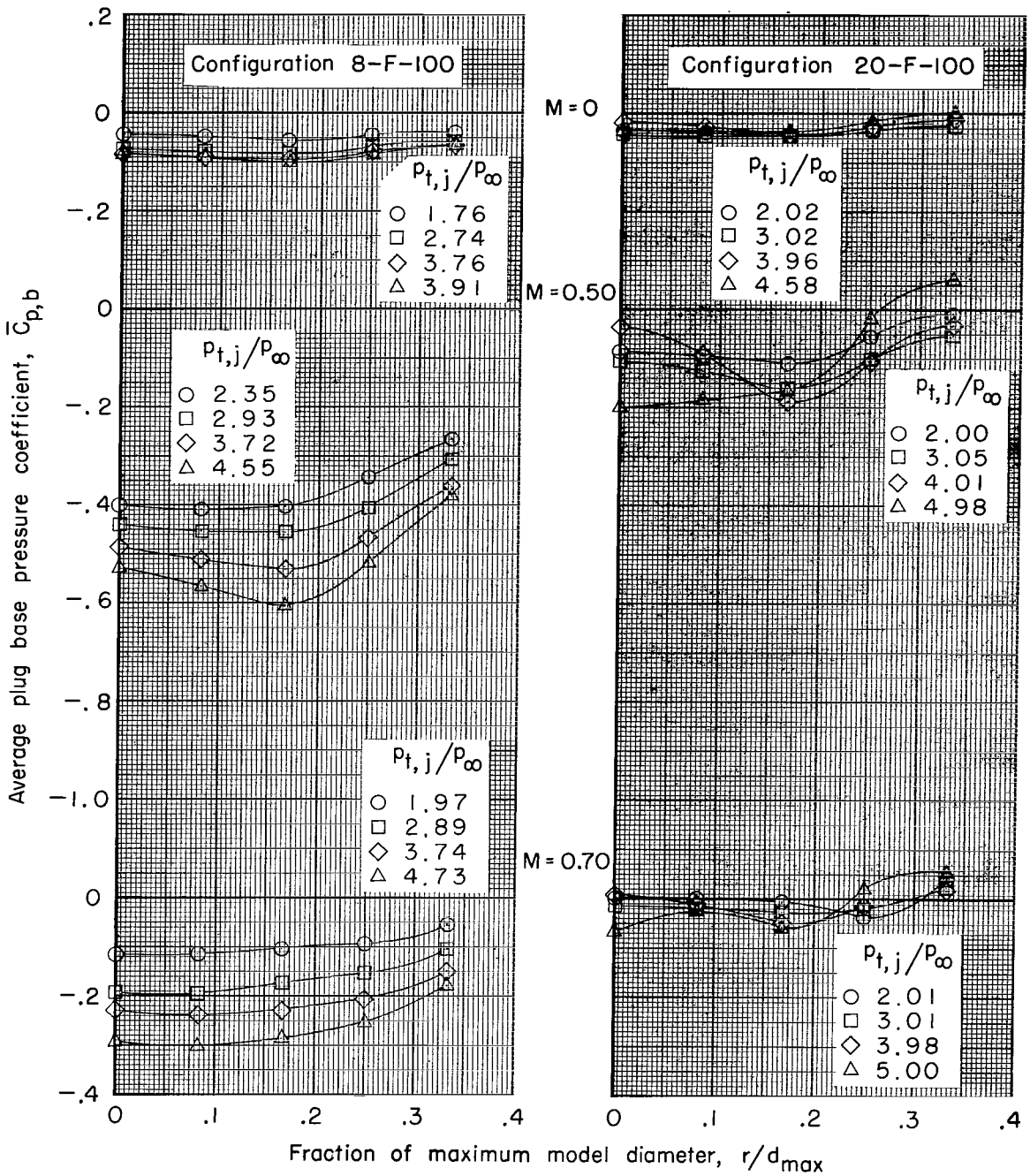

(a) M = 0 to M = 0.70.

Figure 20.- Effect of jet total-pressure ratio on average plug base pressure distributions of configurations 8-F-100 and 20-F-100 for various Mach numbers.

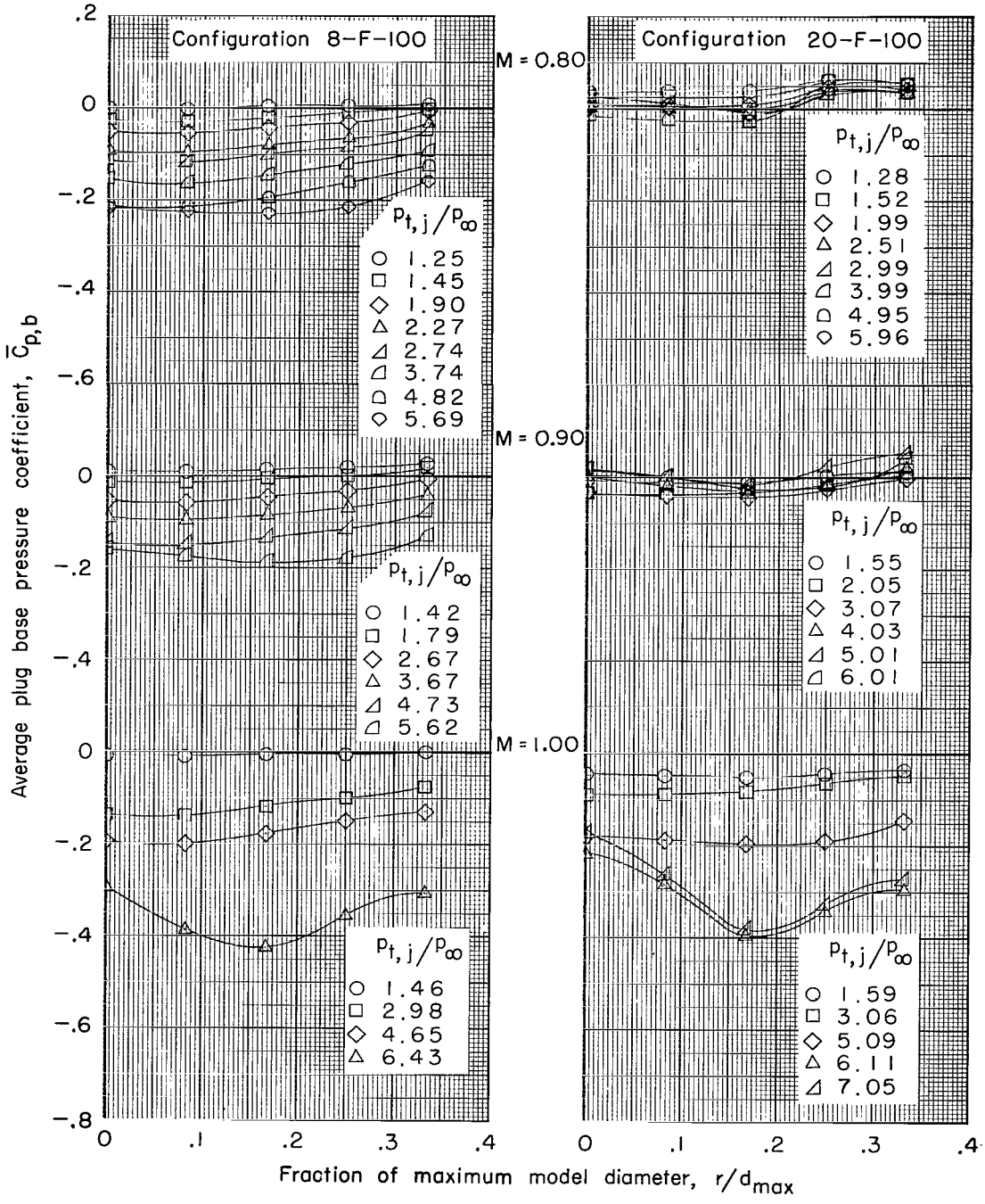

(b) M = 0.80 to M = 1.00.

Figure 20.- Continued.

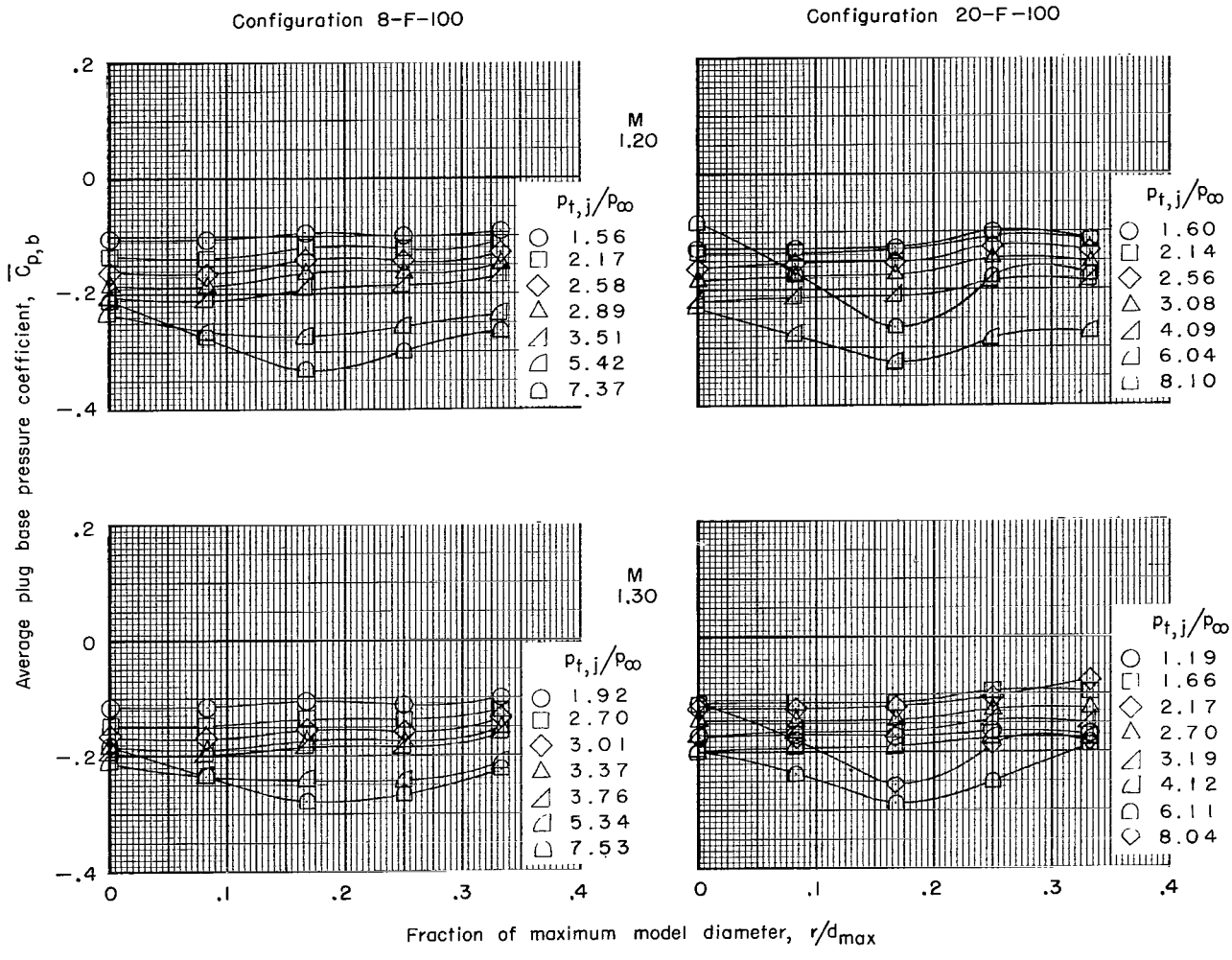

(c) M = 1.20 and M = 1.30.

Figure 20.- Concluded.

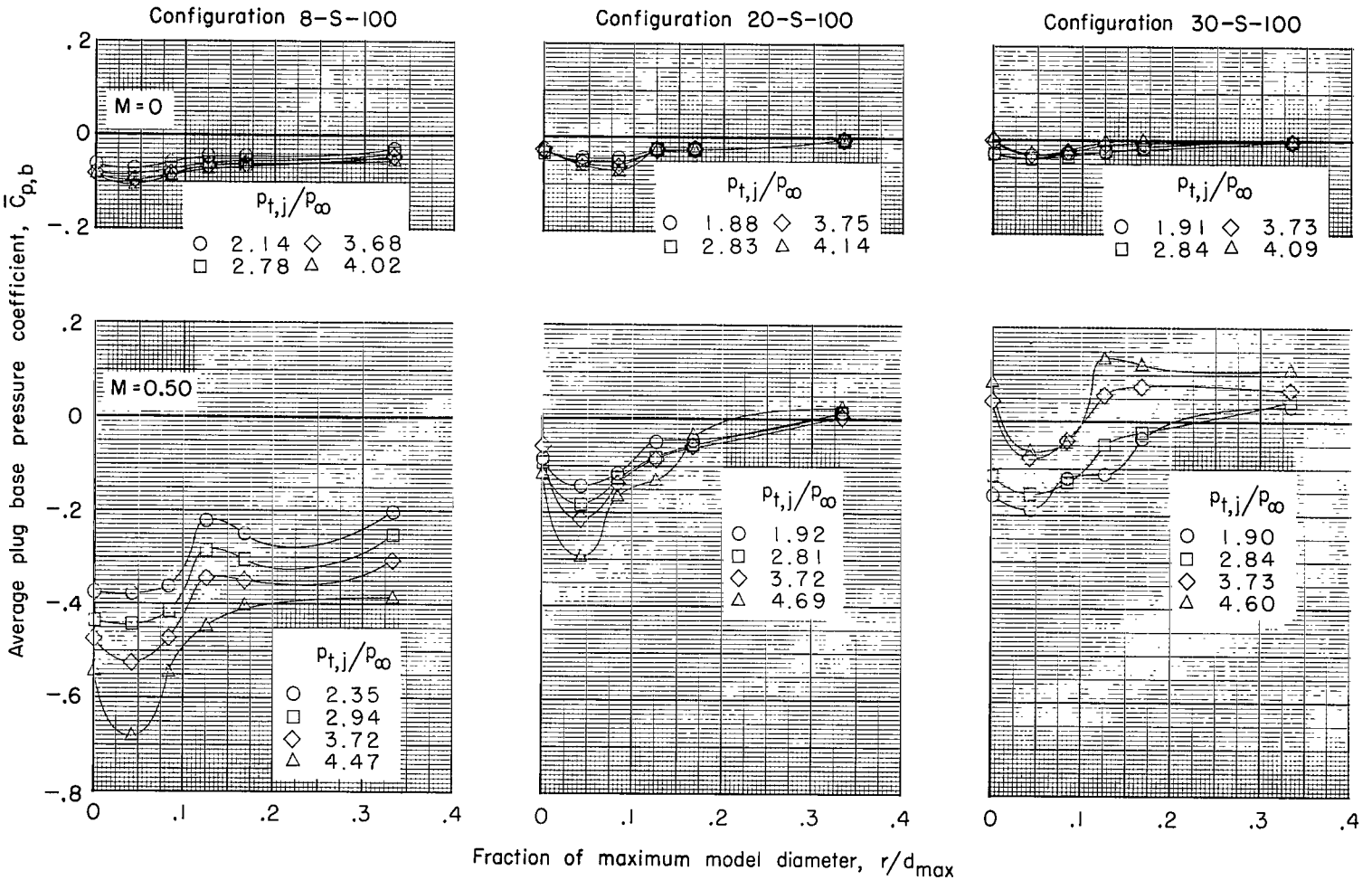

(a) M = 0 and M = 0.50.

Figure 21.- Effect of jet total-pressure ratio on average plug base pressure distributions of configurations 8-S-100, 20-S-100, and 30-S-100 for various Mach numbers.

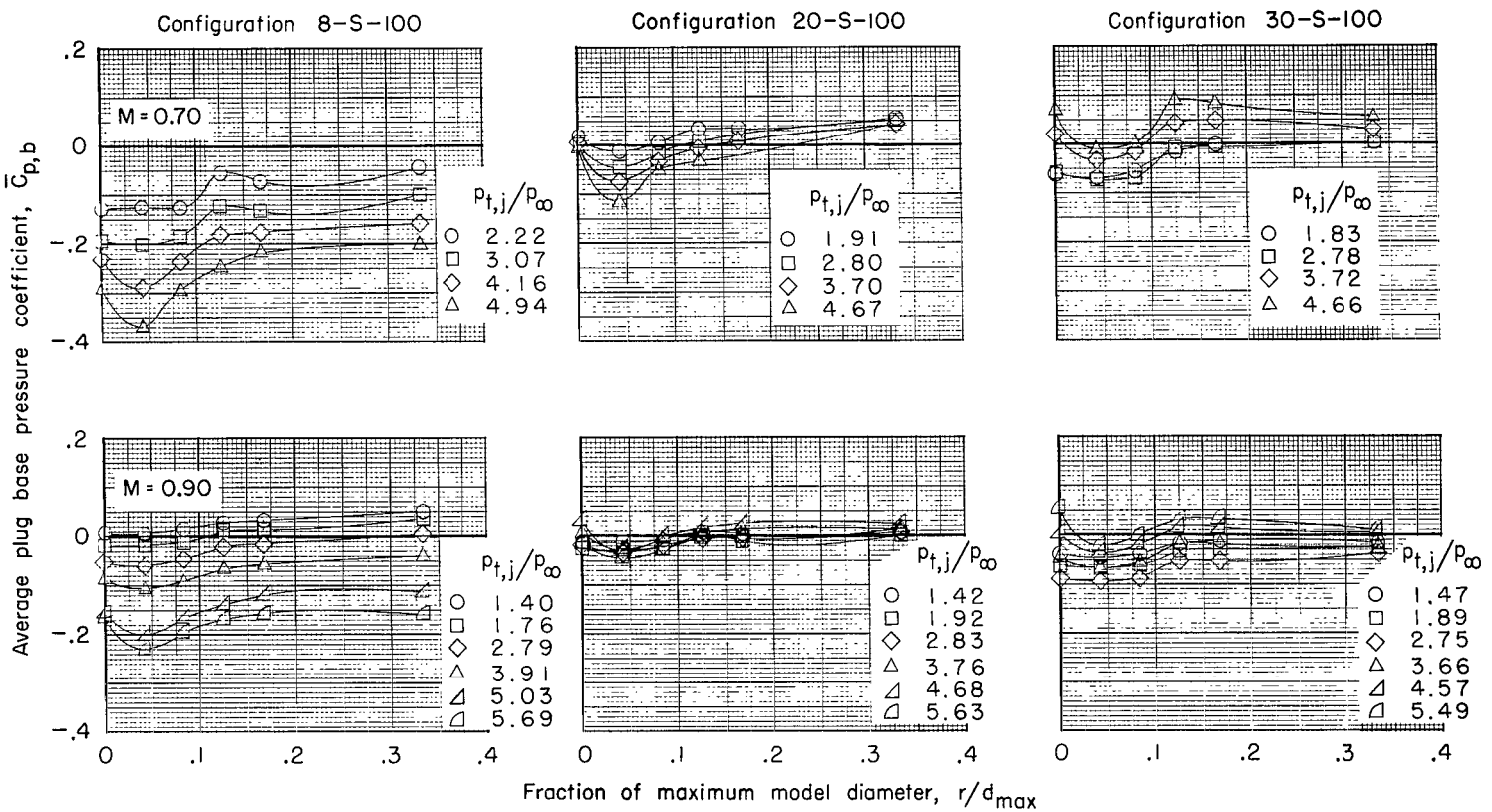

(b) M = 0.70 and M = 0.90.

Figure 21.- Continued.

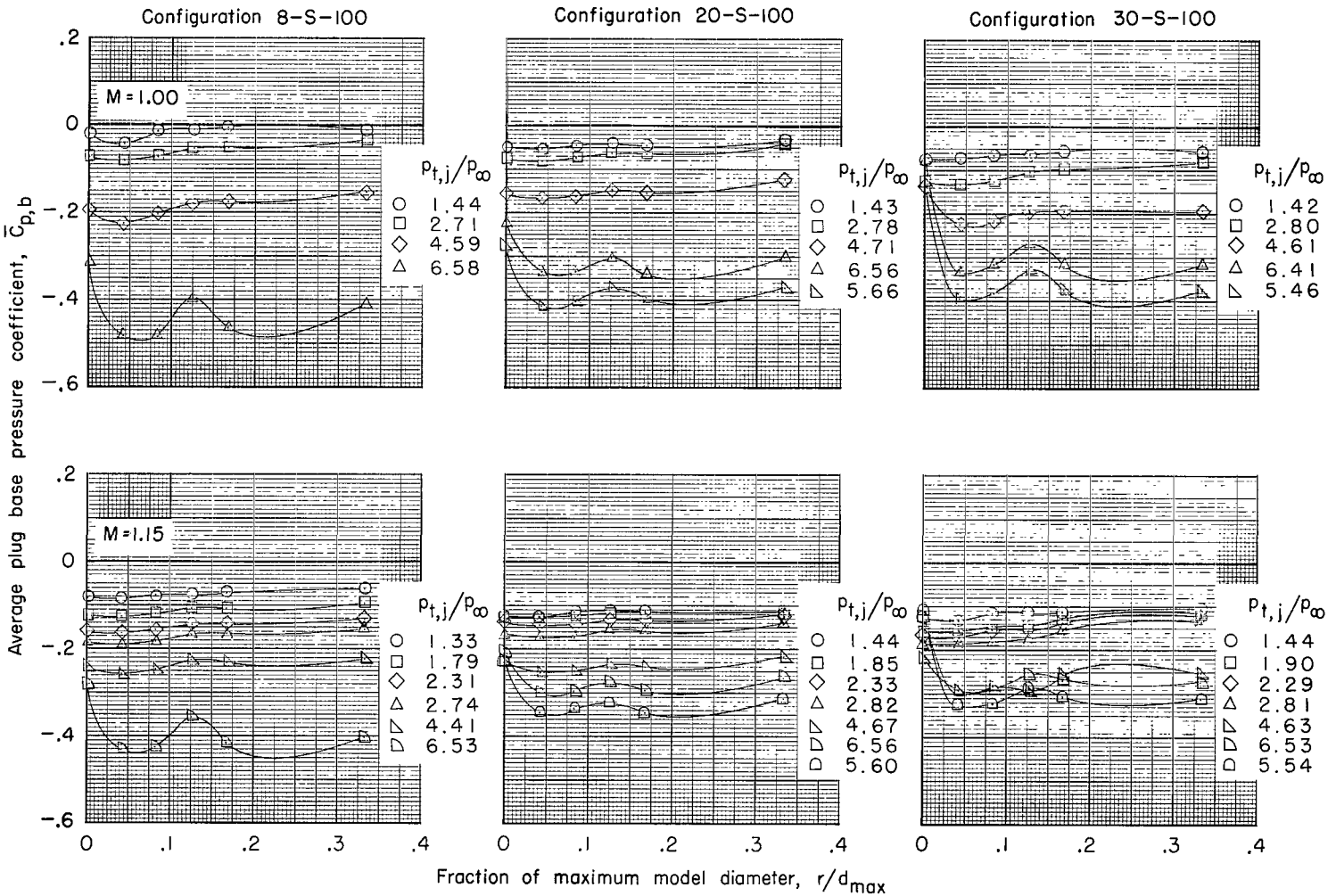

(c) M = 1.00 and M = 1.15.

Figure 21.- Continued.

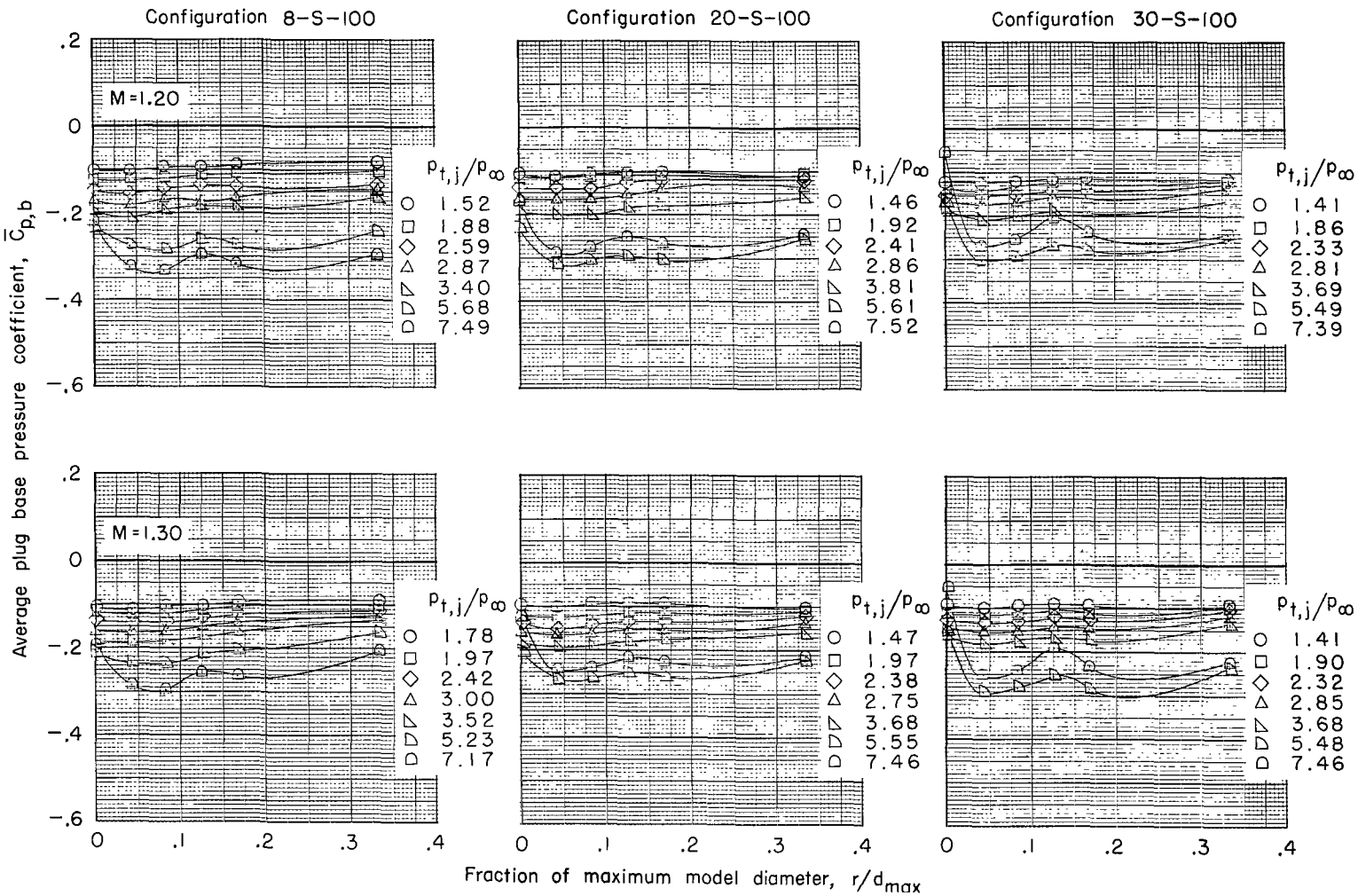

(d) M = 1.20 and M = 1.30.

Figure 21.- Concluded.

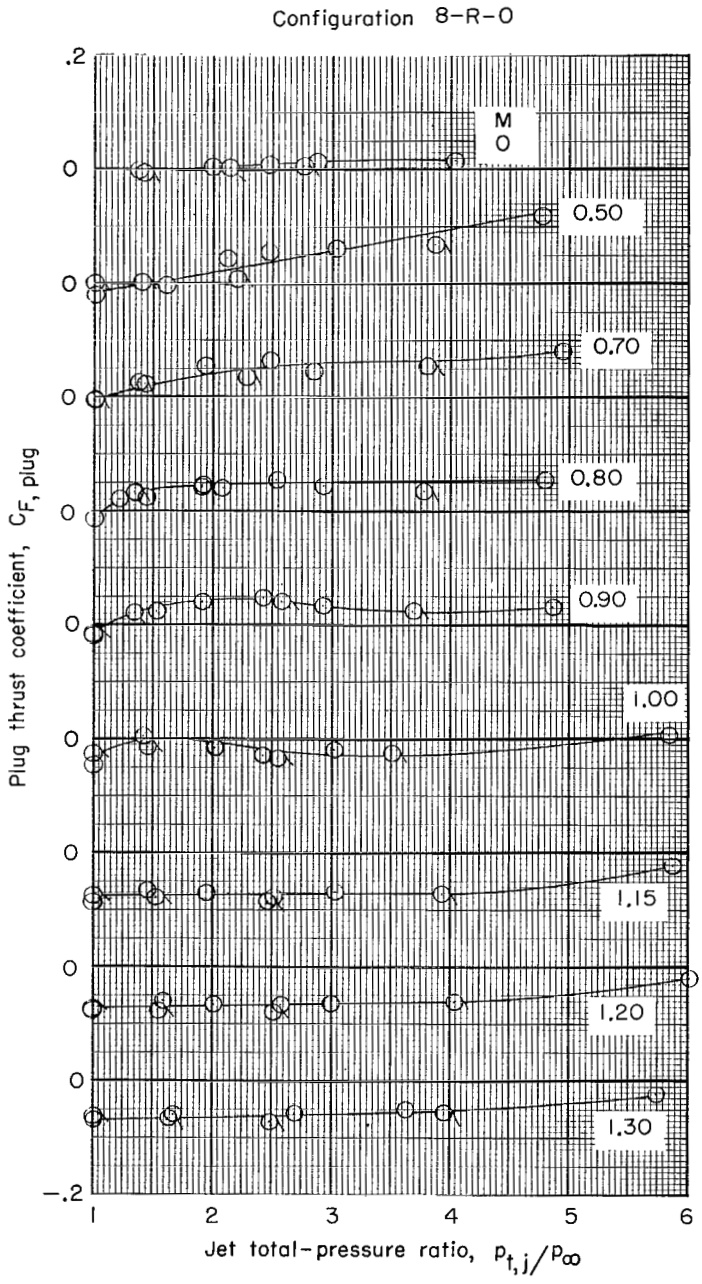

(a) Configuration 8-R-0.

Figure 22.- Variation of plug thrust coefficient with jet total-pressure ratio and Mach number. Tailed symbols indicate decreasing pressure ratios. (Note shifting scales.)

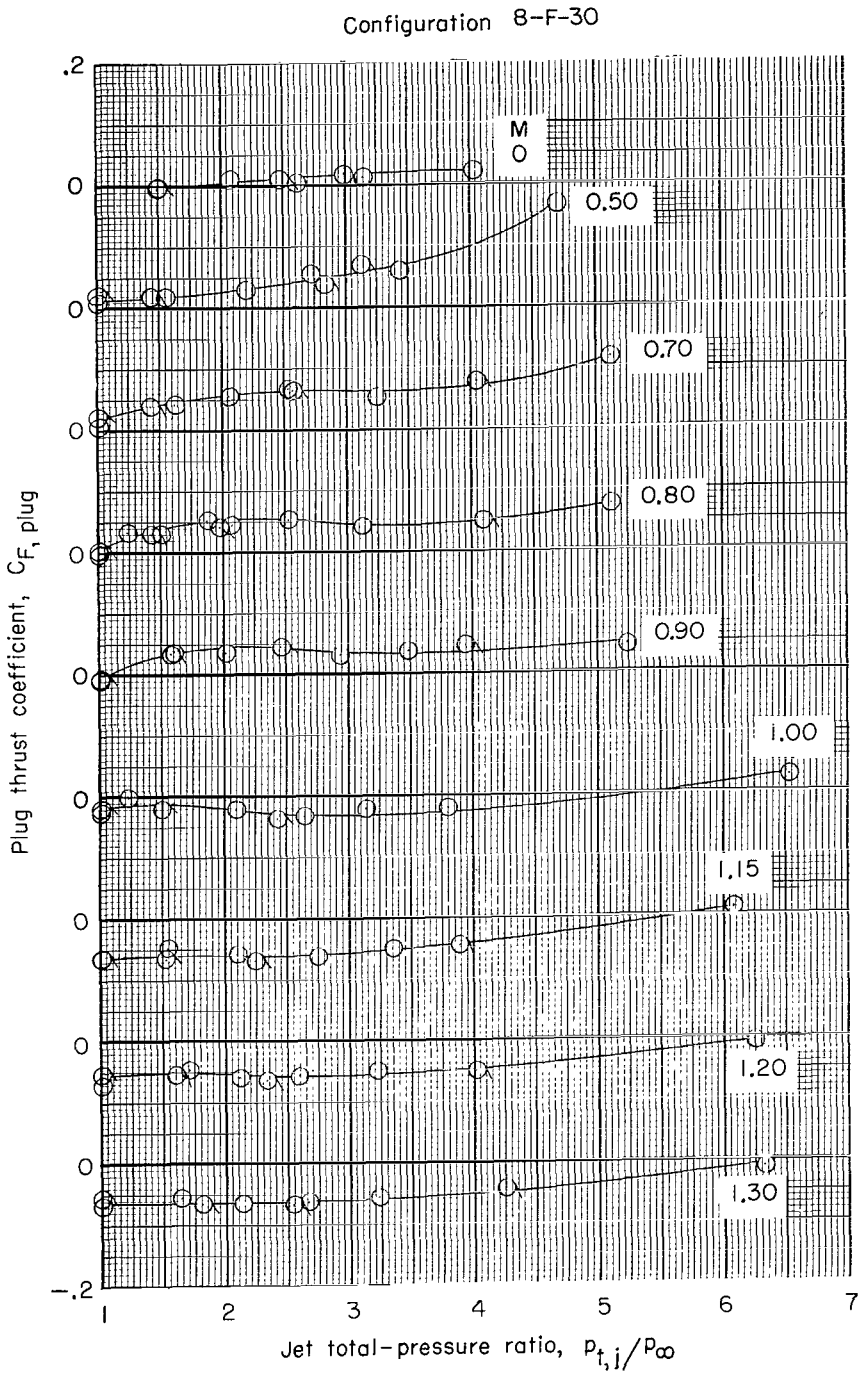

(b) Configuration 8-F-30.

Figure 22.- Continued.

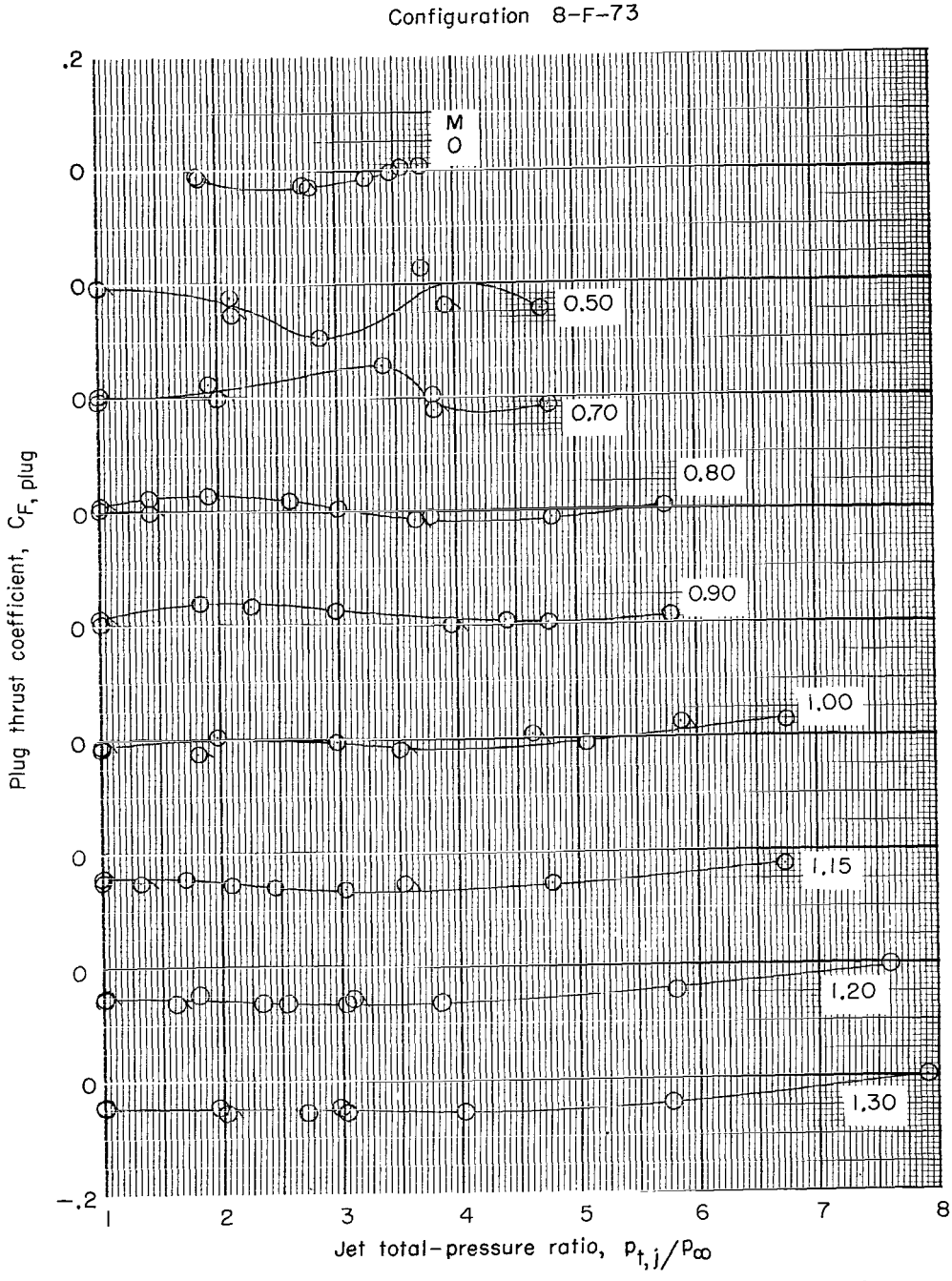

(c) Configuration 8-F-73.

Figure 22.- Continued.

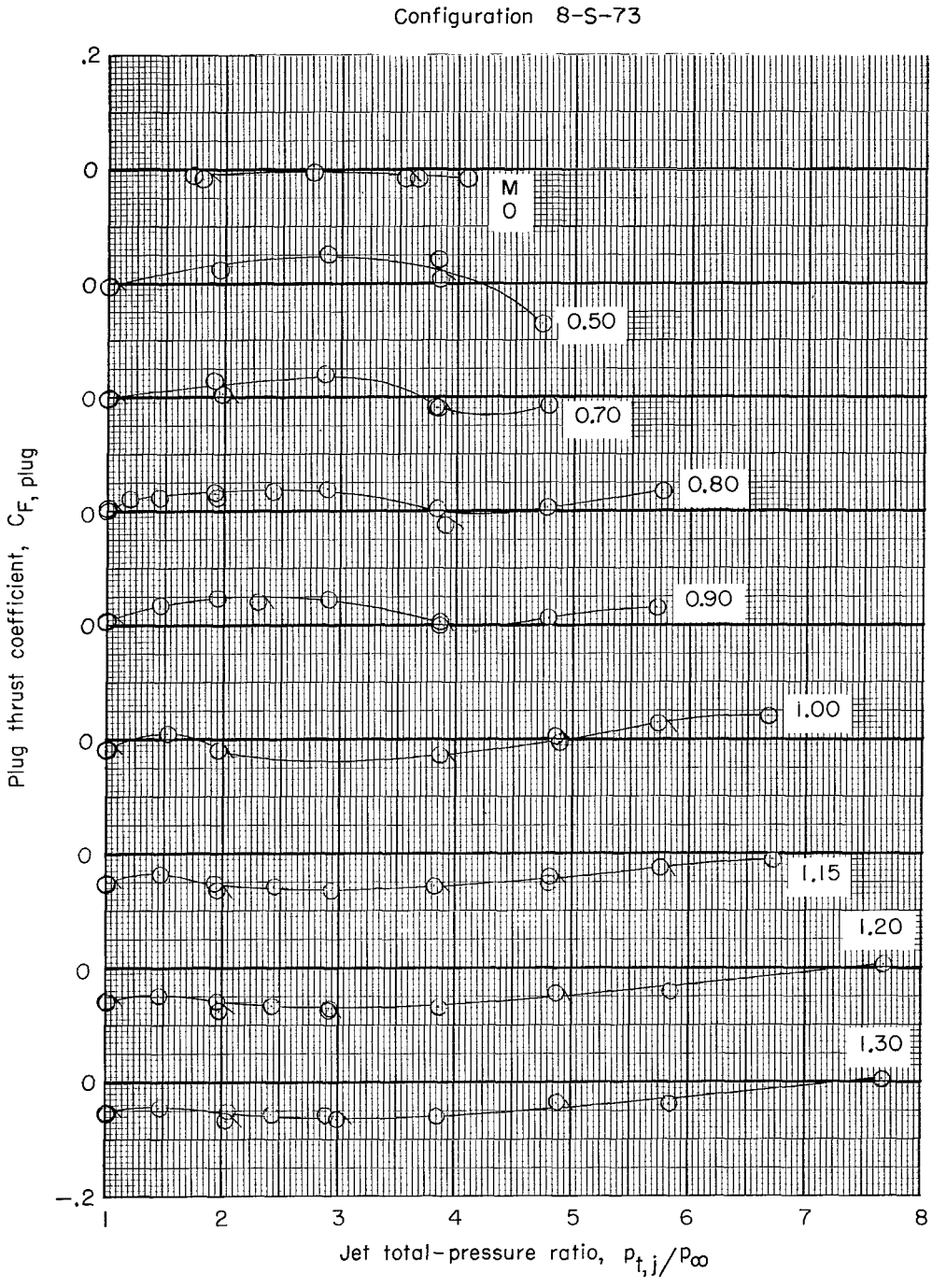

(d) Configuration 8-S-73.

Figure 22.- Continued.

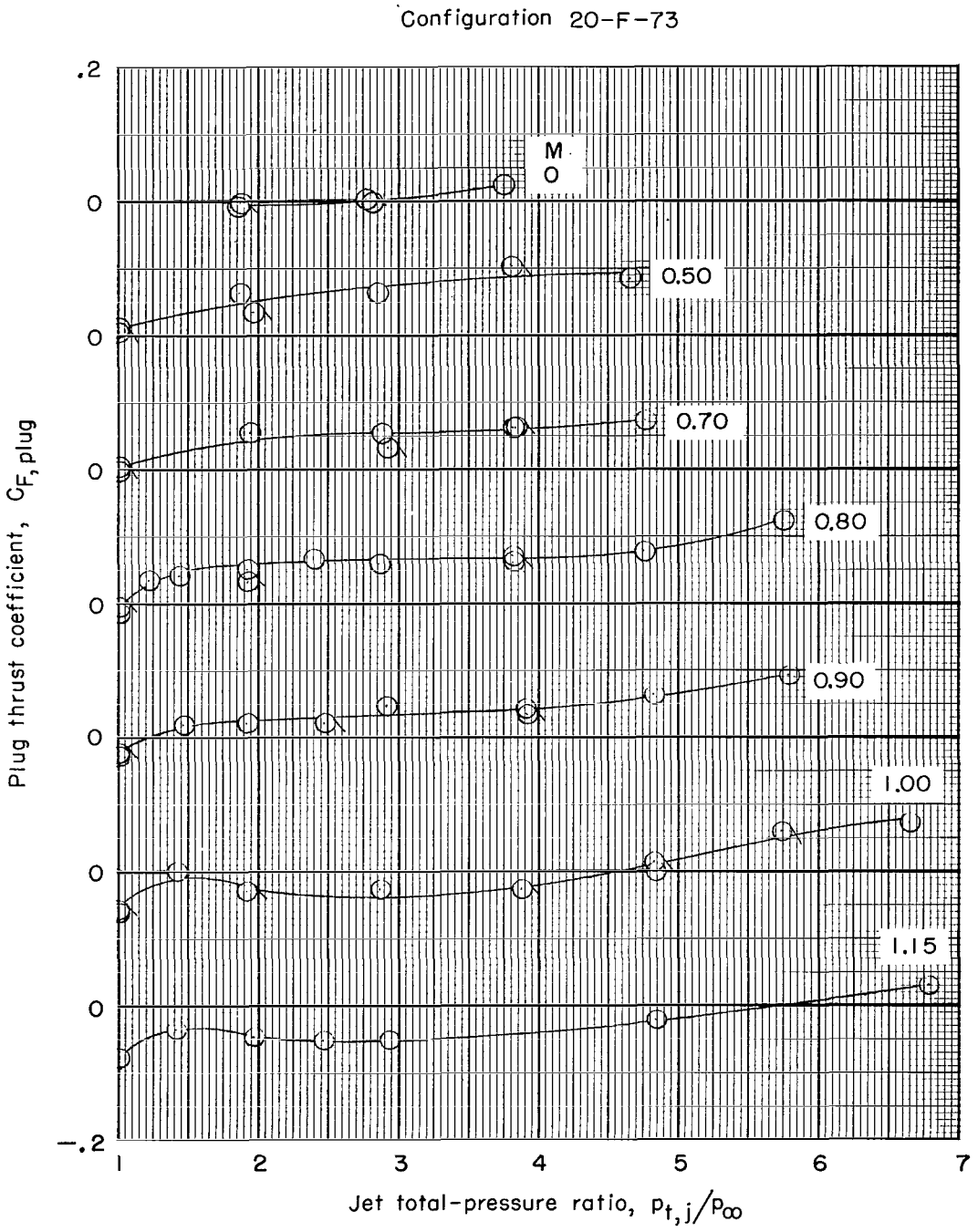

(e) Configuration 20-F-73.

Figure 22.- Continued.

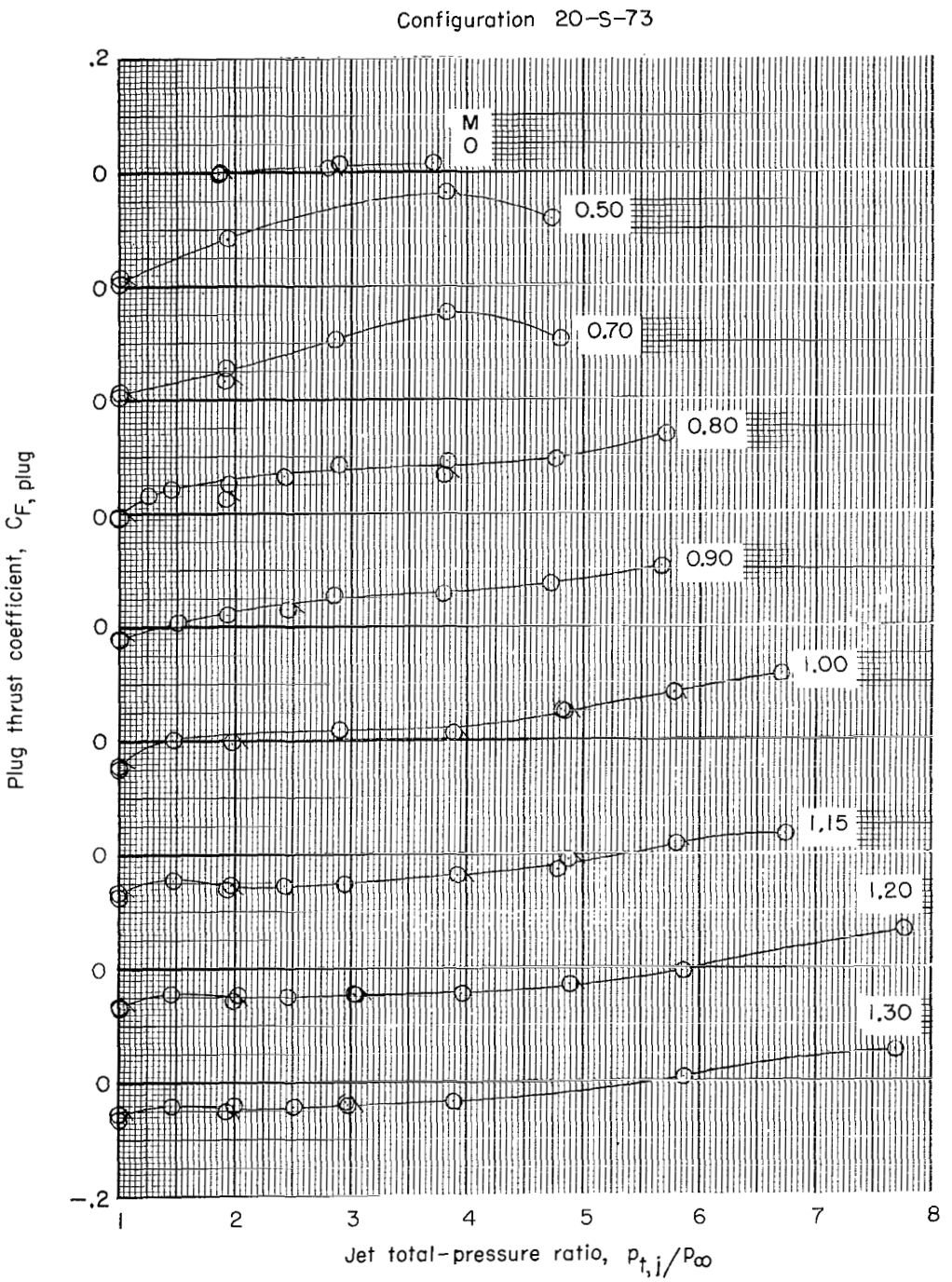

(f) Configuration 20-S-73.

Figure 22.- Continued.

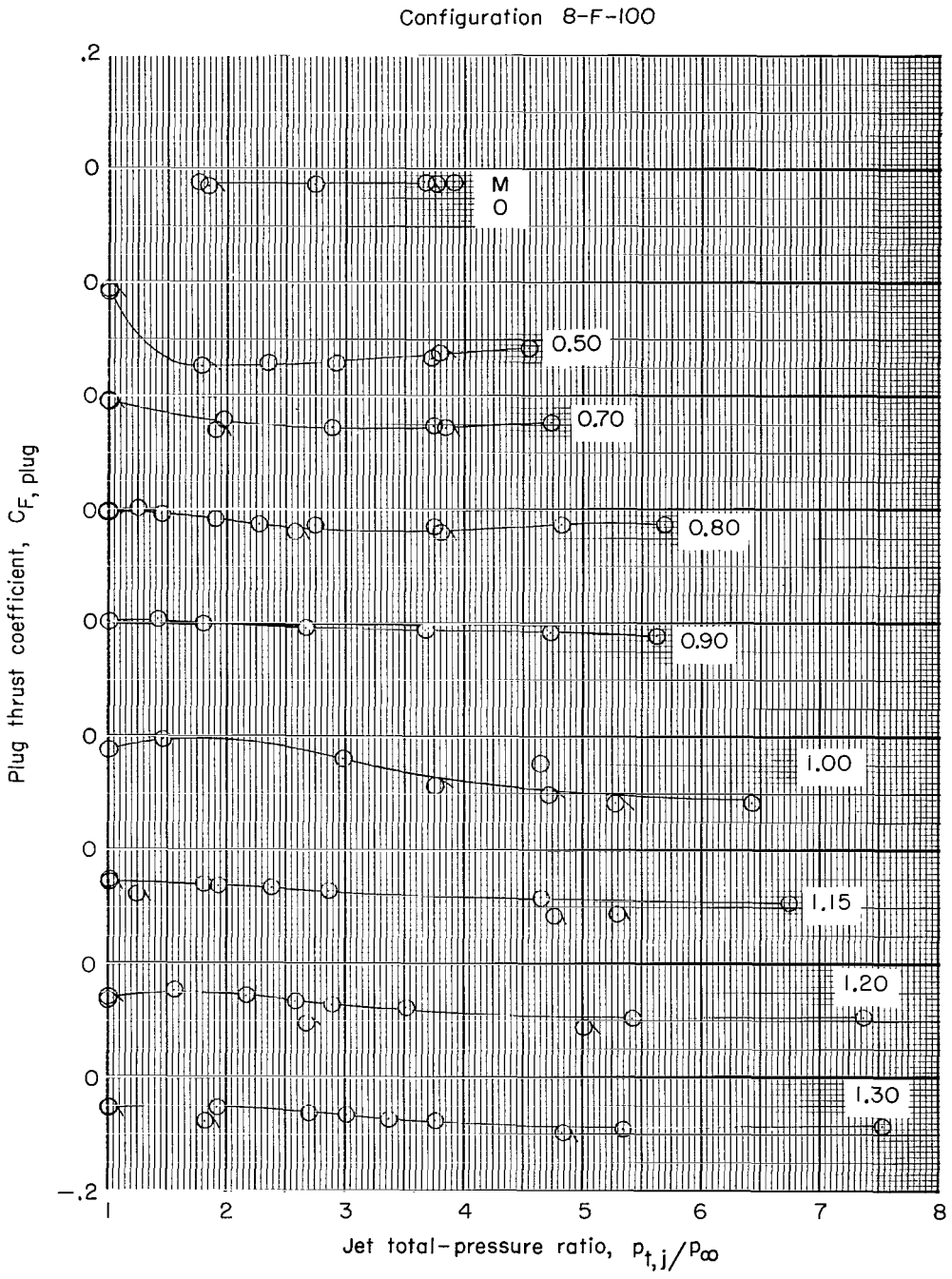

(g) Configuration 8-F-100.

Figure 22.- Continued.

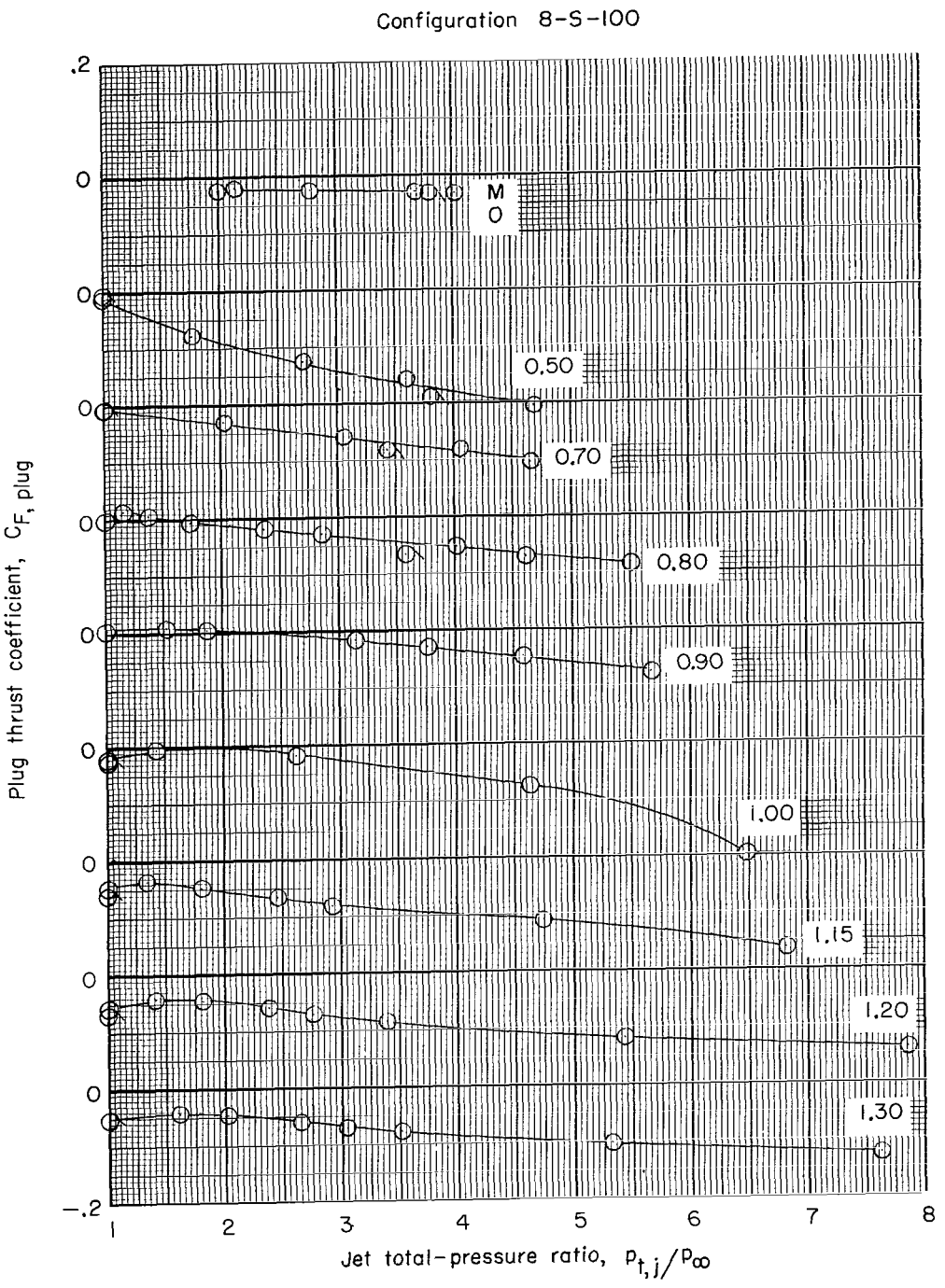

(h) Configuration 8-S-100.

Figure 22.- Continued.

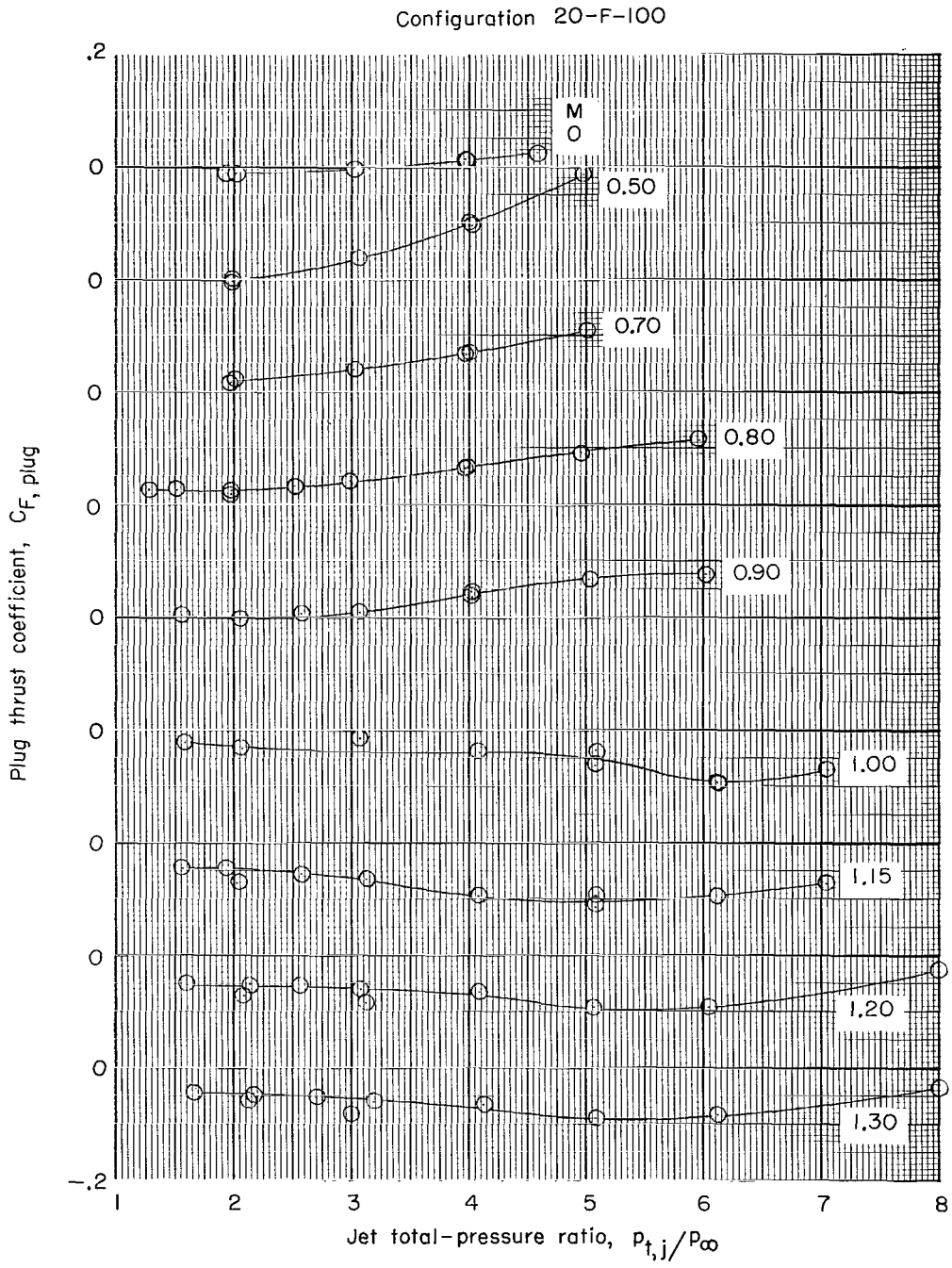

(i) Configuration 20-F-100.

Figure 22.- Continued.

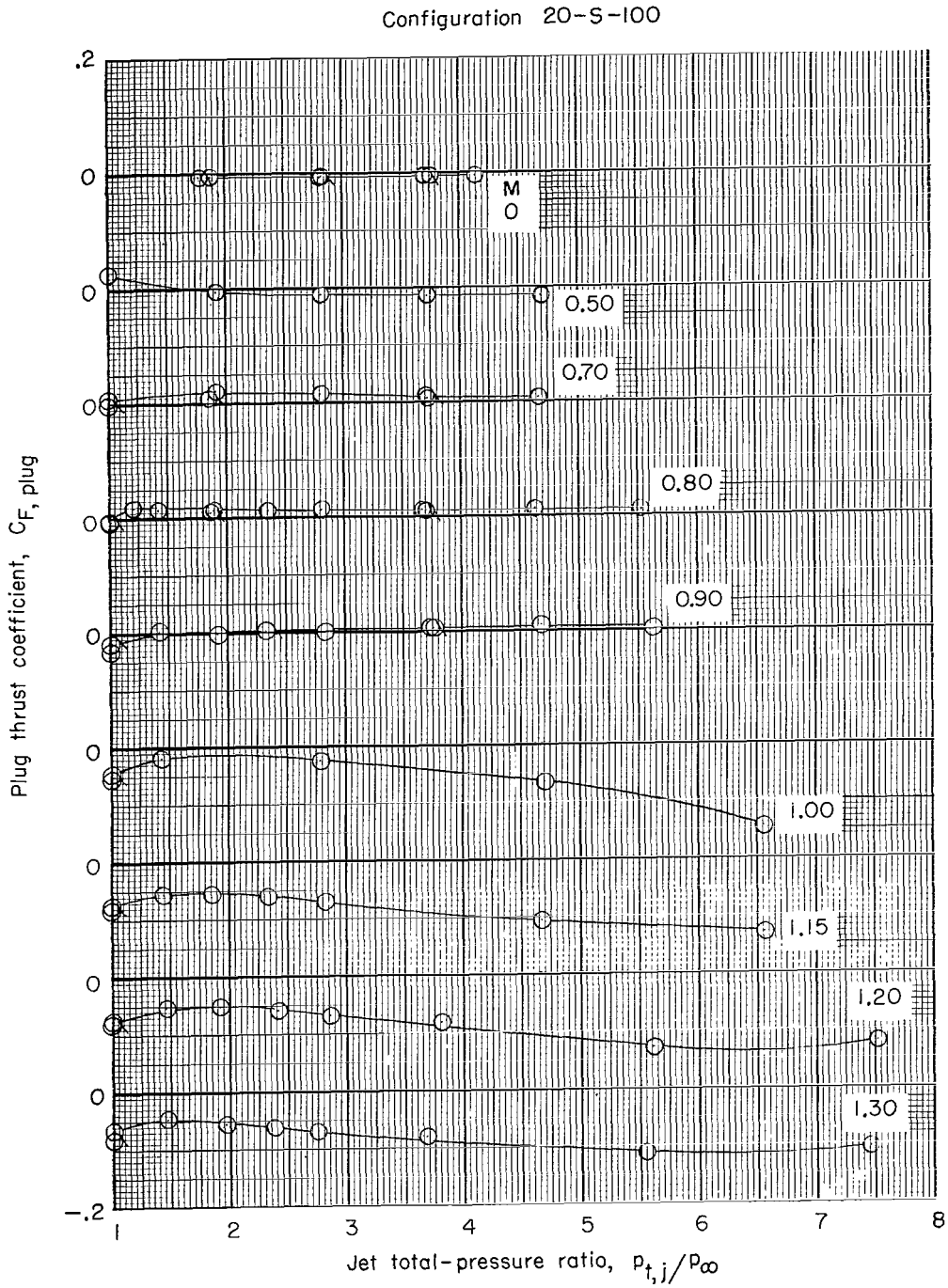

(j) Configuration 20-S-100.

Figure 22.- Continued.

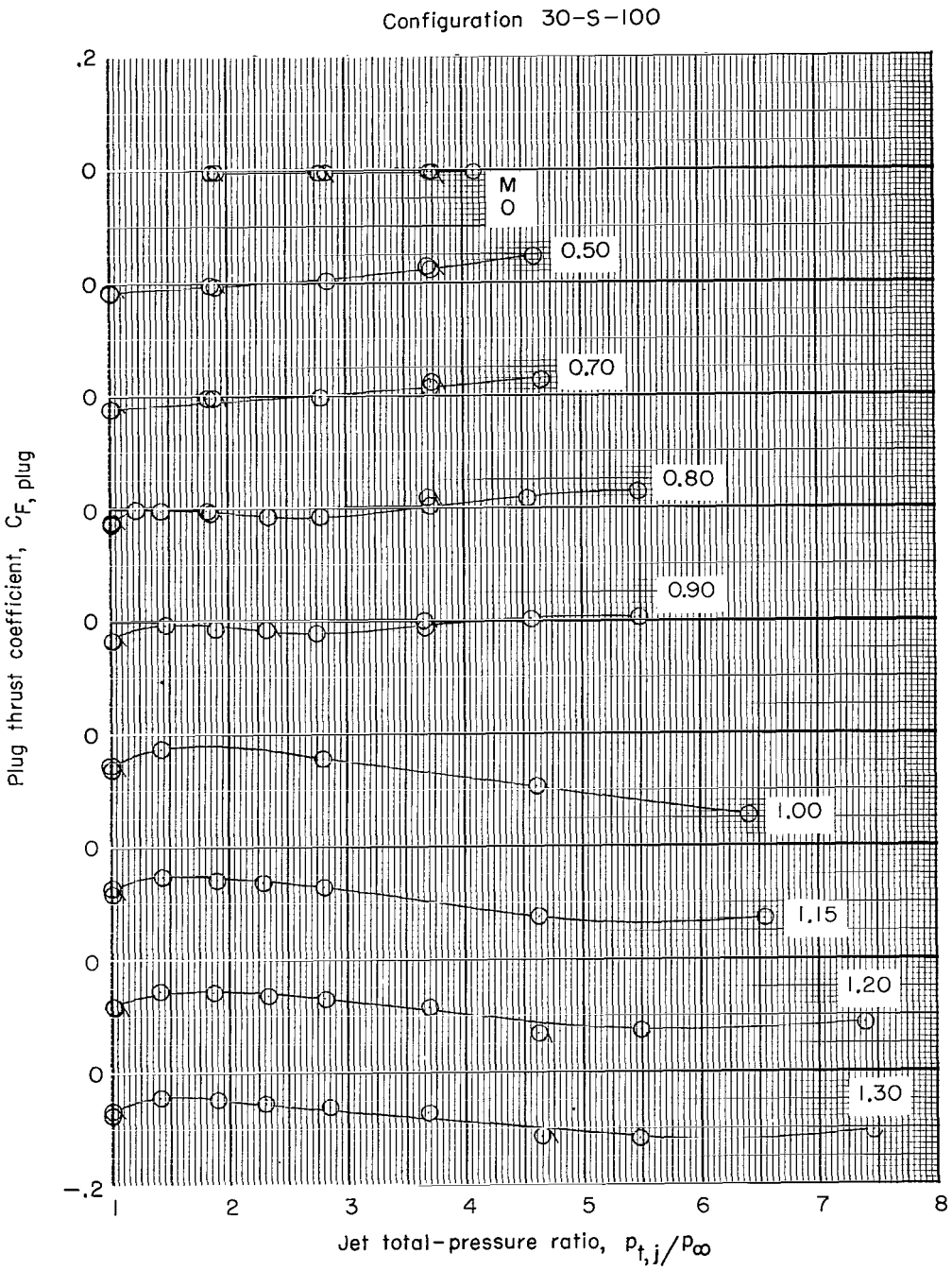

(k) Configuration 30-S-100.

Figure 22.- Concluded.

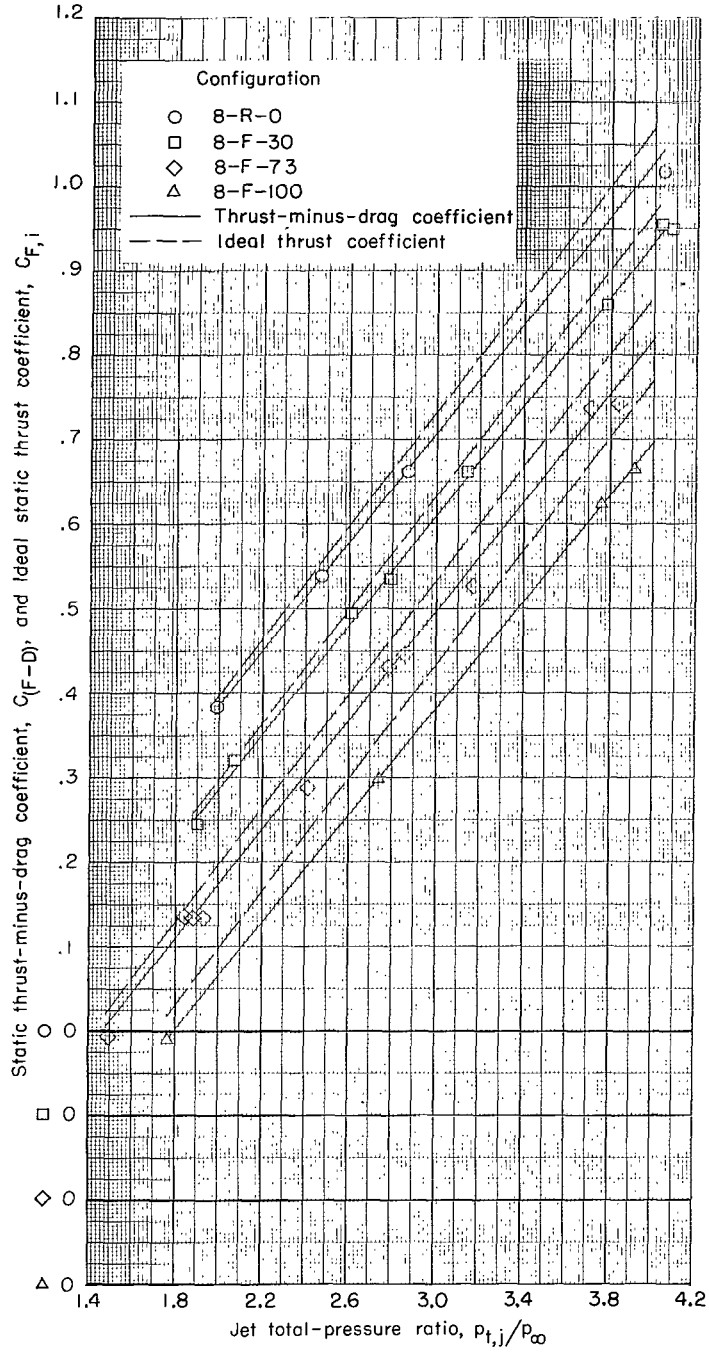

(a) $\beta = 8^0$; flat base.

Figure 23.- Variation of static thrust-minus-drag coefficient and ideal static thrust coefficient with jet total-pressure ratio.

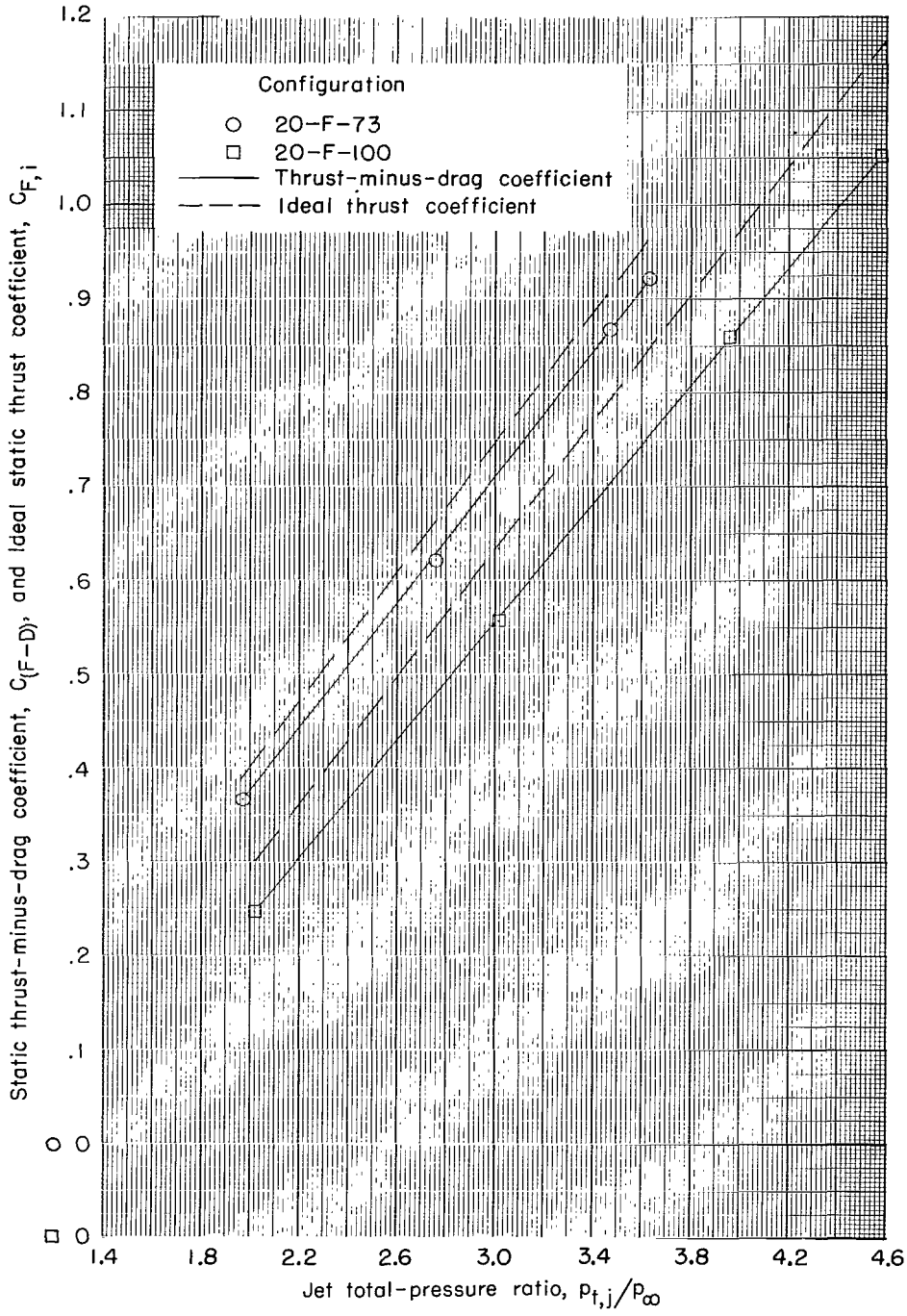

(b) $\beta = 20^0$; flat base.

Figure 23.- Continued.

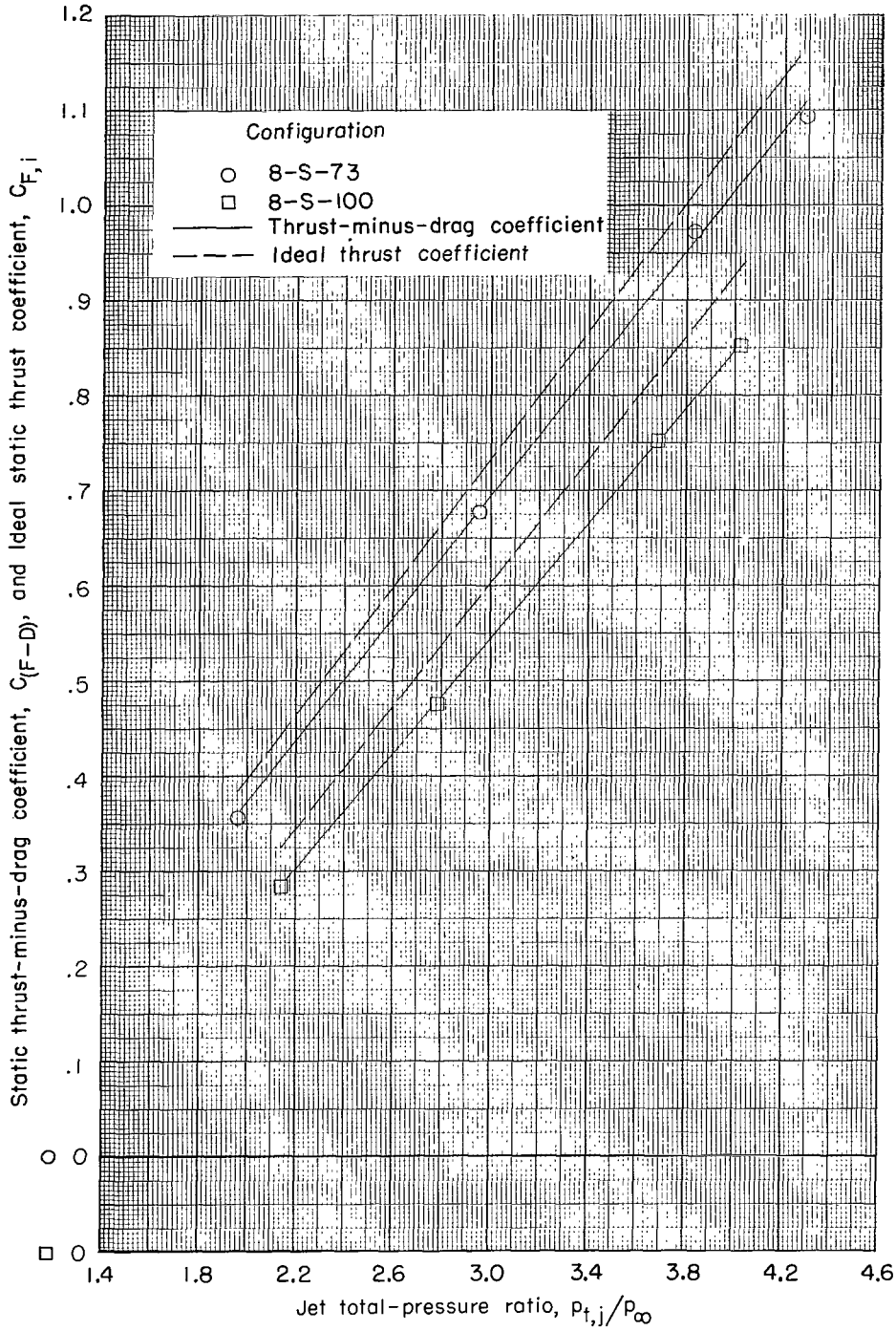

(c) $\beta = 8^0$; semitoroidal base.

Figure 23.- Continued.

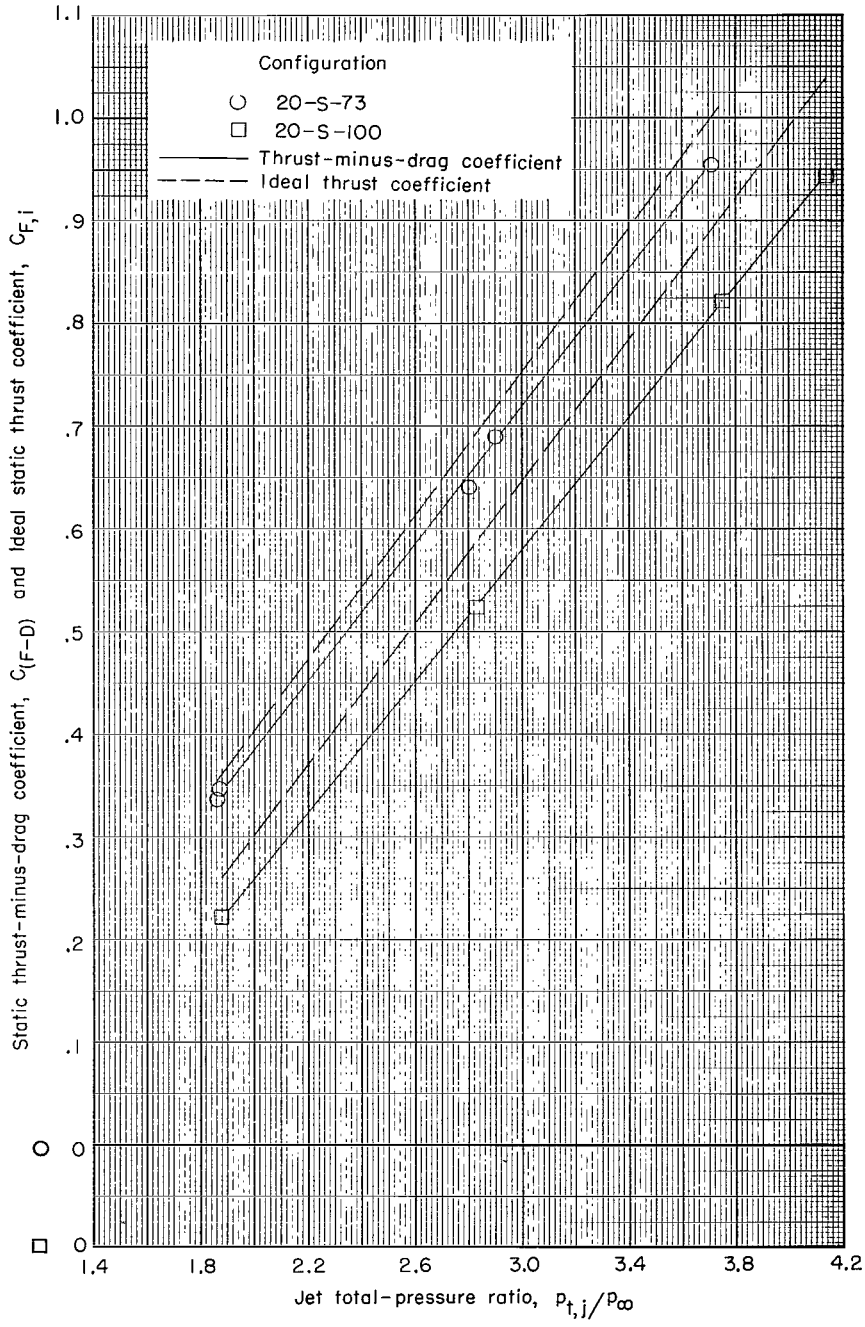

(d) $\beta = 20^0$; semitoroidal base.

Figure 23.- Continued.

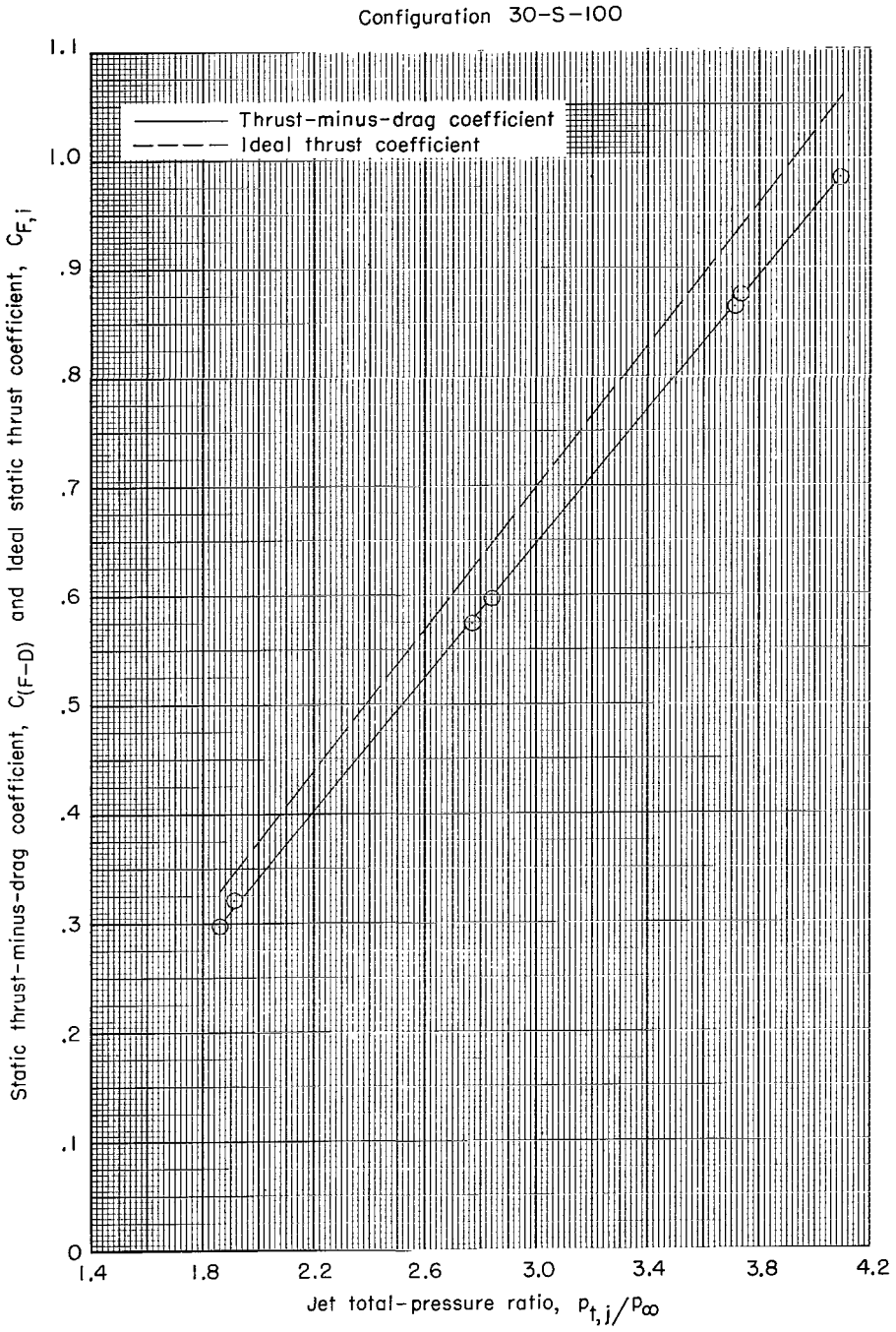

(e) $\beta = 30^0$; semitoroidal base.

Figure 23.- Concluded.

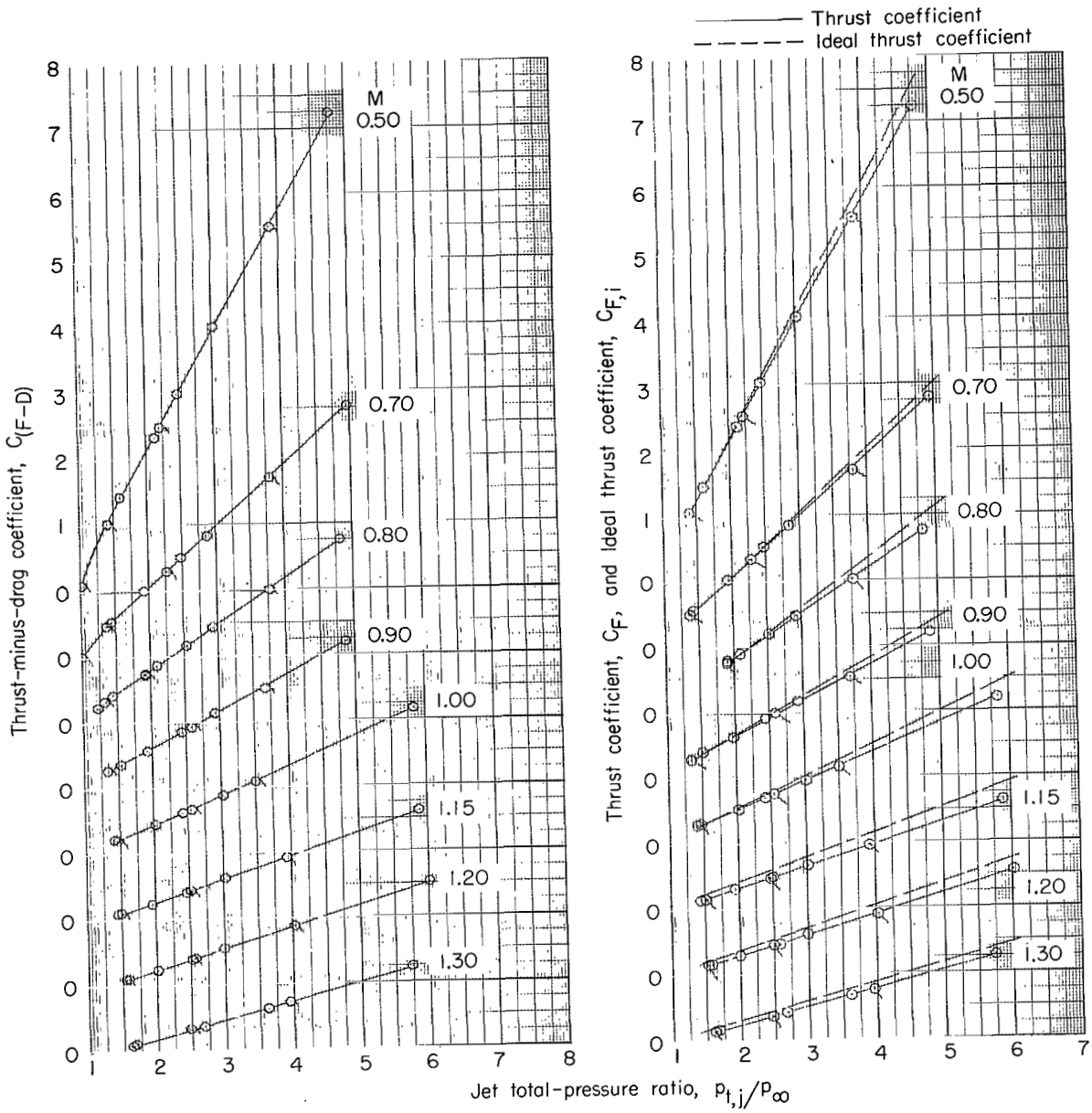

(a) Configuration 8-R-0.

Figure 24.- Variation of thrust-minus-drag, thrust, and ideal thrust coefficients with jet total-pressure ratio for various Mach numbers. Tailed symbols denote decreasing pressure ratio. (Note shifting scales.)

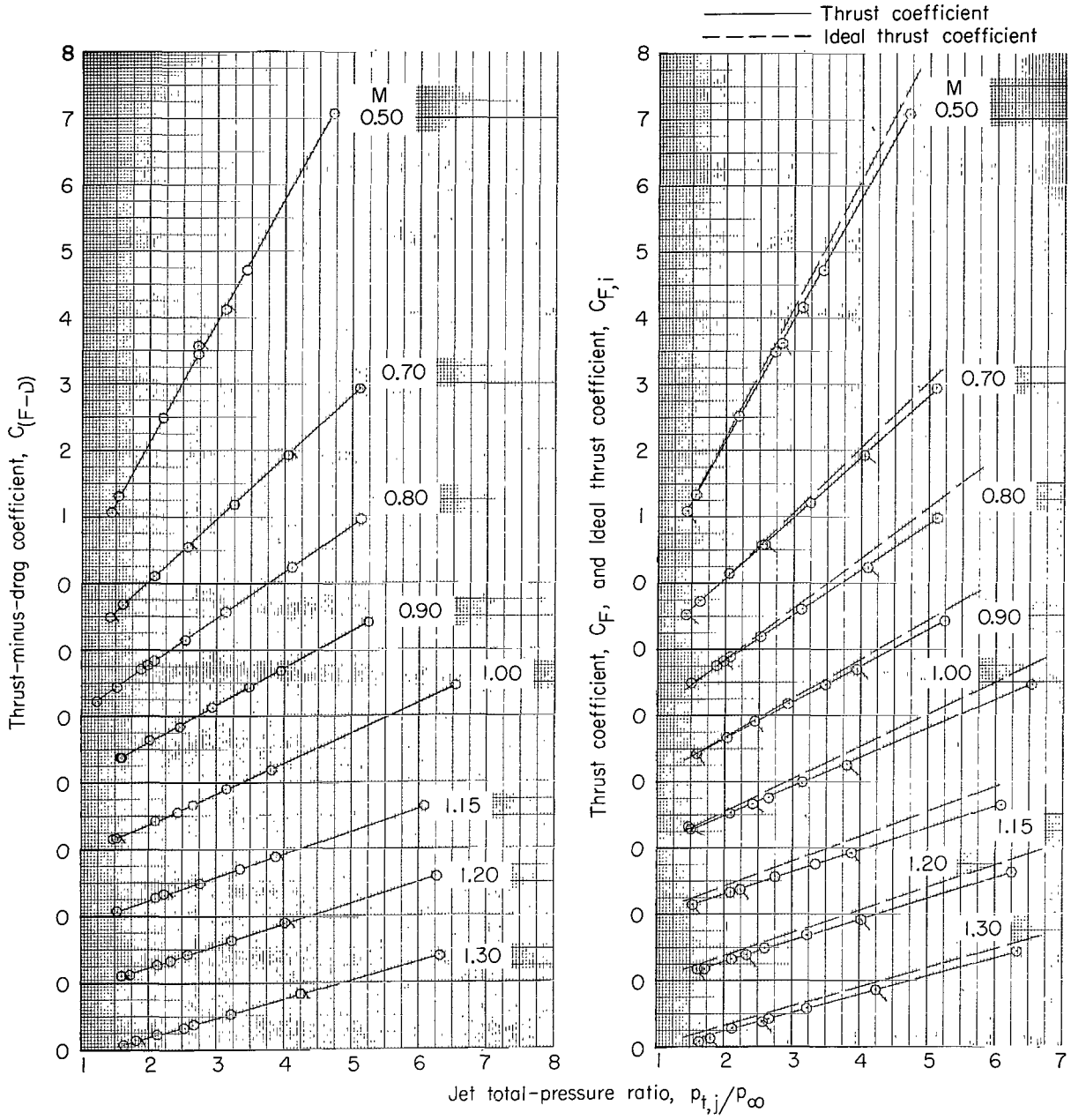

(b) Configuration 8-F-30.

Figure 24.- Continued.

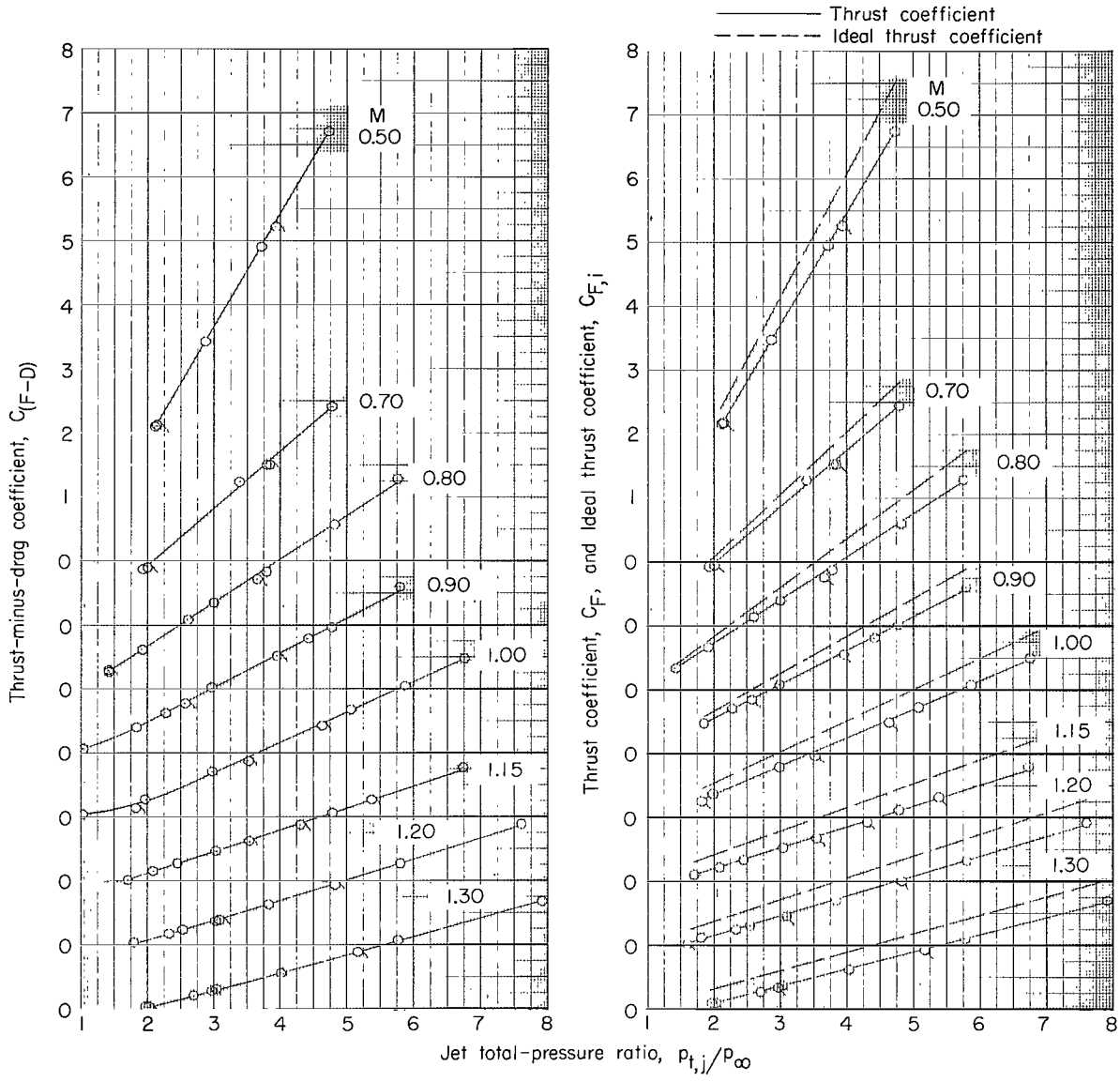

(c) Configuration 8-F-73.

Figure 24.- Continued.

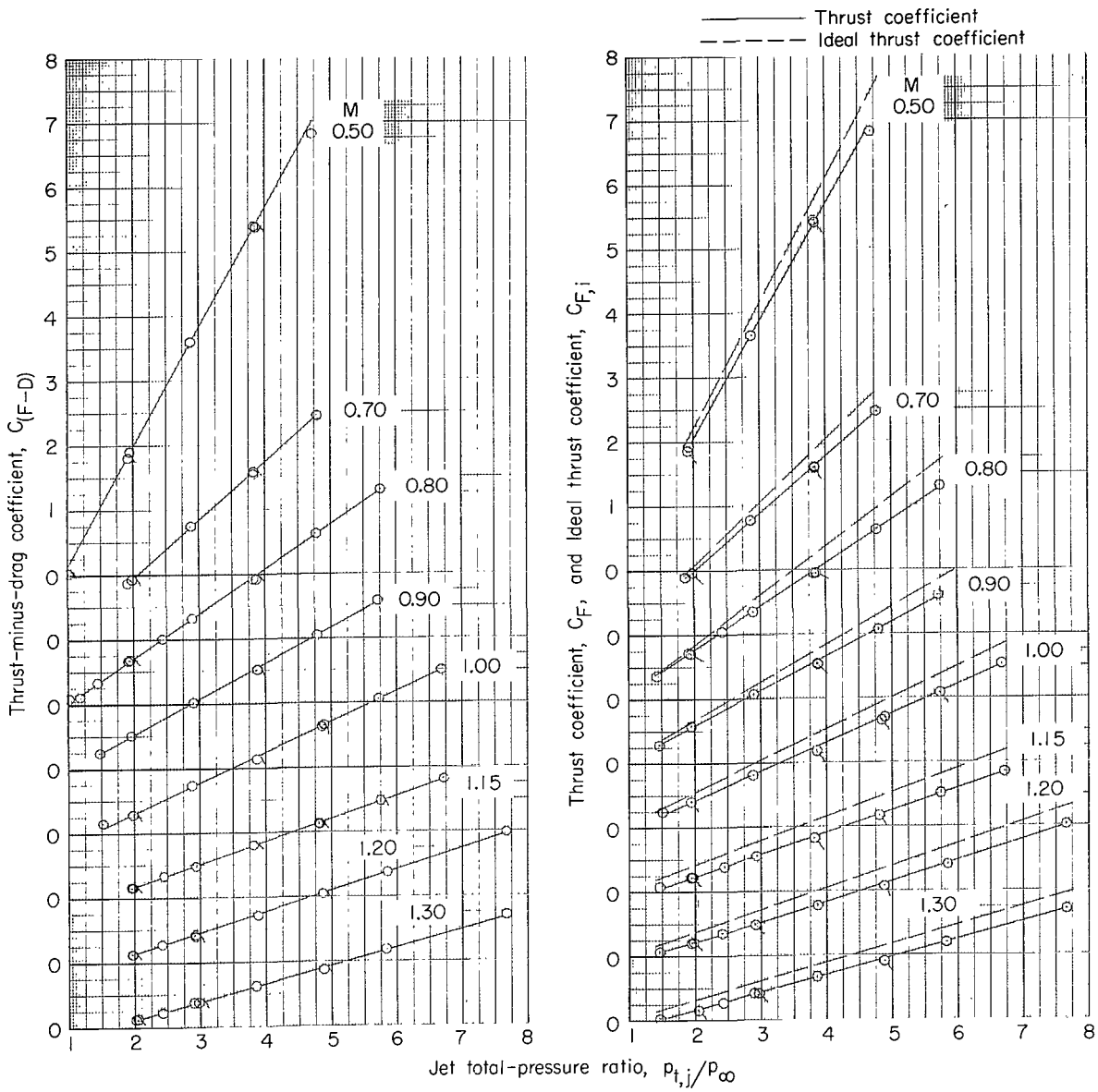

(d) Configuration 8-S-73.

Figure 24.- Continued.

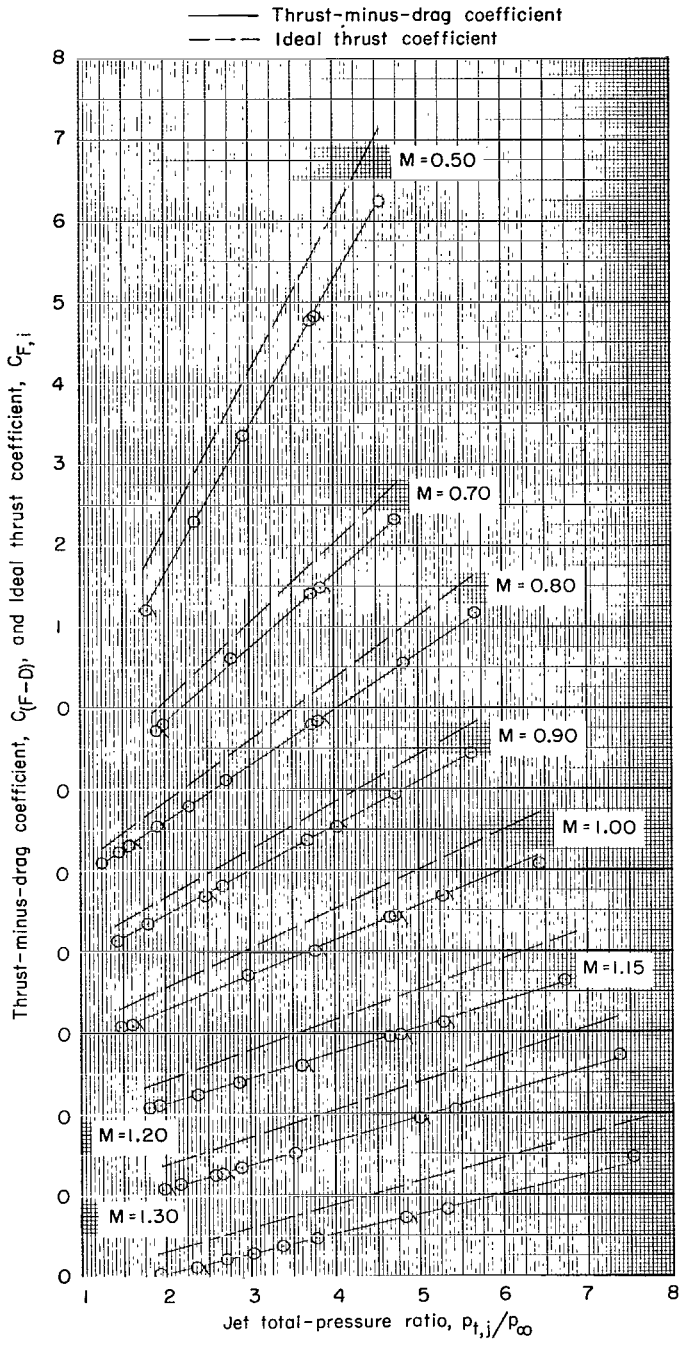

(e) Configuration 8-F-100.

Figure 24.- Continued.

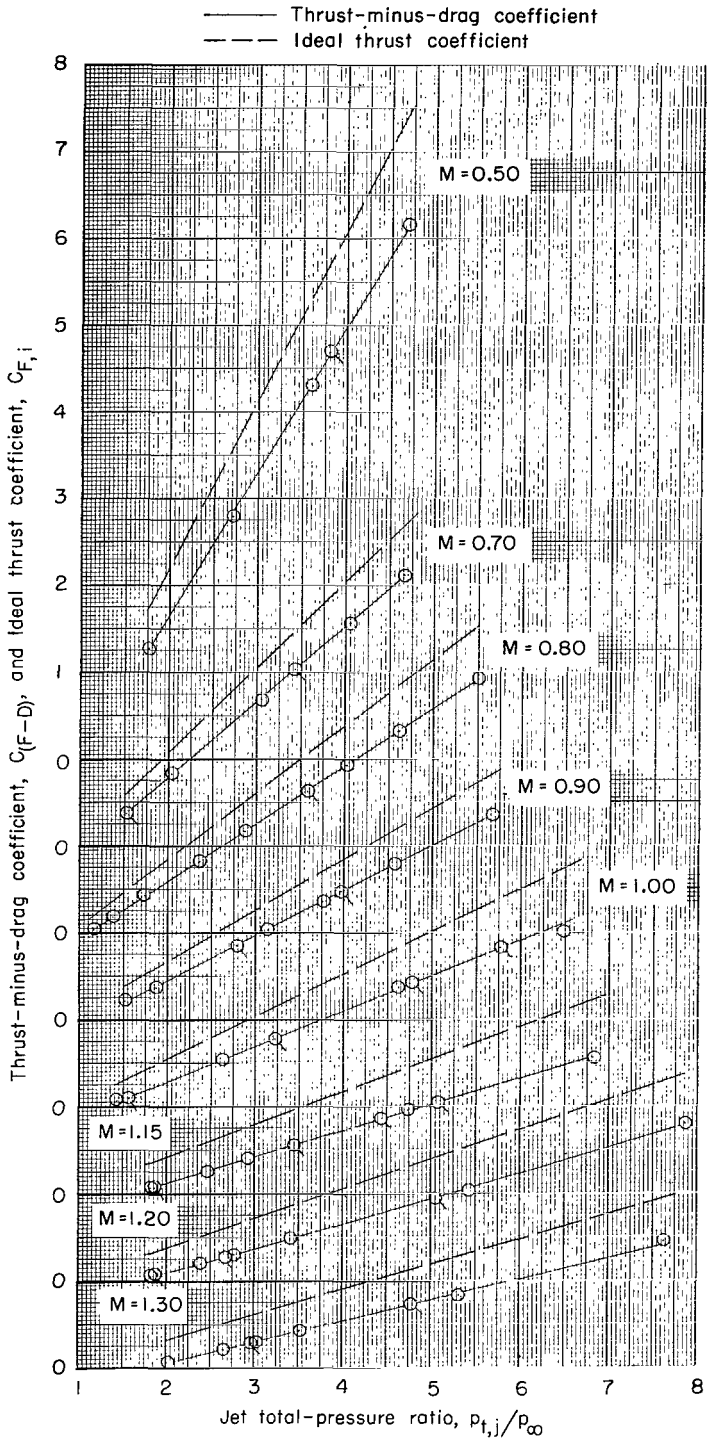

(f) Configuration 8-S-100.

Figure 24.- Continued.

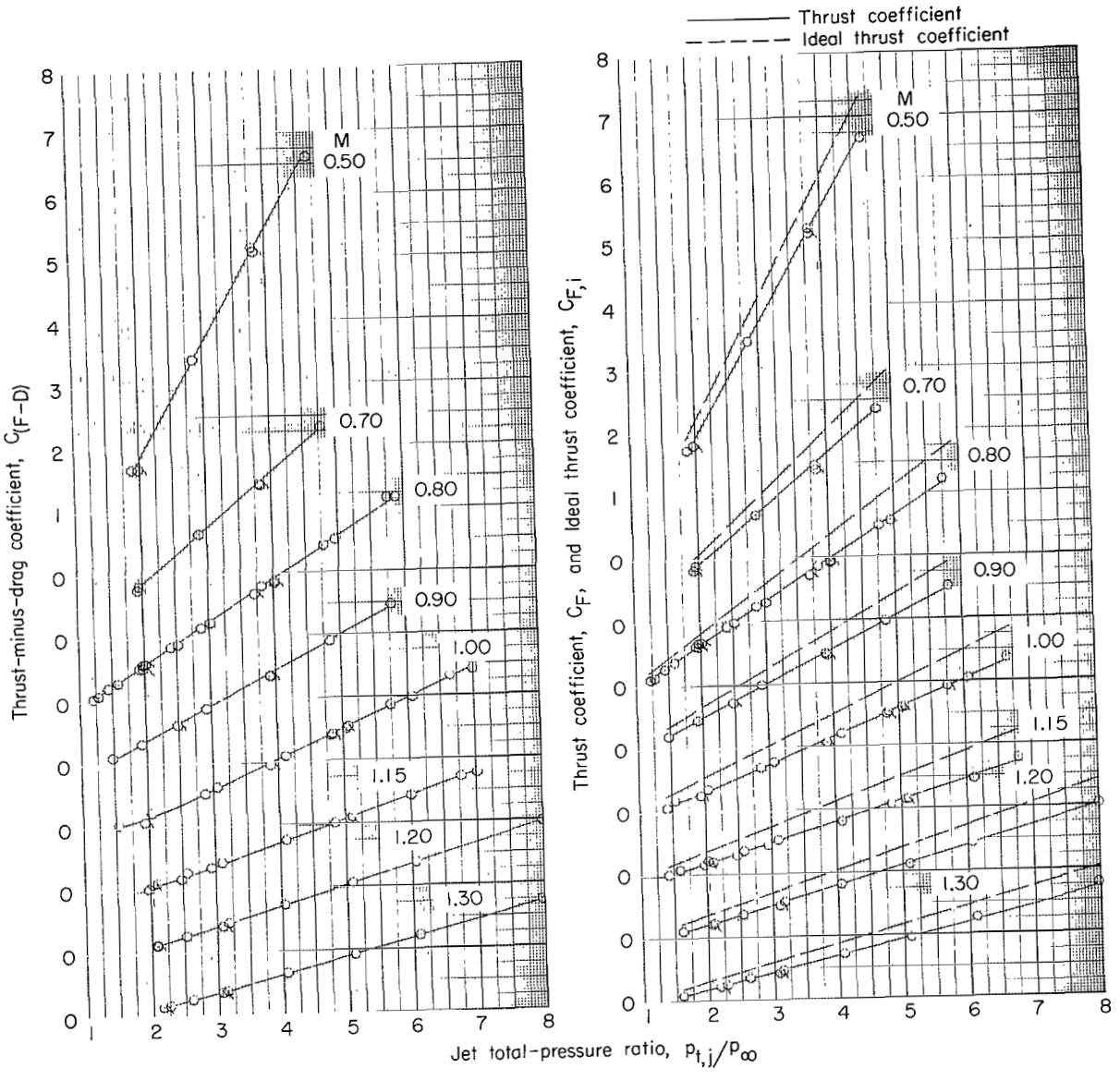

(g) Configuration 20-F-73.

Figure 24.- Continued.

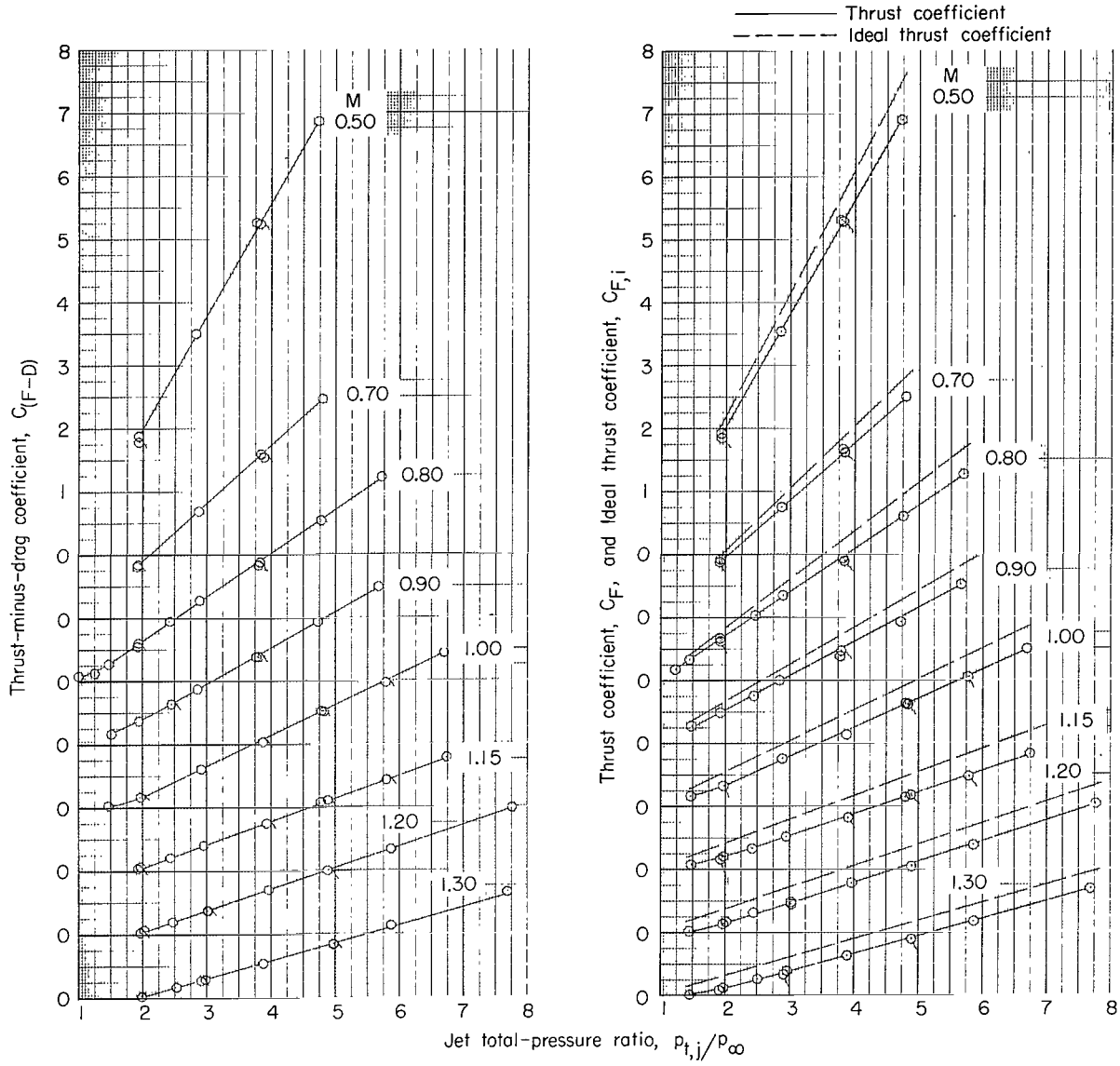

(h) Configuration 20-S-73.

Figure 24.- Continued.

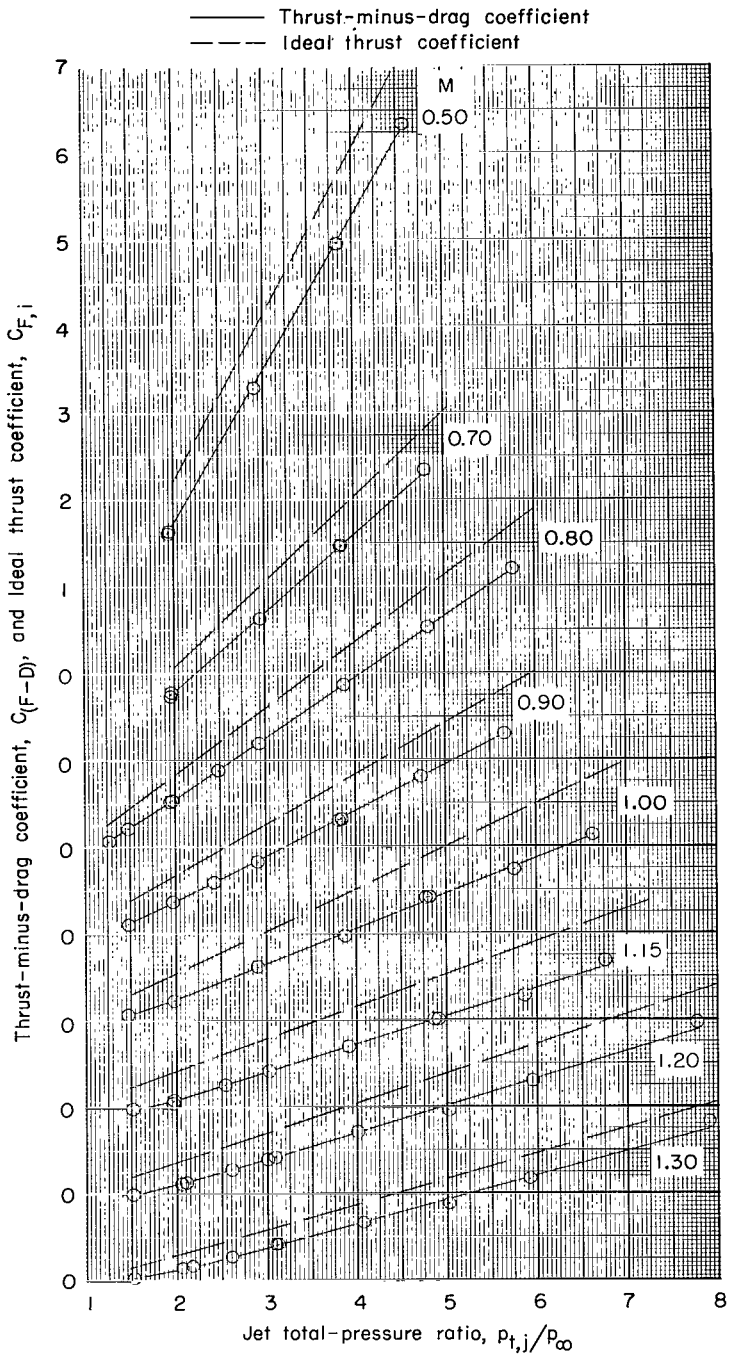

(i) Configuration 20-F-100.

Figure 24.- Continued.

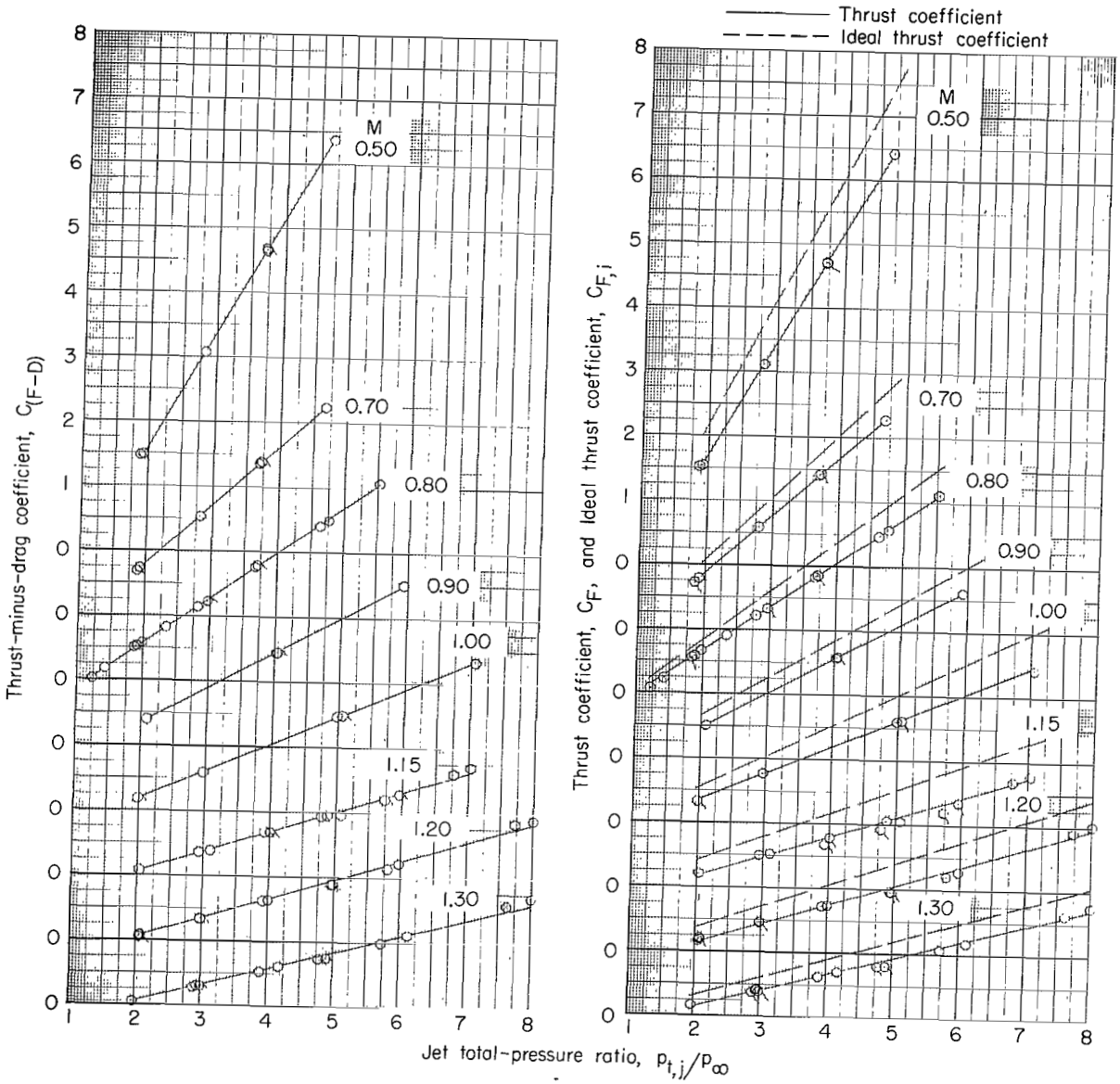

(j) Configuration 20-S-100.

Figure 24.- Continued.

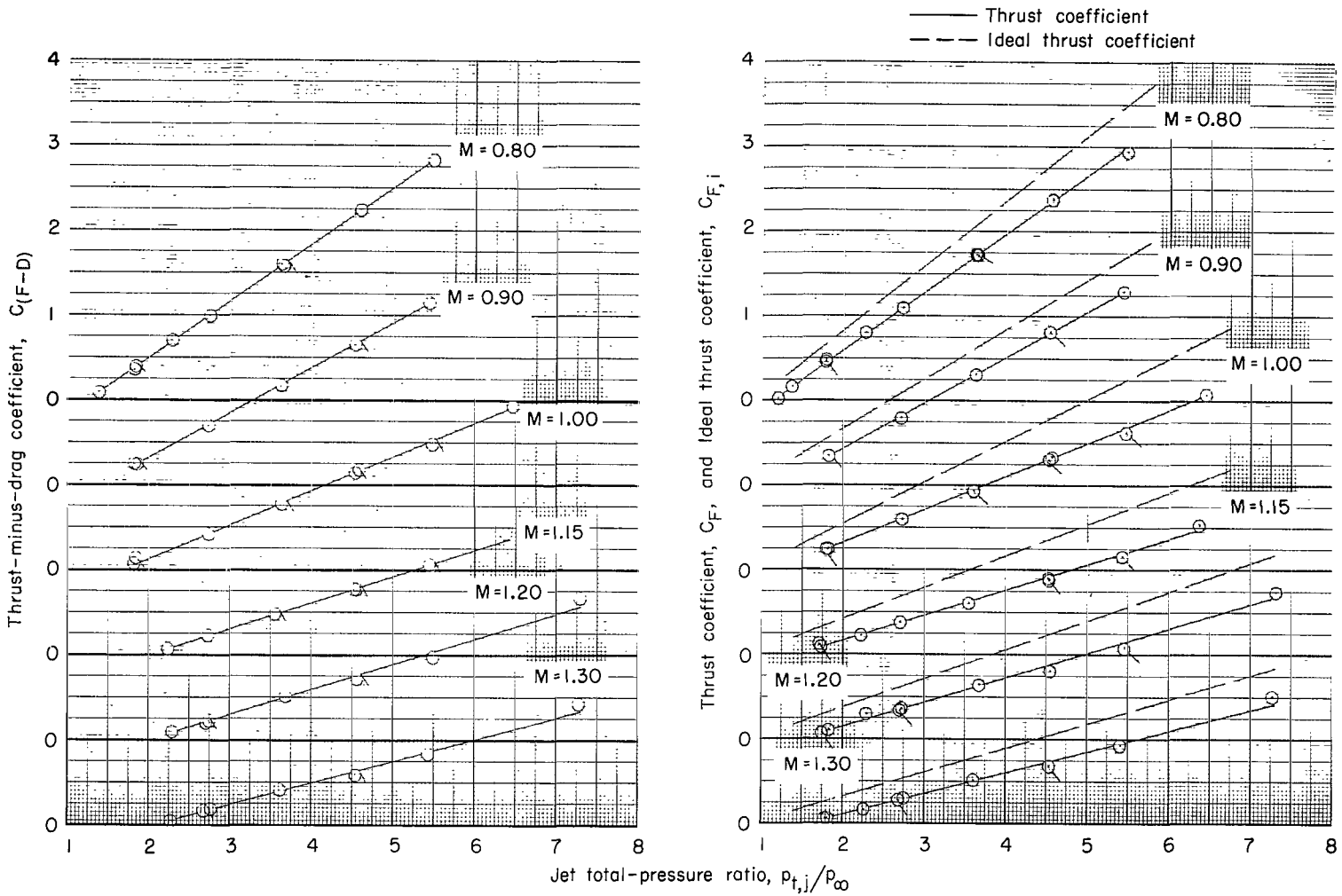

(k) Configuration 30-S-100.

Figure 24.- Concluded.

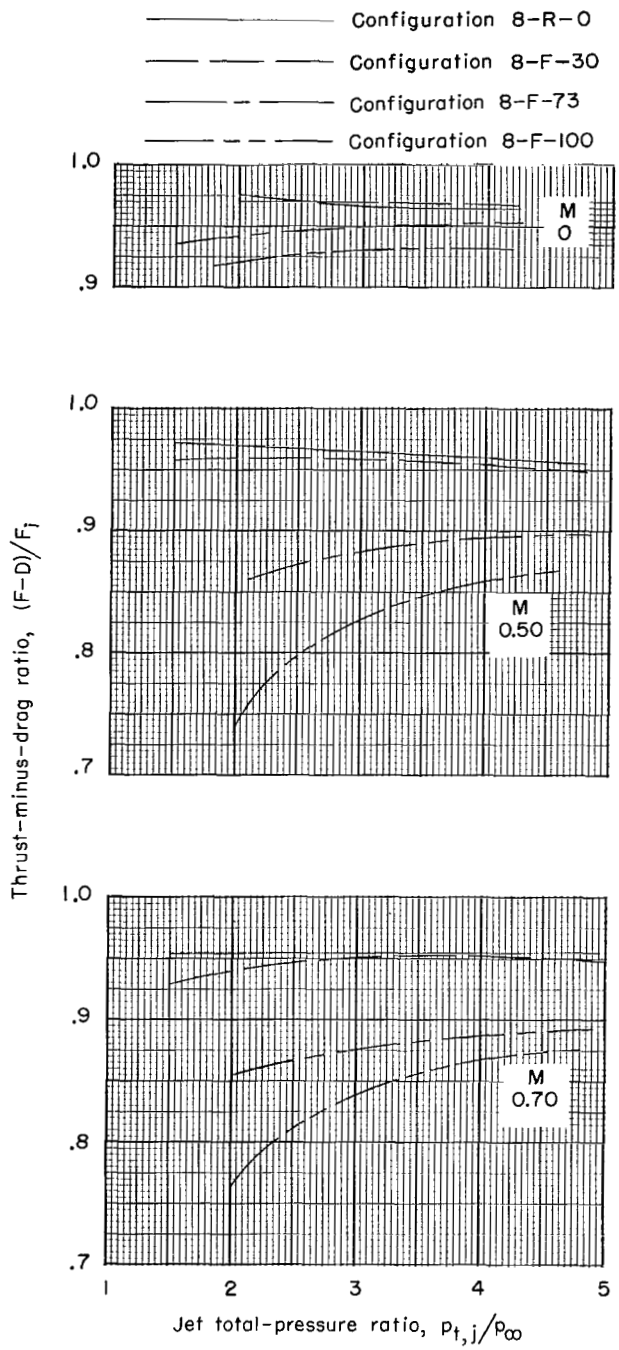

(a) M = 0 to M = 0.70.

Figure 25.- Effect of jet total-pressure ratio and plug truncation on thrust-minus-drag ratio. 8^0 boattail angle; flat plug base.

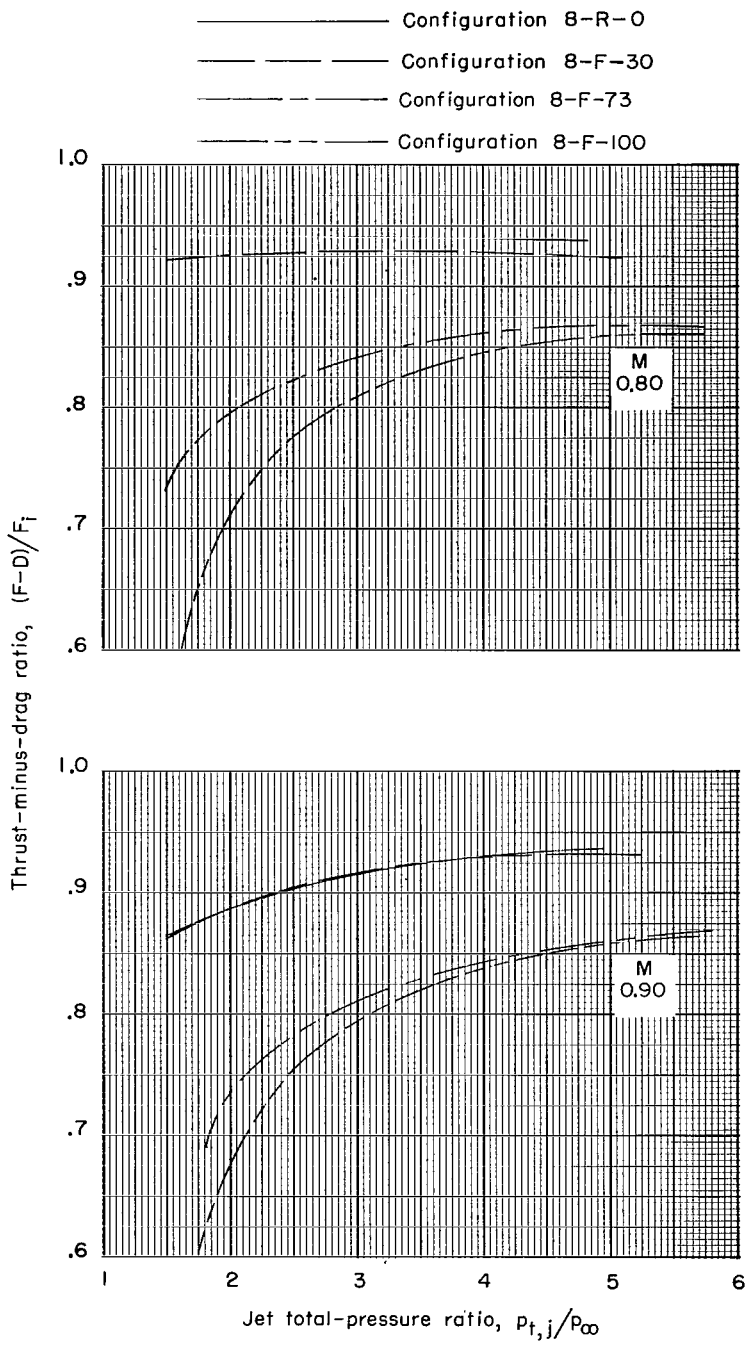

(b) M = 0.80 and M = 0.90.

Figure 25.- Continued.

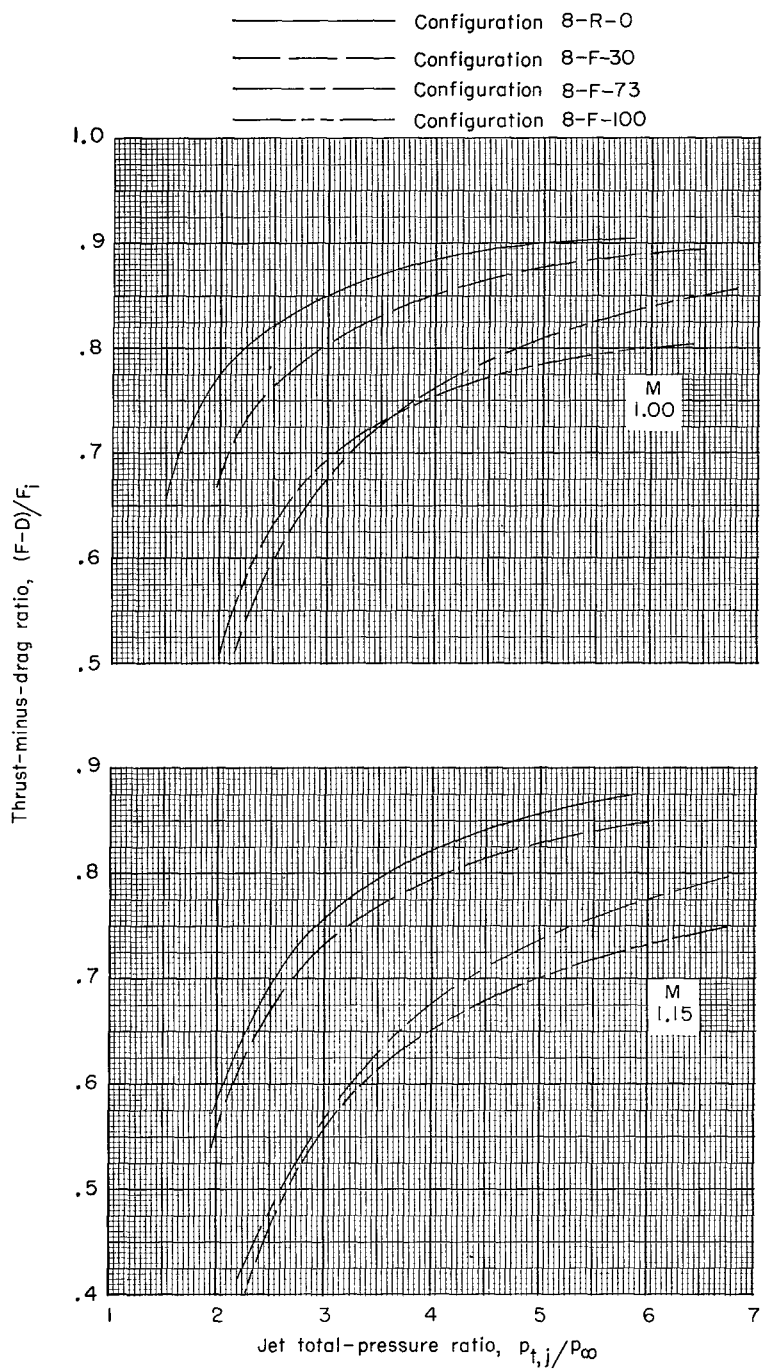

(c) M = 1.00 and M = 1.15.

Figure 25.- Continued.

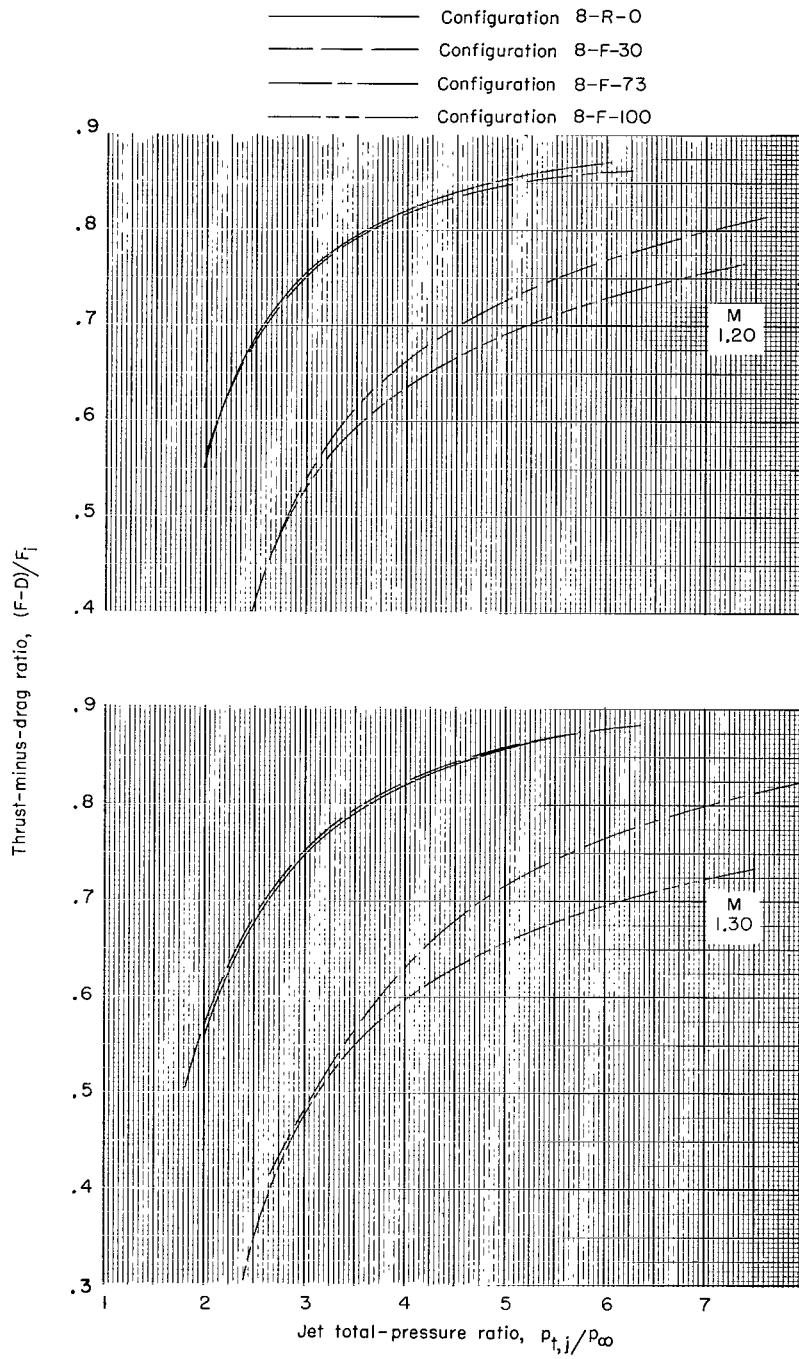

(d) M = 1.20 and M = 1.30.

Figure 25.- Concluded.

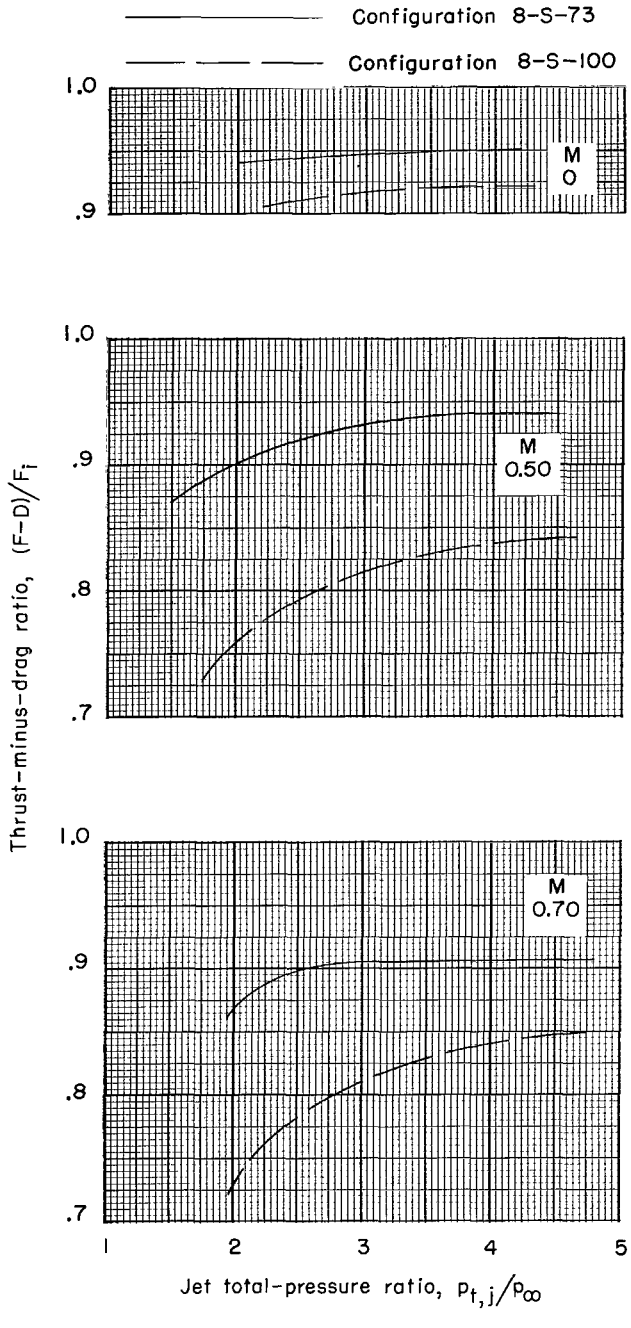

(a) M = 0 to M = 0.70.

Figure 26.- Effect of jet total-pressure ratio and plug truncation on thrust-minus-drag ratio. 8° boattail angle; semitoroidal plug base.

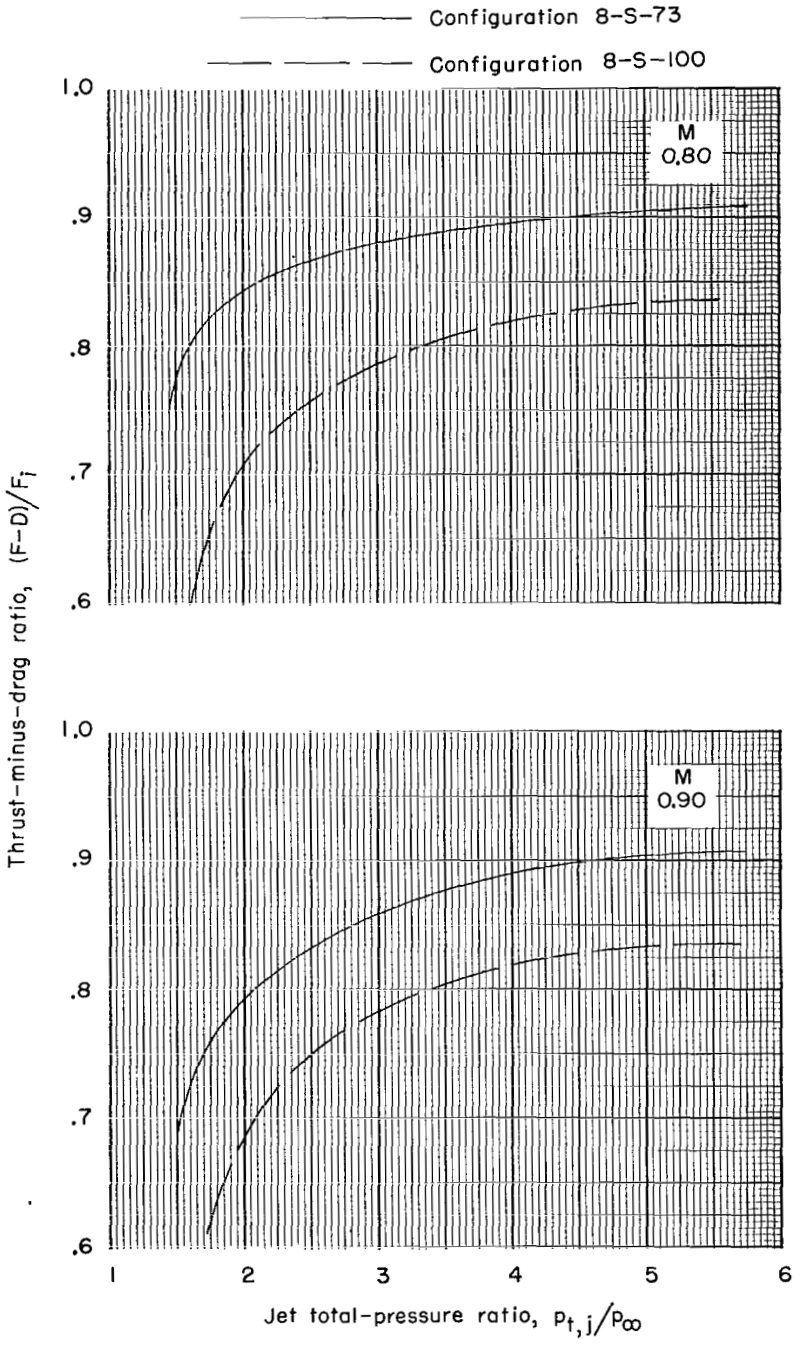

(b) M = 0.80 and M = 0.90.

Figure 26.- Continued.

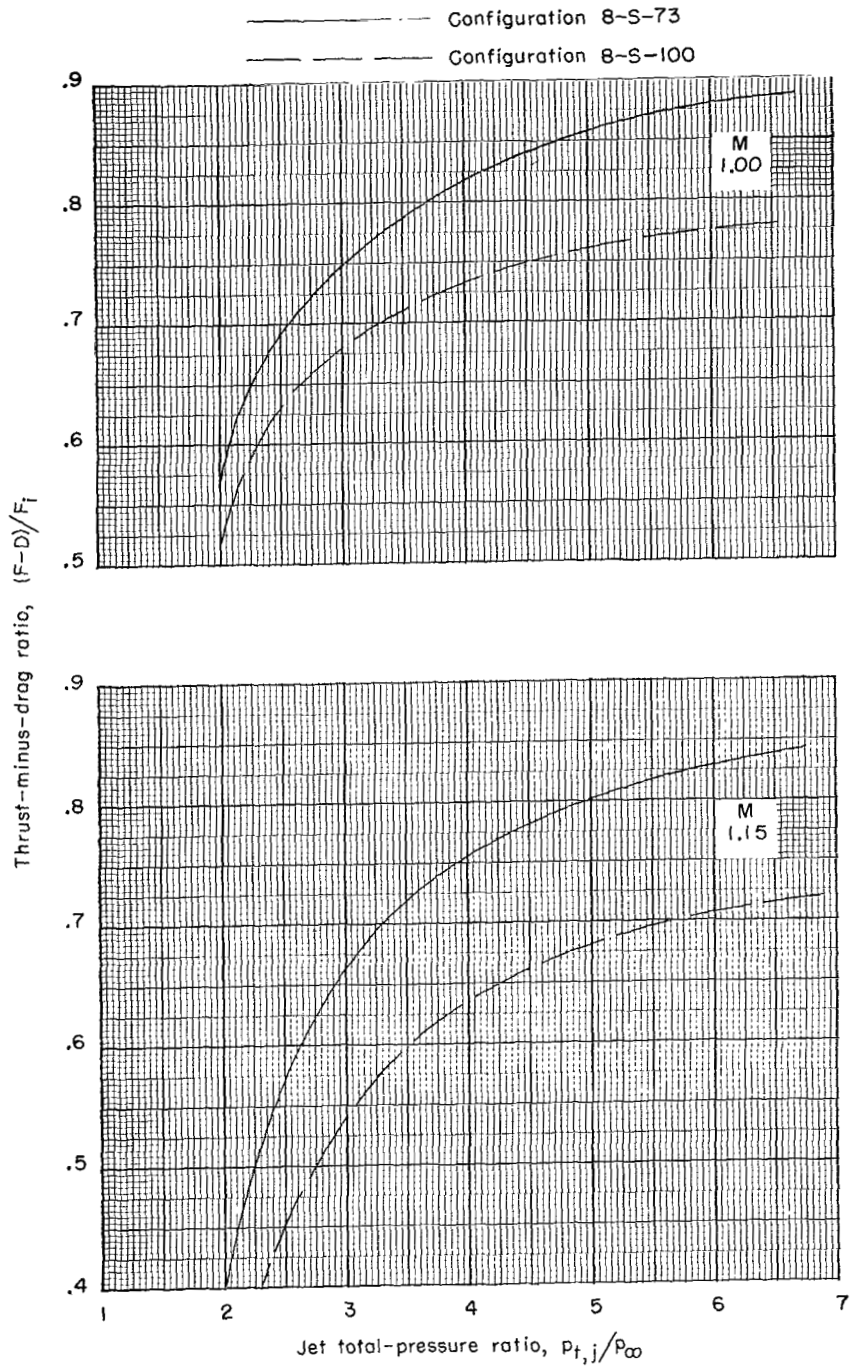

(c) M = 1.00 and M = 1.15.

Figure 26.- Continued.

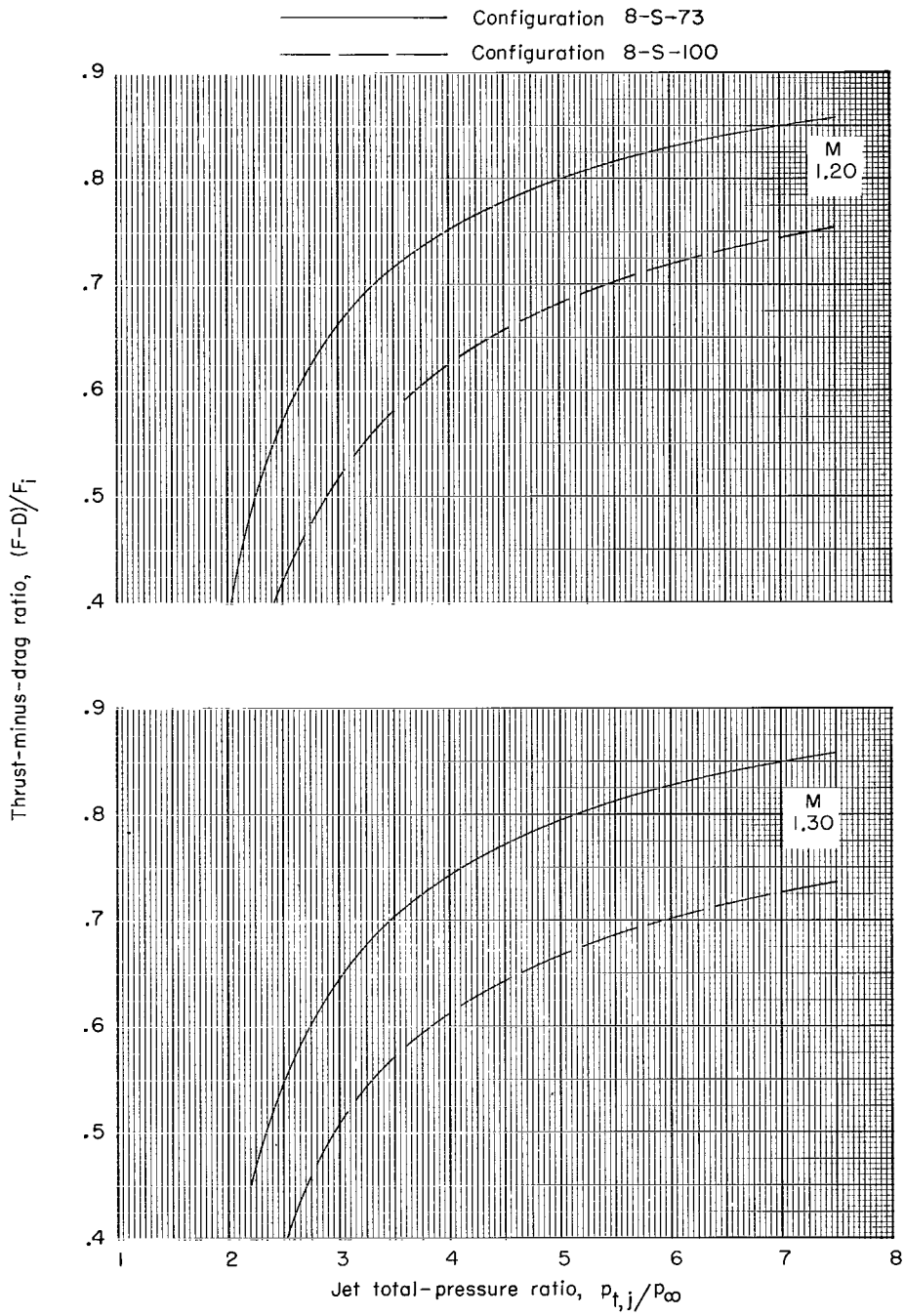

(d) M = 1.20 and M = 1.30.

Figure 26.- Concluded.

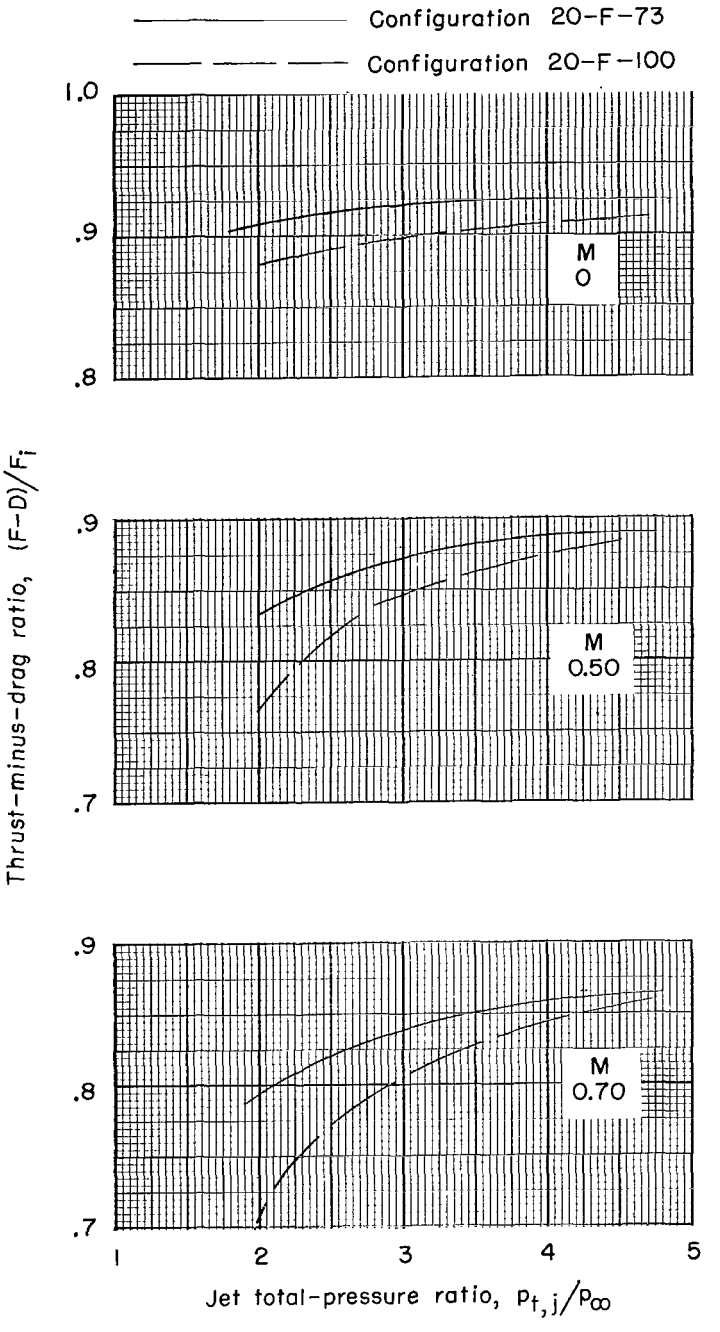

(a) M = 0 to M = 0.70.

Figure 27.- Effect of jet total-pressure ratio and plug truncation on thrust-minus-drag ratio. 20^0 boattail angle; flat plug base.

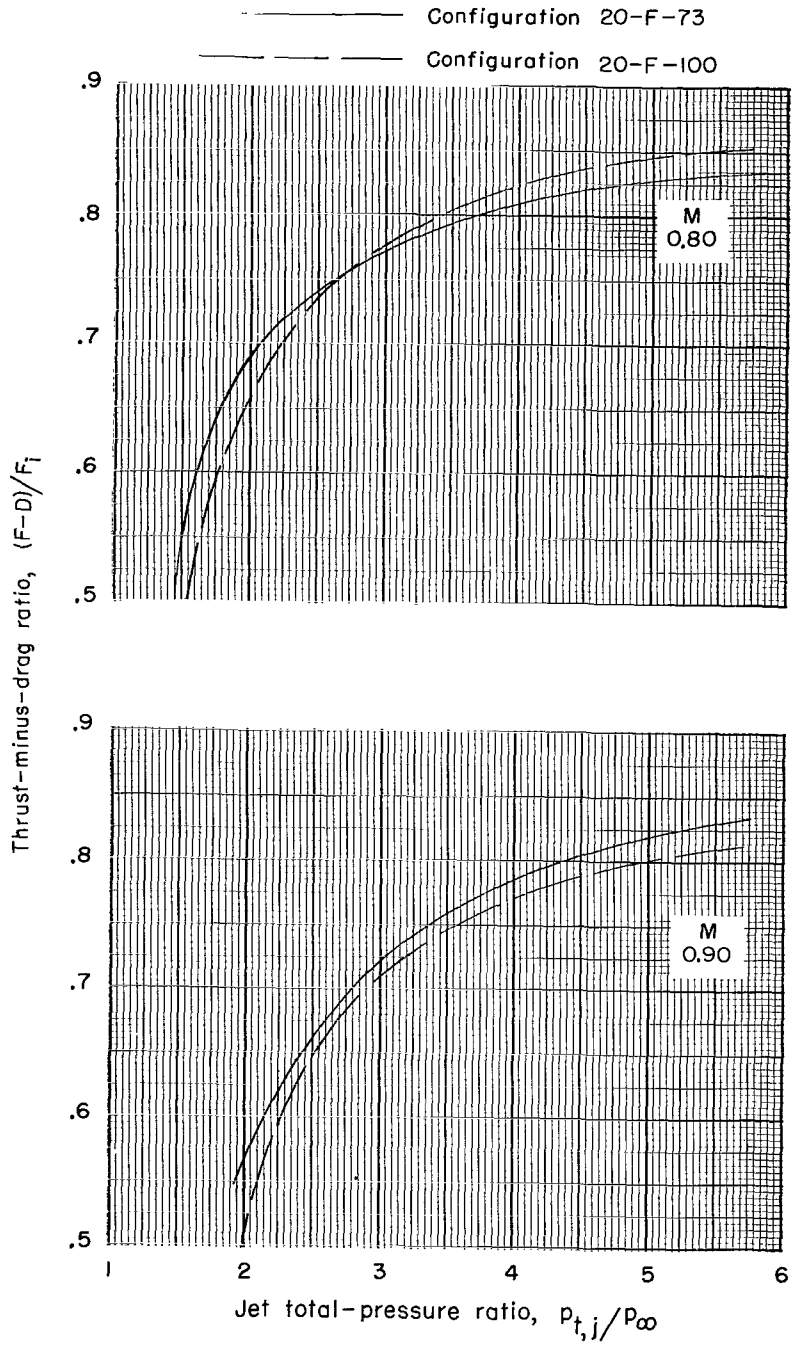

(b) M = 0.80 and M = 0.90.

Figure 27.- Continued.

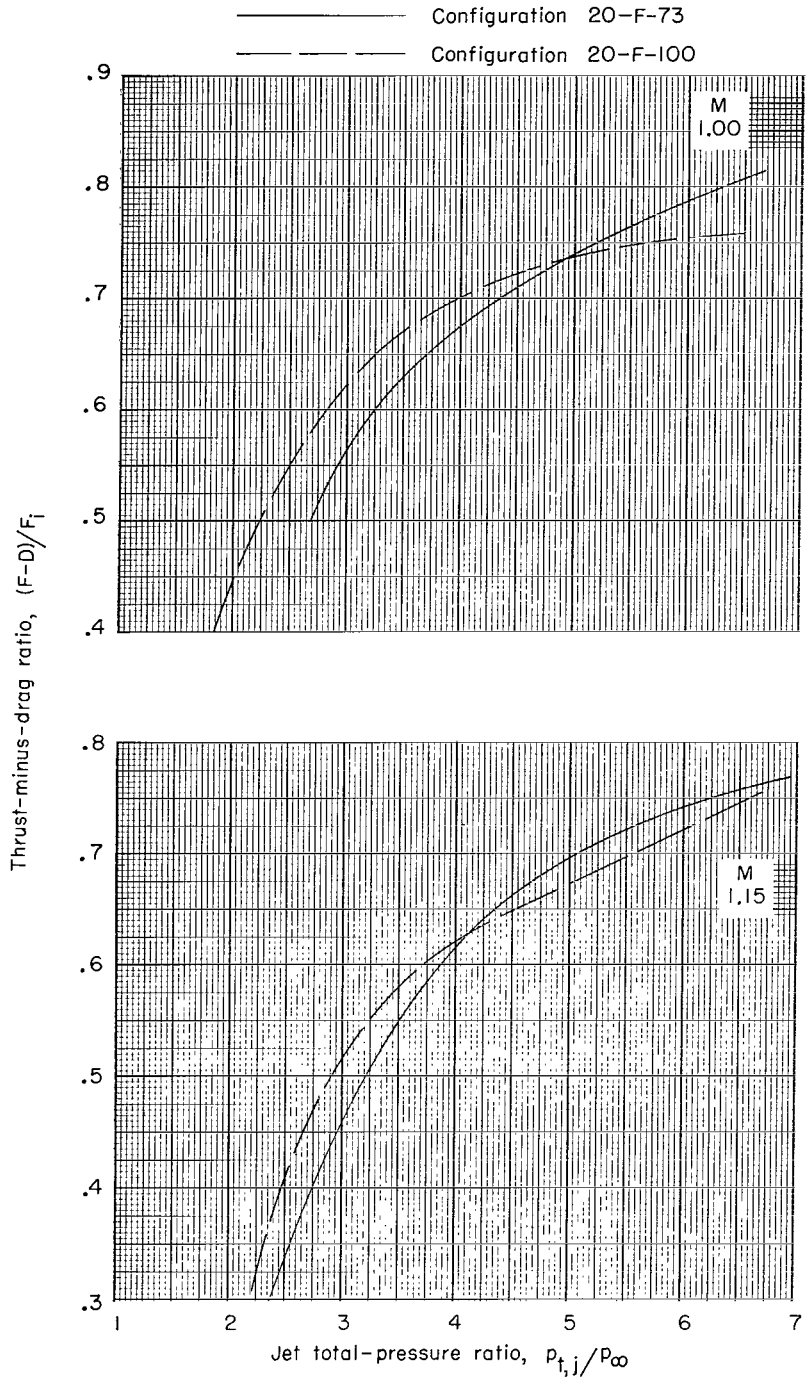

(c) M = 1.00 and M = 1.15.

Figure 27.- Continued.

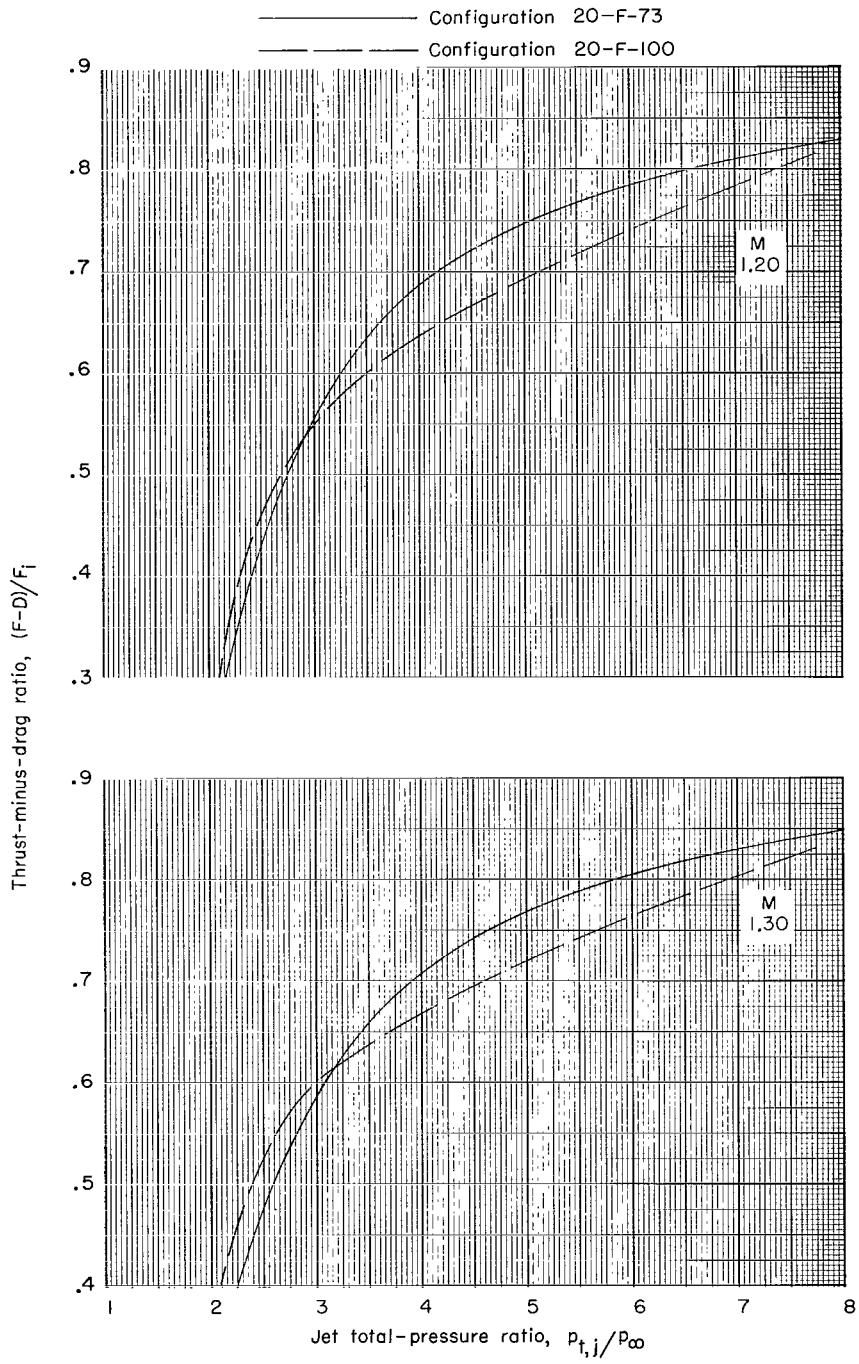

(d) M = 1.20 and M = 1.30.

Figure 27.- Concluded.

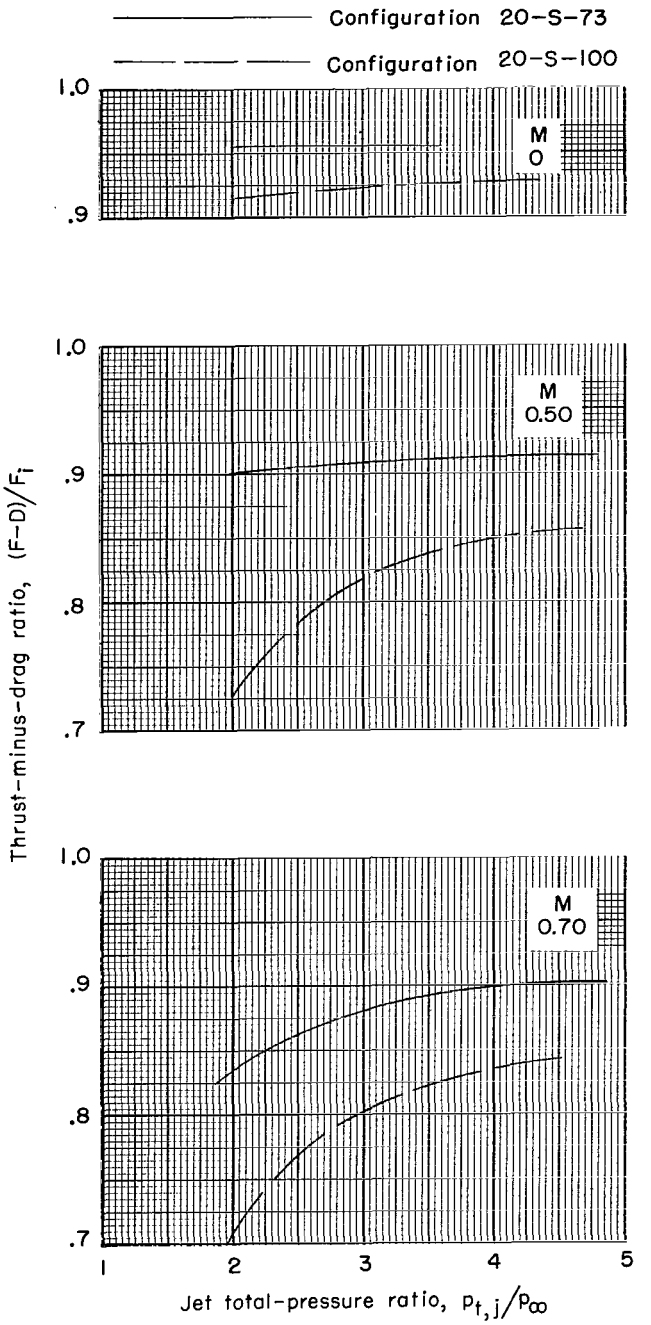

(a) M = 0 to M = 0.70.

Figure 28.- Effect of jet total-pressure ratio and plug truncation on thrust-minus-drag ratio. 20^0 boattail angle; semitoroidal plug base.

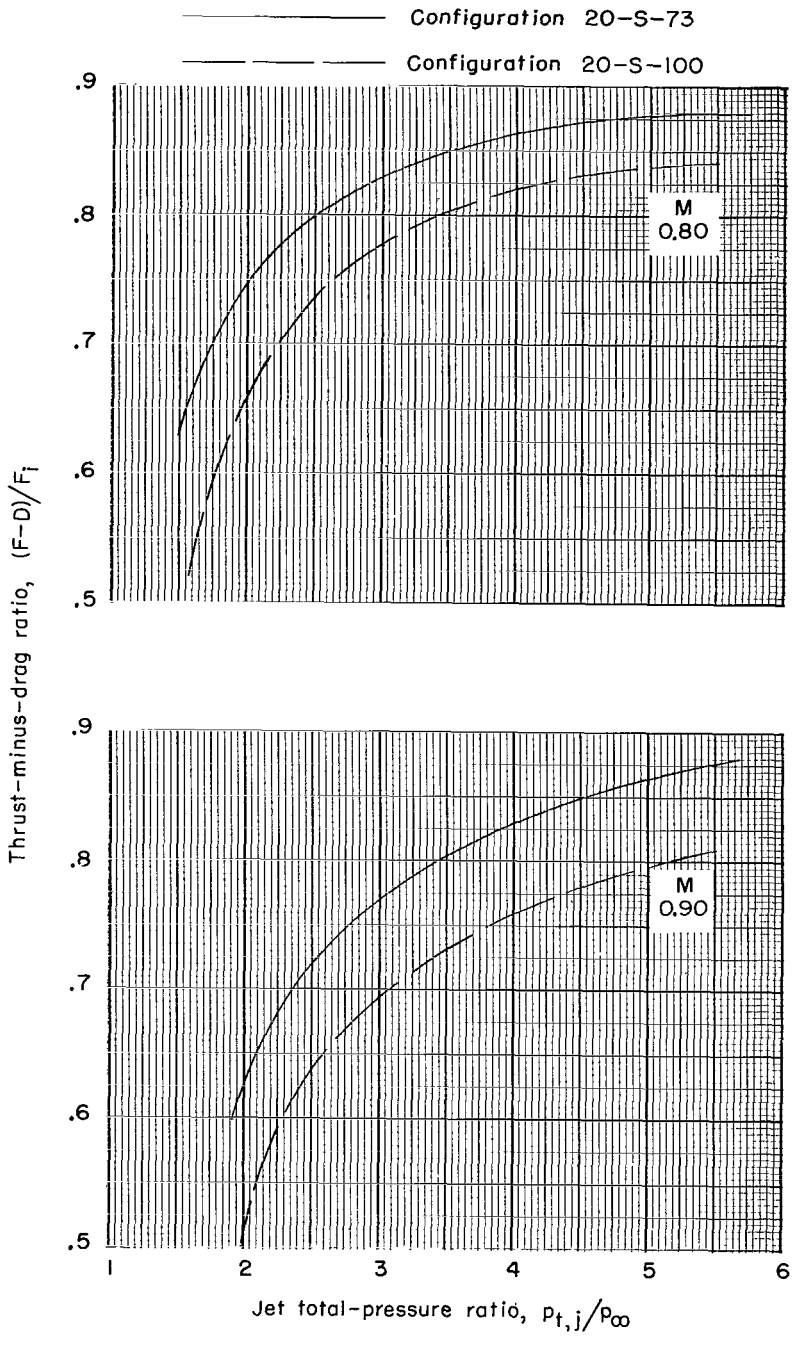

(b) M = 0.80 and M = 0.90.

Figure 28.- Continued.

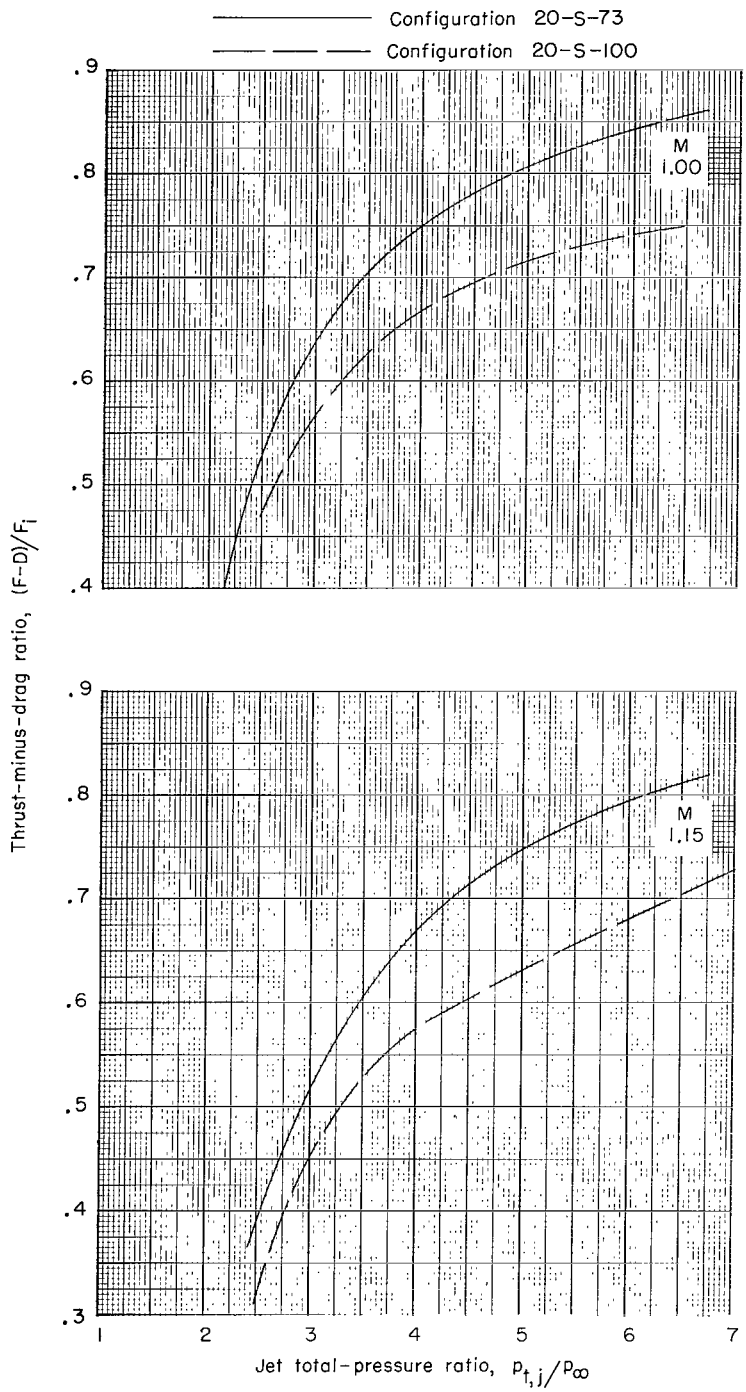

(c) M = 1.00 and M = 1.15.

Figure 28.- Continued.

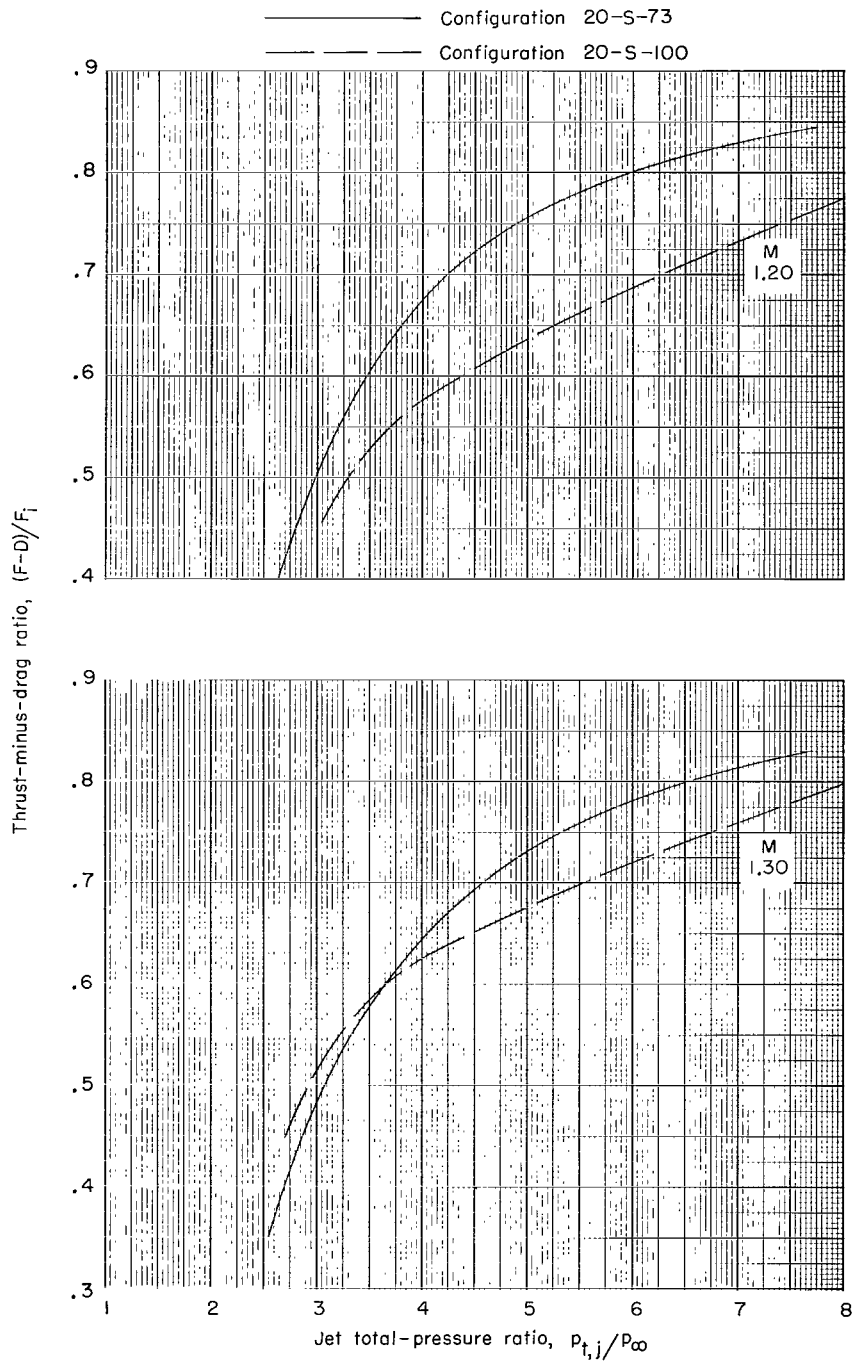

(d) M = 1.20 and M = 1.30.

Figure 28.- Concluded.

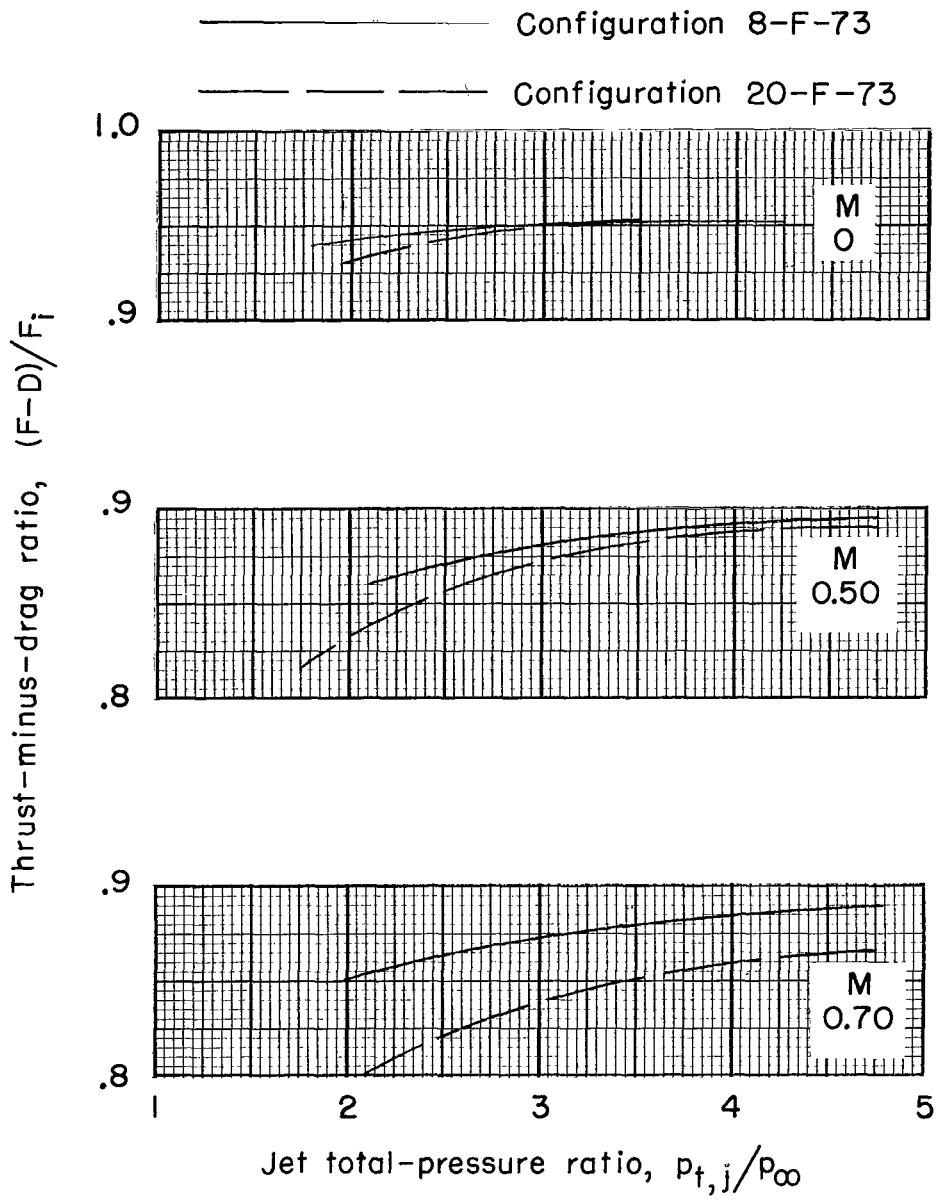

(a) M = 0 to M = 0.70.

Figure 29.- Effect of jet total-pressure ratio and boattail angle on thrust-minus-drag ratio. 72.5-percent truncation; flat plug base.

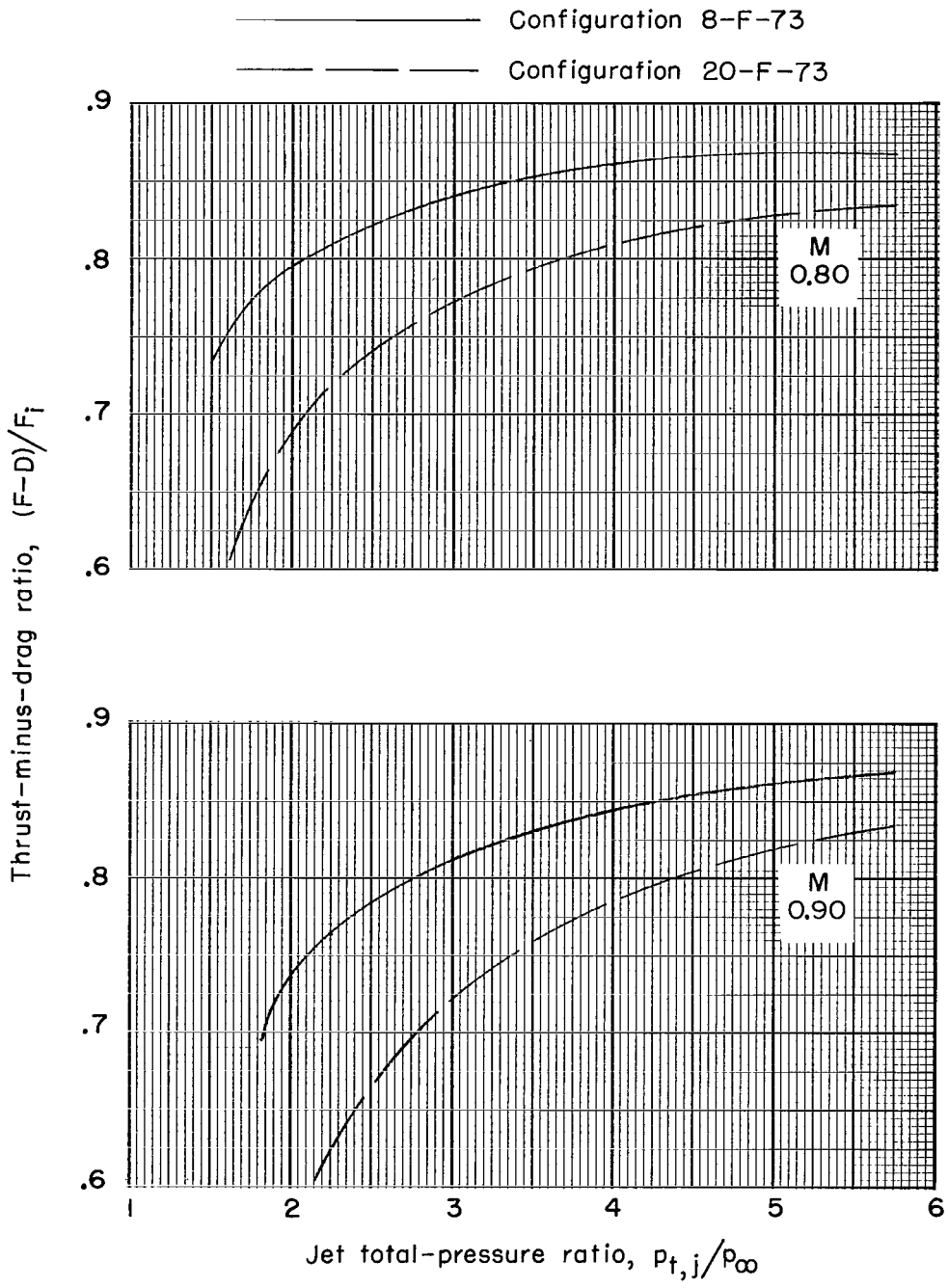

(b) M = 0.80 and M = 0.90.

Figure 29.- Continued.

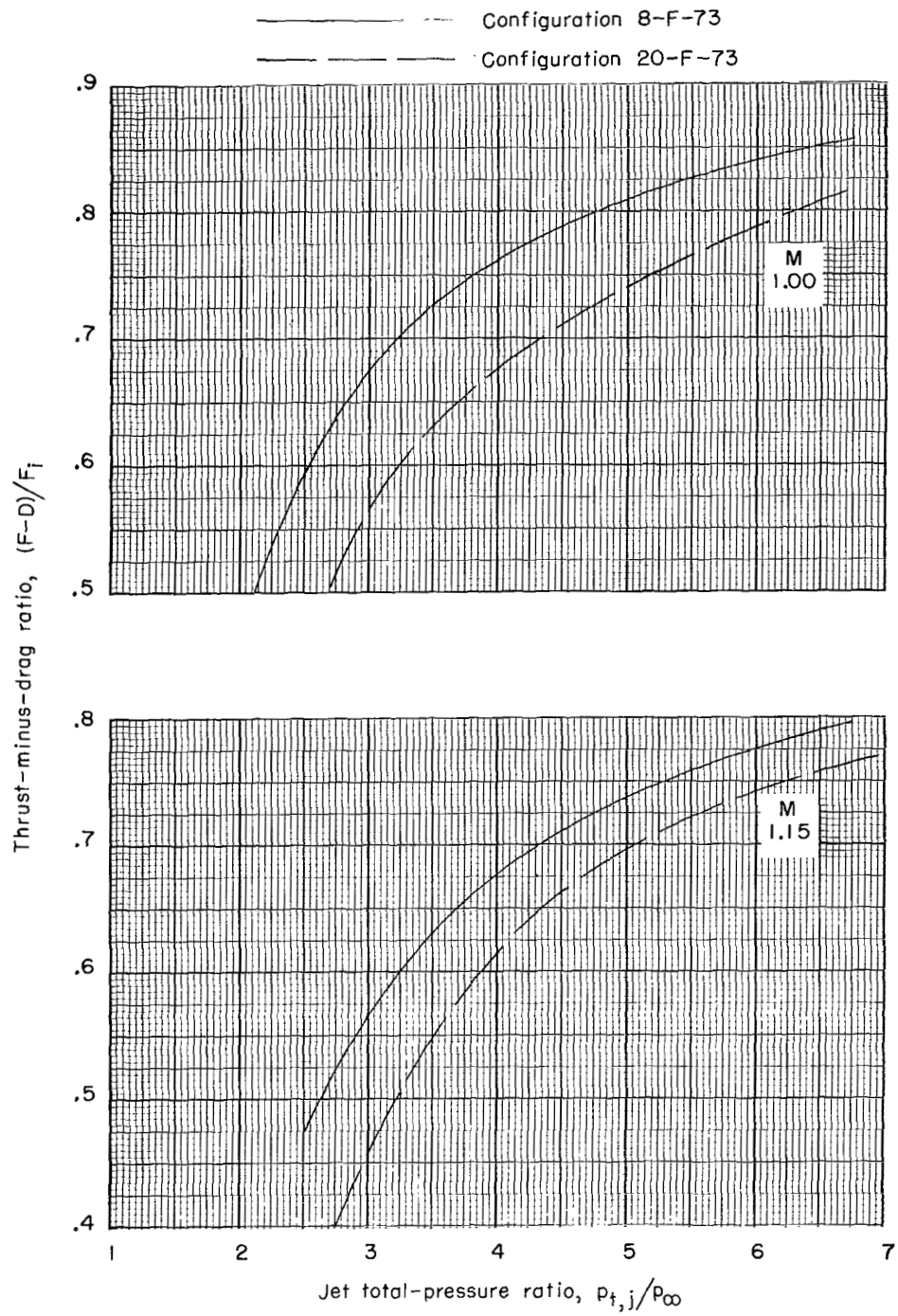

(c) M = 1.00 and M = 1.15.

Figure 29.- Continued.

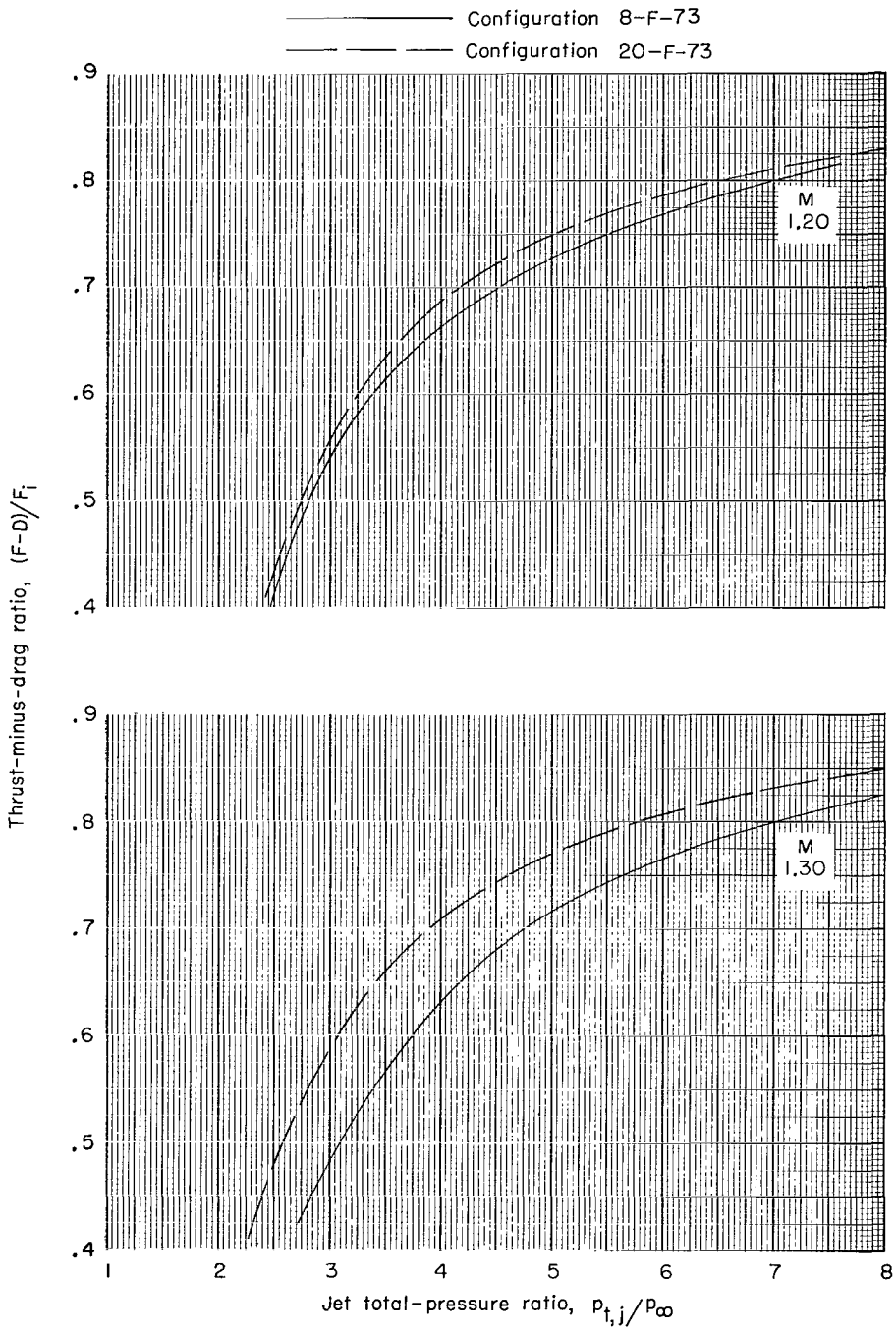

(d) M = 1.20 and M = 1.30.

Figure 29.- Concluded.

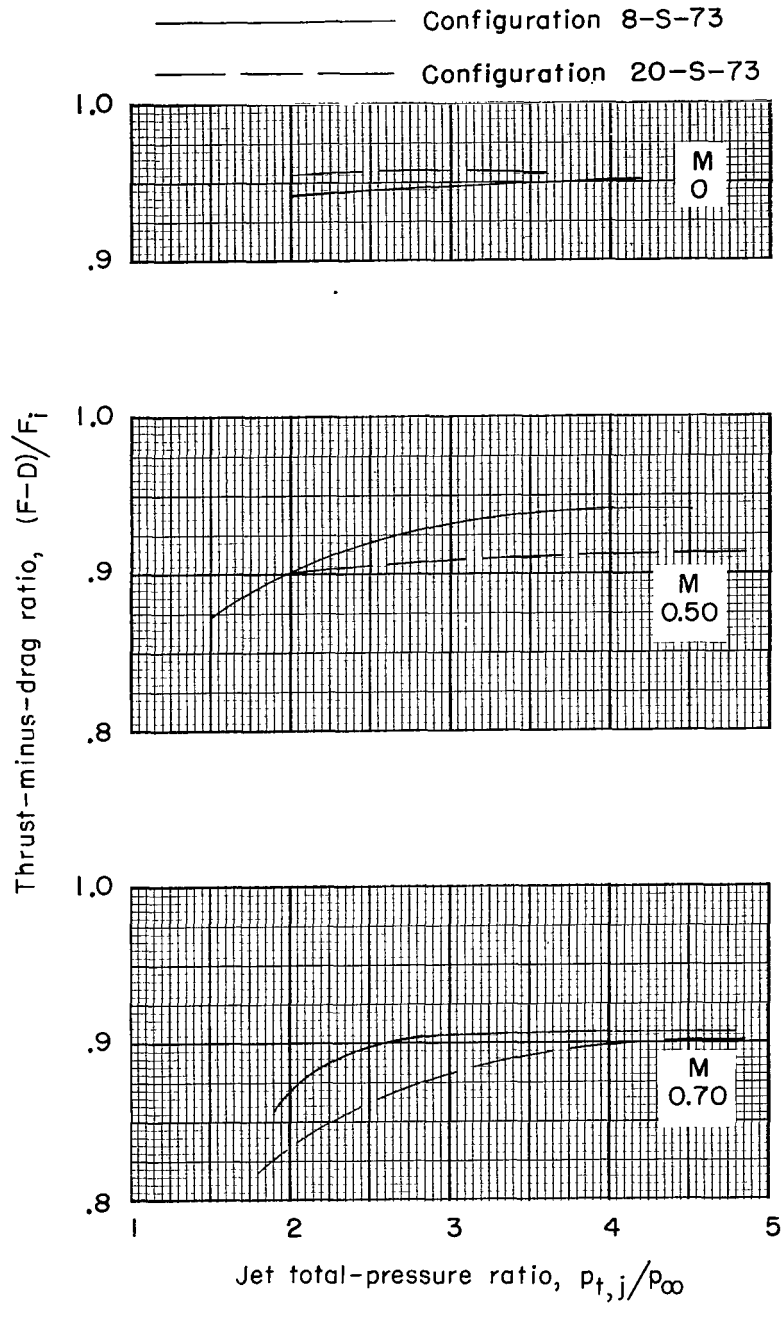

(a) M = 0 to M = 0.70.

Figure 30.- Effect of jet total-pressure ratio and boattail angle on thrust-minus-drag ratio. 72.5-percent truncation; semitoroidal plug base.

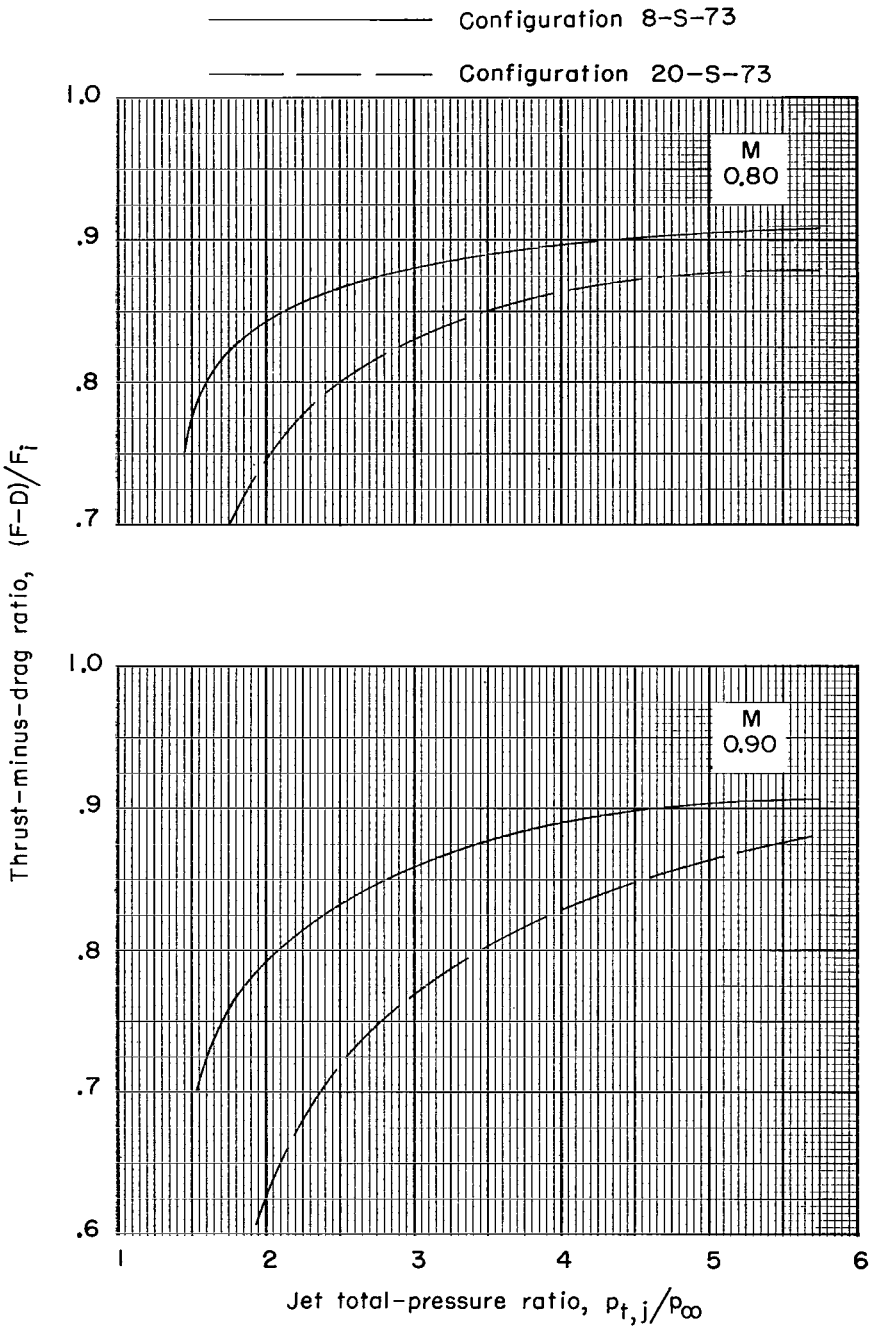

(b) M = 0.80 and M = 0.90.

Figure 30.- Continued.

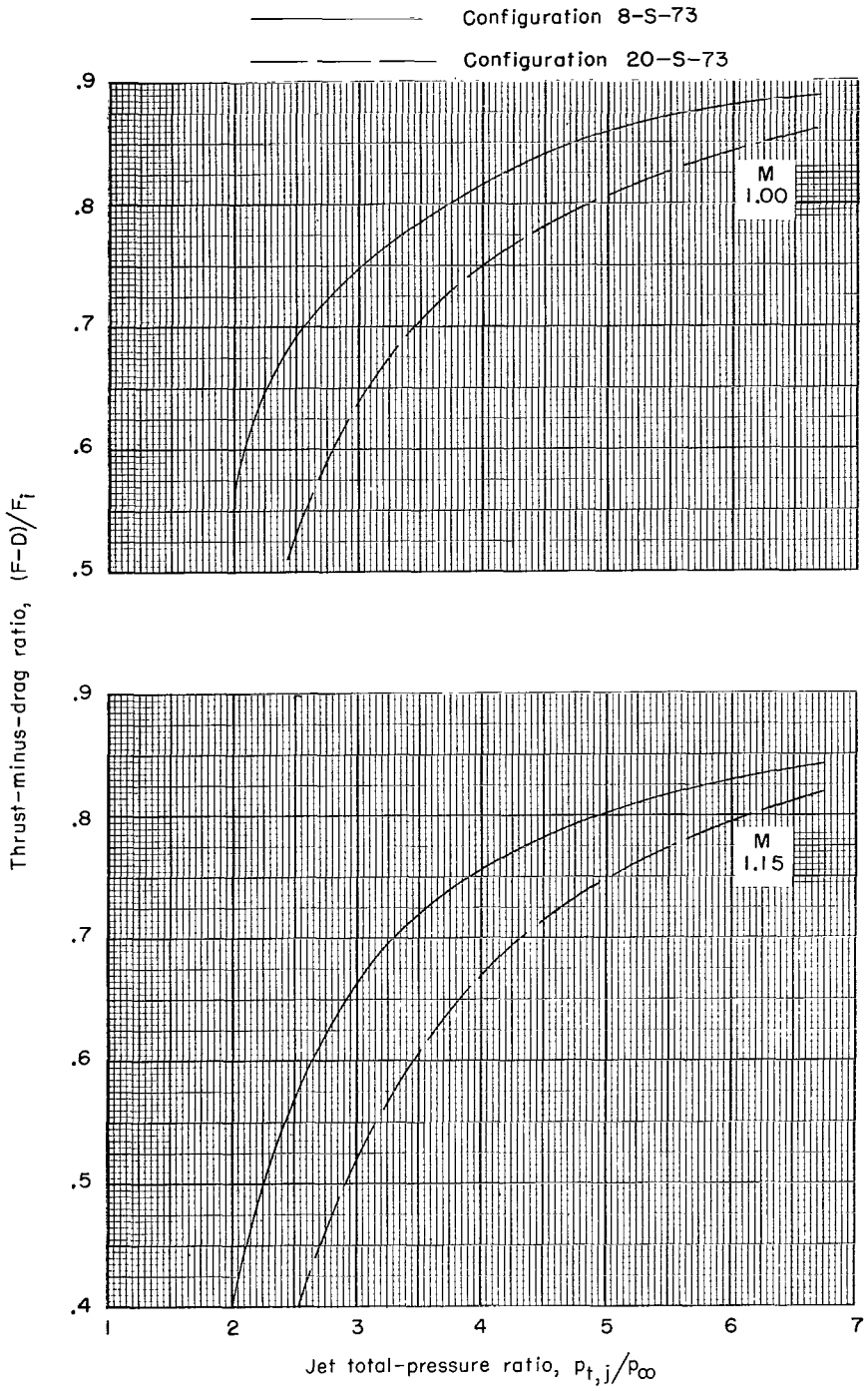

(c) M = 1.00 and M = 1.15.

Figure 30.- Continued.

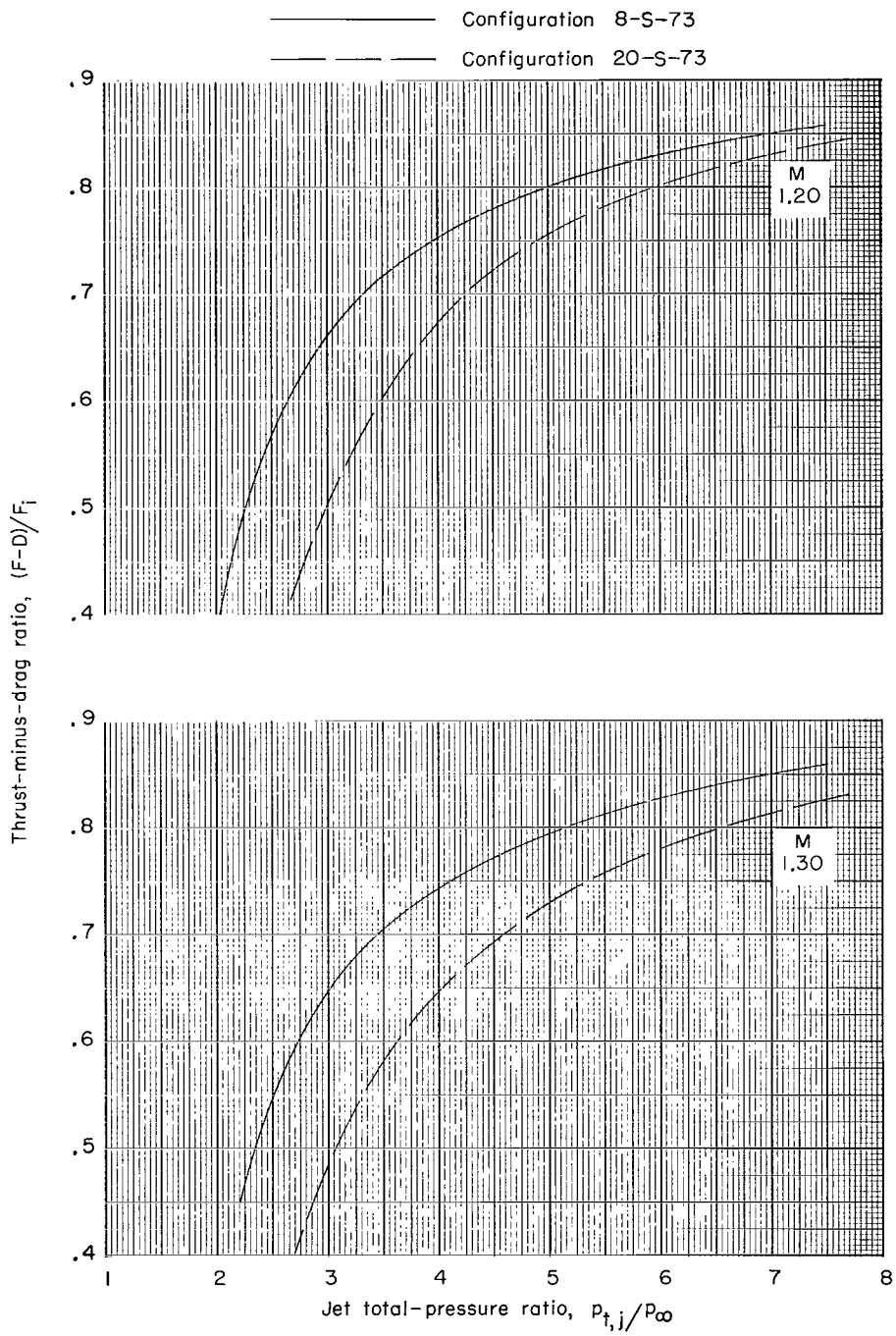

(d) M = 1.20 and M = 1.30.

Figure 30.- Concluded.

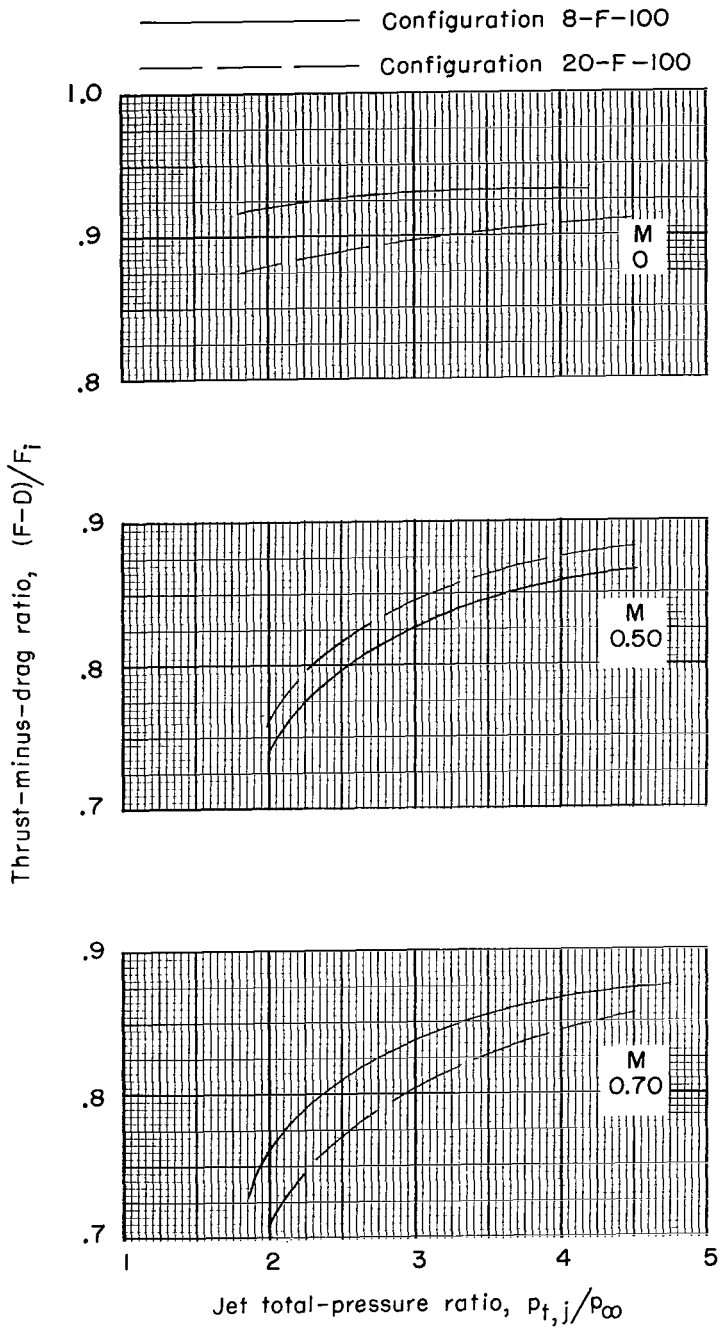

(a) M = 0 to M = 0.70.

Figure 31.- Effect of jet total-pressure ratio and boattail angle on thrust-minus-drag ratio. 100-percent truncation; flat plug base.

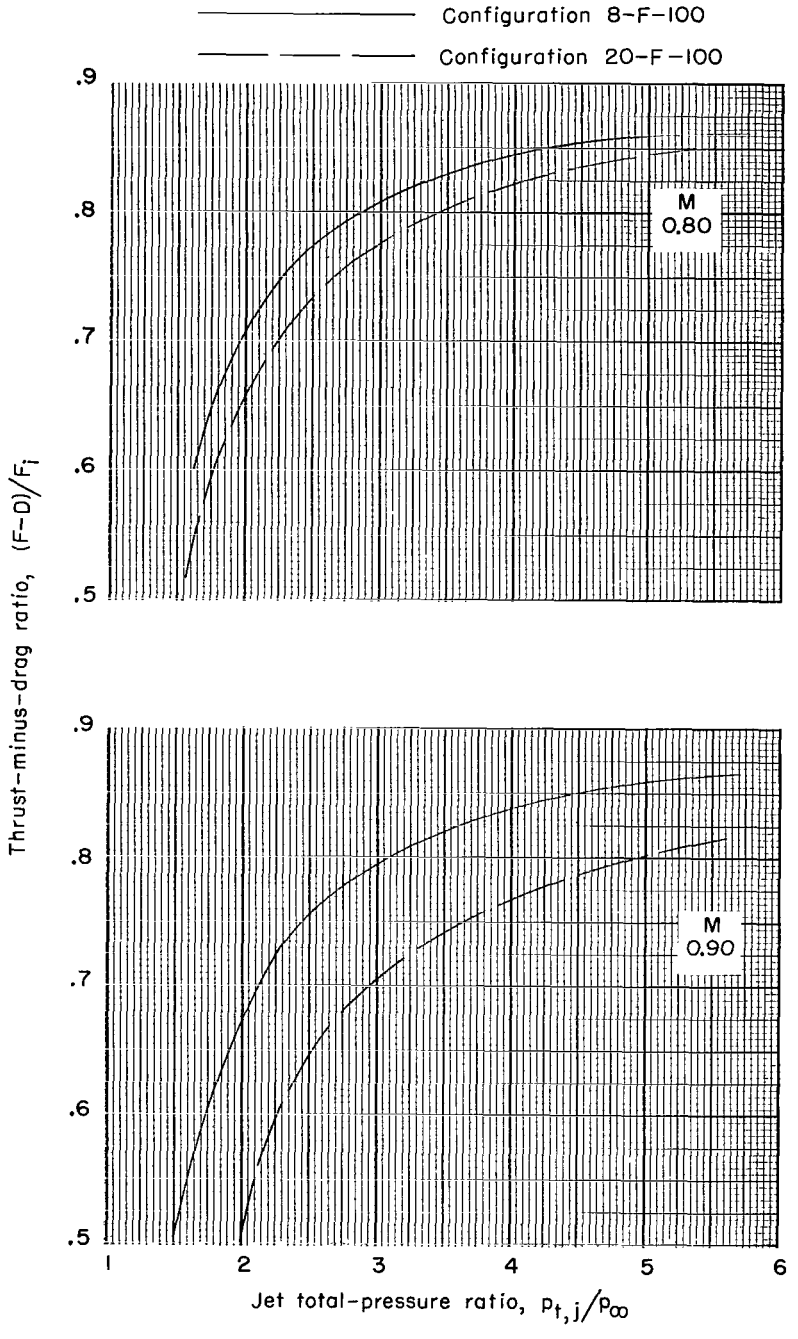

(b) M = 0.80 and M = 0.90.

Figure 31.- Continued.

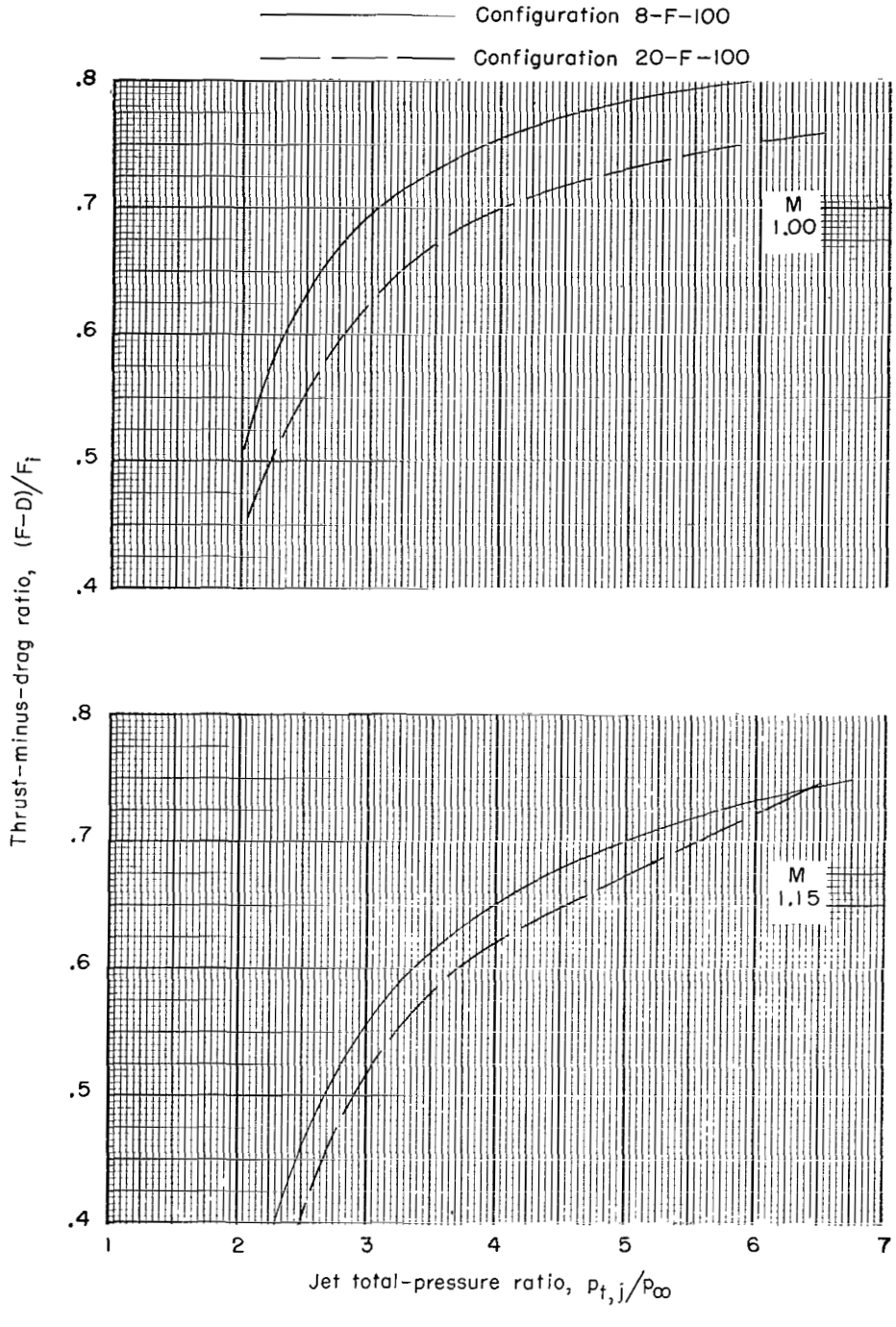

(c) M = 1.00 and M = 1.15.

Figure 31.- Continued.

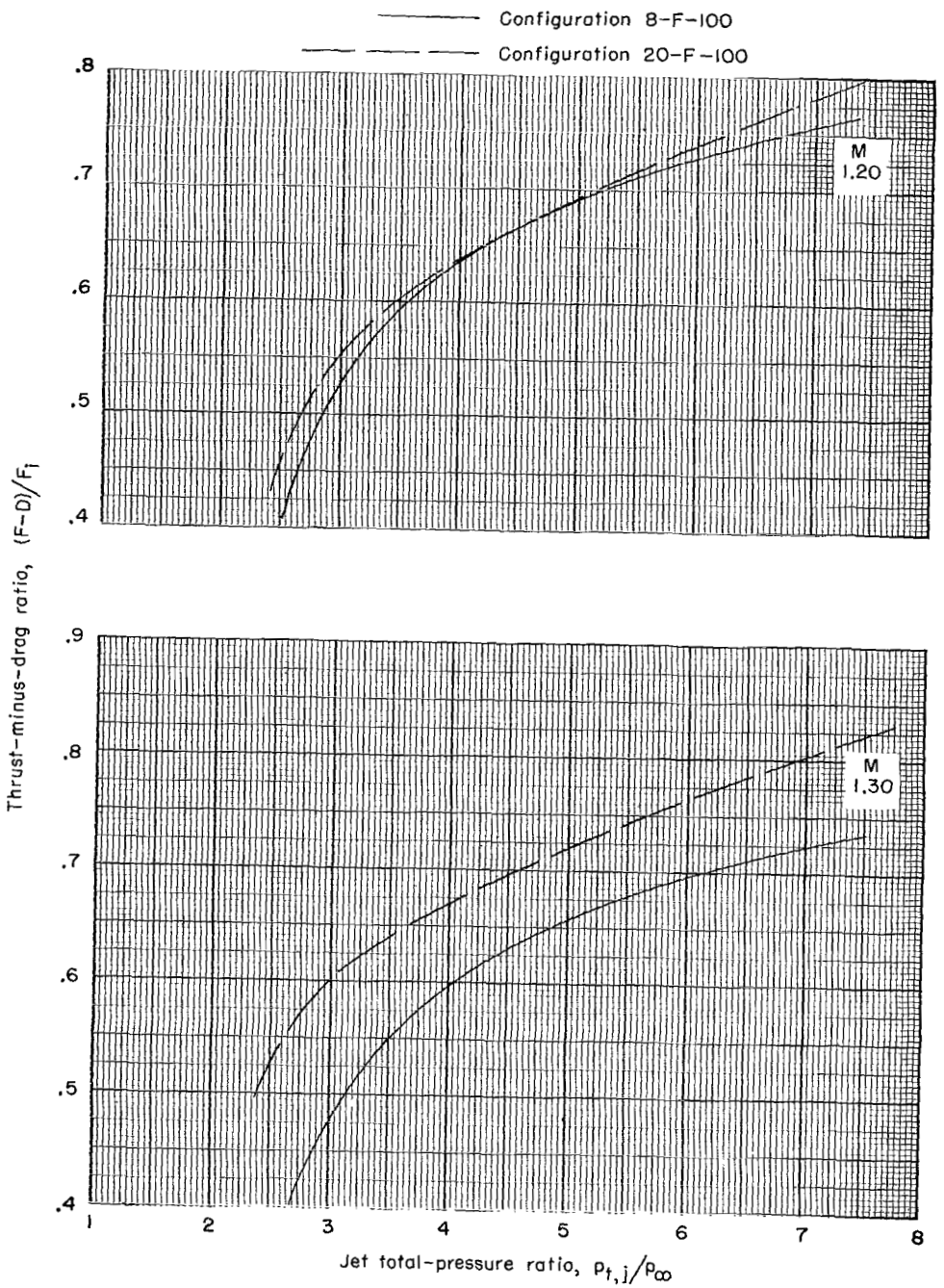

(d) M = 1.20 and M = 1.30.

Figure 31.- Concluded.

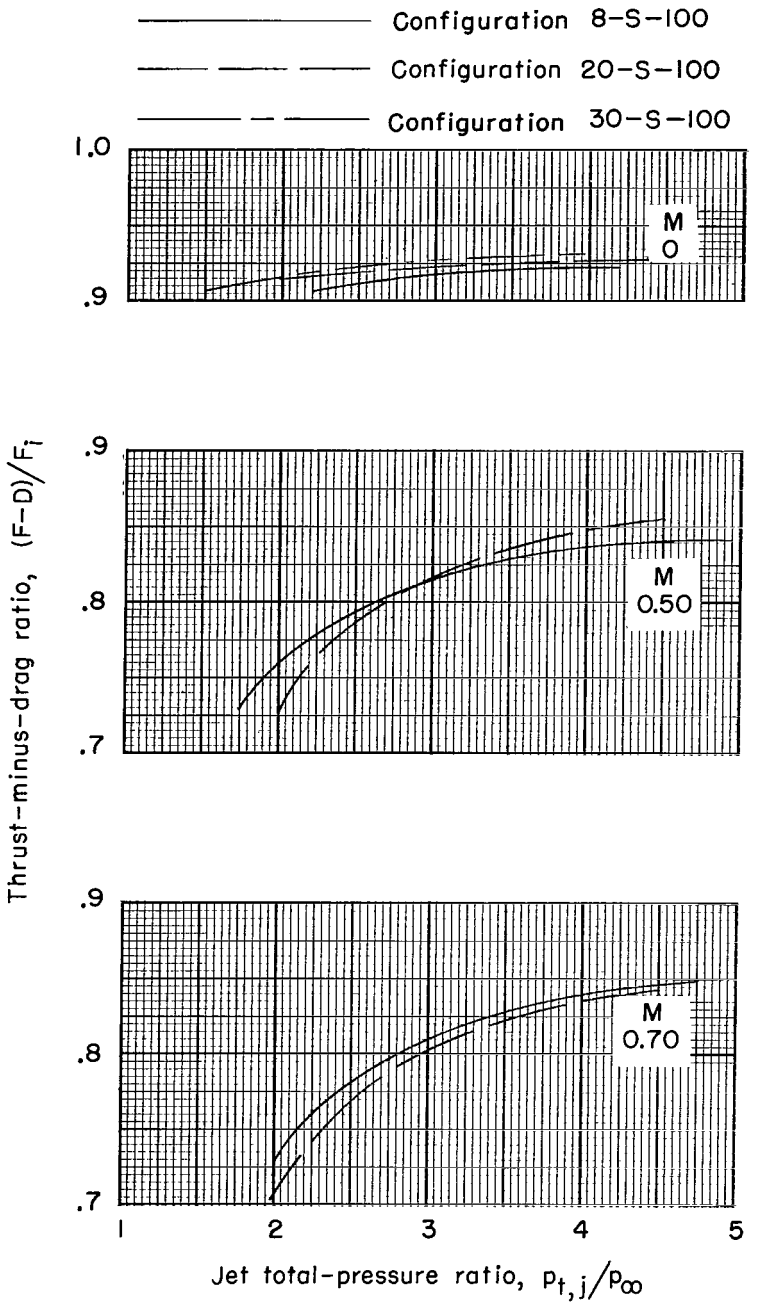

(a) M = 0 to M = 0.70.

Figure 32.- Effect of jet total-pressure ratio and boattail angle on thrust-minus-drag ratio. 100-percent truncation; semitoroidal plug base.

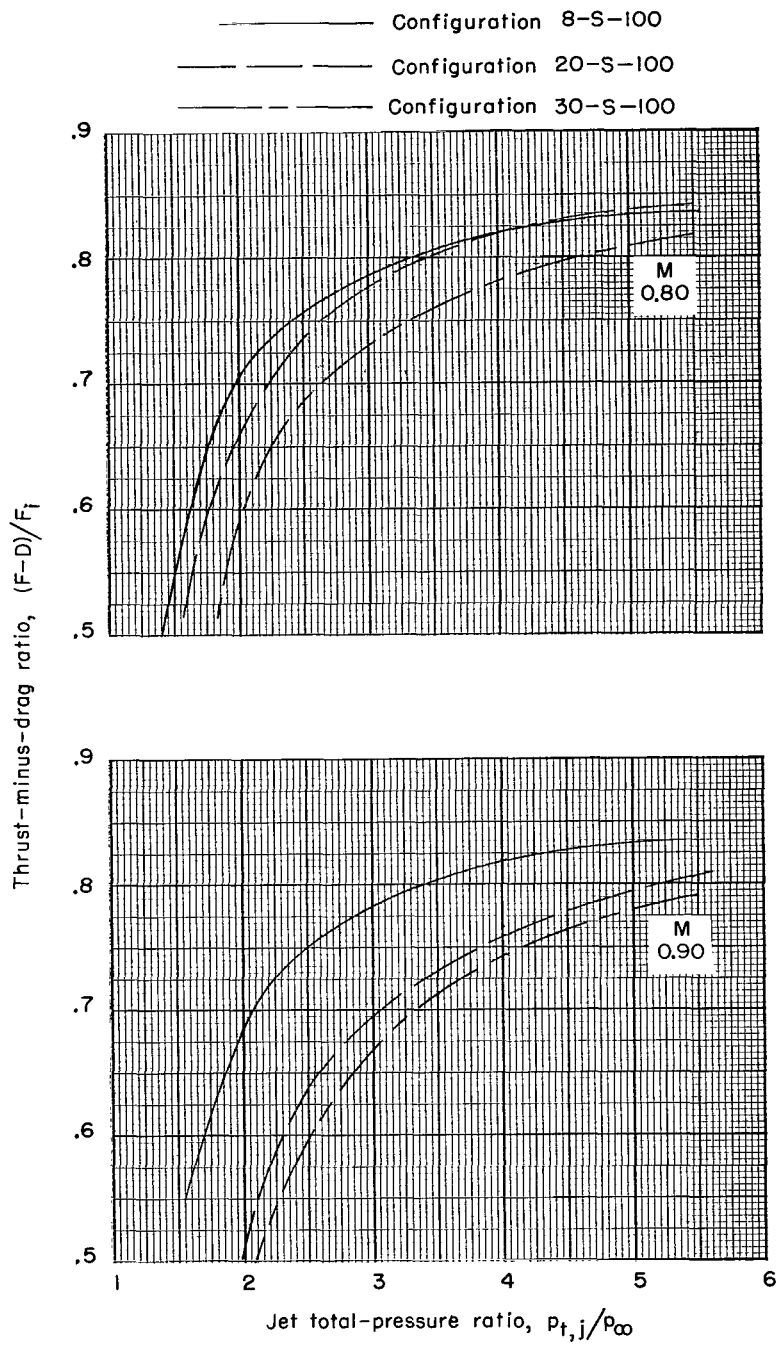

(b) M = 0.80 and M = 0.90.

Figure 32.- Continued.

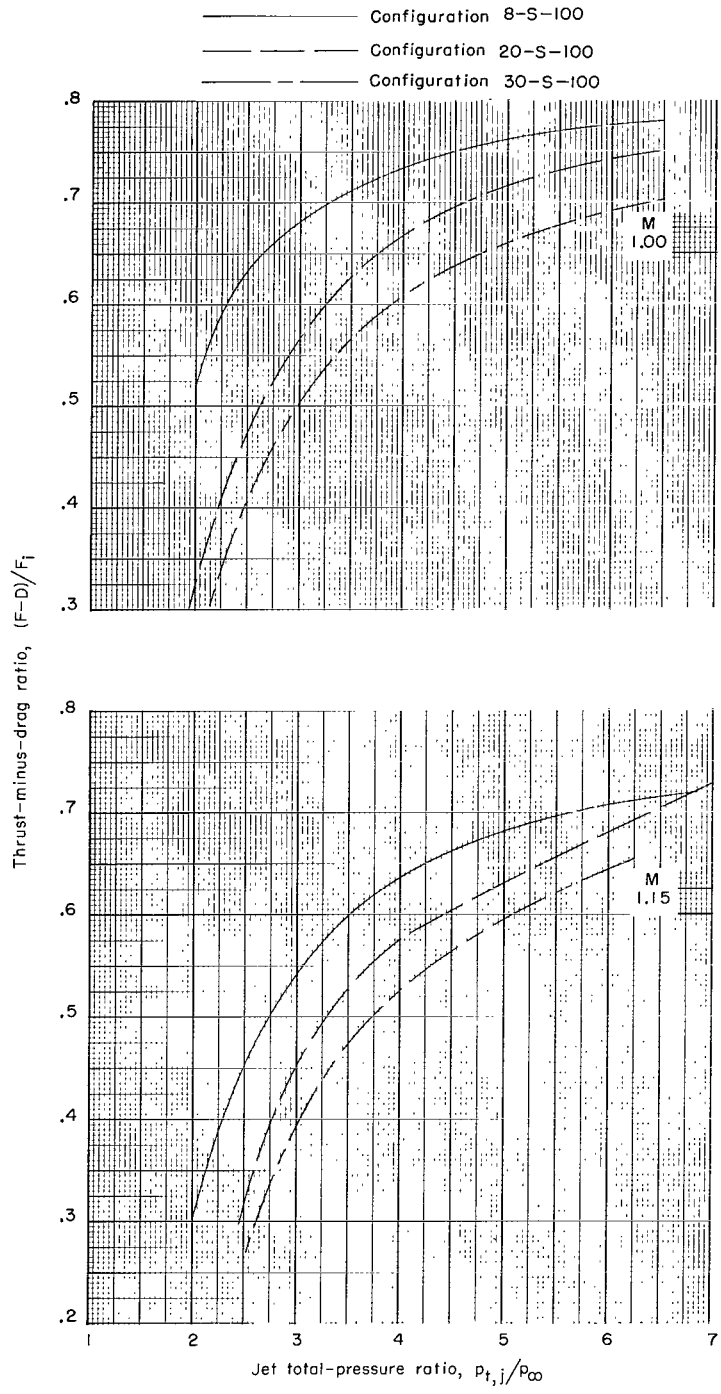

(c) M = 1.00 and M = 1.15.

Figure 32.- Continued.

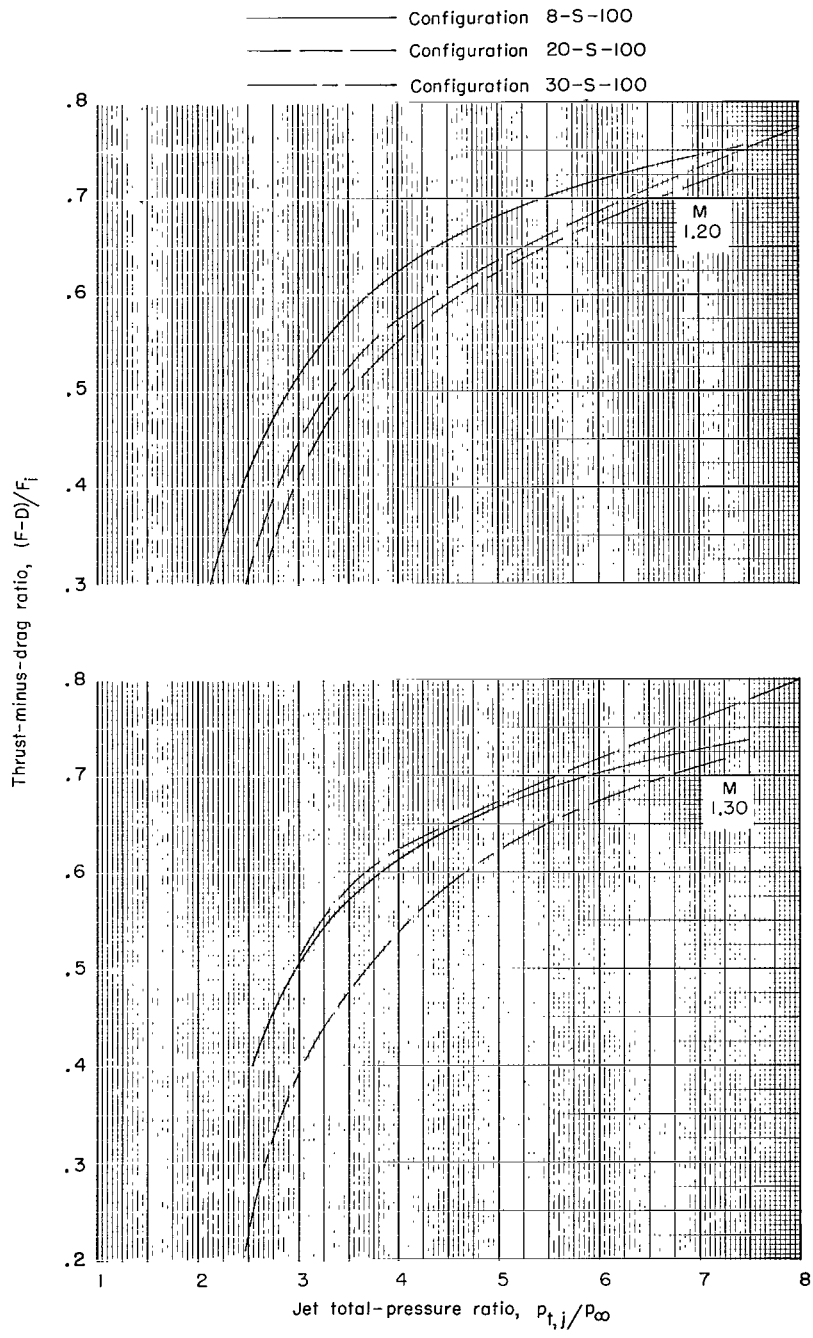

(d) M = 1.20 and M = 1.30.

Figure 32.- Concluded.

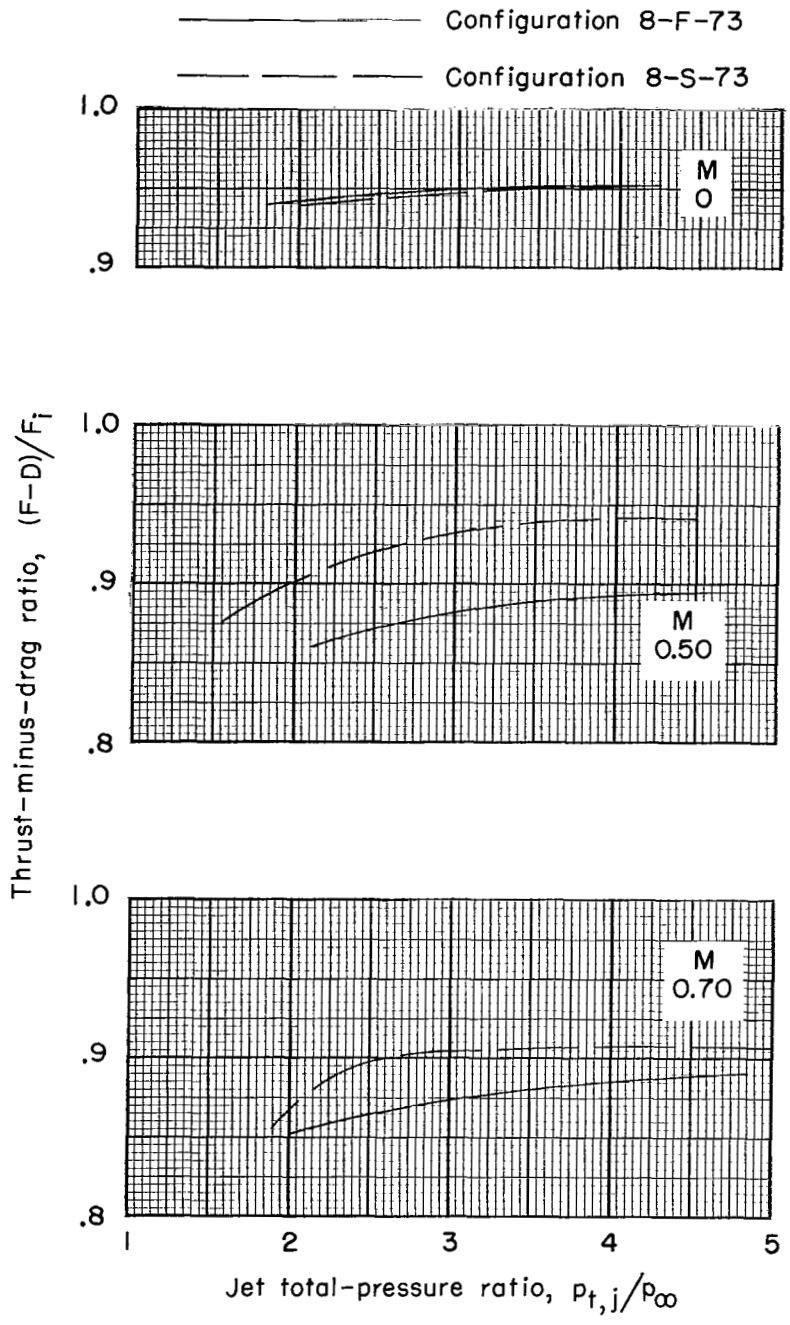

(a) M = 0 to M = 0.70.

Figure 33.- Effect of jet total-pressure ratio and plug base shape on thrust-minus-drag ratio. 8^0 boattail angle; 72.5-percent truncation.

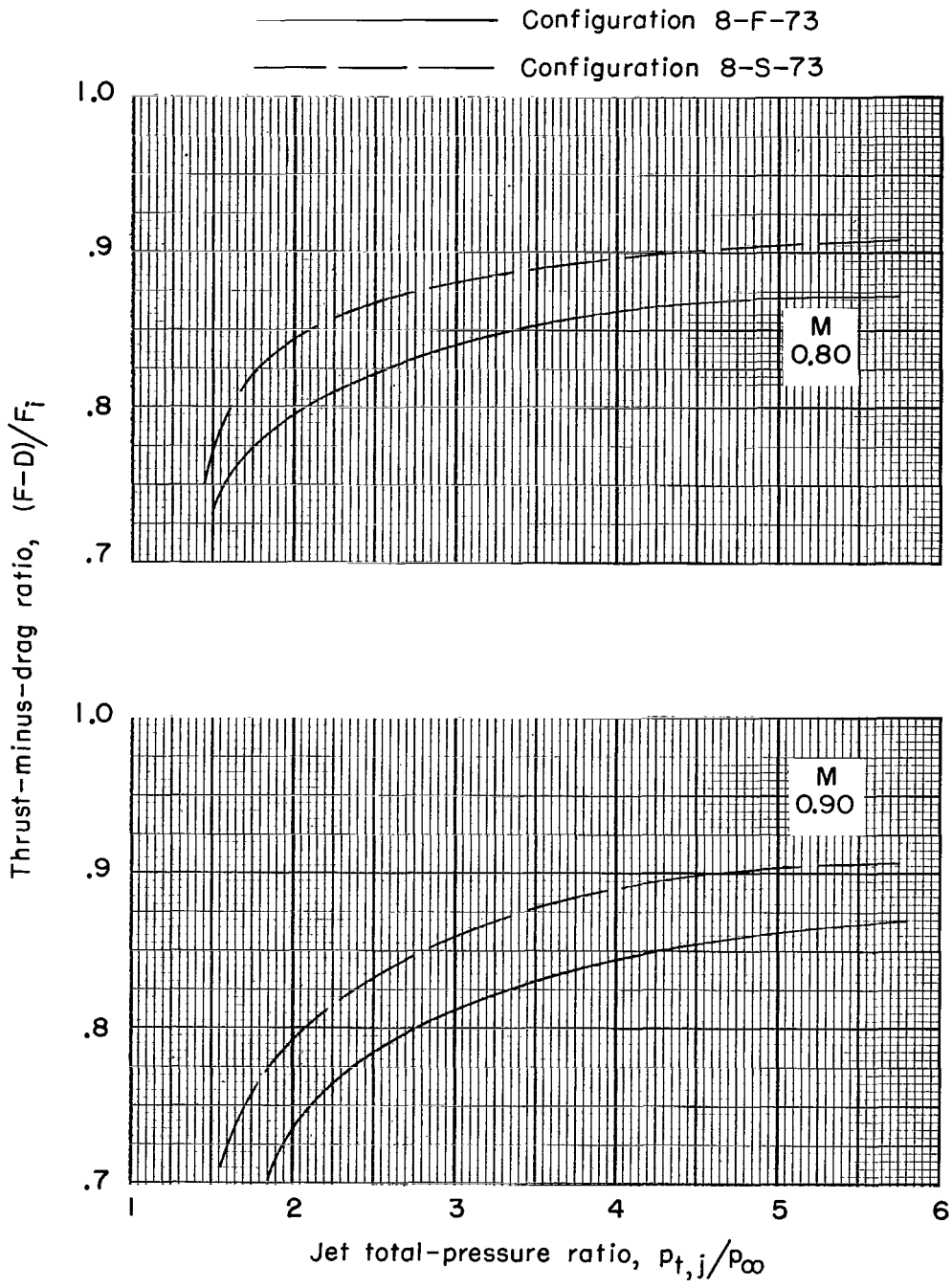

(b) M = 0.80 and M = 0.90.

Figure 33.- Continued.

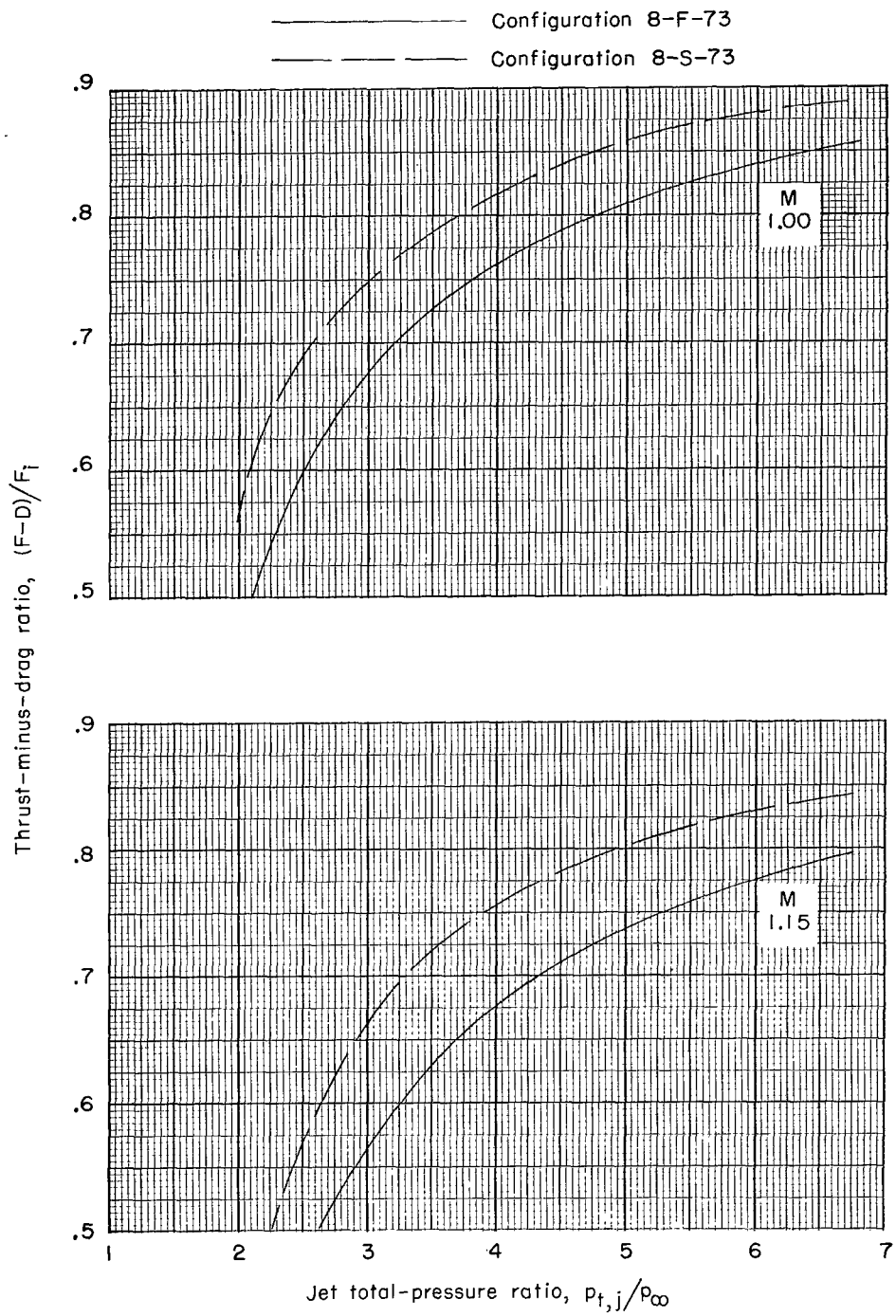

(c) M = 1.00 and M = 1.15.

Figure 33.- Continued.

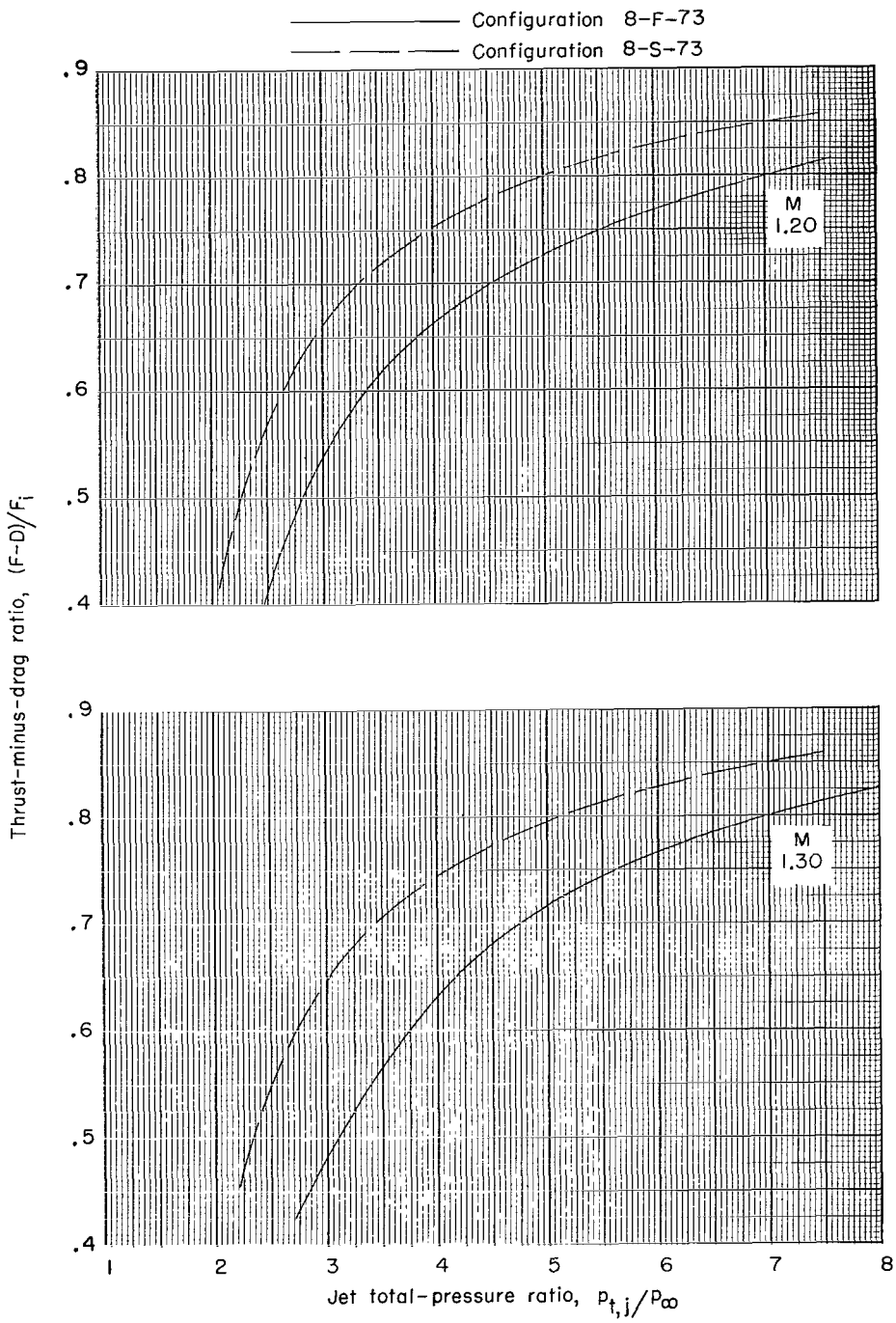

(d) M = 1.20 and M = 1.30.

Figure 33.- Concluded.

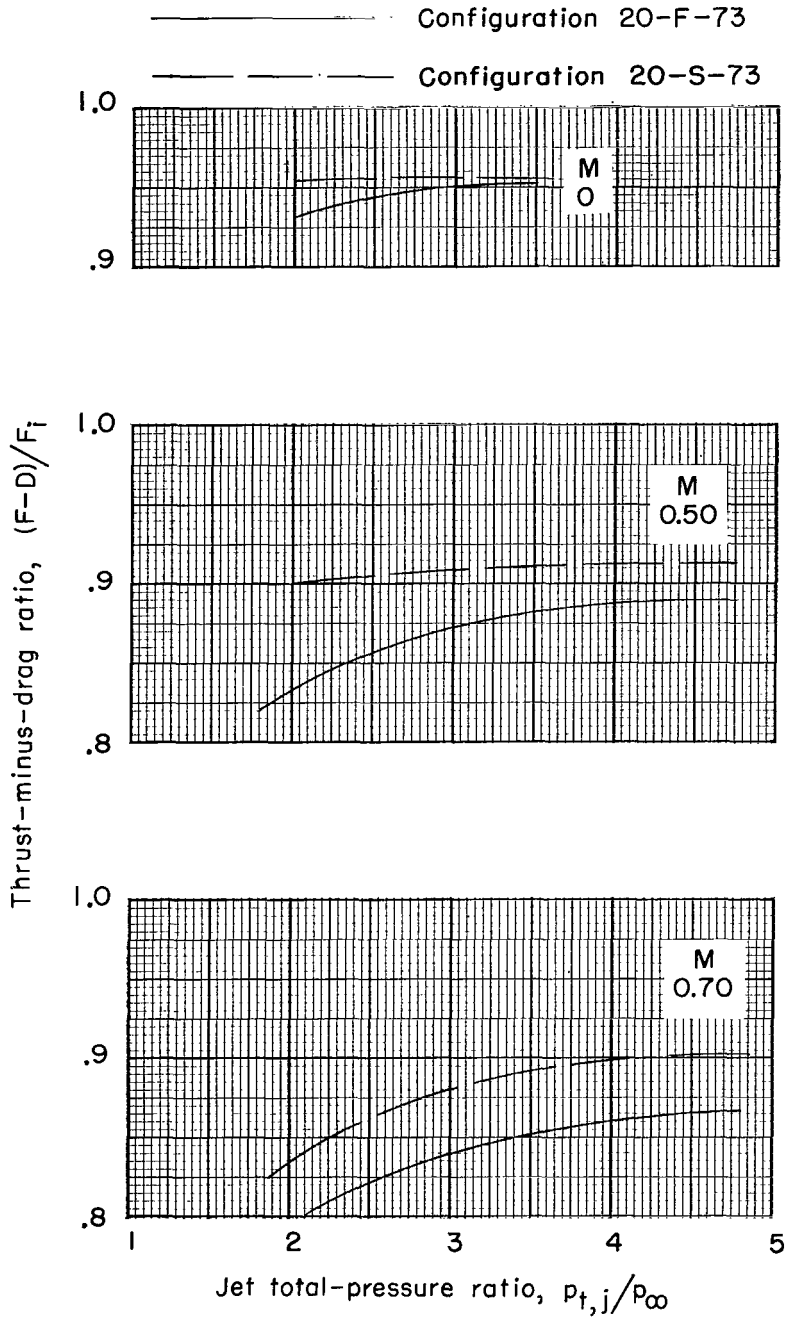

(a) M = 0 to M = 0.70.

Figure 34.- Effect of jet total-pressure ratio and plug base shape on thrust-minus-drag ratio. 20^0 boattail angle; 72.5-percent truncation.

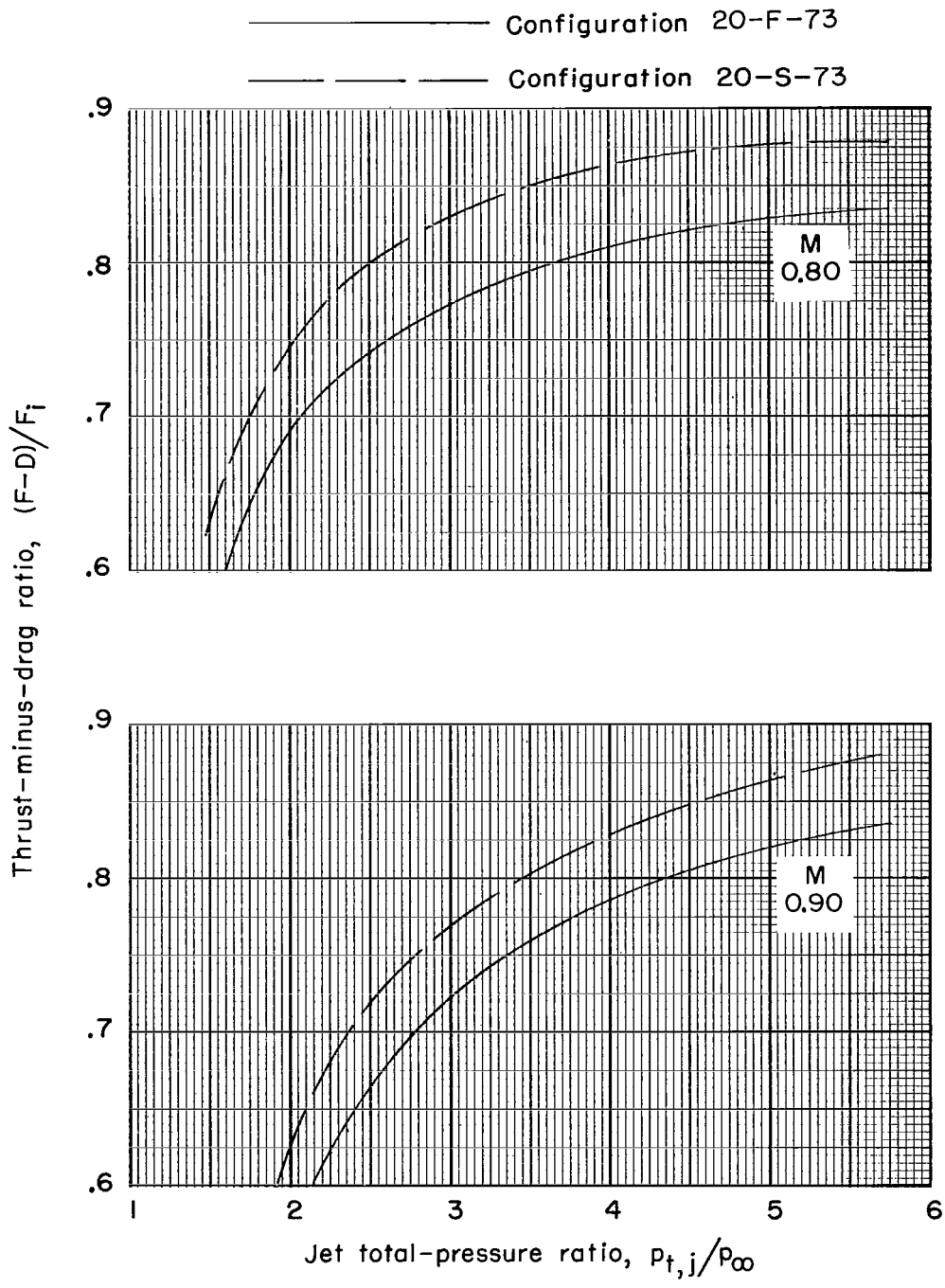

(b) M = 0.80 and M = 0.90.

Figure 34.- Continued.

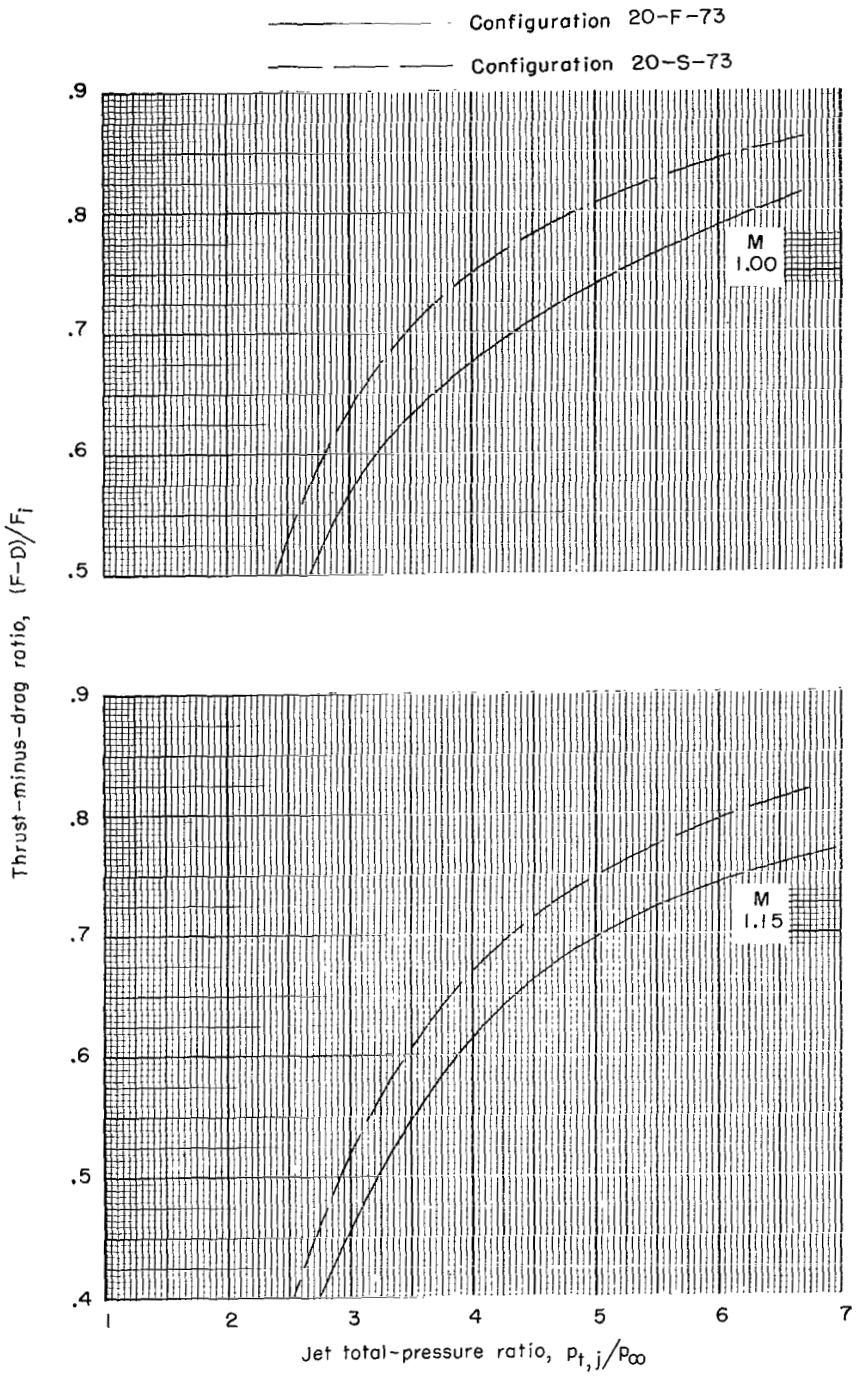

(c) M = 1.00 and M = 1.15.

Figure 34.- Continued.

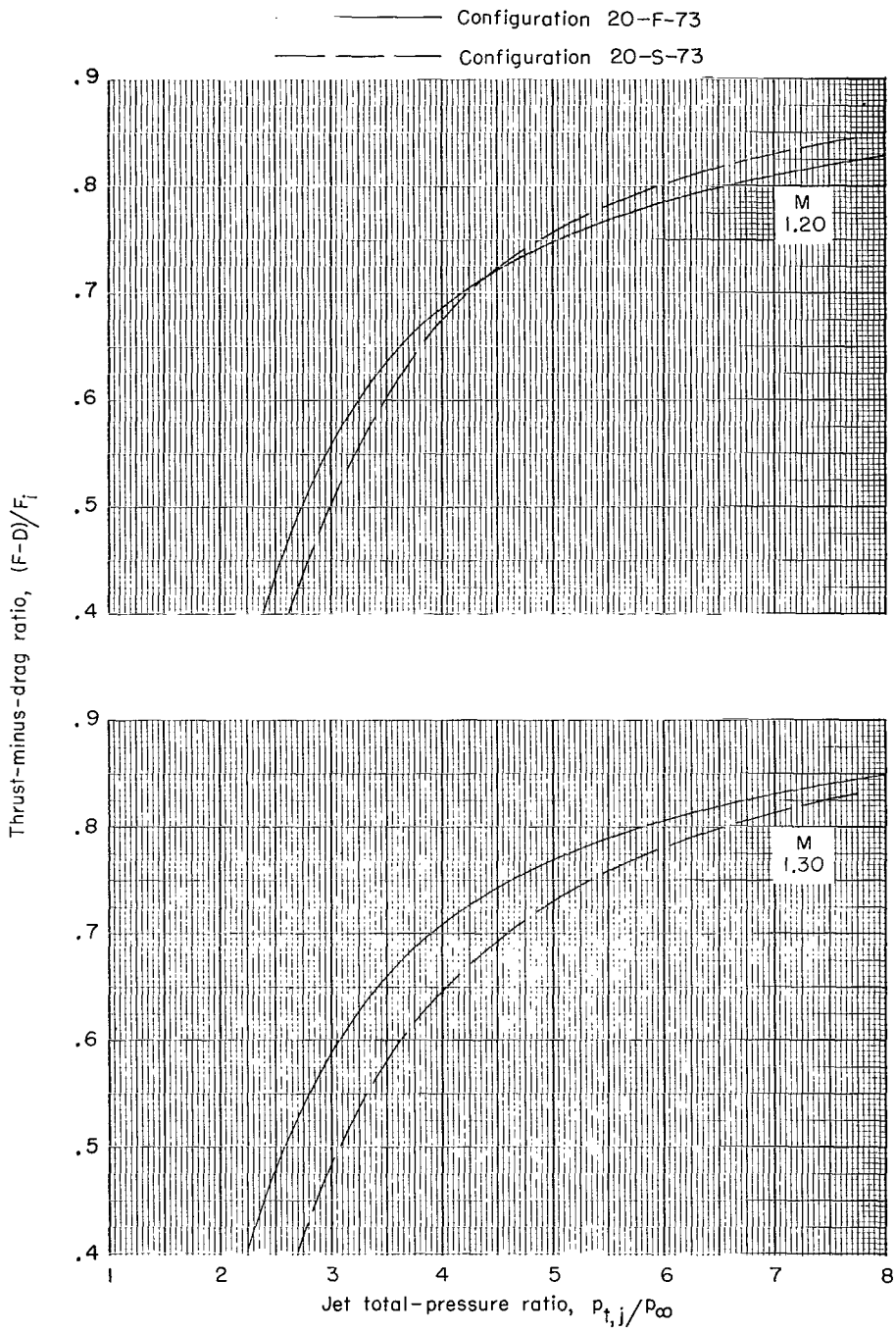

(d) M = 1.20 and M = 1.30.

Figure 34.- Concluded.

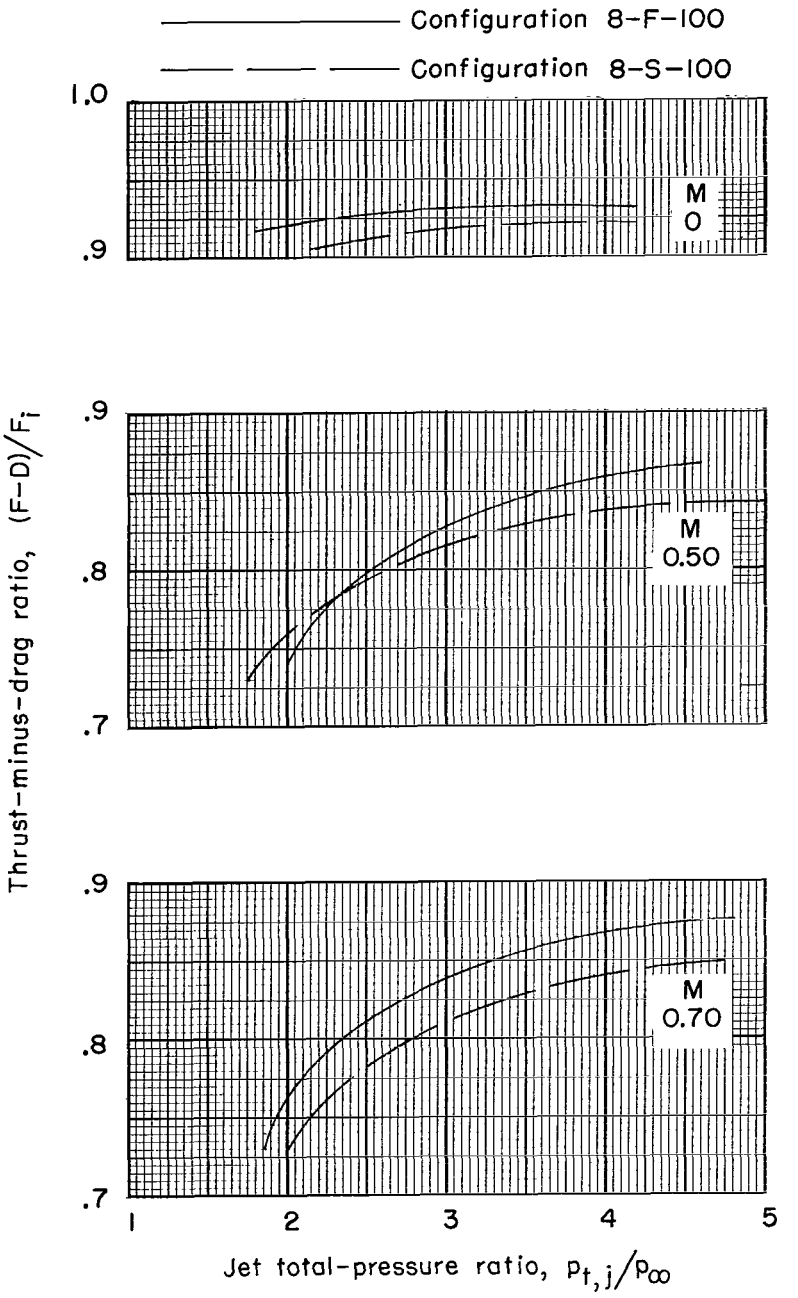

(a) M = 0 to M = 0.70.

Figure 35.- Effect of jet total-pressure ratio and plug base shape on thrust-minus-drag ratio. 8° boattail angle; 100-percent truncation.

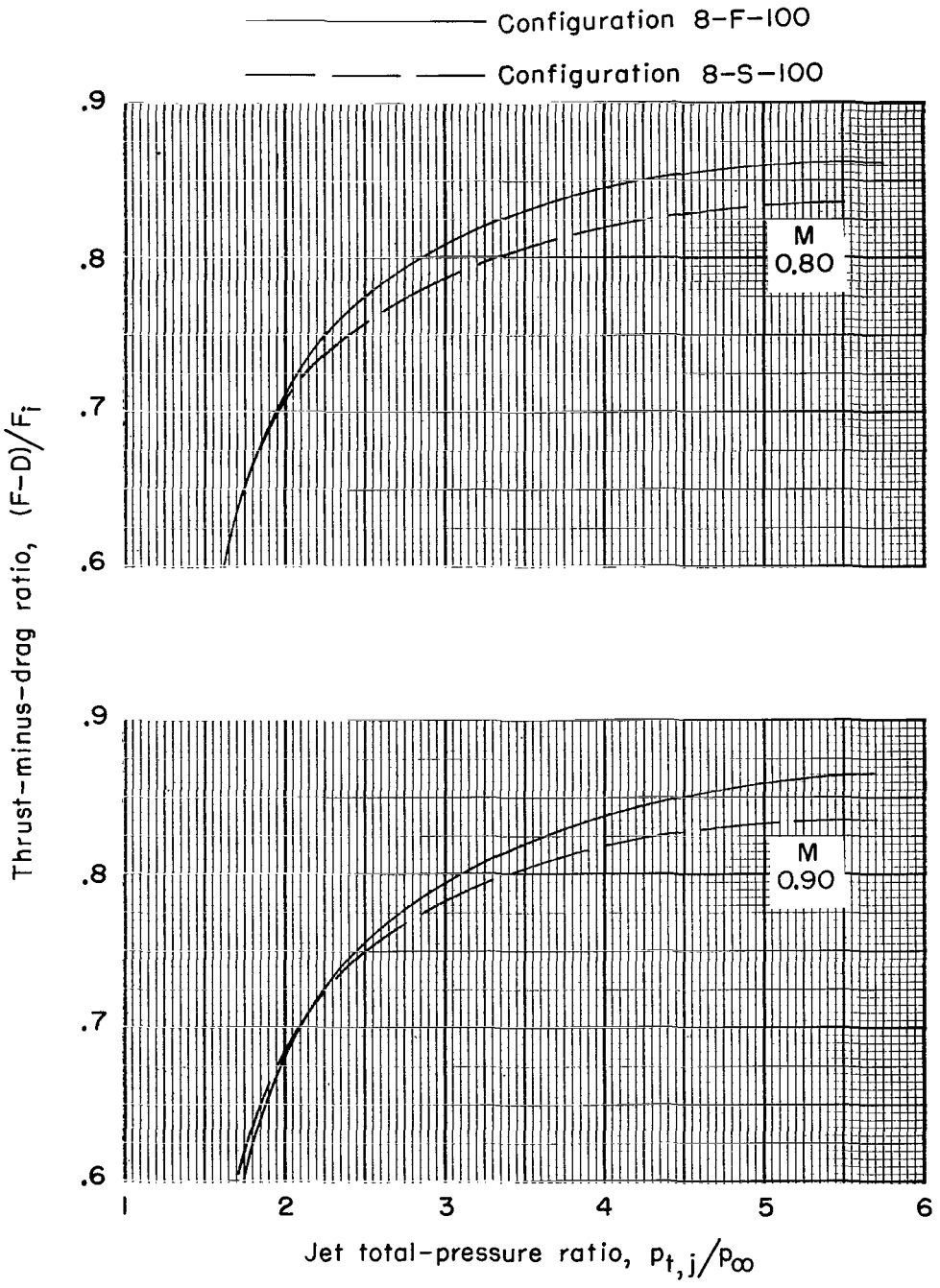

(b) M = 0.80 and M = 0.90.

Figure 35.- Continued.

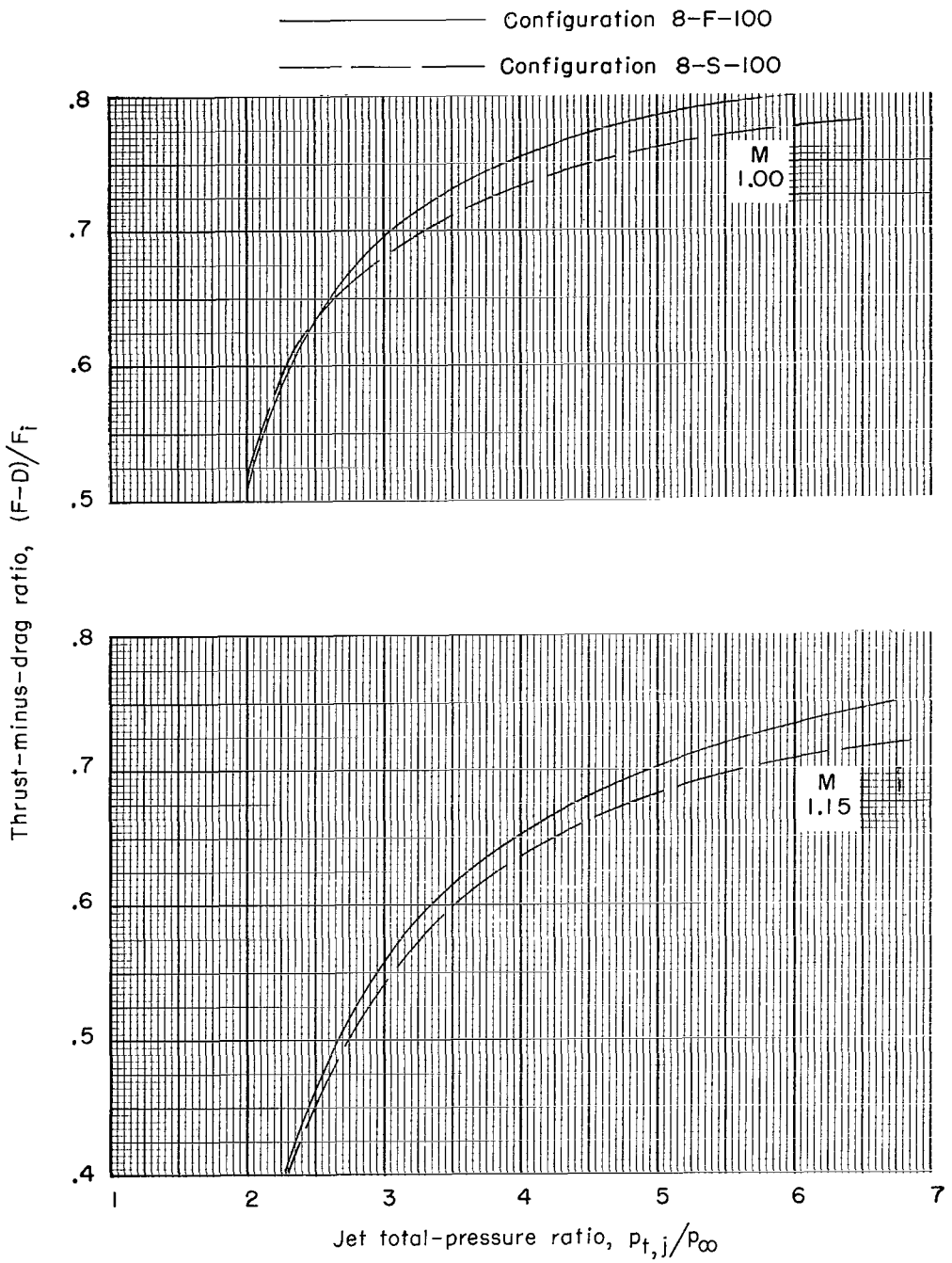

(c) M = 1.00 and M = 1.15.

Figure 35.- Continued.

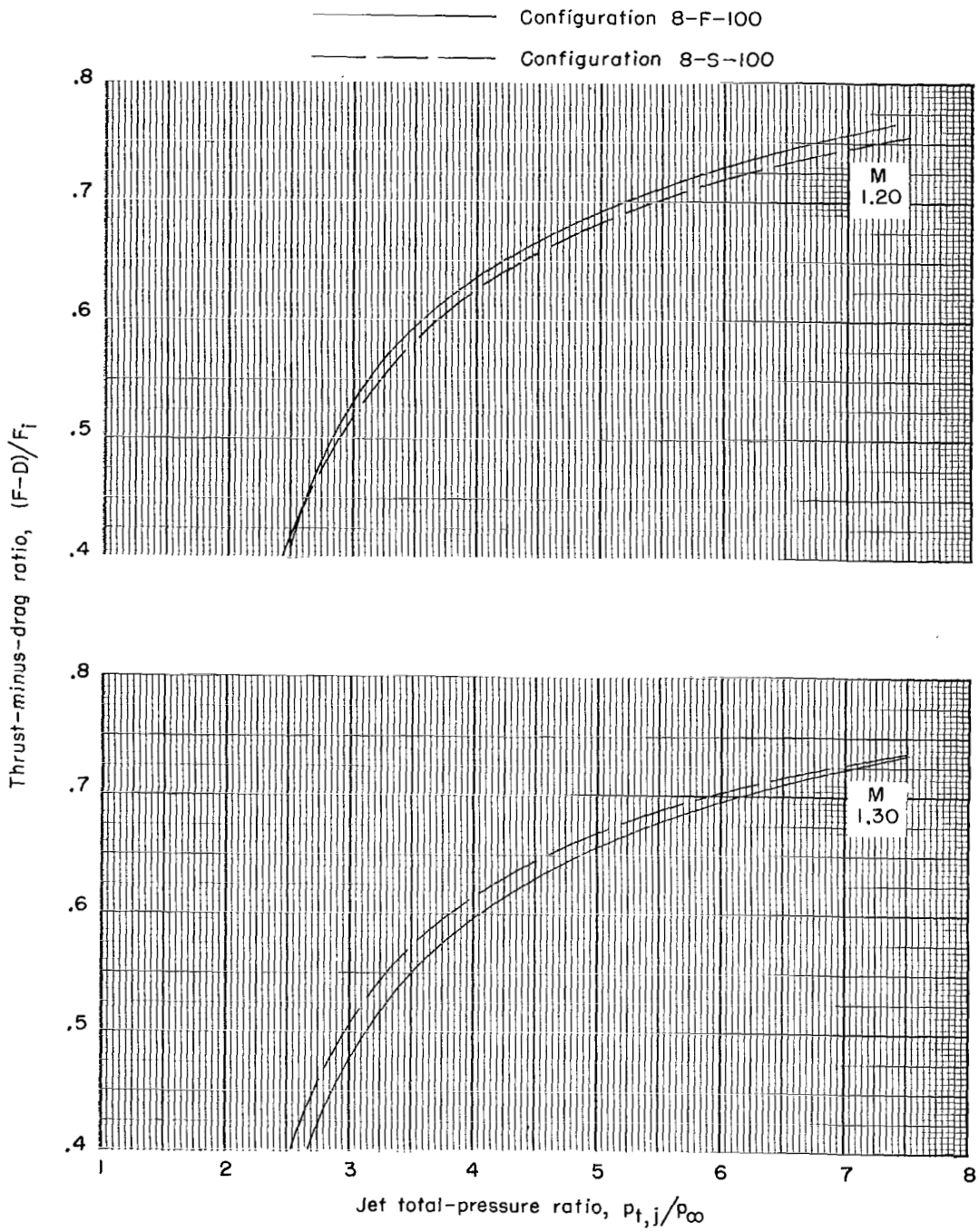

(d) M = 1.20 and M = 1.30.

Figure 35.- Concluded.

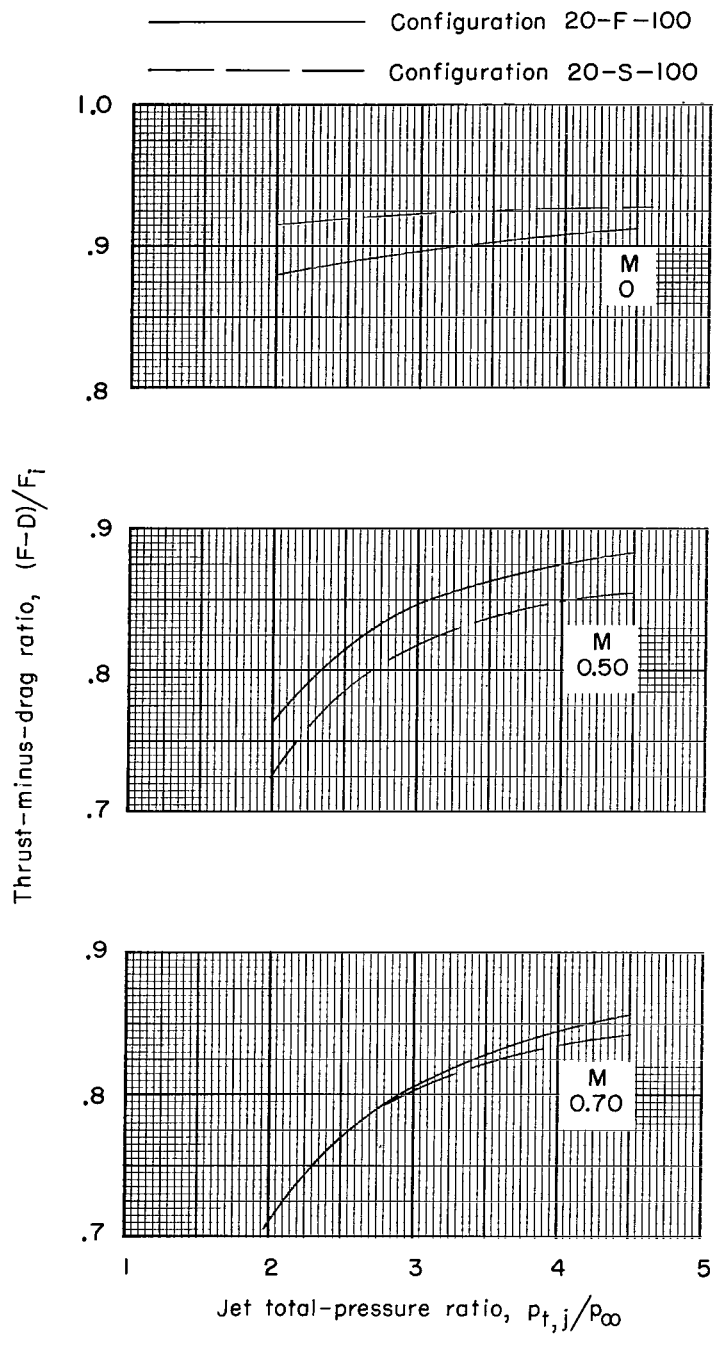

(a) M = 0 to M = 0.70.

Figure 36.- Effect of jet total-pressure ratio and plug base shape on thrust-minus-drag ratio. 20° boattail angle; 100-percent truncation.

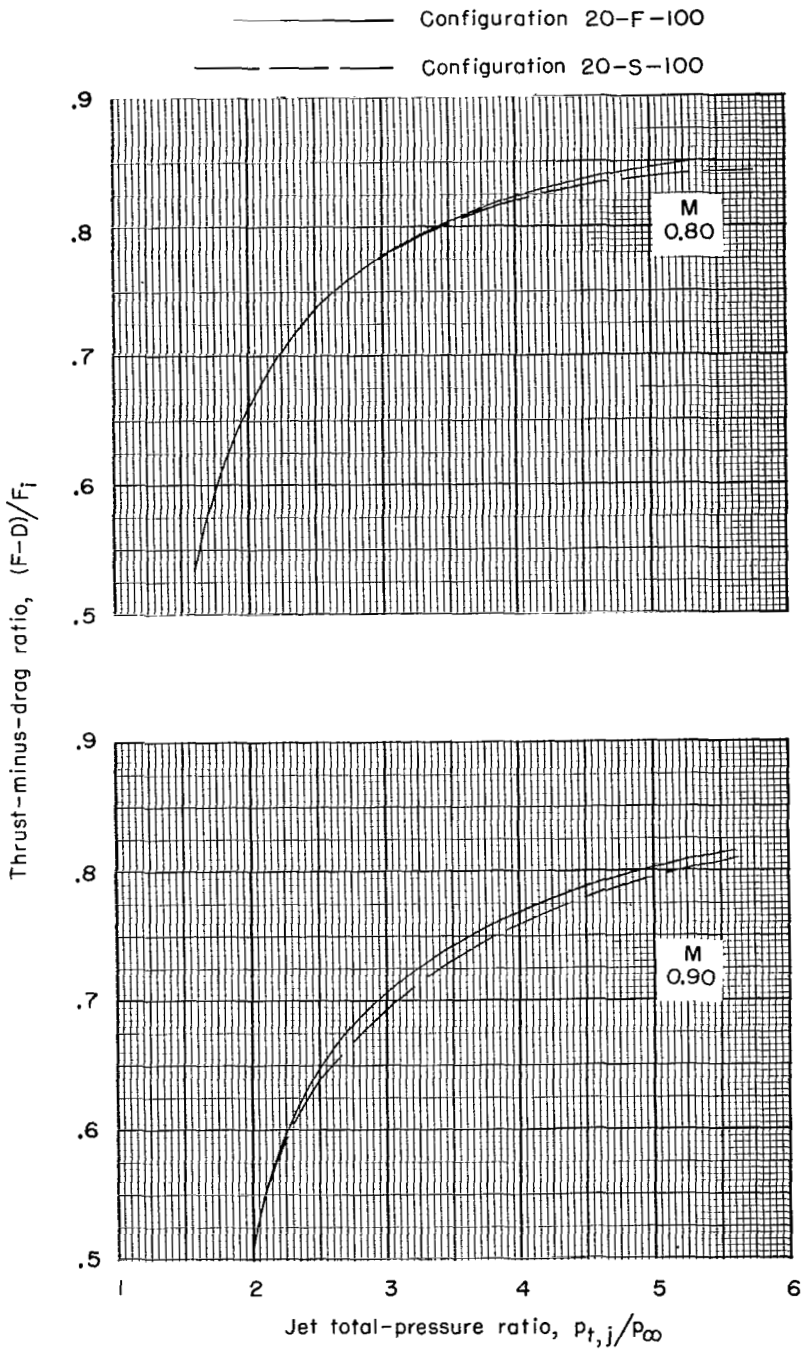

(b) M = 0.80 and M = 0.90.

Figure 36.- Continued.

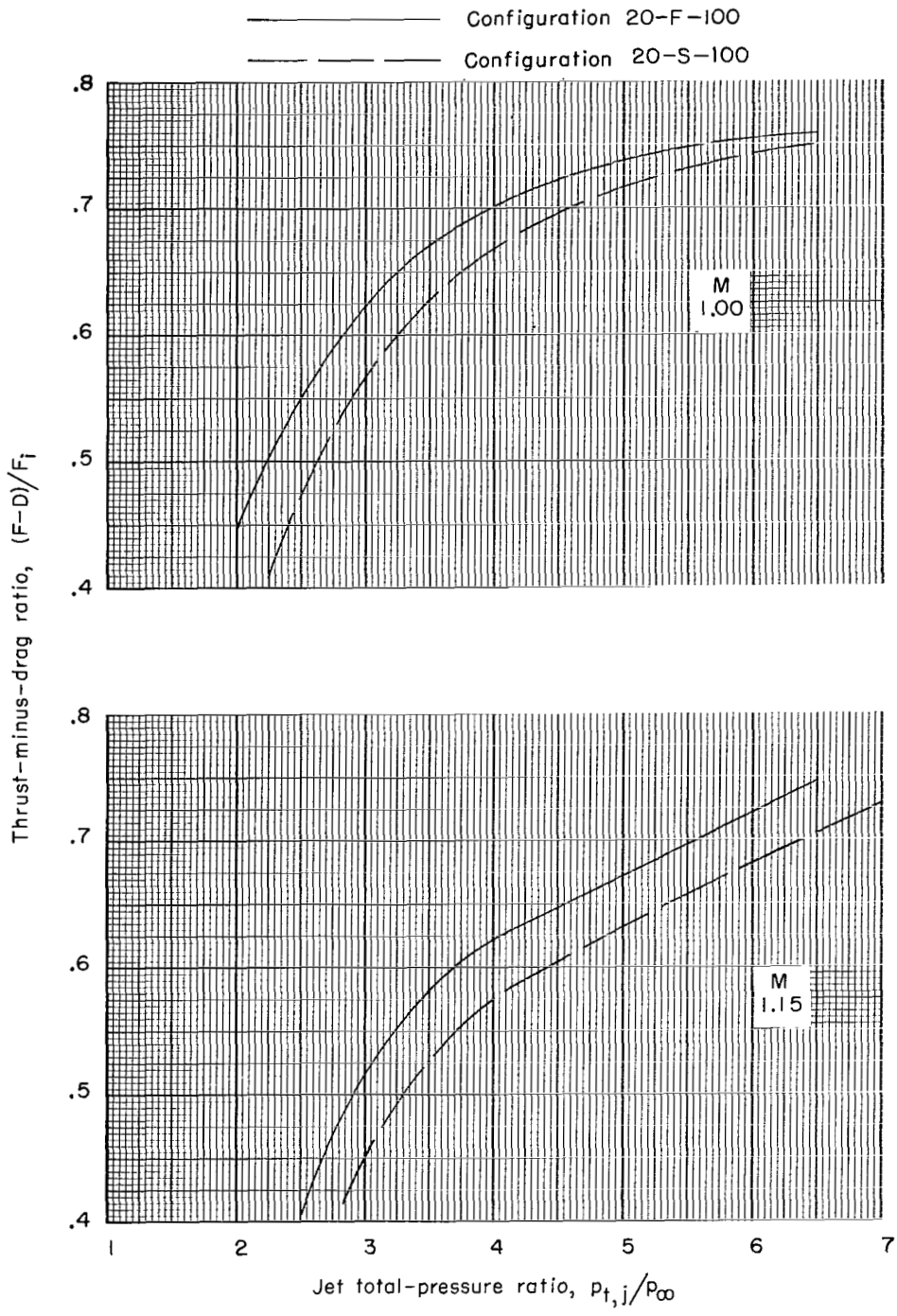

(c) M = 1.00 and M = 1.15.

Figure 36.- Continued.

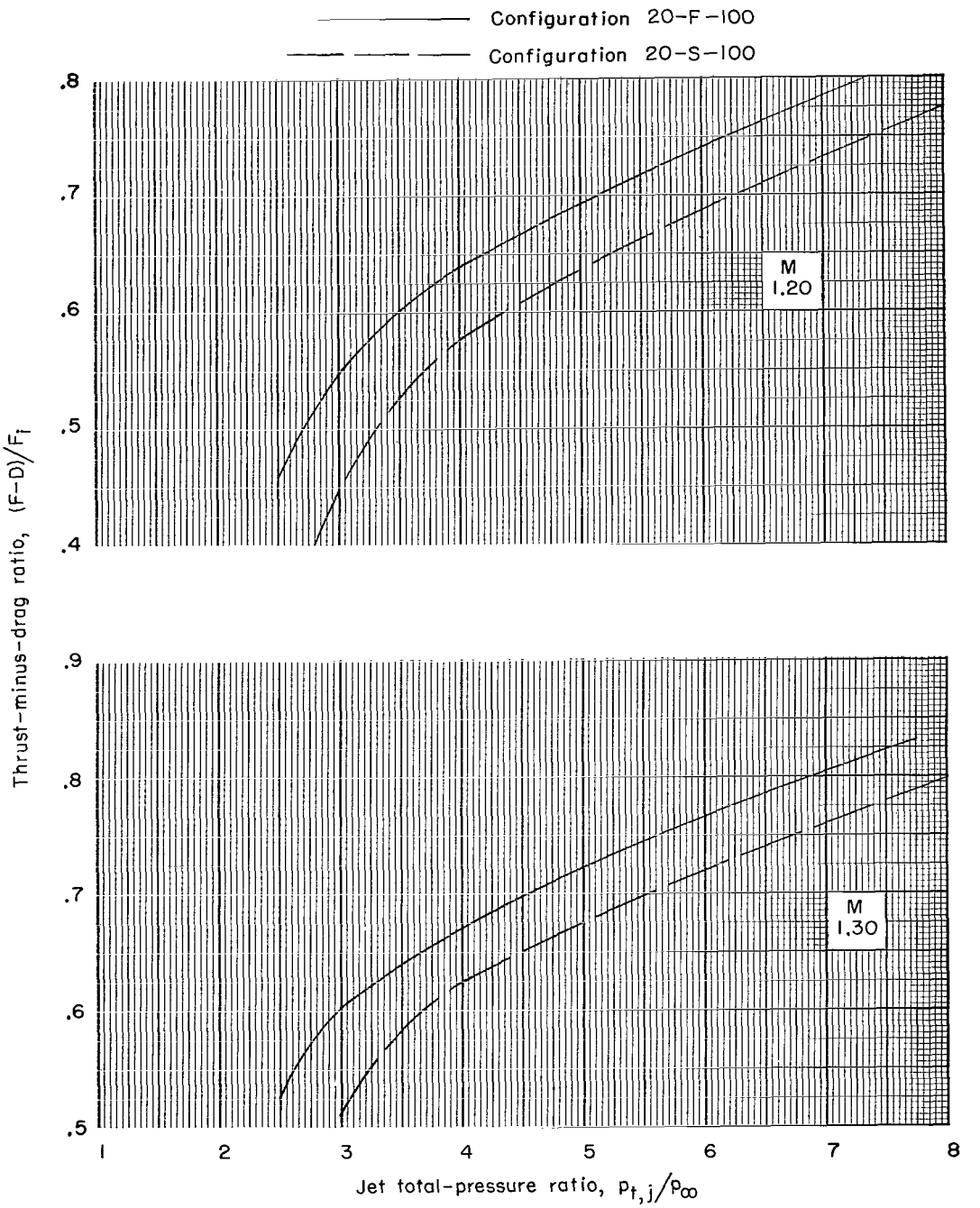

(d) M = 1.20 and M = 1.30.

Figure 36.- Concluded.

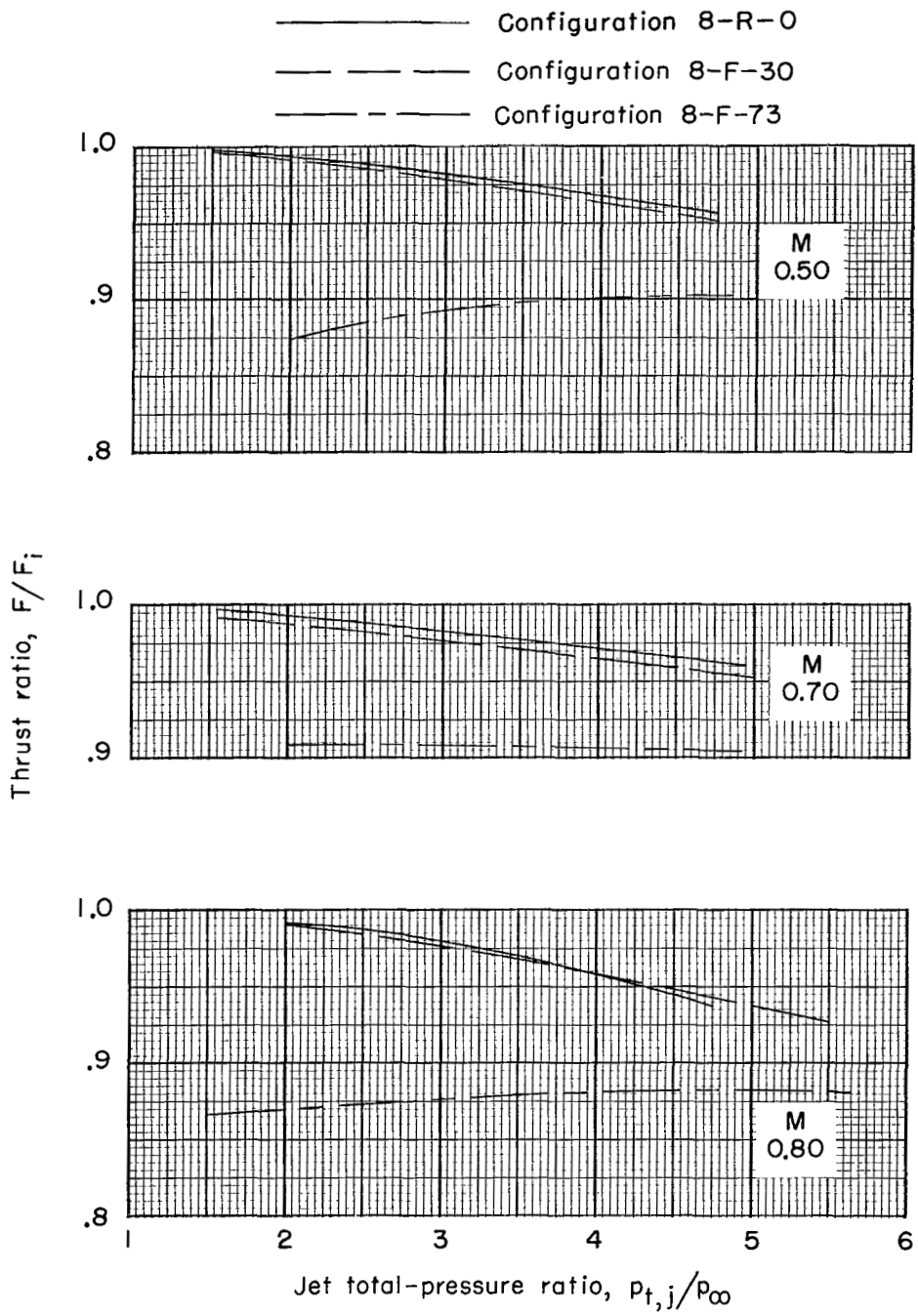

(a) M = 0.50 to M = 0.80.

Figure 37.- Effect of jet total-pressure ratio and plug truncation on thrust ratio. 8^0 boattail angle; flat plug base.

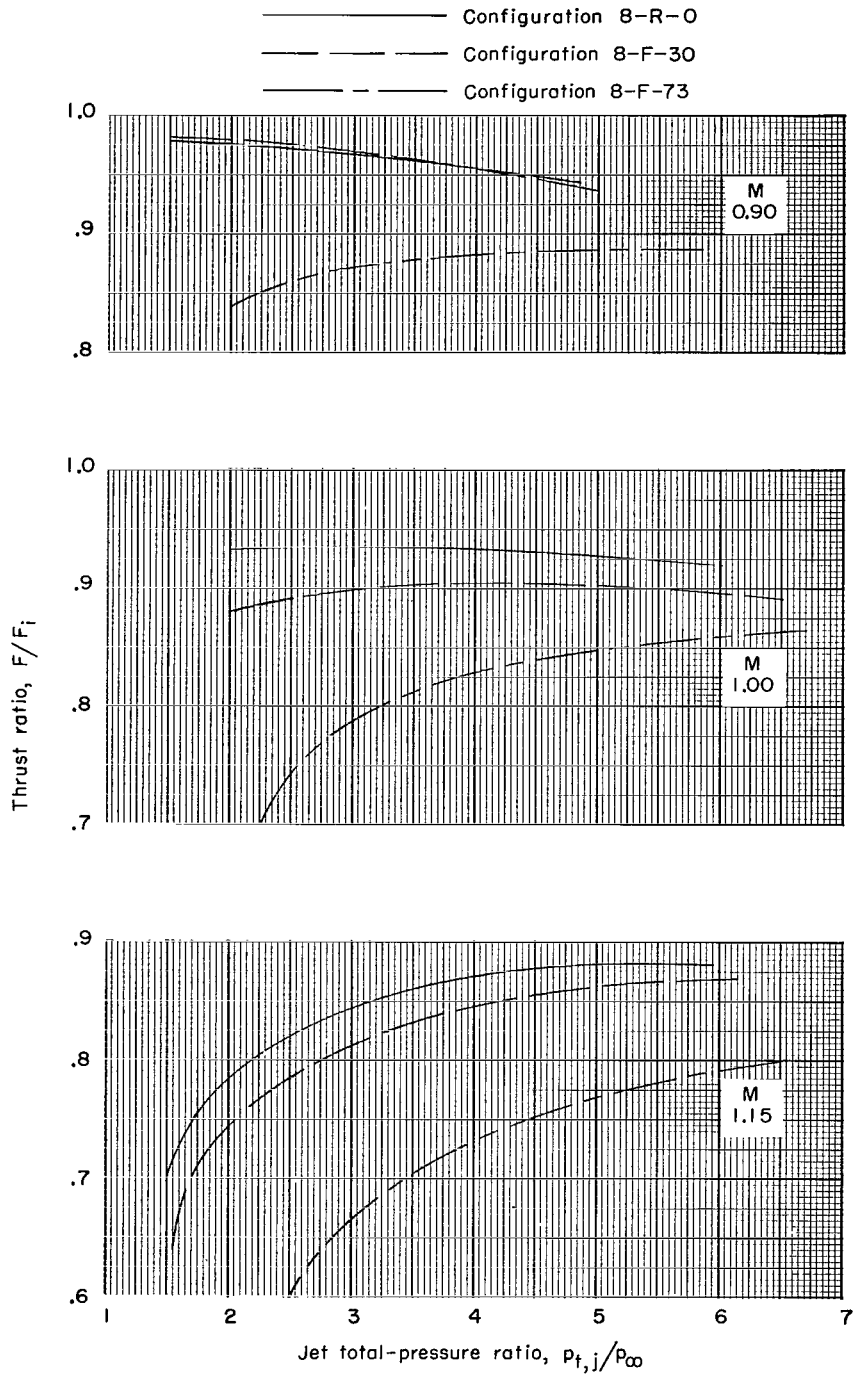

(b) M = 0.90 to M = 1.15.

Figure 37.- Continued.

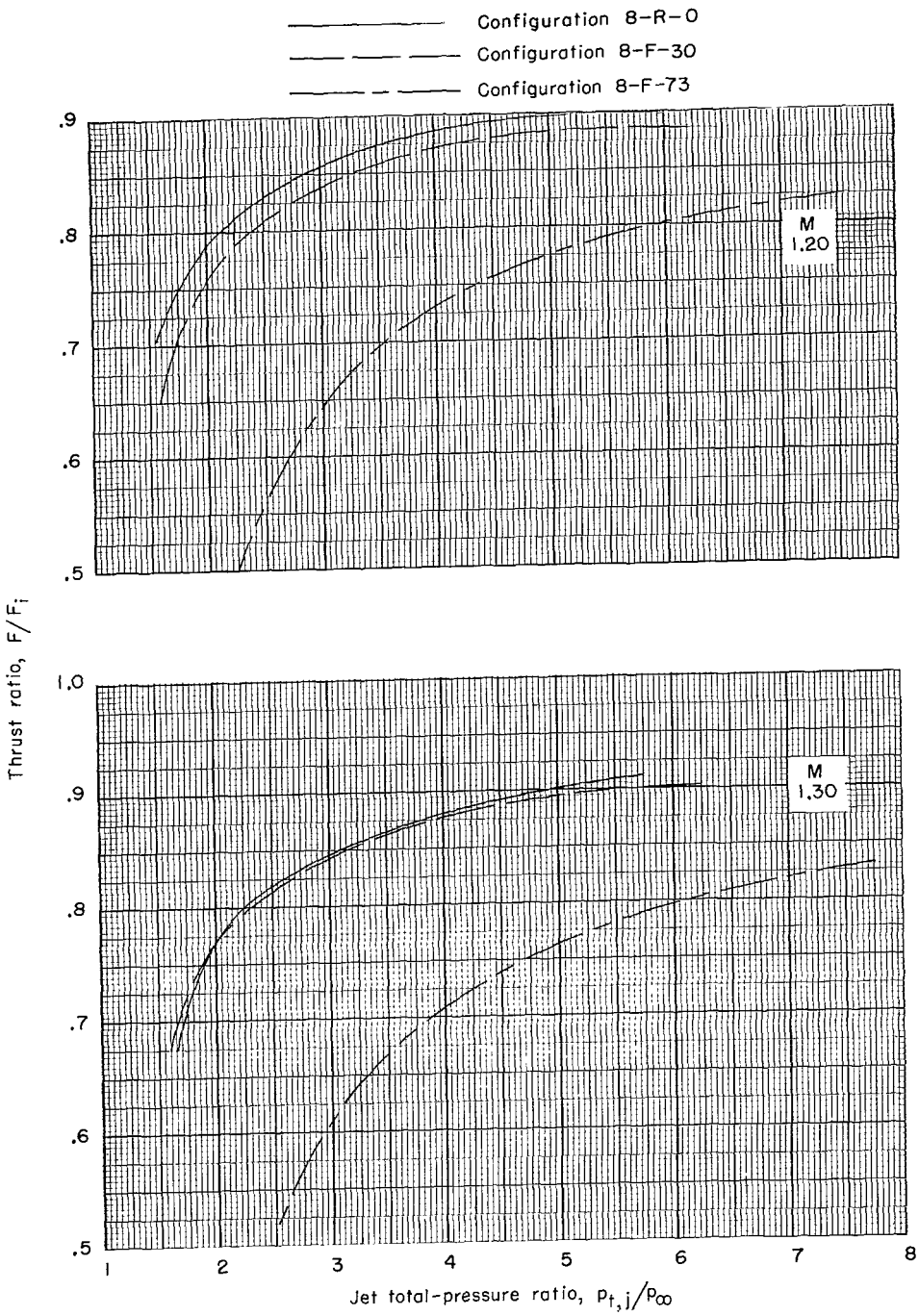

(c) M = 1.20 and M = 1.30.

Figure 37.- Concluded.

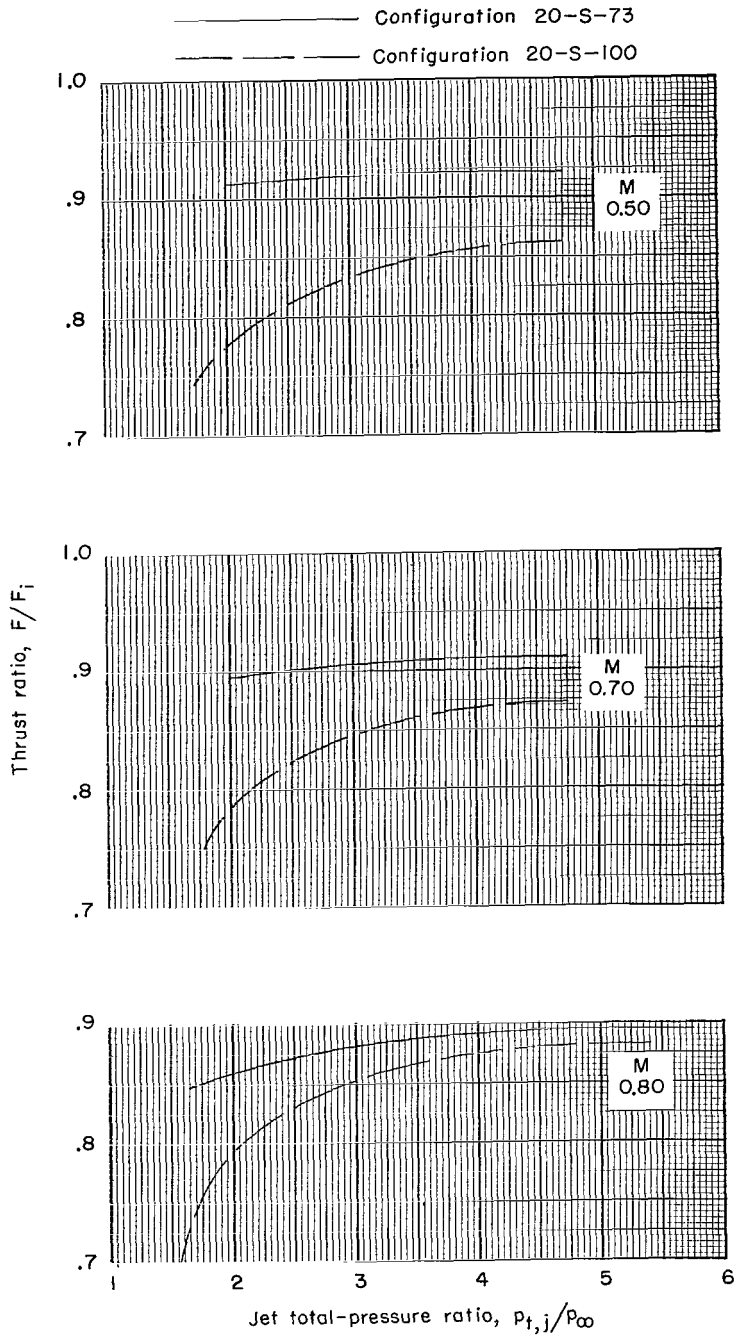

(a) M = 0.50 to M = 0.80.

Figure 38.- Effect of jet total-pressure ratio and plug truncation on thrust ratio. 20° boattail angle; semitoroidal plug base.

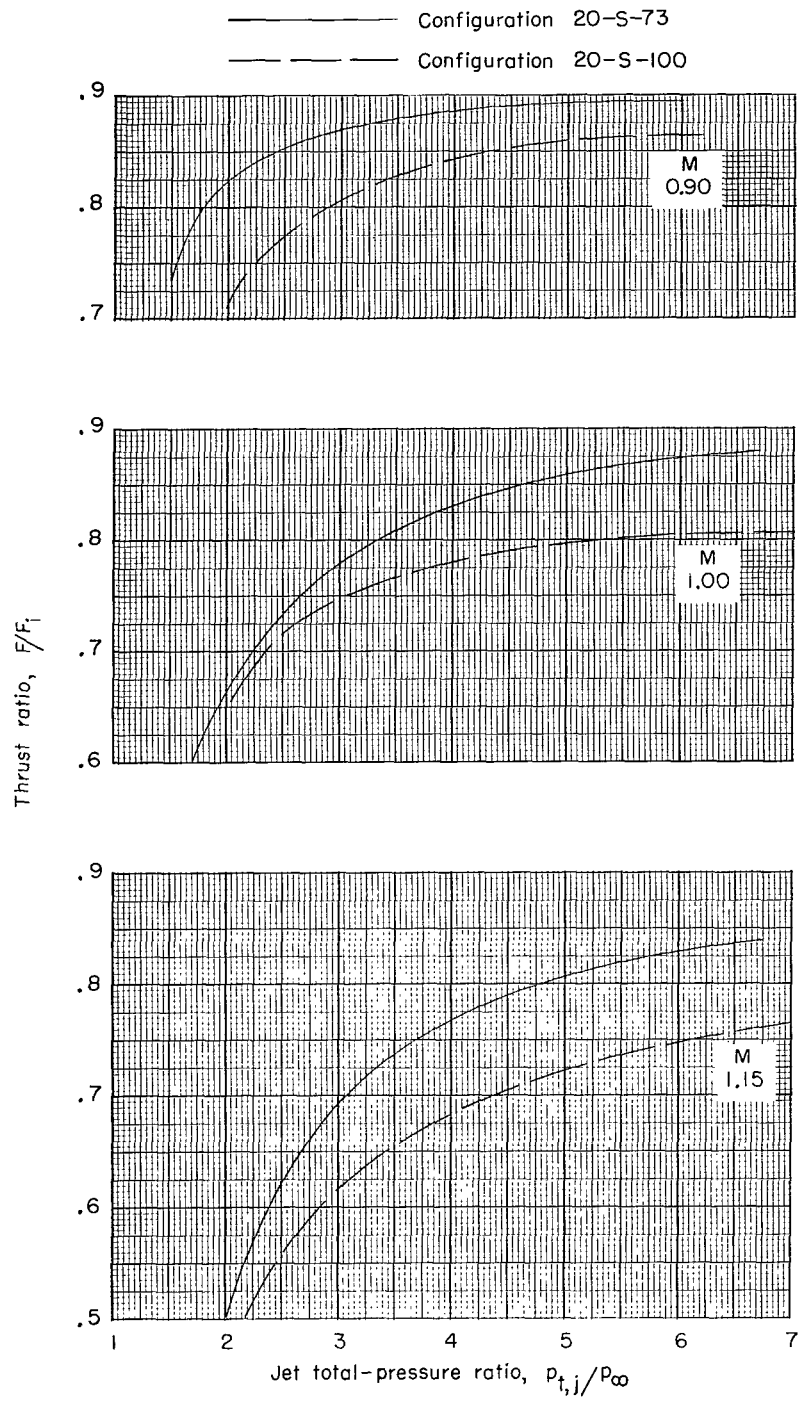

(b) M = 0.90 to M = 1.15.

Figure 38.- Continued.

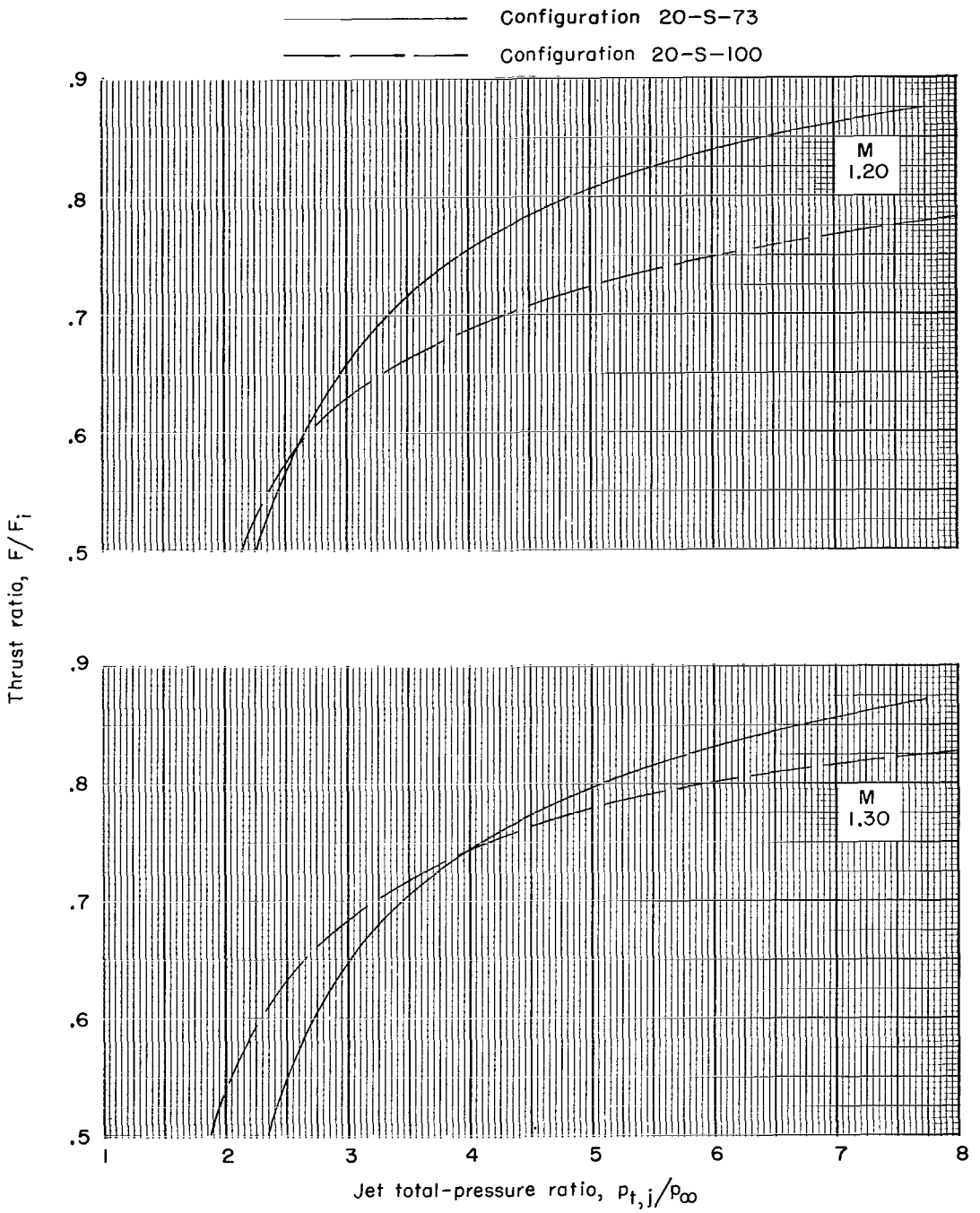

(c) M = 1.20 and M = 1.30.

Figure 38.- Concluded.

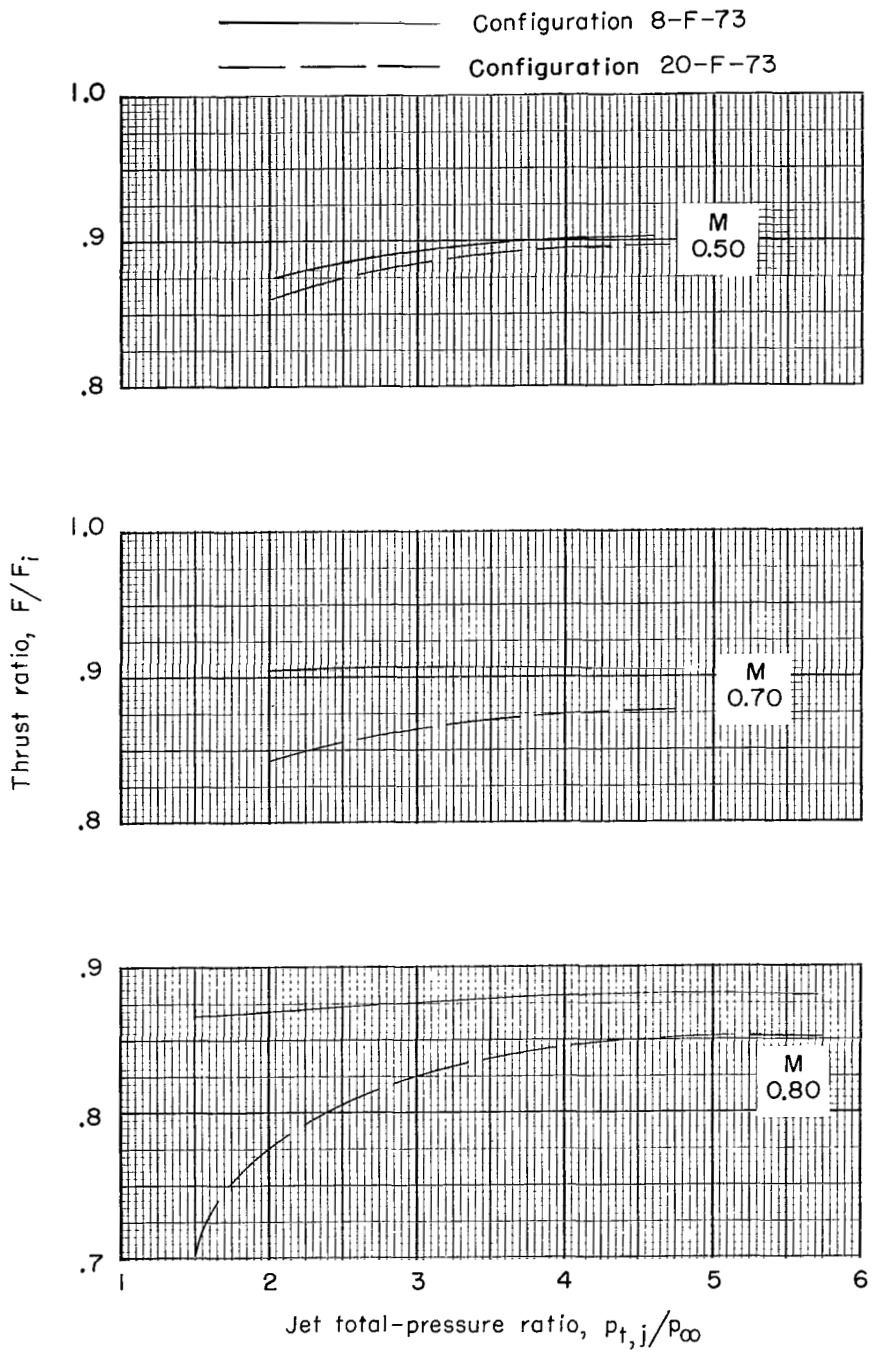

(a) M = 0.50 to M = 0.80.

Figure 39.- Effect of jet total-pressure ratio and boattail angle on thrust ratio. 72.5-percent truncation; flat plug base.

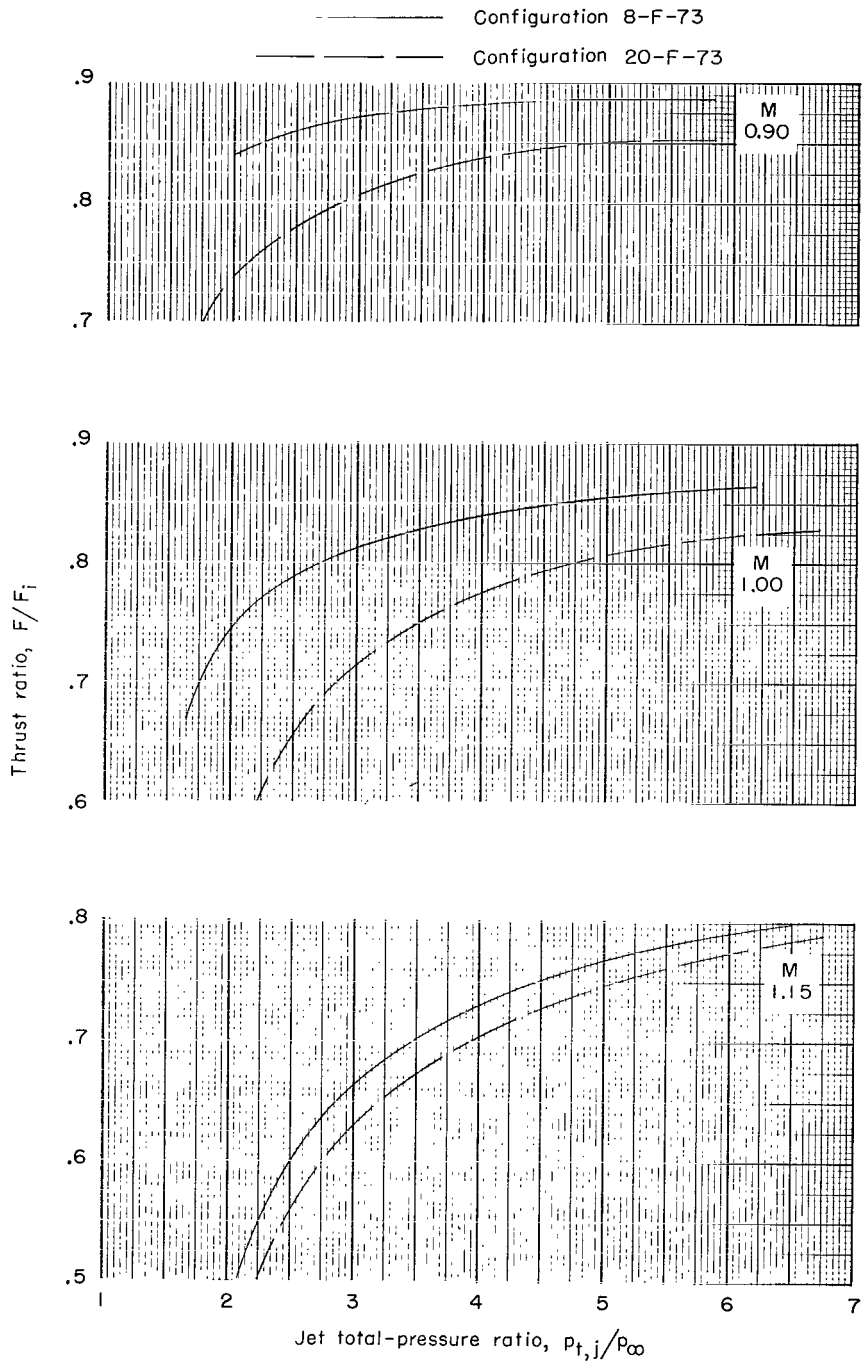

(b) M = 0.90 to M = 1.15.

Figure 39.- Continued.

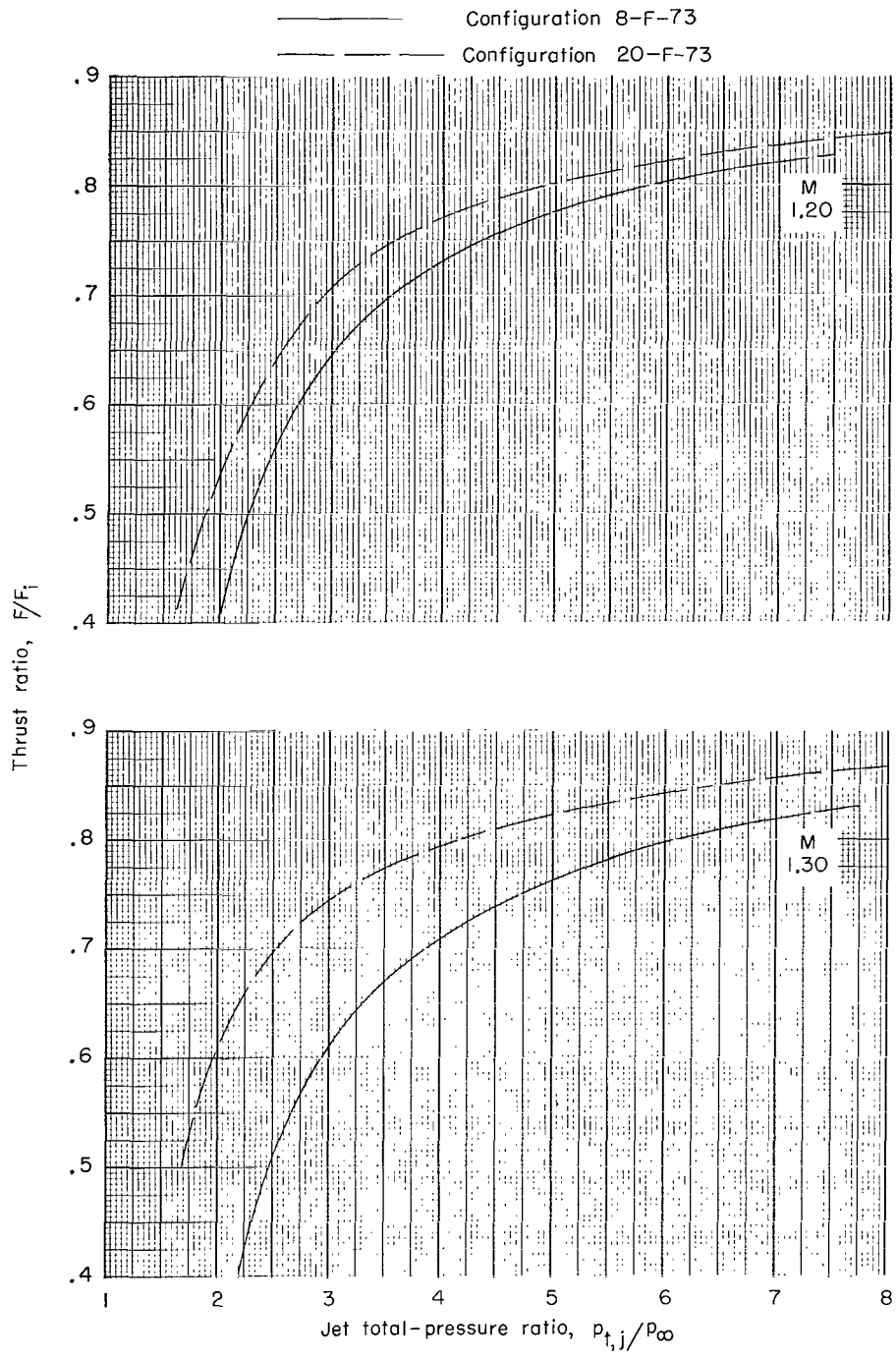

(c) M = 1.20 to M = 1.30.

Figure 39.- Concluded.

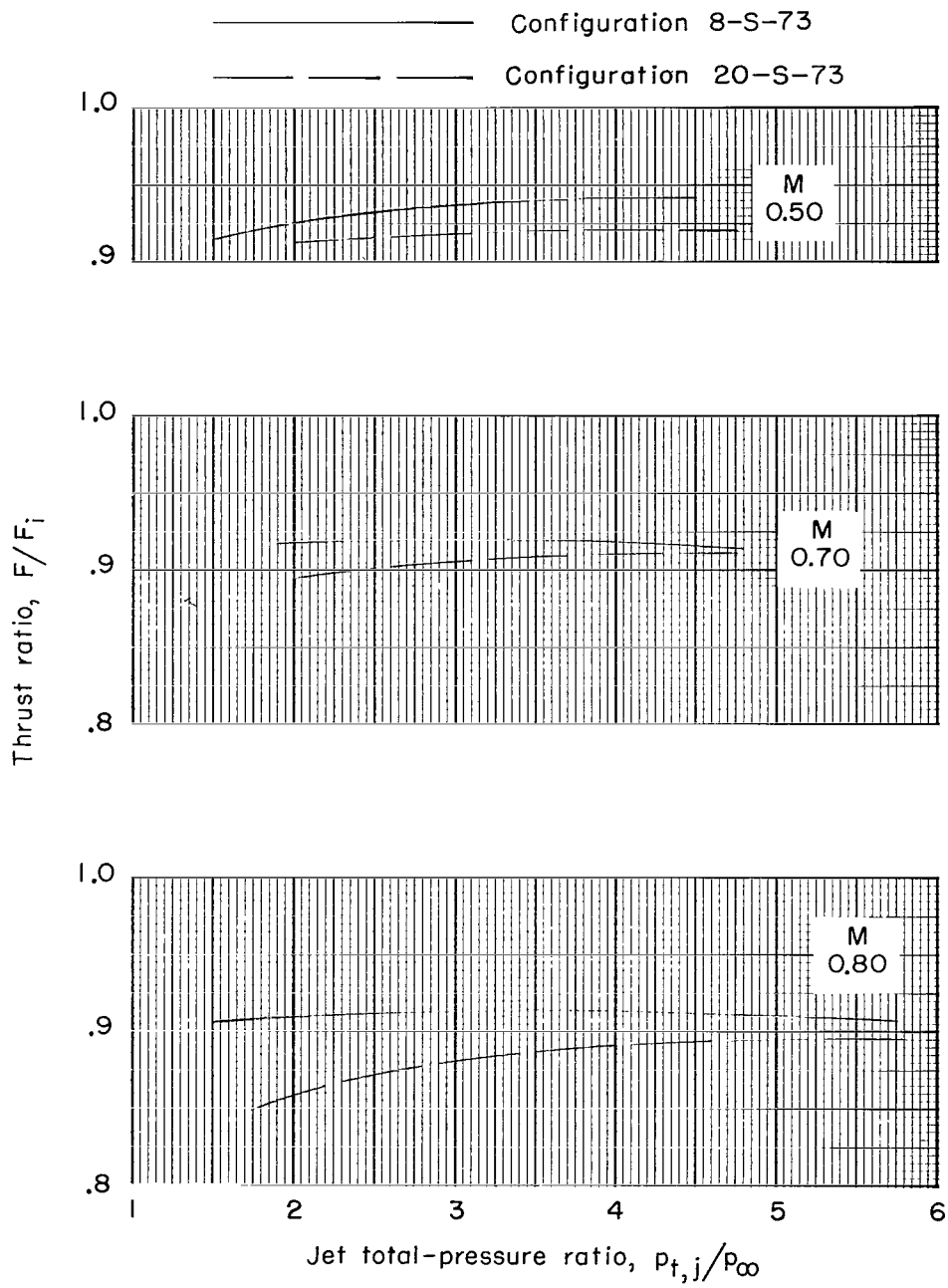

(a) M = 0.50 to M = 0.80.

Figure 40.- Effect of jet total-pressure ratio and boattail angle on thrust ratio. 72.5-percent truncation; semitoroidal plug base.

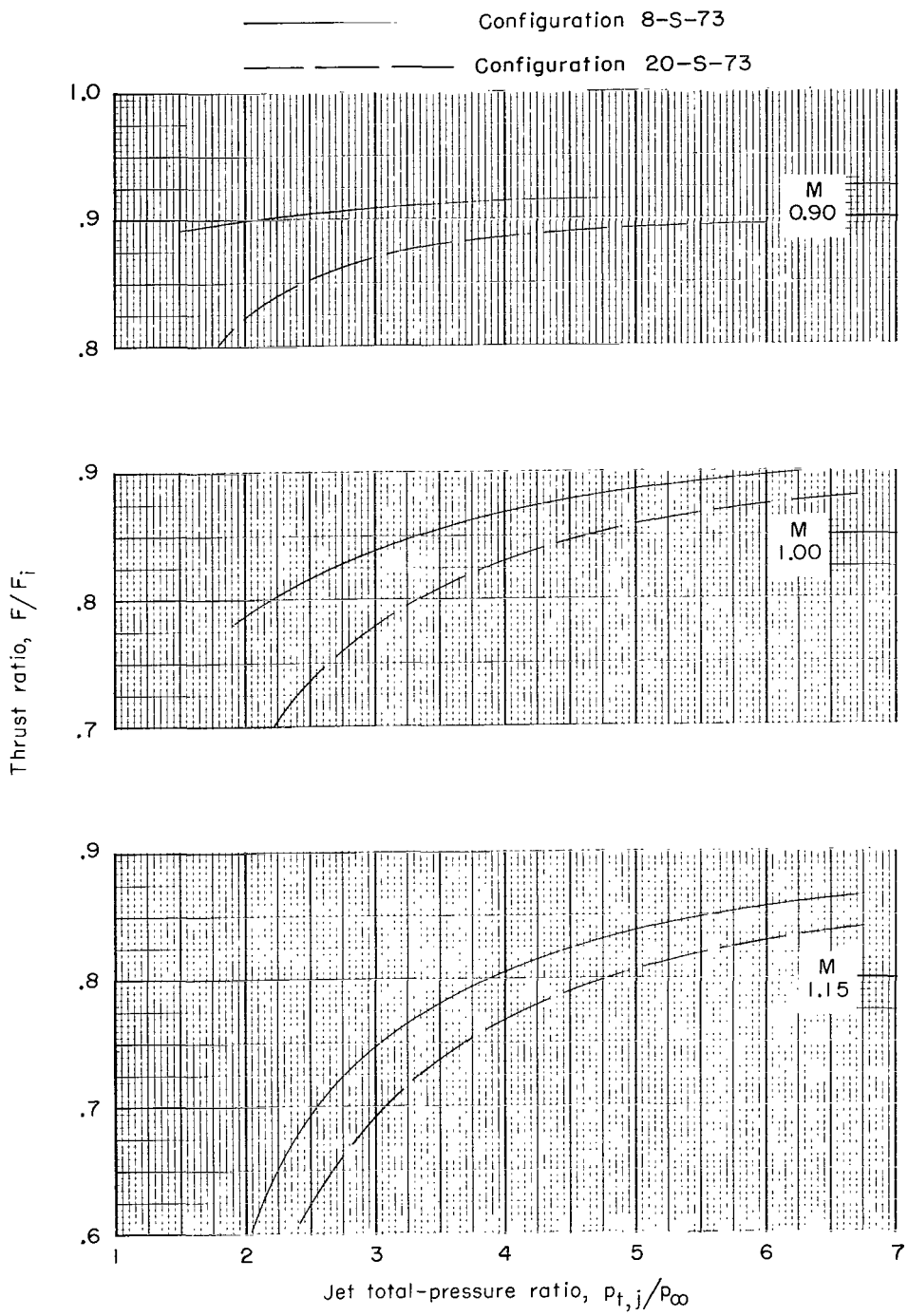

(b) M = 0.90 to M = 1.15.

Figure 40.- Continued.

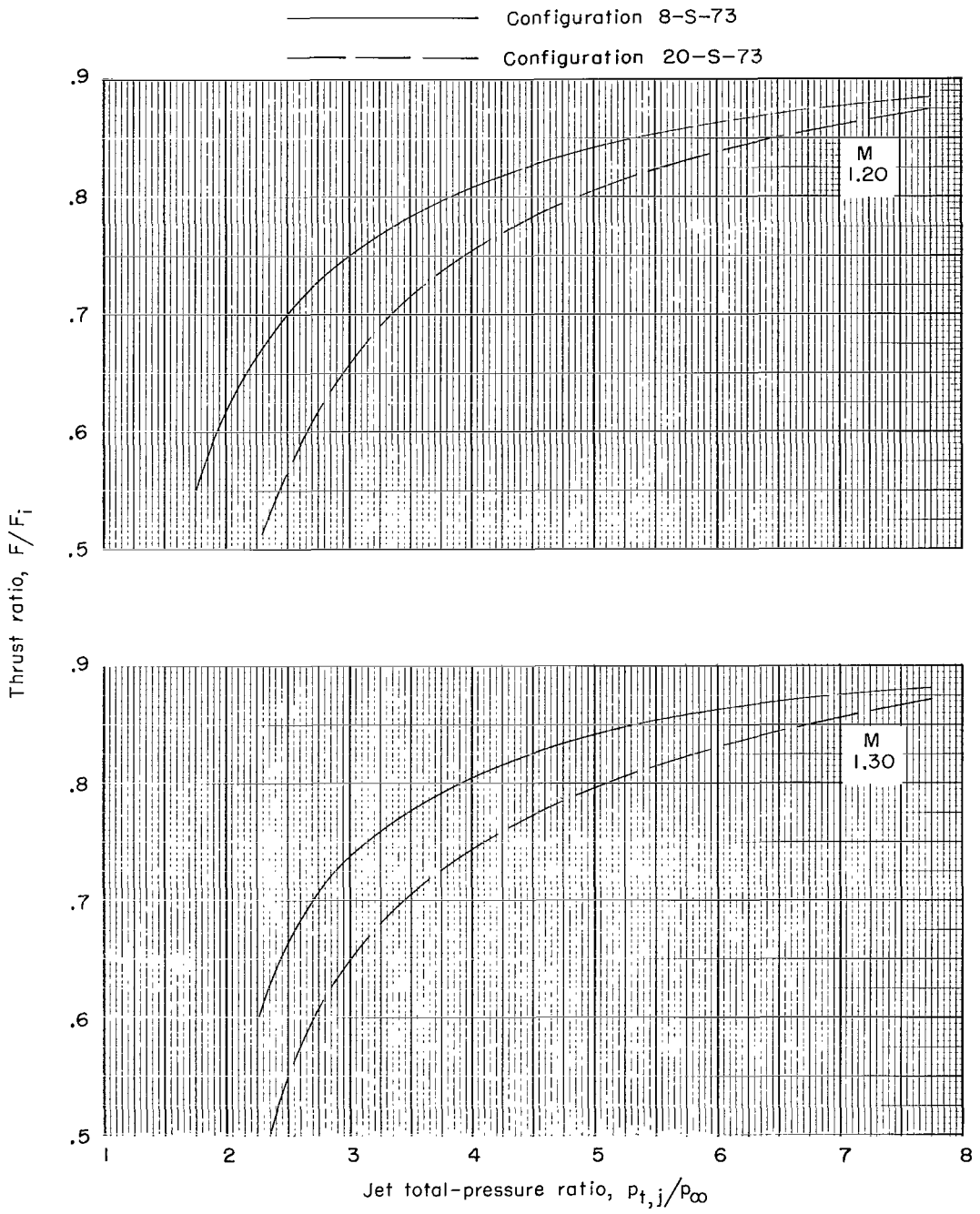

(c) M = 1.20 to M = 1.30.

Figure 40.- Concluded.

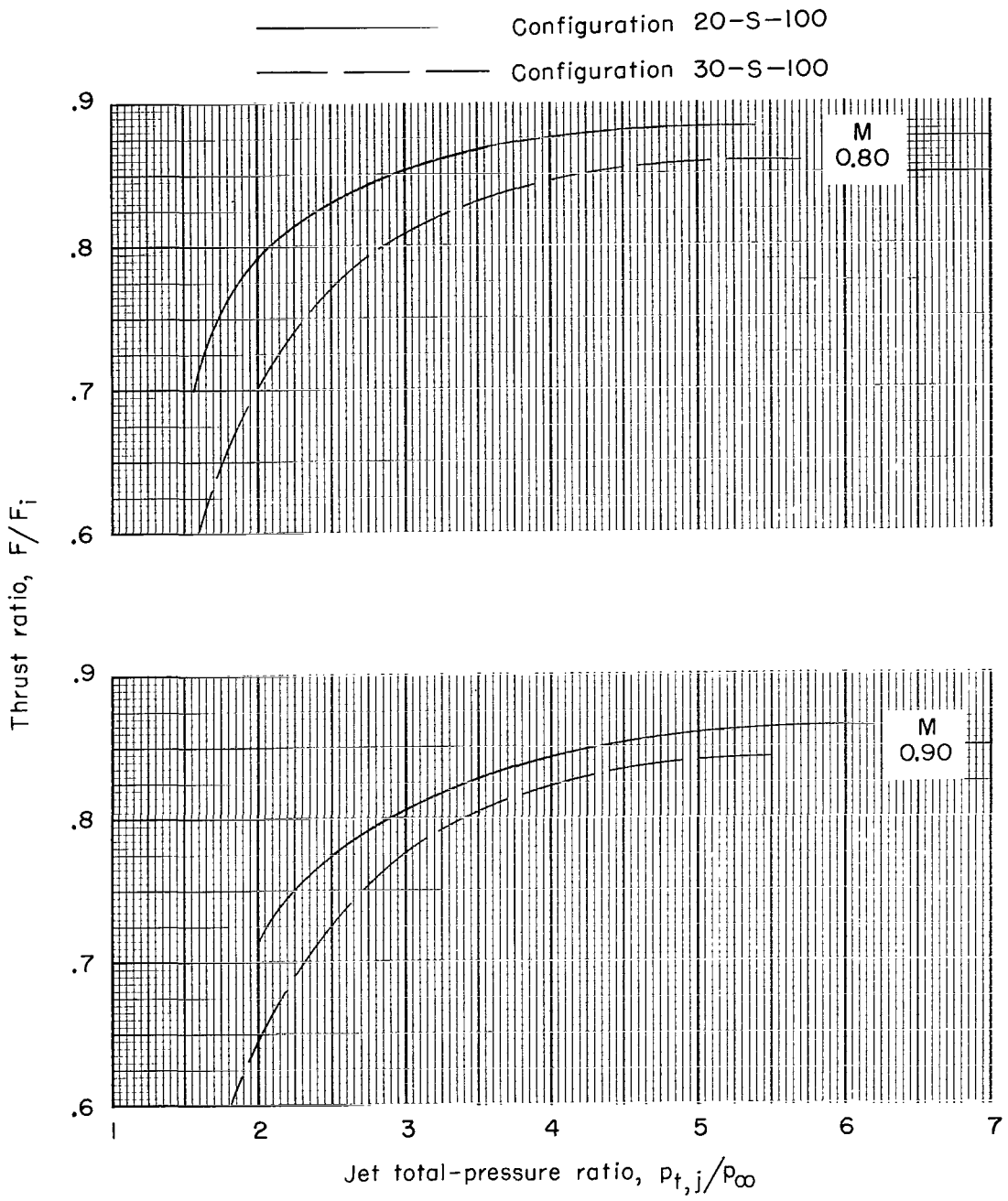

(a) M = 0.80 and M = 0.90.

Figure 41.- Effect of jet total-pressure ratio and boattail angle on thrust ratio. 100-percent truncation; semitoroidal plug base.

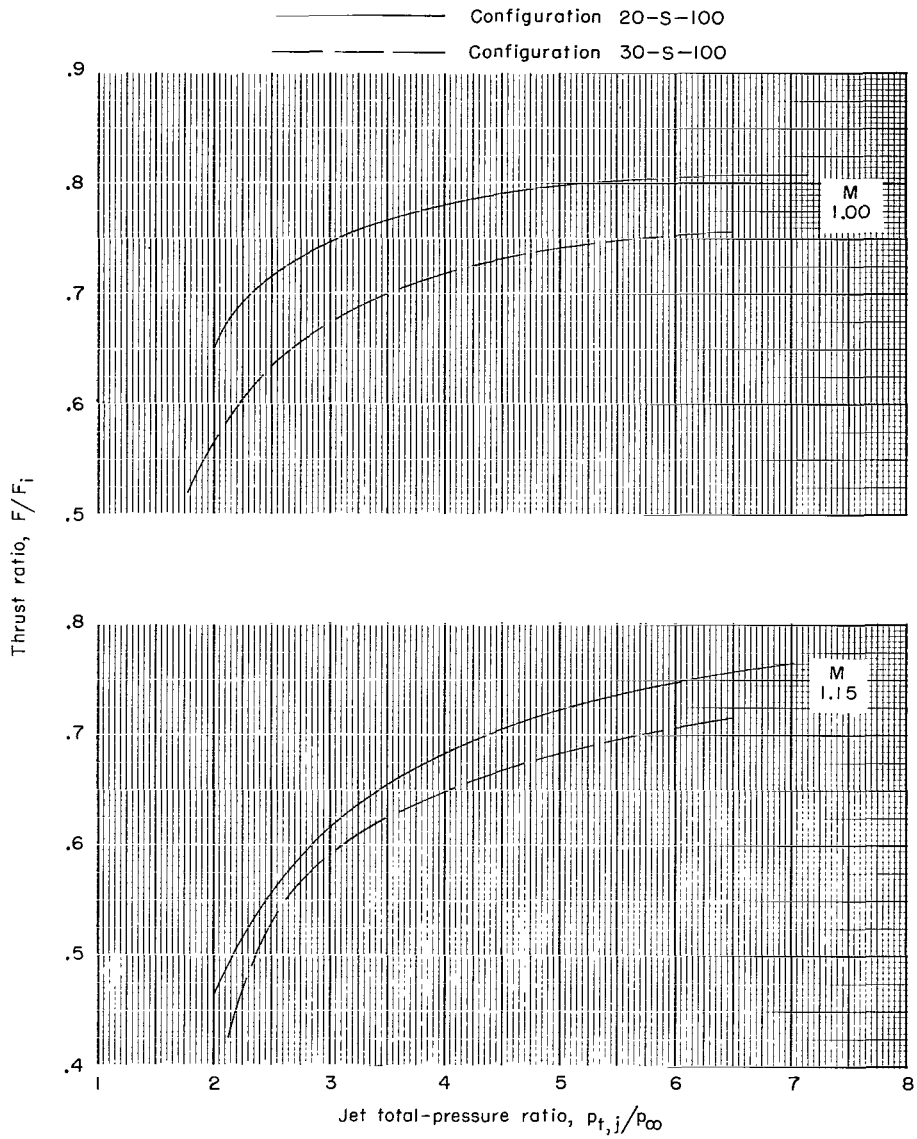

(b) M = 1.00 and M = 1.15.

Figure 41.- Continued.

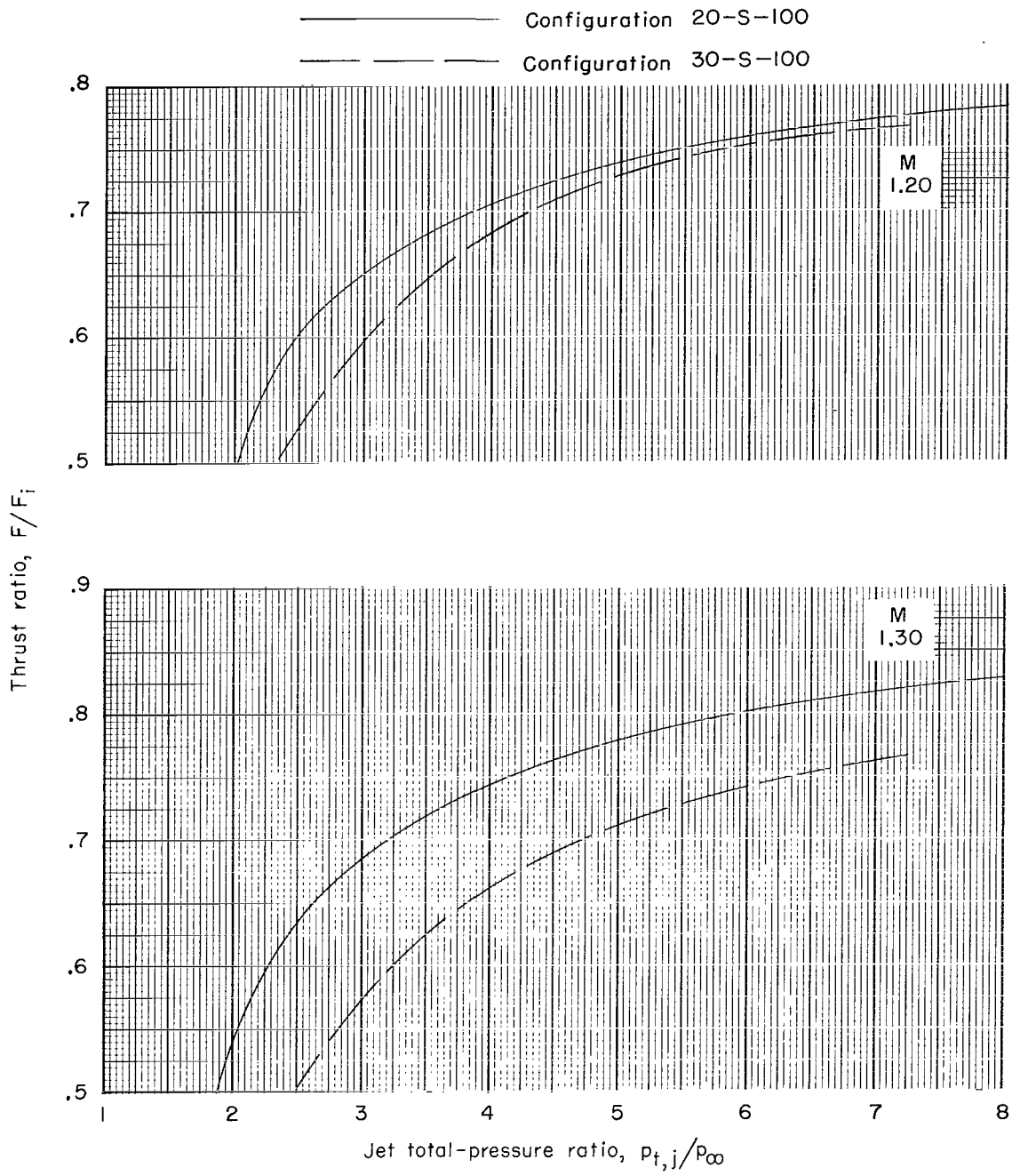

(c) M = 1.20 and M = 1.30.

Figure 41.- Concluded.

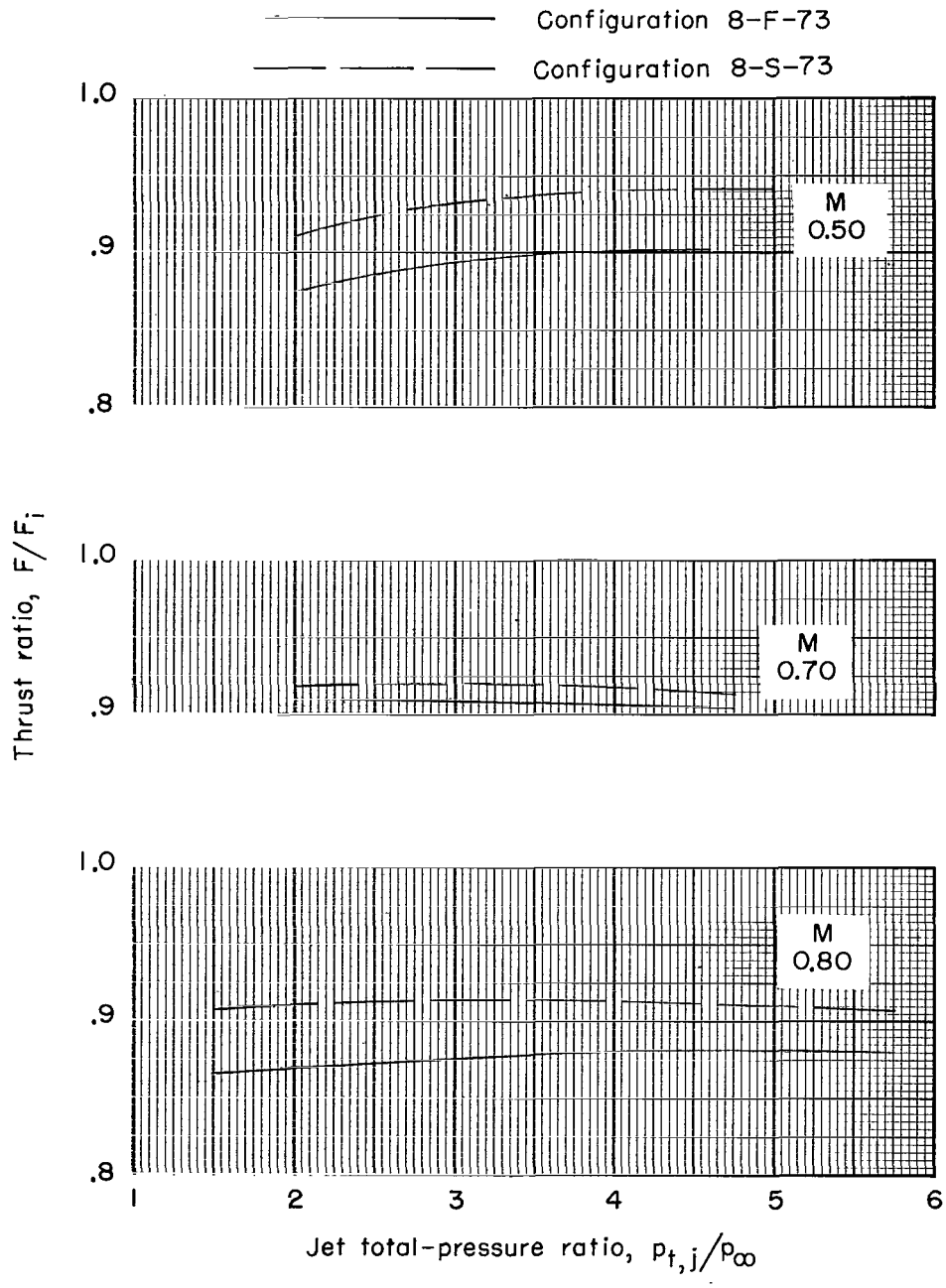

(a) M = 0.50 to M = 0.80.

Figure 42.- Effect of jet total-pressure ratio and plug base shape on thrust ratio. 8^0 boattail angle; 72.5-percent truncation.

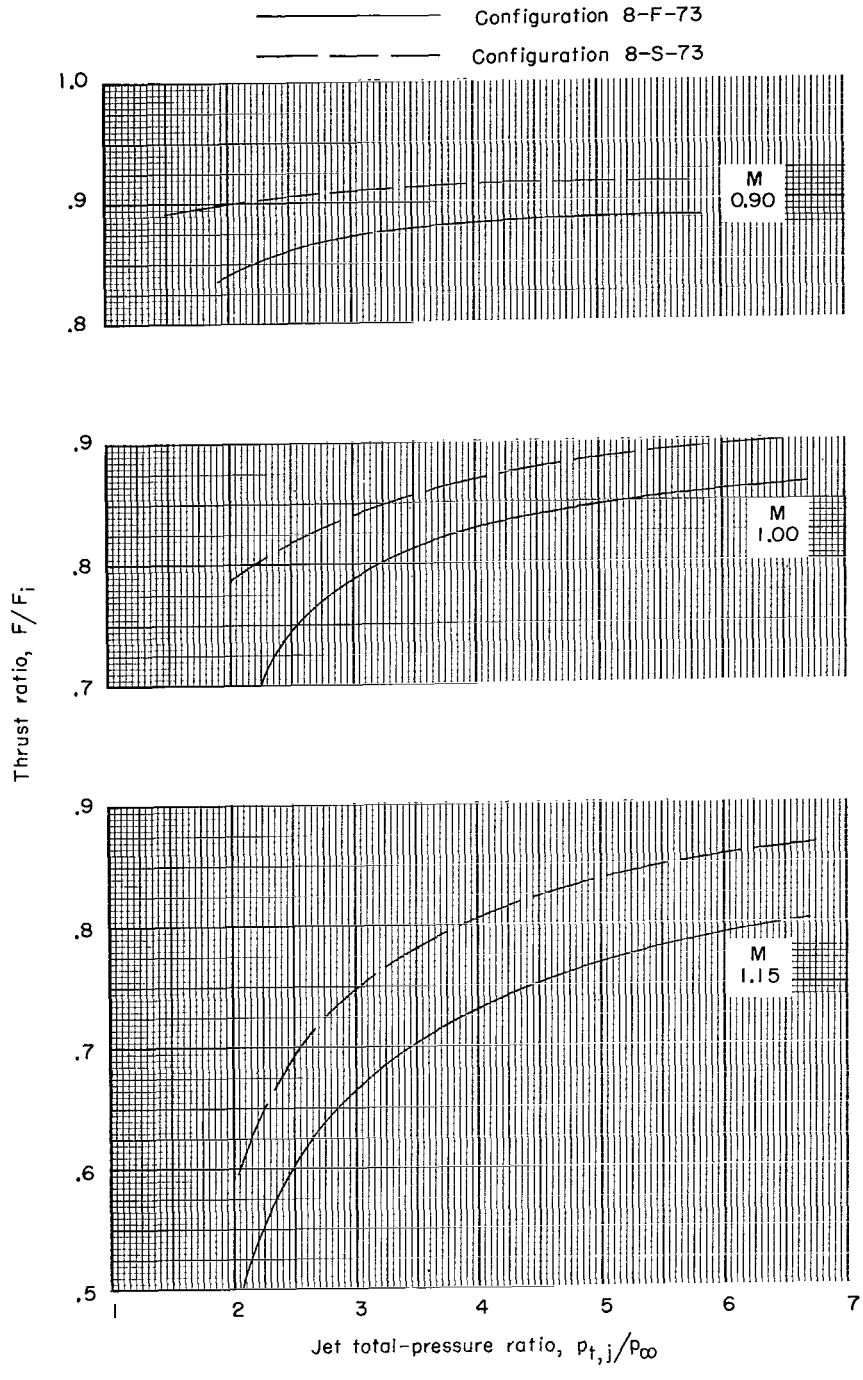

(b) M = 0.90 to M = 1.15.

Figure 42.- Continued.

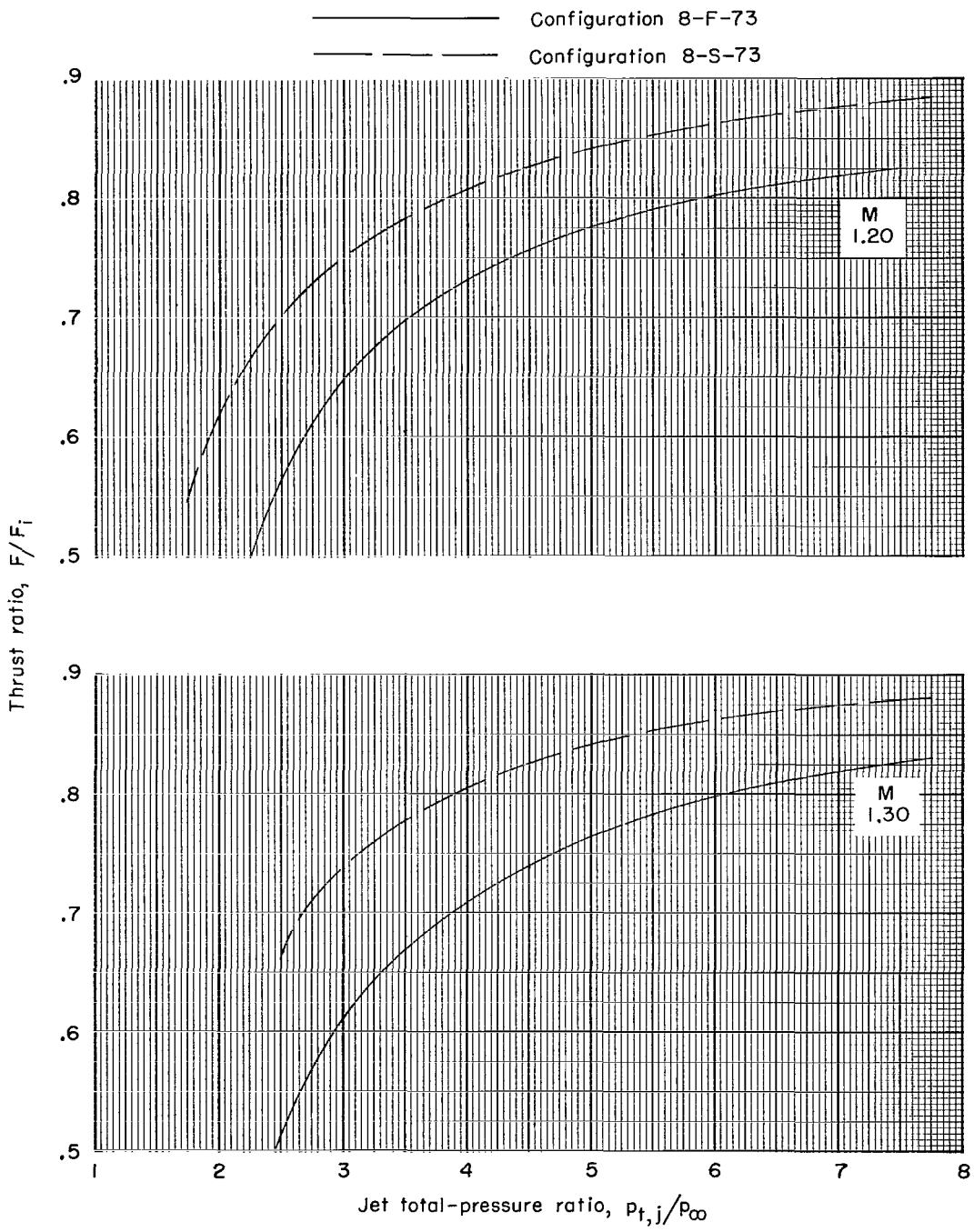

(c) M = 1.20 and M = 1.30.

Figure 42.- Concluded.

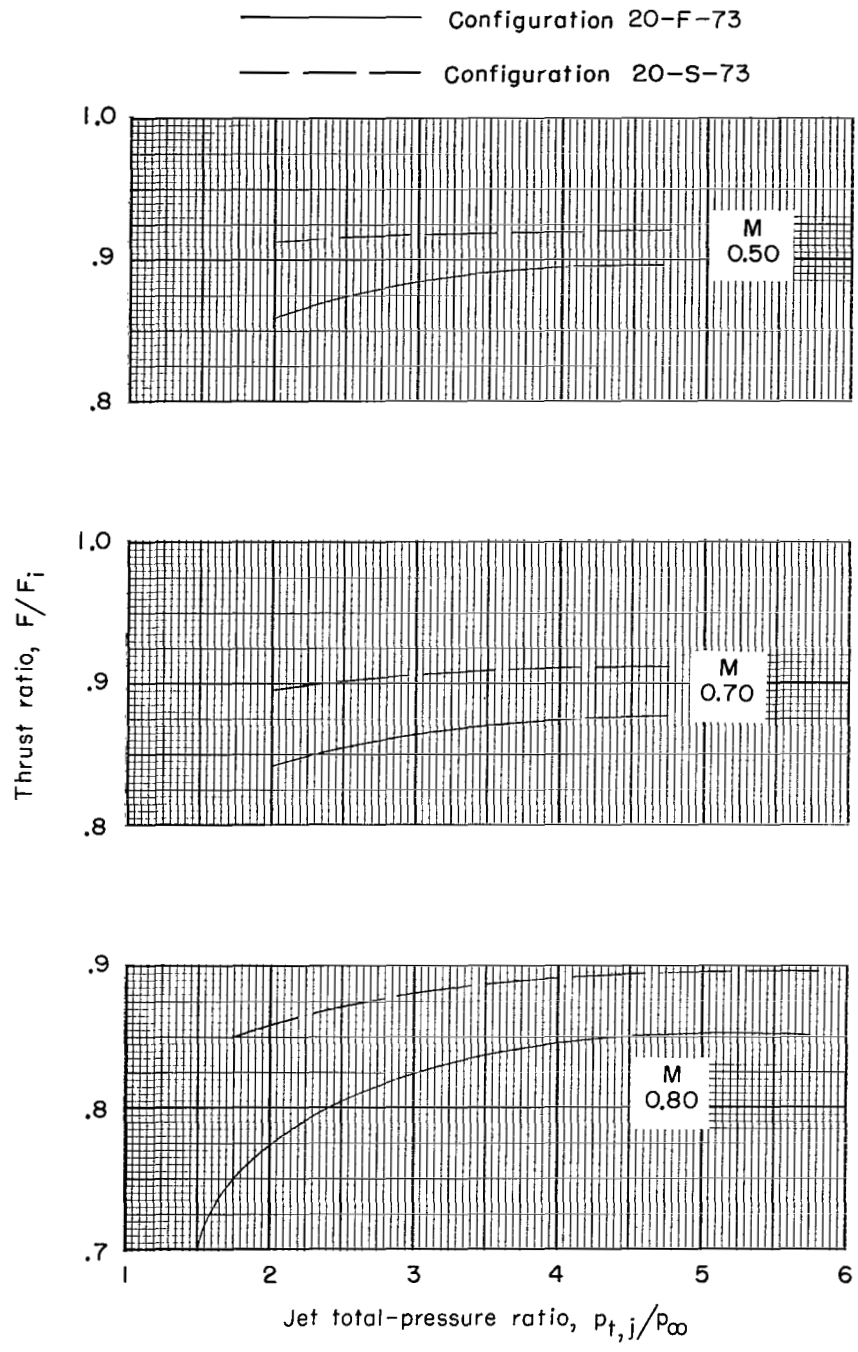

(a) M = 0.50 to M = 0.80.

Figure 43.- Effect of jet total-pressure ratio and plug base shape on thrust ratio. 20° boattail angle; 72.5-percent truncation.

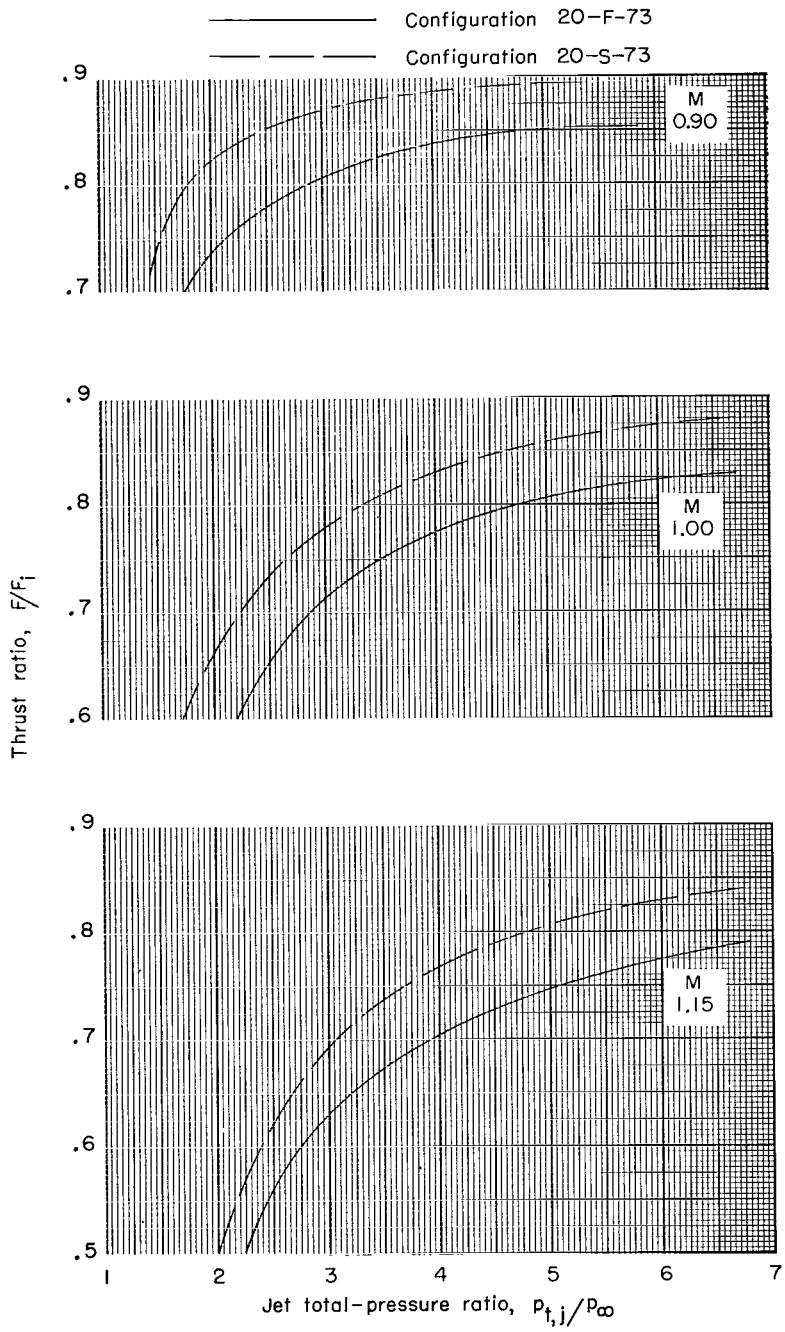

(b) M = 0.90 to M = 1.15.

Figure 43.- Continued.

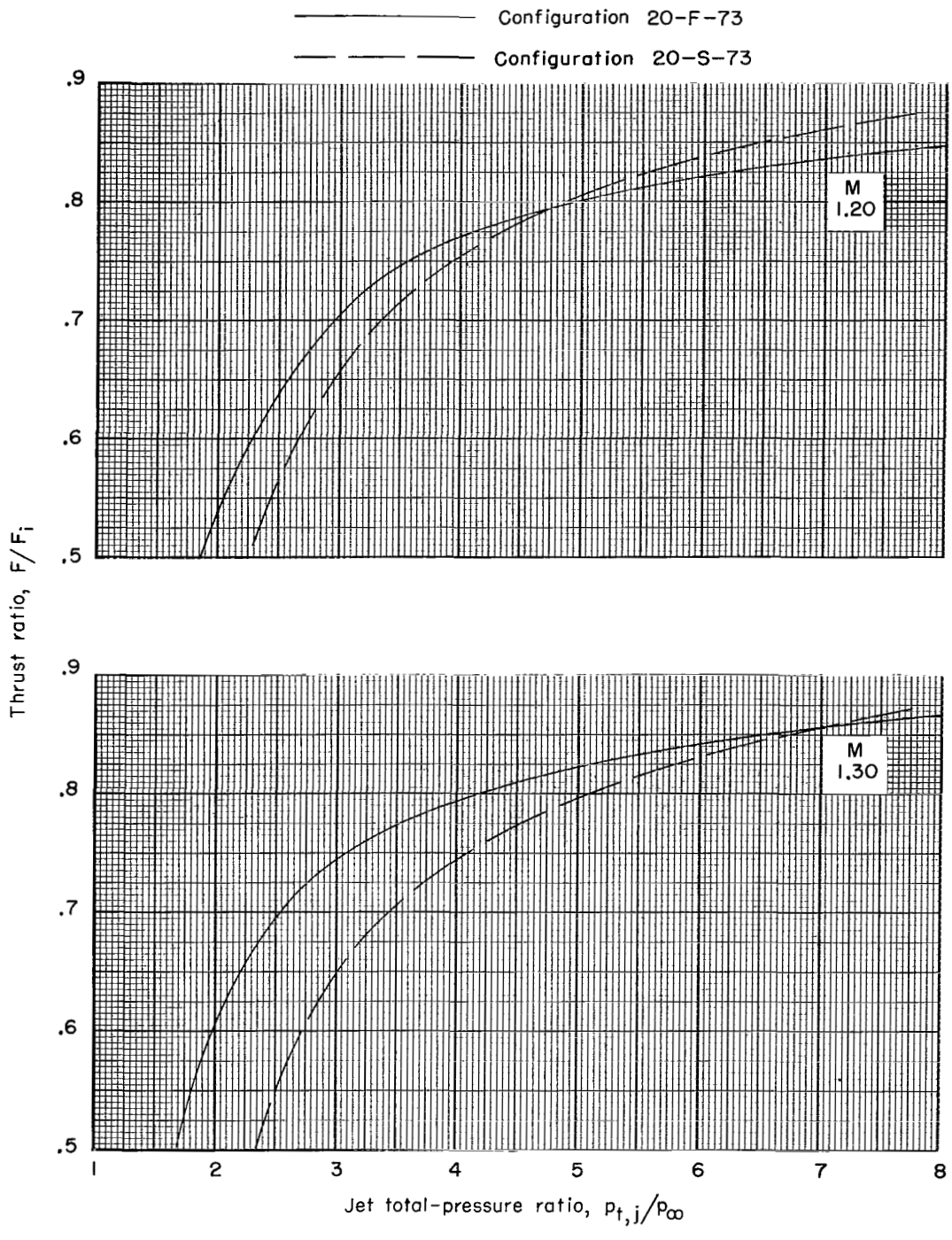

(c) M = 1.20 and M = 1.30.

Figure 43.- Concluded.

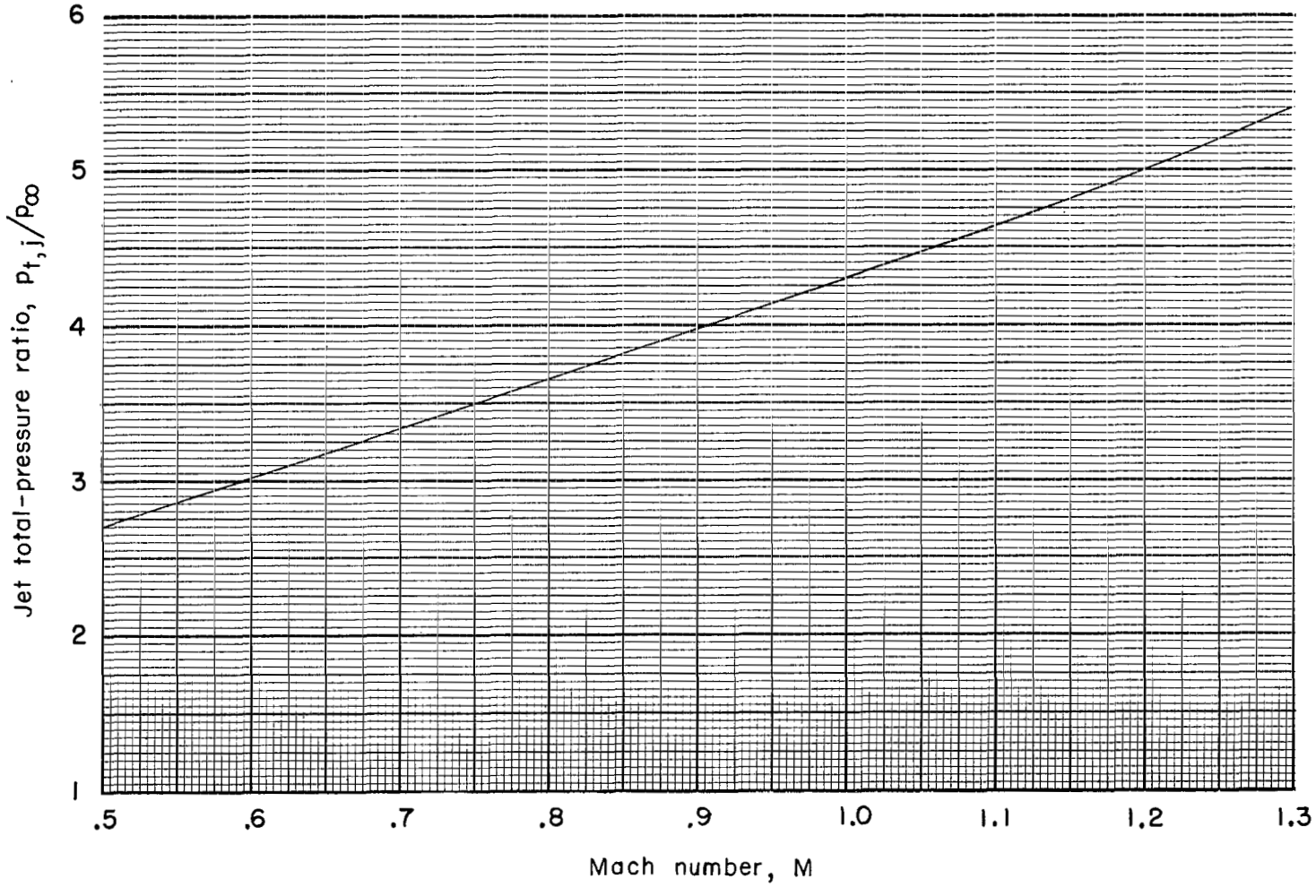

Figure 44.- Typical jet total-pressure-ratio schedule for turbojet-engine configuration.

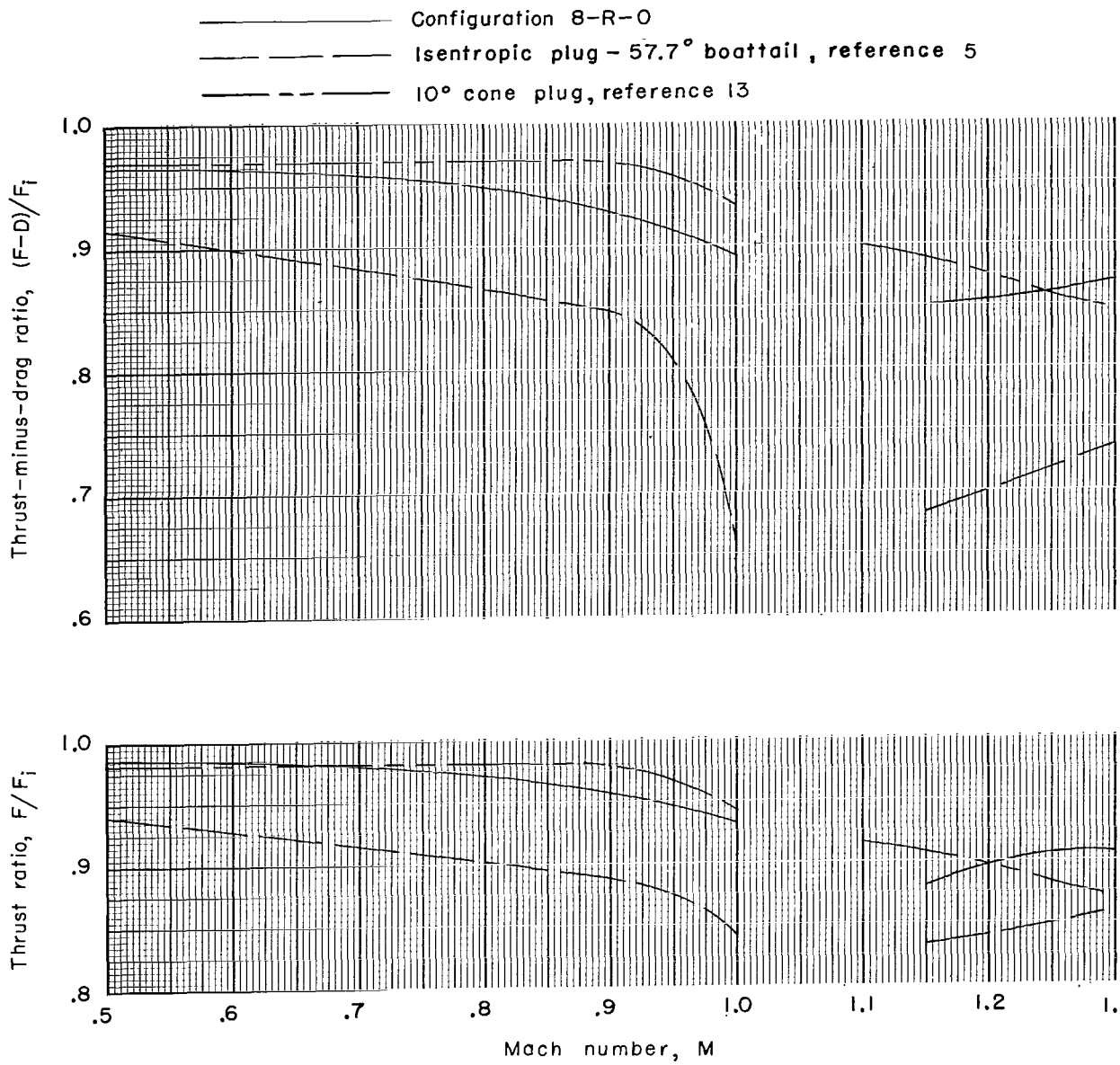

(a) Comparison of plug types.

Figure 45.- Variation of thrust-minus-drag ratio and thrust ratio with Mach number for typical jet total-pressure-ratio schedule.

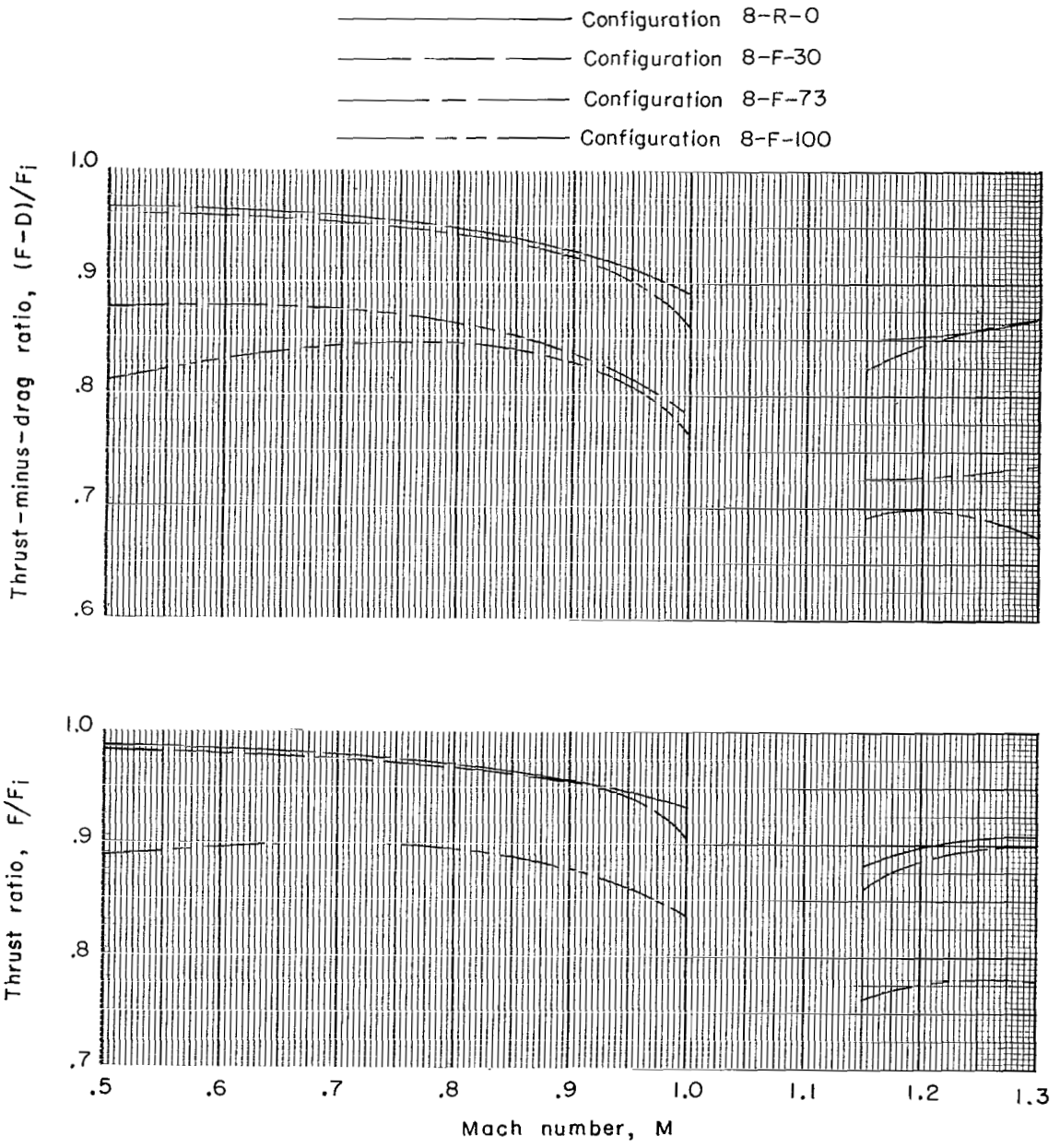

(b) Effect of truncation.

Figure 45.- Continued.

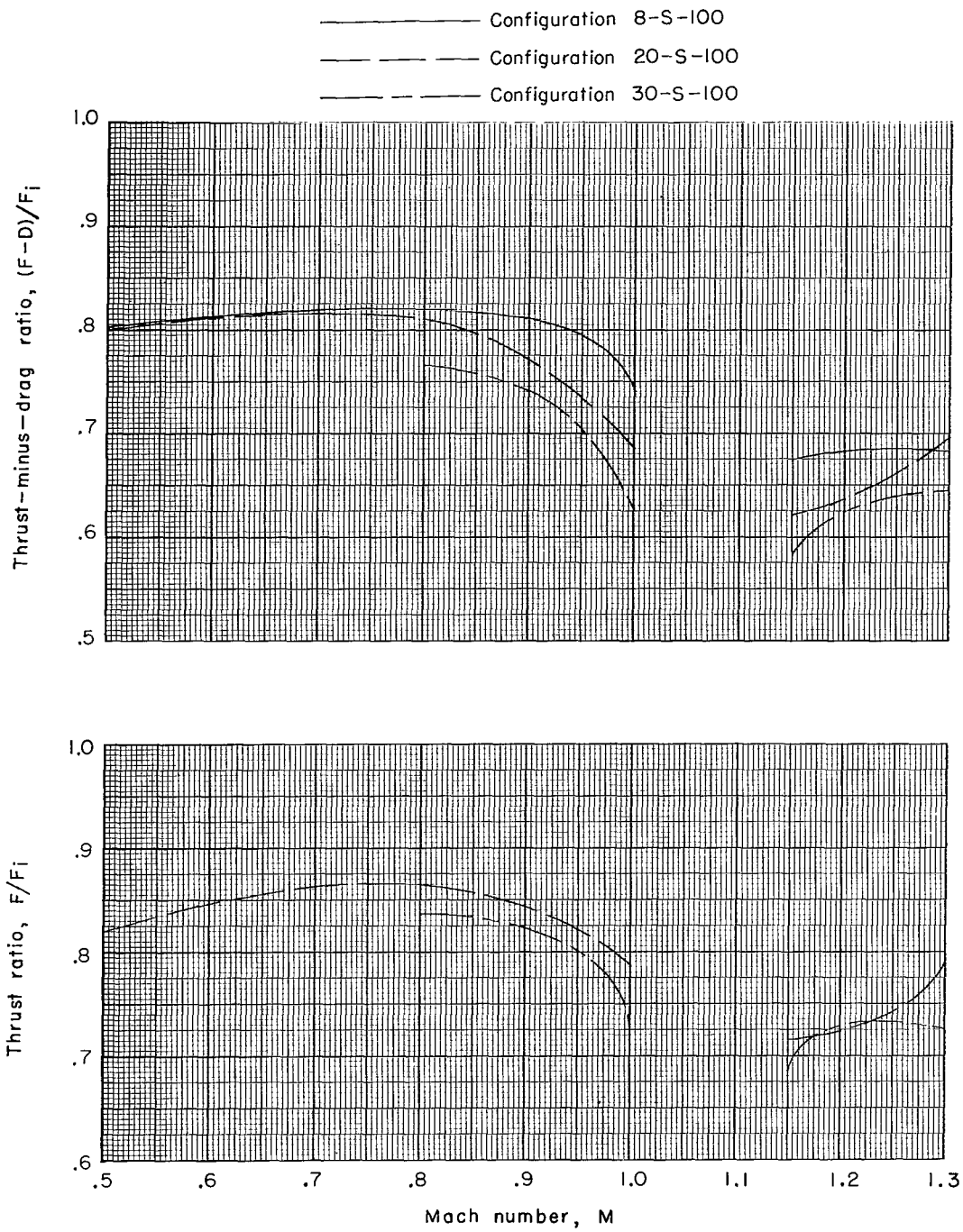

(c) Effect of boattail angle.

Figure 45.- Concluded.

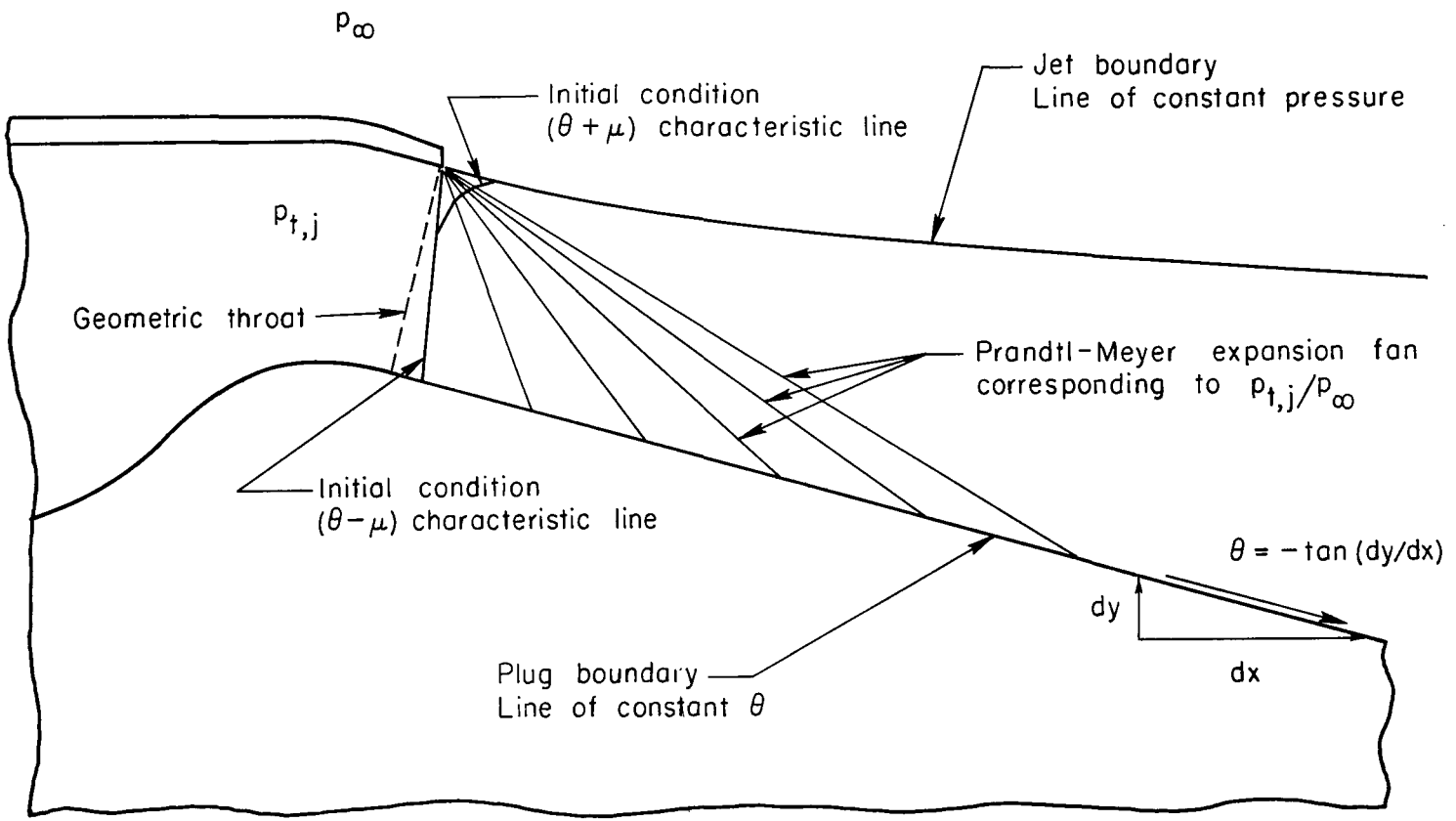

Figure 46.- Sketch showing boundary and initial conditions required for method-of-characteristics computer program.

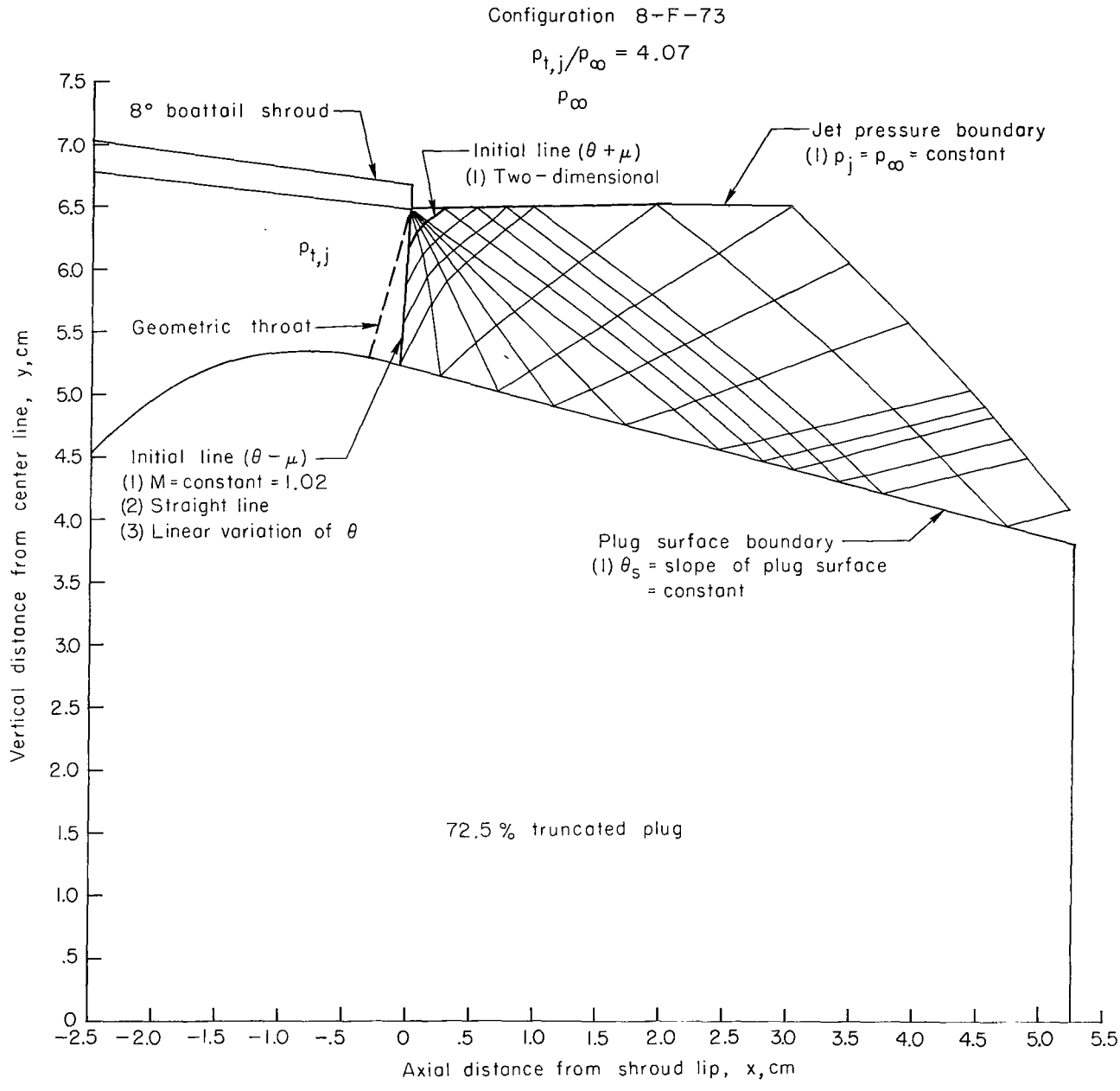

(a) Configuration 8-F-73.

Figure 47.- Characteristic net for cone plug nozzles.

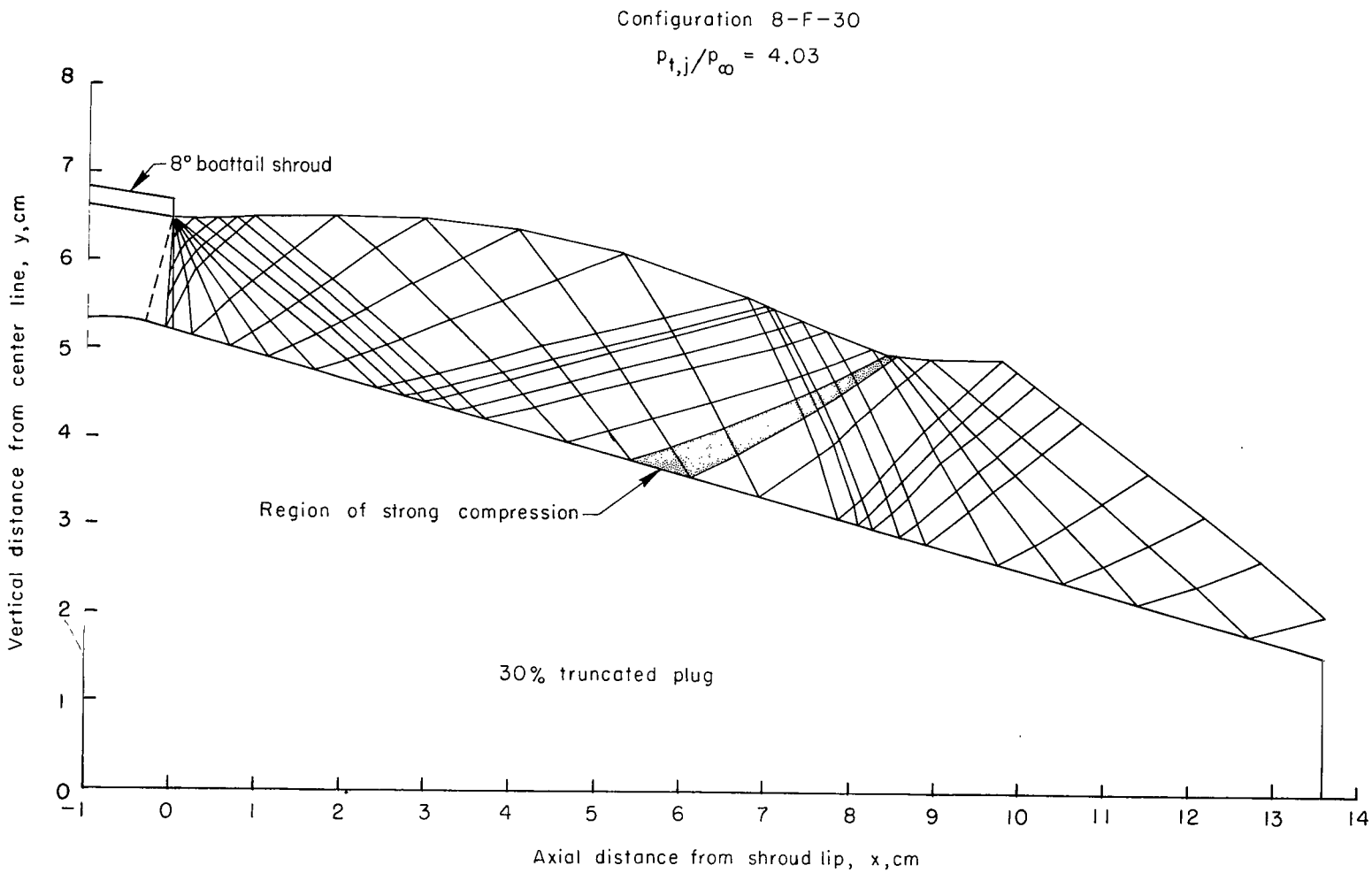

(b) Configuration 8-F-30.

Figure 47.- Concluded.

NATIONAL AERONAUTICS AND SPACE ADMINISTRATION
WASHINGTON, D. C. 20546

OFFICIAL BUSINESS

FIRST CLASS MAIL

POSTAGE AND FEES PAID
NATIONAL AERONAUTICS A
SPACE ADMINISTRATION

POSTMASTER: If Undeliverable (Section 1
Postal Manual) Do Not Ret

"The aeronautical and space activities of the United States shall be conducted so as to contribute . . . to the expansion of human knowledge of phenomena in the atmosphere and space. The Administration shall provide for the widest practicable and appropriate dissemination of information concerning its activities and the results thereof."

—NATIONAL AERONAUTICS AND SPACE ACT OF 1958

NASA SCIENTIFIC AND TECHNICAL PUBLICATIONS

TECHNICAL REPORTS: Scientific and technical information considered important, complete, and a lasting contribution to existing knowledge.

TECHNICAL NOTES: Information less broad in scope but nevertheless of importance as a contribution to existing knowledge.

TECHNICAL MEMORANDUMS: Information receiving limited distribution because of preliminary data, security classification, or other reasons.

CONTRACTOR REPORTS: Scientific and technical information generated under a NASA contract or grant and considered an important contribution to existing knowledge.

TECHNICAL TRANSLATIONS: Information published in a foreign language considered to merit NASA distribution in English.

SPECIAL PUBLICATIONS: Information derived from or of value to NASA activities. Publications include conference proceedings, monographs, data compilations, handbooks, sourcebooks, and special bibliographies.

TECHNOLOGY UTILIZATION PUBLICATIONS: Information on technology used by NASA that may be of particular interest in commercial and other non-aerospace applications. Publications include Tech Briefs, Technology Utilization Reports and Notes, and Technology Surveys.

Details on the availability of these publications may be obtained from:

SCIENTIFIC AND TECHNICAL INFORMATION DIVISION

NATIONAL AERONAUTICS AND SPACE ADMINISTRATION

Washington, D.C. 20546